Synthesis of Non-alternant Polyaromatic Hydrocarbon-containing Cycloparaphenylenes and Phenanthroline-containing Cycloparaphenylenes toward Mechanically Interlocked Polymers

by

Lan Chen

A dissertation accepted and approved in partial fulfillment of the

requirements for the degree of

Doctor of Philosophy

in Chemistry

Dissertation Committee:

Prof. Mike Haley, Chair

Prof. Ramesh Jasti, Advisor

Prof. Amanda Cook, Core Member

Prof. Richard Taylor, Institutional Representative

University of Oregon

Summer 2026

© 2026 Lan Chen

DISSERTATION ABSTRACT

Lan Chen

Doctor of Philosophy in Chemistry

Title: Synthesis of Non-alternant Polyaromatic Hydrocarbon-containing Cycloparaphenylenes and Phenanthroline-containing Cycloparaphenylenes toward Mechanically Interlocked Polymers

Cycloparaphenylene (CPPs), representing the shortest segments of armchair carbon nanotubes (CNTs), exhibit unique size-dependent photophysical properties and enhanced solubility in common organic solvents compared to their linear counterparts. While significant research has focused on developing the robust synthetic methodology to access CPP derivatives featuring various functional units, and on revealing how these components introduce strain and modulate photophysical behavior, the incorporation of non-alternant polycyclic aromatic hydrocarbons (PAHs) into the CPP backbone remains a largely uncharted area. It has been shown that integrating non-alternant PAH moiety into the CPP framework perturbs the electronic properties of the parent nanohoops and decreases their overall aromaticity. Inspired by this, one focus of this work is to expand the library of non-alternant PAH-containing CPPs. Specifically, Chapter II details the synthesis and photophysical investigation of azulene-embedded CPPs, while Chapter III shows the preliminary results on cyclopenta[*hi*]aceanthrylene (CPA)-embedded analogues.

Another research focus involves utilizing CPP derivatives as macrocyclic templates for the construction of π-conjugated, complex molecular architectures. Leveraging their radially π-conjugated structures and good solubility, we aim to construct fully π-conjugated, mechanically interlocked polymers and probe the electronic communication between the constituent components. The second half of this dissertation details efforts toward the synthesis of mechanically interlocked rotaxane and catenane monomers suitable for polymerization. Chapter IV discusses the synthesis of [2]rotaxane featuring Phen[*n*]CPPs (where $n = 5, 6$) and anthracene-terminated axle components, as well as initial studies into their polymerization capability. Chapter V presents the preliminary synthetic progress toward [2]catenane featuring 1,10-phenanthroline and alkyne-based functional handles.

ACKNOWLEDGMENTS

First and foremost, I would like to thank my supervisor, Professor Ramesh Jasti, for providing me with this incredible opportunity to carry out my doctoral studies in his lab and for his support and guidance during my time at UO. Your mentorship and unshakable belief in me mean a lot to me.

To the Haley lab, I would like to extend my gratitude to Prof. Haley, who kindly picked me up from the airport, treated me to my first meal in the USA, and has always offered help when needed as my thesis committee chair. I am also appreciative of my first rotation mentor, Dr. Gabrielle Warren, for allowing me to stay in her apartment for a week and providing guidance that extends far beyond research into life itself. I also would like to thank Dr. Nolan McNeill, Dr. Efrain Vidal, Dr. Bella Demachkie and Michael Miller for their help and support. Also thank you Megan and Nathan for the good time shared during the Haley/Jasti joint meetings.

To the Brozek lab, I would like to thank Dr. Brozek for giving me the opportunity to learn MOF chemistry and for pairing me with an amazing mentor, Dr. Checker Marshall, who taught me a lot during my rotation. I also would like to thank the rest of the Brozek lab members for making my rotation a good experience and Dr. Audrey Davenport for your guidance when I was taking a role in one of the organizations.

To the Jasti lab, I am grateful to all the talented colleagues who have taught me so much and bore with me when I was doing all kinds of silly things. I want to thank my amazing mentor Dr. James May for introducing me to the fascinating world of mechanically interlocked systems and for entrusting me with a project that I am thrilled to see come to certain fruition at the end of my doctoral studies. Your actions speak louder than your words and you are a true role model. Your passion toward chemistry and work efficiency has been a constant inspiration. Thank you to Dr. Tavis Price, our lab "dad," for helping me master new techniques and for always being a supportive presence for everyone in the group and people from other labs. To Dr. Julia Fehr, thank you for being a role model of both hard work and scientific artistry. To Dr. Tara Clayton, thank you for your friendship and our happy Saturday hangouts, you have a unique way of equilibrating between the realities of life and your own safe place, where you can contemplate with a profound depth of thought. To, Dr. Harrison Reid, thank you for being a great community builder and helping the lab. Your dedication to the marathon and your passion for polymer chemistry are

amazing. To Dr. Veronica Spaulding, thank you for being a cool, brave scientist whose perspectives have consistently helped me think beyond my own limitations and let me believe that I can dream big. Furthermore, I cannot thank my fellow group members enough, particularly Dr. Gabriella Bailey. It was not an easy journey for you, but your perseverance and resilience inspired me, and I know you will shine wherever you go! Thank you for your encouragement. I would like to thank Victor, who always holds a positive mindset despite all the challenges he has faced. Your genuine love toward chemistry is truly inspiring, and thank you for sharing some many cool ideas and being my late-night working bro. To Katy, you always have so many good ideas and execute fast! You will be an amazing chemist for sure. To Noah, the king of mechanically interlocked structures, your hardworking and the ability to bounce back from failures is really something that I look up to! To Josh, thank you for your encouragement and your contagious laughter. I know you will get some cool results very soon.

I would also like to thank my mentees for their trust. Although I was not always at my best while working with you, I hope you gained valuable skills and techniques during our time together. My gratitude extends to my undergraduate students, Ethan and Brandon, as well as my rotation students, Natalie and Ally. Also, I would like to thank Katelyn, Audrey, Laila, Lulu, Melvika, Sam, Robert, Tracee, Brenna, Dominic, Daphne and Kristina for their support! Your presence and belief in me helped me persevere and affirmed my decision to continue in doctoral study.

To the supporting staff at UO, I would like to thank Natalie and Dylan in the Sci store, Seth, Ben, Laurie, Laura and Jenny in the EHS, Carrissa, Christi, Helen, Janet, Zoe and Leah in the Chem office, and Becky, Wanda, Michael in the ISSS offices for their support.

I am forever grateful to my undergraduate PI, Prof. Rik Tykwinski, for welcoming me into your group and allowing me to participate in so many fascinating projects regarding acenes. Your support and belief in me remain a cornerstone of my academic path. I cannot achieve what I have without your support. I also like to thank my Physics and Chemistry teachers in high school and at UA for laying the foundations that allowed me my early wins and encouraged me to pursue a path in STEM.

I also want to thank my friends, Xinyue, Meng, Kate for their continuous support and Connor for your encouragement and advice for rotaxanes!!

Most importantly, I would like to thank my family. To my parents, thank you for your unwavering support and for giving me the opportunity to experience a life I could never have

imagined. To my husband, Henrik, thank you for loving me unconditionally and for your willingness to navigate every challenge with me and what comes in front of us. And thank you to my parents-in-law for all your support and help during the visa applications.

I would like to thank Dr. Cook and Dr. Taylor for being my committee member and seeing me grow during the past four years.

DEDICATION

This page is dedicated to all the scientists and medical professionals who have devoted their lives to the advancement of science and saving people. Thank you for your stubborn love of this field: it is your passion and work ethics that inspire young generations to pursue careers in STEM, to push the boundaries of science, technology and medicine, and to build a better world.

TABLE OF CONTENTS

Chapter Page

I. TOWARD CPP-BASED NON-ALTERNANT PAH-CONTAINING CPPS AND MECHANICALLY INTERLOCKED POLYMER AND 17

I.1. Non-alternant PAH embedded cycloparaphenylenes 17

I.2. Mechanically Interlocked Polyrotaxane and Polycatenanes 20

I.3. Bridge to Chapter I 25

II. SYNTHESIS OF AZULENE-EMBEDDED CYCLOPARAPHENYLENES WITH ANTI-KASHA BEHAVIOR 26

II.1. Introduction 26

II.2. Results and Discussion 28

II.3. Conclusions 34

II.4. Methods and Materials 34

II.4.1. Synthetic procedures 37

II.4.2. Single crystal X-ray diffraction information 44

II.4.3. Computational results of 1,3-Az[*n*]CPPs 50

II.5. Bridge to Chapter II 61

III. SYNTHESIS OF CYCLOPENTA[*HI*]ACEANTHRYLENE-CONTAINING CYCLOPARAPHENYLENES 62

III.1. Introduction 62

III.2. Results and Discussions 64

III.3. Conclusions 68

III.4. Methods and Materials 69

III.4.1. Synthetic procedures 70

III.4.2. Computational results of FMOs of 4,9-CPA[7]CPP 77

III.5. Bridge to chapter IV 78

IV. SYNTHESIS AND DESIGN OF [2]ROTAXANE FEATURING PHEN[*N*]CPP MACROCYCLE AND ANTHRACENE BASED THREAD 79
IV.1. Introduction 79
IV.2. Results and Discussion 89
IV.2.1. Method Design 89
IV.2.2. Synthesis of Phen[*n*]CPPs (*n* = 5–7) 91
IV.2.3. Synthesis of anthracene-based half-axle, free thread and [2]rotaxanes 93
IV.2.4. ^{1}H NMR spectrum, crystal structure and photophysical properties of Phen[*n*]CPPs 95
IV.2.5. ^{1}H NMR spectrum, crystal structure and photophysical properties of [2]rotaxanes 97
IV.2.6. Functionalization of the [2]rotaxane with fluorenyl derivatives 100
IV.3. Conclusions 103
IV.4. Methods and Materials 103
IV.4.1. Synthetic procedures 104
IV.5. Bridge to chapter V 113
V. SYNTHESIS AND DESIGN OF [2]CATENANE FEATURING 1,10-PHENANTHROLINE AND ALKYNE FUNCTIONAL HANDLE 114
V.1. Introduction 114
V.2. Results and Discussions 124
V.3. Conclusions 126
V.4. Methods and Materials 127
V.4.1. Synthetic Procedures 128
VI. CONCLUDING REMARKS 134
CITED REFERENCES 135

LIST OF FIGURES

Figure Page

Figure I.1. Selective examples of alternant and non-alternant PAH molecules that have been successfully incorporated into CPPs as reported in the literature. 17
Figure I.2. Photophysical properties of cycloparaphenylenes: CPPs share common absorption profiles, size-dependent emission, as well as high molar absorptivity and variable quantum yields. The photograph of [*n*]CPP solutions in vials was provided by Dr. Fehr. 18
Figure I.3. Selective examples of nonalternant systems embedded in the CPP framework. 19
Figure I.4. Selective examples polyrotaxane and polycatenanes (I.1–I.4). 21
Figure II.1. Resonance structures of azulene and its halochromic behavior upon protonation and deprotonation through a reversible process. 27
Figure II.2. A selection of previous CPP derivatives exhibiting anti-Kasha behavior (highlighted in blue), halochromic properties (highlighted in pink), both properties (displayed in a blue-pink gradient box) and [*n*]Cycloparaazulene (highlight in green, where *n* = 6, 8 and 10). 28
Figure II.3. Compilation of the ^{1}H NMR spectra of 1,3-Az[*n*]CPPs (*n* = 5, 7 and 11) acquired in CD_2Cl_2 30
Figure II.4. X-ray crystallographic analysis of 1,3-Az[*n*]CPPs (*n* = 5, 7 and 11), from left to right. The structure on the left side shows the size of the cavity in Å. The space-filling and capped stick models shown on the right side illustrate the crystal packing motif. Solvent molecules are omitted for clarity. 31
Figure II.5. UV-Vis absorption of 1,3-Az[*n*]CPPs (solid lines) and model compound II.7 (dotted line), and fluorescence spectra (dashed lines) in CH_2Cl_2 at room temperature. 32
Figure II.6. a. The calculated ground state FMOs of 1,3-Az[5]CPP (a, left side) and after protonation, $[1,3\text{-Az[5]CPP+H}]^+$ (a, right side). b. Corresponding orbitals involved in the calculated $S_5 \rightarrow S_0$ fluorescence emission of 1,3-Az[7]CPP (LUMO+2 → HOMO and LUMO → HOMO-2). 33
Figure II.7. Crystal structure of 1,3-Az[5]CPP: (a) 1,3-Az[5]CPP with solvent molecule inside; (b) top view. (c) side view. H atoms have been omitted for clarity. Thermal ellipsoids at the 50% probability level. (d) C-H···π interaction (distances are reported in Å). Disordered atoms in the cavity are shown with all resolved orientations. 44

Figure II.8. Crystal structure of 1,3-Az[7]CPP: (a) 1,3-Az[7]CPP with solvent molecule inside; (b) top view. (c) side view. H atoms have been omitted for clarity. Thermal ellipsoids at the 50% probability level. (d) C-H···π interaction (distances are reported in Å). 45
Figure II.9. Crystal structure of 1,3-Az[11]CPP: (a) 1,3-Az[11]CPP with solvent molecule inside; (b) top view. (c) side view. H atoms have been omitted for clarity. Thermal ellipsoids at the 50% probability level. (d) C-H···π interaction (distances are reported in Å). 45
Figure II.10. Molar extinction coefficient measurements of 1,3-Az[*n*]CPPs and model compound II.7. II.7 (P0), 1,3-Az[5]CPP (P1), 1,3-Az[7]CPP (P2), 1,3-Az[11]CPP (P3). 46
Figure II.11. pH-responsiveness experiment of 1,3-Az[5]CPP conducted using excess *d*-TFA in CD_2Cl_2. A detailed analysis of the signal H_4–H_8 were not attempted but the assignment for H_2 is certain. 47
Figure II.12. pH-responsiveness experiment of 1,3-Az[7]CPP conducted using excess *d*-TFA in CD_2Cl_2. A detailed analysis of the signal H_4–H_8 were not attempted but the assignment for H_2 is certain. 47
Figure II.13. pH-responsiveness experiment of 1,3-Az[11]CPP conducted using excess *d*-TFA in DCM (left: P3, right: *d*-TFA added) 48
Figure II.14. TD-DFT calculated UV-Vis absorption spectra of (a) 1,3-Az[5]CPP, (b) 1,3-Az[7]CPP, (c) 1,3-Az[11]CPP, and (d) 1,3-Az[9]CPP. 48
Figure II.15. TD-DFT calculated fluorescence spectra of (a) 1,3-Az[5]CPP, (b) 1,3-Az[7]CPP, (c) 1,3-Az[11]CPP. 49
Figure II.16. Computed energy gaps (HOMO, LUMO, LUMO+1) of 1,3-Az[*n*]CPP (*n* = 5, 7 and 11) and 1,3-Az[9]CPP (blue trend) and protonated species (red trend). 49
Figure II.17. HRMS (EI^+-TOF, AccuTOF) chart of 1,3-Az[5]CPP and its calculated isotopic distribution (calcd. for $C_{40}H_{26}$; $[M]^+$). 59
Figure II.18. HRMS (EI^+-TOF) chart of 1,3-Az[7]CPP and its calculated isotopic distribution (calcd. for $C_{52}H_{34}$; $[M]^+$). 60
Figure II.19. HRMS (MALDI-TOF) chart of 1,3-Az[11]CPP and its calculated isotopic distribution (calcd. for $C_{76}H_{50}$; $[M]^+$). 61
Figure III.1. (a) Cyclopenta[*hi*]aceanthrylene (CPA) is a subsegment of C_{70}. (b) The resonance structure of CPA. Upon accepting two electrons, the resulting dianion is fully aromatic. 62

Figure III.2. The synthetic evolution of aceanthrylene derivative III.2 and CPA derivatives (III.5, III.7– III.9). 63
Figure III.3. (a) Selective examples of CPA-based structures demonstrating the tunability of the CPA core upon appending different functional groups, highlighting their applications in materials and polymer applications. (b) Resonance structures illustrating the diradical character of CPA. 64
Figure III.4 UV-Vis spectra of 4,9-CPA[7]CPP & III.29 in CH_2Cl_2 and the literature reported compound III.30 (The UV-Vis figure is plotted by Brandon). 67
Figure III.5. (a) Synthesis schemes of 2,7-CPA[7]CPP. (b) ^1H NMR spectra of the starting materials and the crude reaction mixture. The gradient lines track the chemical shift changes of the characteristic peaks on the CPA unit before and after the macrocyclization. 68
Figure III.6. Proposed synthetic strategy for the [3]rotaxane with a CPA-containing thread. 69
Figure IV.1. (a) Host-guest chemistry of C_{60} and [10]CPP. (b) Concave-convex π-π template method toward Fullerene-CPP rotaxane developed by the von Delius group. 80
Figure IV.2. (a) Host-guest interaction between [6]CPP-12OMe and adiponitrile (b) [2]rotaxane synthesis featuring [6]CPP-12OMe macrocycle and bulky adamantyl stoppers. 81
Figure IV.3. (a) Covalent azo-group template for the synthesis of improbable rotaxanes with all benzene scaffolds. (b) Chemical stimuli experiment of aniline derived rotaxane IV.13. 82
Figure IV.4. Synthesis of [2]rotaxanes via AT-CC and AT-CuAAC methods through *meta*-aza[6] and *meta*-aza[8]CPP 84
Figure IV.5. (a) Rotaxane IV.17 shows a turn-on fluorescence property upon treatment with TBAF. (b) Rotaxane fluorescent sensor toward RSS, H_2S, which exists at SH^- at physiological condition. 85
Figure IV.6. (a) Enhanced solution-phase stability of a polyyne [3]rotaxane insulated by *meta*-aza[6]CPP compared to phenanthroline-based macrocycle IV.20. 86
Figure IV.7. Synthesis of [3]rotaxane IV.28 via AT-CC utilizing diaza[8]macrocycle IV.24. 87
Figure IV.8. Evaluation of the nitrogen-atom positioning on the macrocycles during the AT-CC reaction, highlighting the requirement of multiple heteroatom coordination sites. 88
Figure IV.9. Near-quantitative yield from the AT-CuAAC synthesis using the prearomatized macrocycle IV.31 with butyl protecting groups. 89

Figure IV.10. Selected failed attempts toward [2]rotaxane formation using macrocycle IV.24 and *meta*-aza[6]CPP using the AT-CuAAC synthesis. 90
Figure IV.11. Overview of the synthetic library of Phen[*n*]CPP-based rotaxanes and their potential for downstream cross-coupling applications toward conjugated polymers. 91
Figure IV.12. (a) Synthesis of Phen[7]CPP-$ZnCl_2$ complex. (b) Photophysical property measured in CH_2Cl_2 (absorbance traces are shown as solid lines and emission trace as dashed line: light yellow: Phen[7]CPP, orange line: Phen[7]CPP-$ZnCl_2$). 93
Figure IV.13. Synthesis of [2]rotaxanes (IV.52–IV.55) via AT-CC coupling reaction. 94
Figure IV.14. (a) ^{1}H NMR compilation of Phen[*n*]CPP (*n* = 5–8). (b) dihedral angles measured from the single-crystal X-ray structure. 96
Figure IV.15. Single-crystal structure of Phen[*n*]CPPs. Cavity dimensions and intermolecular C-H···π and N···C-H interaction distances are reported in Å. The table summarizes the number of the favored intermolecular contacts and the specific crystallization conditions for each macrocycle. 97
Figure IV.16. UV-Vis absorption and fluorescence data of Phen[*n*]CPP measured in CH_2Cl_2 solutions. 97
Figure IV.17. (a) ^{1}H NMR spectra compilation of [2]rotaxane IV.52 and its individual components measured in $CDCl_3$. Upon formation of the interlocked structure, H_A and H_B undergo an upfield shift to $H_{A'}$ and $H_{B'}$, attributed to the shielding effect of the Phen[5]CPP. (b) Single crystal structure of IV.52 shown in space-filling model. (c) The intramolecular C-H···π interaction between the axle component and macrocycle. (d) The intermolecular C-H···π and π-π interaction between [2]rotaxane. 98
Figure IV.18. (a) Qualitative UV-Vis absorption (solid lines) and fluorescence (dashed lines) of the dichloromethane solution of [2]rotaxane IV.52, free thread IV.51 and Phen[5]CPP. The fluorescence spectra of Phen[5]CPP were measured upon excitation at 315 nm, and the spectra of IV.51 and IV.52 were measured upon excitation at 320 nm. (b) The proposed fluorescence mechanism with asterisk (*) represents the component in the excited state. 99
Figure IV.19. Representative anthracene-based derivatives (IV.56–IV.61) used in display technology. 100

Figure IV.20. (a) Synthetic route of fluorenyl with terminal alkyne IV.64 and the subsequent Sonogashira cross coupling reaction with free thread IV.51 to yield the model compound IV.65, and with the rotaxane IV.52 to afford the monomer analog IV.66. (b) ^{1}H NMR spectra comparison confirms the targeted fluorenyl-functionalized [2]rotaxane IV.66 was obtained. .. 102
Figure IV.21. UV–Vis and fluorescence spectra of [2]rotaxane IV.52, fluorenyl-functionalized free thread IV.65 and that of [2]rotaxane IV.66 measured in CH_2Cl_2. The product shows bright blue emission under UV irradiation or direct sunlight..... 103
Figure V.1. The first reported identification of [2]catenanes consists of CPPs..... 114
Figure V.2. [2]catenane consists of two Mobiüs conjugated nanohoops. 115
Figure V.3. Synthesis of [2]catenanes and trefoil knot using covalent template method via spirosilane motif..... 116
Figure V.4. Synthesis of [2]catenane consists of two *meta*-[9]CPPs using covalent template method via azo linker..... 117
Figure V.5. Synthesis of C60/[10]CPP-based catenanes using Pd-nanocapsule as a mask to enhance regioselectivity..... 118
Figure V.6. Synthesis of a [3]catenane V.34 via a ring-in-ring strategy using a ternary template to promote intramolecular CuAAC..... 119
Figure V.7. Synthetic scheme of CPP-bipyridine V.38 via AT method via Ni-mediated homocoupling condition. 120
Figure V.8. [2]rotaxane synthesized via the AT-CC method for the construction of fully π-conjugated [2]catenanes (V.42(a-b), V.45) and [3]catenane (V.49)..... 121
Figure V.9. [2]rotaxane synthesized via AT-AAC for the construction of fully π-conjugated [2]catenanes (V.52 and V.56). 122
Figure V.10. Literature examples of CPP-based catenanes capable of post-synthetic modification. 123

LIST OF SCHEMES

Scheme Page

Scheme II.1. Synthesis of 1,3-Az[*n*]CPPs (where *n* = 5, 7 and 11). 29
Scheme III.1. Synthetic schemes for 2,7-CPA[*n*]CPP (*n* = 6,11 and 12). 65
Scheme III.2. Synthetic schemes of 4,9-CPA[7]CPP and the planar model compound III.29. ... 67
Scheme IV.1. Synthetic scheme to Phen[*n*]CPPs (where *n* = 5–7). 92
Scheme IV.2. Synthetic approach to anthracene-based half-axle components and the free thread IV.51 for comparison. 94
Scheme V.1. Synthetic scheme toward a [2]catenane (V.76) featuring a phenanthroline-containing macrocycle and tri*iso*propylsilyl-protected alkyne handle 125
Scheme V.2. Proposed synthetic pathway toward a [2]catenane (V.80) featuring a phenanthroline-containing macrocycle and azulene-appended alkyne handle. 127

LIST OF TABLES

Table Page

Table II.1. Tilt angle of the plane of azulene and plane defined by the two adjacent phenylene carbons (blue dots). Tilt angle for the neutral compounds is measured from their crystal structures, while those for the protonated structures are measured from optimized geometries. Reported dihedral angles represent average values. 34
Table II.2. Major electronic transitions of 1,3-Az[5]CPP calculated by TD-DFT method 50
Table II.3. Major electronic transitions of 1,3-Az[7]CPP calculated by TD-DFT method 51
Table II.4. Major electronic transitions of 1,3-Az[11]CPP calculated by TD-DFT method 52
Table II.5. Major electronic transitions of 1,3-Az[9]CPP calculated by TD-DFT method 53
Table II.6. Major electronic transitions (emission) of 1,3-Az[5]CPP calculated by TD-DFT method 54
Table II.7. Major electronic transitions (emission) of 1,3-Az[7]CPP calculated by TD-DFT method 55
Table II.8. Major electronic transitions (emission) of 1,3-Az[11]CPP calculated by TD-DFT method 56
Table II.9. FMOs of neutral compounds, 1,3-Az[*n*]CPPs, where *n* = 5,7,9 and 11 57
Table II.10. FMOs of protonated 1,3-Az[n]CPPs, where *n* = 5,7,9 and 11. 58
Table III.1. Major electronic transitions (absorption) of 4,9-CPA[7]CPP calculated by TD-DFT method 77
Table III.2. Major electronic transitions (absorption) of 4,9-CPA[7]CPP calculated by TD-DFT method 78

CHAPTER I TOWARD CPP-BASED NON-ALTERNANT PAH-CONTAINING CPPS AND MECHANICALLY INTERLOCKED POLYMER AND

I.1. Non-alternant PAH embedded cycloparaphenylenes

Non-alternant π-systems are a distinct class of conjugated organic molecules characterized by the presence of rings with an odd number of atoms, most commonly five- and seven-membered rings. As illustrated in Figure I.1, a primary method to distinguish between alternant and non-alternant systems involves the alternating labeling of carbon atoms as 'A' or 'B' throughout the π-system. If any adjacent carbons share the same label, the system is non-alternant. Taking azulene as an example, the carbons on the C-C bond shared between the five- and seven-membered rings are labeled as 'B' at both termini, indicating its non-alternant nature. This structural feature accounts for the asymmetric orbital distribution of non-alternant systems compared to their alternant counterparts, frequently resulting in an intrinsic dipole moment, a narrower HOMO-LUMO gap and a degree of antiaromaticity that distinguishes them from their alternant counterparts and endows them with redox-active electronic properties.[1] To date, the integration of non-alternant polycyclic aromatic hydrocarbons (PAHs) into the cycloparaphenylene (CPP) backbone remains relatively uncharted compared to their alternant counterparts.

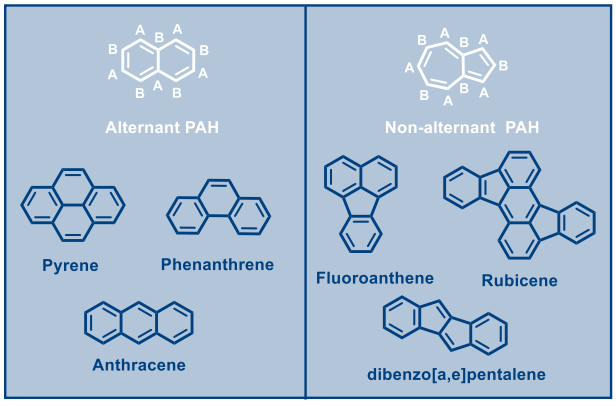


Figure I.1. Selective examples of alternant and non-alternant PAH molecules that have been successfully incorporated into CPPs as reported in the literature.

Since 2008, extensive studies on cycloparaphenylenes (CPPs) have demonstrated their unique optoelectronic properties, characterized by tunable emission, high extinction coefficients, and size-dependent quantum yields (Figure I.2).[2,3] These attributes render them promising candidates for electronic applications. Furthermore, bottom-up synthetic approaches provide a

versatile platform for incorporating various functional units into the CPP backbone in place of the phenylene, yielding derivatives with unique electronic properties distinct from parent [*n*]CPPs. Consequently, an emergent area of research in this field, as shown in Figure I.3, involves the substitution of phenylene units with non-alternant PAHs, which possess unique characteristics such as chirality, stimuli-responsive properties, while providing a platform to modulate the structural and electronic properties of the parent nanohoop system.

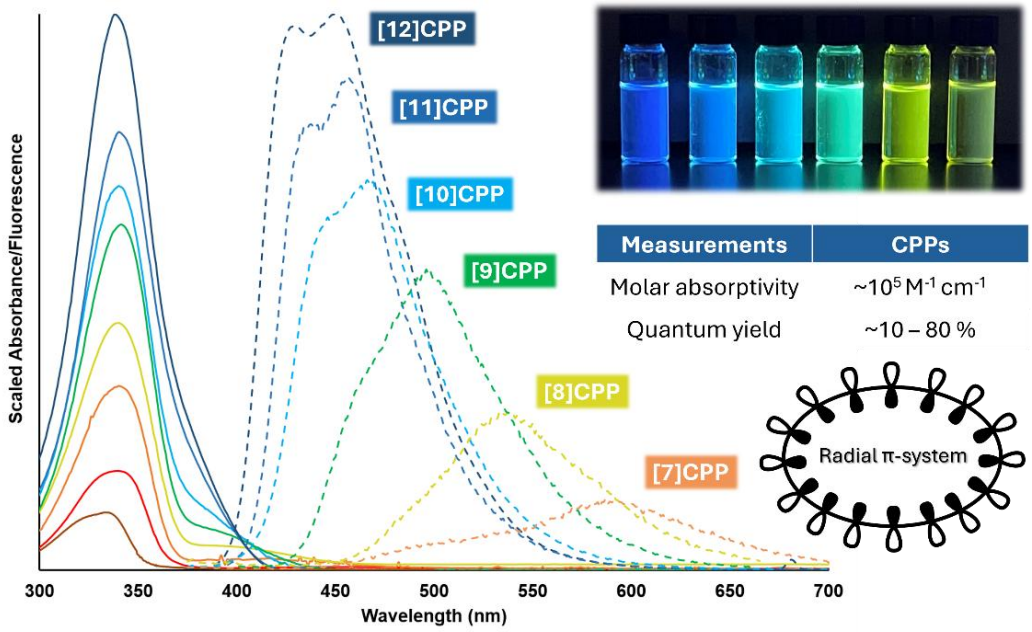


Figure I.2. Photophysical properties of cycloparaphenylenes: CPPs share common absorption profiles, size-dependent emission, as well as high molar absorptivity and variable quantum yields. The photograph of [*n*]CPP solutions in vials was provided by Dr. Fehr.

In 2020, the Itami group synthesized a methylene-bridged [6]CPP from a pillar[6]arene, reporting the first example of a non-alternant aromatic belt.[4] Structurally, this compound can be viewed as a [6]CPP derivative in which each phenylene unit is tethered by a methylene bridge. The presence of these bridges reduces the torsion angle between the phenylene units, which enhances π-conjugation and results in a narrower HOMO-LUMO gap compared to the parent [6]CPP. This work tackled the synthetic challenges and provided a detailed analysis of its properties in comparison to [*n*]CPPs, as well as its linear analog, the ladder-type oligophenylenes. In the same year, the Du group successfully incorporated a fluoranthene unit into a CPP backbone to yield a fluoreanthene-[9]CPP.[5] This molecular crown acts as a structural mimic for a fullerene C_{240} fragment and serves as a good effective supramolecular host to encapsulate C_{60}. Another

example is the incorporation of dibenzo[*a,e*]pentalene (DBP) into the CPP backbone. The Esser group showed that by integrating the DBP into the system, its antiaromaticity character decreases.[6] Furthermore, the substituents on the five-membered ring provide a handle to tune the energy gap.

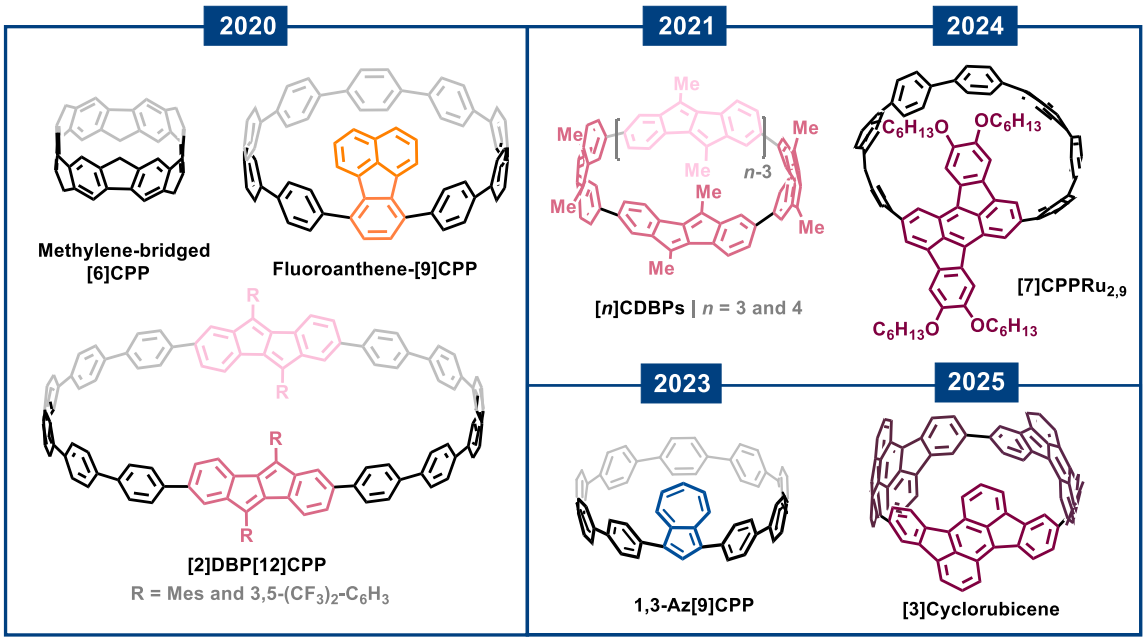


Figure I.3. Selective examples of nonalternant systems embedded in the CPP framework.

In 2021, the same group further advanced in this field and reported the first example of two macrocycles consisting of DBP unit, the trimer - **[3]CDBP** and the tetramer - **[4]CDBP**, synthesized via a platinum-mediated macrocyclization. These antiaromatic macrocycles exhibit an elevated HOMO energy level compared to the parent DBP, which contributes significantly to the narrowed HOMO-LUMO gap.[7] Additionally, the supramolecular interactions of the tetramer with C_{60} and C_{70} were investigated, suggesting its potential as a good supramolecular host.

In 2023, the Jiang group reported the first example of an azulene containing CPP, **1,3-Az[9]CPP**.[8] This study demonstrated that the characteristic anti-Kasha properties of the azulene unit are retained, alongside halochromic behavior upon changes in pH. Additionally, the macrocycle was also shown to act as a supramolecular host for C_{60} and C_{70}.

In 2024, the Du group reported their success in integrating rubicene unit into the nanohoop framework, **[7]CPPRu$_{2,9}$**.[9] Upon bending the planar rubicene units, the resulting macrocycles are obtained as a pair of enantiomers that was successfully separated via chiral HPLC. This works suggests the potential of chiral nanohoops for applications in chiral catalysis. Subsequently, in

2025, the Mastalerz group synthesized **[3]Cyclorubiene**,[10] a macrocycle composed solely of rubicene unit. Utilizing a Ni-mediated Yamamoto coupling, the Mastalerz successfully constructed the macrocyclic scaffold. Notably, the synthesis proceeds with high retention of chirality from the early chiral building blocks, enabling the isolation of the product in quantities sufficient for chiroptical studies.

Learning from these representative examples, it is evident that non-alternant cyclic systems possess unique properties from the parent CPPs, including narrower HOMO-LUMO gaps, the ability to host fullerenes with good binding constants, and unique chiroptical properties that could be applicable for chiral catalysis. Furthermore, the established synthetic methods, ranging from the direct incorporation of non-alternant PAH into the nanohoop backbone, to Pt- and Ni-mediate homocoupling methods, giving us the essential toolkit to expand the library of non-alternant PAH-containing CPPs. In Chapter II and III, research efforts in synthesizing 1,3-Az[*n*]CPPs and 2,7-CPA[*n*]CPP as 4,9-CPA[*n*]CPP were discussed, alongside the study of their photophysical properties.

I.2. Mechanically Interlocked Polyrotaxane and Polycatenanes

Mechanically interlocked molecules (MIMs) have garnered significant interest within the scientific community, particularly following the 2016 Nobel Prize in Chemistry[11–13], which highlighted their fundamental role in the design and construction of molecular machines. Unlike traditional polymers that rely exclusively on covalent connectivity, MIMs are defined by mechanical bonds, wherein molecular components are held together through spatial entanglement rather than direct chemical links. This unique feature enables their application in the development of molecular motors[14] and targeted drug delivery systems.[15,16] Furthermore, incorporation of MIMs into polymer frameworks (MIPs) allows for the enhancement of structural dynamics, providing materials with good toughness and high durality, owing to the inherent mobility of the mechanical bond.[17–19]

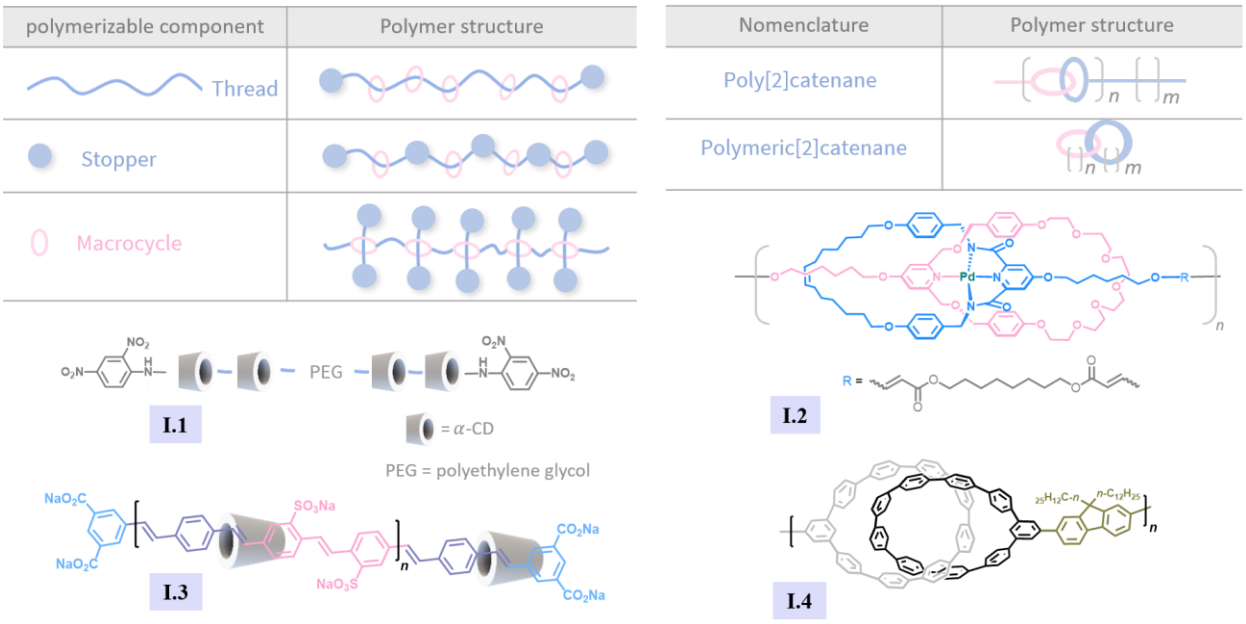


Figure I.4. Selective examples polyrotaxane and polycatenanes (**I.1–I.4**).

As illustrated in Figure I.4, the polymerization of polyrotaxanes and polycatenanes can be achieved through distinct synthetic strategies. For polyrotaxanes, polymerization typically proceeds either through functional handles incorporated into the axle component or via reactive sites on the macrocyclic moiety. In the case of polycatenanes, the framework is generally constructed by either utilizing pre-existing polymeric rings or by employing [2]catenane monomers equipped with functional handles positioned on each ring to facilitate the polymerization. Cyclodextrin (CD)-based polyrotaxanes are the most extensively studied class of mechanically interlocked polymers. This is due to its good water solubility, the ease of functionalizing their hydroxy groups and their structural stability. To take **I.1** as an example, a α,ω-bis-amine-terminated poly(ethylene glycol) (BA-PEG) chain was mixed with α-CD, leading to the formation of a polypseudorotaxane intermediate driven by favorable hydrophobic interactions between the aliphatic PEG backbone and the hydrophobic cavity of the α-CD. Subsequent encapping of the terminal amino groups with dinitrofluorobenzene (DNFB) via S_NAr prevents the dissociation of α-CD, affording the targeted polyrotaxane **I.1**.[20]

In the case of polycatenane, oligo[2]catenane **I.2** serves a prominent example.[21,22] The catenane monomer was synthesized via a Pd(II) templated reaction to position the primary macrocycle (pink ring) and the precursor to the second macrocycle with two terminal alkenes

together (blue ring), followed by ring closing metathesis (RCM) to furnish the second macrocycle. Subsequent removal of the hydroxyl protecting group enabled final polymerization via hydroxy-yne click polymerization to afford **I.2**. A key feature of this system is its superior mechanical performance. Under applied force, the material dissipates energy through a sequential mechanism. The process begins with the dissociation of the dative Pd-N bond, followed by the circumrotation of one macrocycle through the other, and finally, the elongation of the [2]catenane itself.

Another significant advantage of encapsulating conjugated systems within an interlocked motif is the attenuation of π-π stacking, which is often responsible for the poor solubility of highly conjugated systems. By effectively isolating the conjugated backbones using macrocycles, the synthesis of extended conjugated systems becomes plausible. This approach is exemplified by the oligo[2]catenane as shown in Figure I.4 (compound **I.4**), which consists of two ***meta*[9]CPP** units. This target was synthesized from a [2]catenane featuring two Ar–Bpin functional groups on both *meta*-linked phenylene units, which were reacted with fluorenyl derivatives under the Suzuki cross coupling conditions to yield the first reported fully π-conjugated oligo[2]catenane.[23]

In recent years, the use of CPPs as scaffolds for developing conjugated polymers has garnered increased attention. Firstly, these polymers possess extended π-systems that mimic segments of carbon nanotubes (CNTs), serving as potential templates for CNT growth. Secondly, by integrating these macrocycles into linear polymer systems, new electronic states can be accessed, holding promise for future electronic applications. Since 2020, CPP-derived polymers have been developed by different research groups,[24] pioneered by the Jasti and the Du groups. In 2020, the Jasti lab, in collaboration with the Tovar group, utilized Sonogashira cross-coupling conditions between dialkynylated [6]CPP/[8]CPP and tetrasubstituted benzene or thiophene with two reaction sites to successfully access CPP-based polymers, such as **P[8]Ph** as shown in Figure I.5. These polymers, which contain both linear and radial π systems, exhibit new electronic states that differ from the discrete photophysical behavior of their individual components.[25] In 2021, the Jasti group utilized a different polymerization method, known as the ring-opening metathesis polymerization (ROMP), to obtain homopolymers, such as **poly(nb[8]CPP)** (Figure I.5).[26] Additionally, statistical and block copolymers were synthesized by reacting different **nb[*n*]CPPs** (where $n = 9, 10$) using distinct polymerization methods. Interesting photophysical properties were observed in the statistical polymer **poly(nb[8]CPP-*stat*-[10]CPP**), which were attributed to the proximity of macrocycles of different sizes, where the smaller **nb[8]CPP** units act as an energy

acceptor and the larger **nb[10]CPP** unit serve as the donor. This work highlights the significance of controlled polymerization and its ability to access a variety of CPP-based copolymers with tunable emission profiles. In the same year, the Du group synthesized **P[10]CPP** via Ni-mediated homocoupling from a dichlorinated CPP-based monomer.[27] The architecture of this polymer can be described as a poly(para-phenylene) (PPP) backbone interconnected by [10]CPP units. Similar to the photophysical properties observed for the **poly(nb[*n*]CPP)s**, the emission profile of the polymer is nearly identical to that of the monomer, despite the lower quantum yield likely arising from aggregation. In 2022, the Jasti group further modified the **P[8]Ph** system by decorating the two terminal alkynes onto the [8]CPP scaffold with a separation of three phenylene units, resulting in a disjoint π-conjugated system termed **Pdis[8]Ph**.[28] This structural modification disrupts the conjugation of the linear backbone, which promotes electronic communication between the linear and radial π-systems. The experimental and computational data support this hypothesis, showing that the absorption profile differs significantly from that of the first-generation CPP-based linear polymers reported in 2020. This work further expands the scope of CPP-based conjugated polymers by varying the substitution pattern of the linkages between the adjacent CPP units.

In addition to the achievements established by the Jasti and Du groups independently, in 2023, the Esser group showcased that a dibromo-DBP-CPP can undergo Suzuki-Miyaura polycondensation with three electronically distinct bisboronic esters featuring an electron-accepting dithienyldiketo(pyrrolopyrrol), an electron-neutral fluorene, and an electron-donating carbazole units. This approach yielded the corresponding copolymers (**I.5**–**I.7**).[29] Interestingly, both computational and experimental photophysical data imply that the radial π-conjugation dominates in the latter two copolymers. Furthermore, the antiaromatic nature of the DBP unit imparts ambipolar electronic character to these polymers, allowing for facile reduction and oxidation compared to the pure hydrocarbon-based CPP polymers. Notably, polymer **I.7** outperforms its polymer analogue lacking the nanohoop, highlighting the potential of CPP-based polymers for the future applications in charge storage materials.

In 2026, the Jasti and Du groups independently reported their concurrent success in synthesizing polymers featuring the PPV-CPP motif. Specifically, the Jasti lab utilized the base-activated Gilch polymerization between 2,5-bis(chloromethyl)[8]CPP and MEH-PPV to access conjugated polymers ([8]CPP-PPV) with high molar mass.[30] The Du group employed the Stille coupling method on a 2,5-dichloro[8]CPP to obtain **[8]CPPV** and further demonstrated its solution

processability, great electrochemical stability and high capacity retention as an anode material in lithium-ion batteries, compared to the conventional carbonaceous materials.[31]

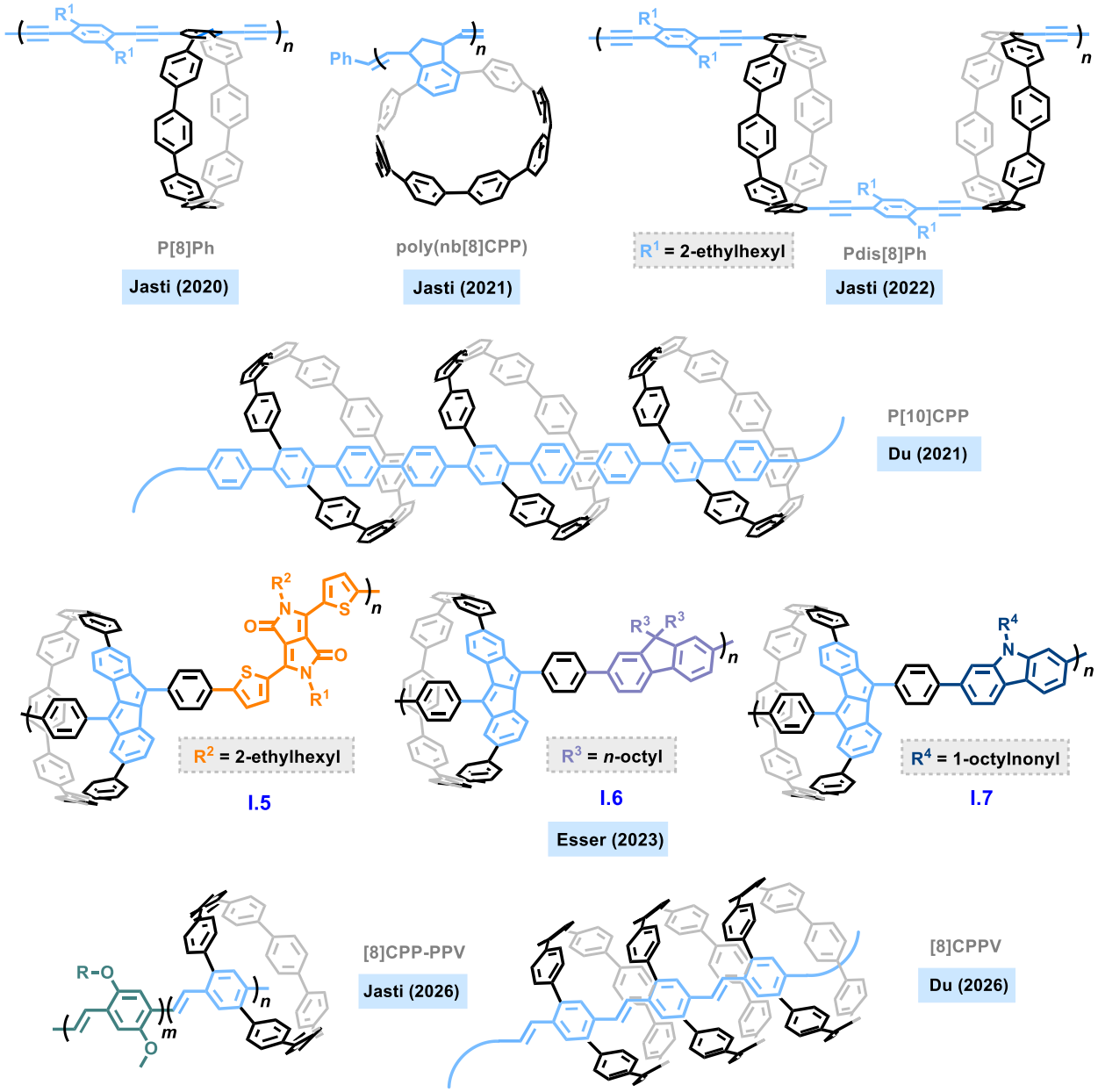


Figure I.5. Representative CPP-based polymers reported in the literature.

Inspired by these developments, we worked to leverage CPP derivatives as macrocyclic components to construct [2]rotaxane monomers featuring anthracene-based axles. The initial success in attaining these monomers, as well as the preliminary tests toward extending the rotaxane via the axle components, is discussed in Chapter IV. Furthermore, Chapter V shows our initial efforts toward the synthesis of phenanthroline-based [2]catenane monomer equipped with

functional handles on the macrocyclic units. Through these studies, we aim to advance the field of fully π-conjugated, CPP-based mechanically interlocked polymers (MIPs), focusing both on the development of the synthetic approaches and on probing the spatial electronic communication within the interlocked systems.

I.3. Bridge to Chapter I

Chapter I provides a brief overview of recent advancements in non-alternant PAH-containing CPPs, as well as the potential of CPP-based macrocycles in the construction of π-conjugated mechanically interlocked polymers (MIPs). Chapter II focuses on the synthesis of 1,3-Az[n]CPPs and the investigation of their photophysical properties.

CHAPTER II SYNTHESIS OF AZULENE-EMBEDDED CYCLOPARAPHENYLENES WITH ANTI-KASHA BEHAVIOR

This chapter outlines a manuscript submitted to *Organic Letters* that is currently under revision. Chen, L.; Lakanen, N. M.; Wagner, A. E.; Salpino, V. M.; Zakharov, L. N.; Jasti, R. Azulene-Embedded Cycloparaphenylenes: Synthesis and Size-Dependent Anti-Kasha Photophysics. *ChemRxiv* **2026**, *2026* (0525). https://doi.org/10.26434/chemrxiv.15003879/v1. This manuscript was written by me with editorial assistance from Professor Ramesh Jasti. The synthetic work was performed equally by Natalie, Allyson and Lan. The photophysical analysis was performed by Lan, and the computation work was performed by Lan under the guidance of Victor. The single-crystal X-ray diffraction data collection and analysis were performed by Dr. Lev N. Zakharov.

II.1. Introduction

Significant efforts have focused on incorporating alternant polycyclic aromatic hydrocarbons (PAHs), such as naphthalene,[32–36] anthracene,[37–41] and pyrene,[42–44] into cycloparaphenylene (CPP) backbones to extend their π-systems toward carbon nanotube-like architectures with tunable electronic properties. In contrast, incorporation of non-alternant PAHs into CPPs remains rare,[14–19] largely due to synthetic challenges and their reduced aromatic stabilization. Nevertheless, these systems are increasingly attractive, as their inherently uneven electron distribution can introduce donor–acceptor character and enable unusual photophysical behavior, including anti-Kasha emission.

Azulene, a dark blue compound composed of a fused seven-membered and five-membered ring, is a distinctive example of a non-alternant π-system. It possesses a net dipole-moment (1.08 D), with the five-membered ring being electron-rich and the seven-membered ring electron-poor (Figure II.1). Unlike its alternant isomer naphthalene, which exhibits evenly distributed molecular orbital coefficients, azulene displays a non-centrosymmetric orbital distribution in which the S_0 and S_2 states have similar electron density while the S_1 state is nearly inverted. This unusual electronic structure results in a large S_2–S_1 energy gap that suppresses internal conversion, enabling direct $S_2 \rightarrow S_0$ emission, known as anti-Kasha behavior.[45–49]

In addition, azulene exhibits pronounced position-dependent reactivity, with odd-numbered positions being relatively electron-rich and even-numbered positions comparatively

electron-poor. Because of that, protonation readily occurs at the 1- or 3-position, driven by formation of a stabilized tropylium-like aromatic substructure.[50] This process narrows the S_2–S_1 energy gap and often leads to turn-on fluorescence accompanied by a distinct color change. Such pH-dependent behavior, known as halochromism, renders azulene an attractive scaffold for responsive materials,[51–53] and has motivated its incorporation into electrochromic systems,[54–56] anion sensors,[57] and nonlinear optical materials.[58,59]

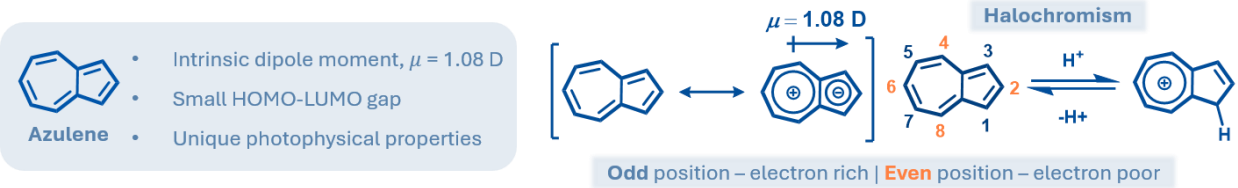


Figure II.1. Resonance structures of azulene and its halochromic behavior upon protonation and deprotonation through a reversible process.

To date, only a limited number of CPP derivatives exhibiting anti-Kasha emission[8,60–63] or pH-responsive behavior[8,64,65] have been reported (Figure II.2), with **1,3-Az[9]CPP** uniquely demonstrating both properties. In 2023, Jiang *et al*. reported the first azulene-containing all-carbon CPP, establishing the feasibility of incorporating azulene at the 1,3-position and highlighting its anti-Kasha emission and halochromic response.[8] These unique properties are originated from the innate electronic structure of azulene. It is well-established that substituents at the 2,6-positions predominantly influence the LUMO, whereas substitution at the 1,3-positions primarily perturbs the HOMO and LUMO+1 levels. This difference in the electronic populations of frontier molecular orbitals offers a platform to engineer the bandgap. Building on this, in 2026, the Dumele and Liu group independently reported the synthesis of [6]Cycloparaazulene (**[6]CPA**),[66] and **[8]CPA** /**[10]CPA** with ethyl substituents on 1-position for each azulene,[67] respectively (Figure II.2, highlighted in green). Notably, these macrocycles exhibited remarkably low-lying LUMO levels, establishing a new class of carbon nanorings with very small HOMO-LUMO gaps.

With all these important pioneering works, however, a systematic investigation of how 1,3-azulene incorporation influences size-dependent structural and photophysical properties of the nanohoops remains lacking. Herein, we report the synthesis of a homologous series of **1,3-Az[*n*]CPPs** (*n* = 5, 7, and 11). Together with the previously reported [9]membered analogue, this

series provides a complete odd-membered set, enabling a comprehensive evaluation of how a non-alternant azulene unit perturbs the electronic structure and optical properties of cyclic π-systems.

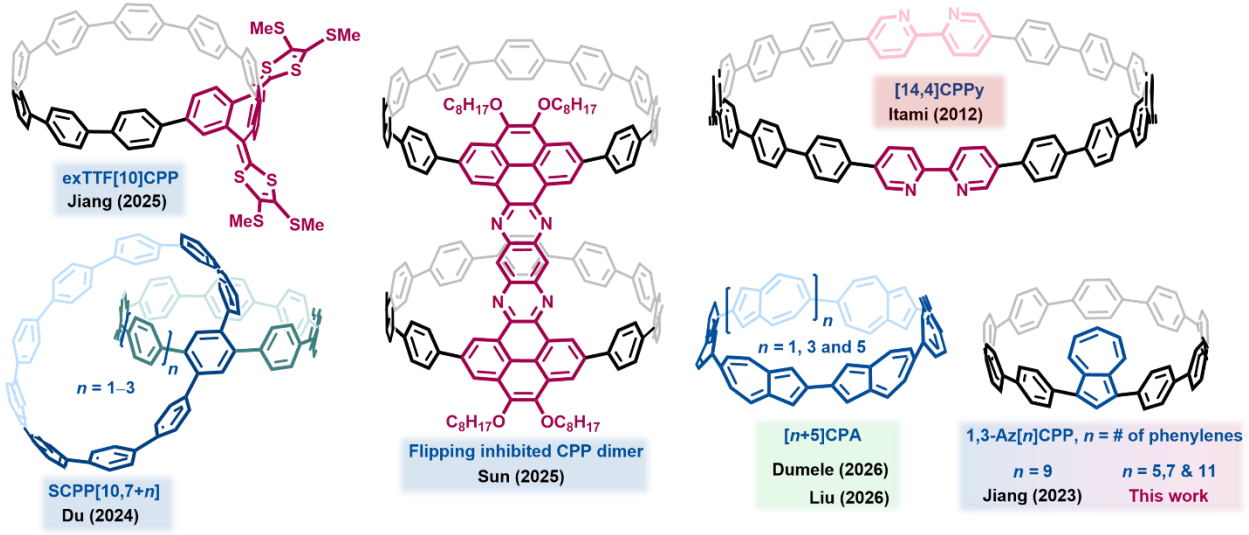


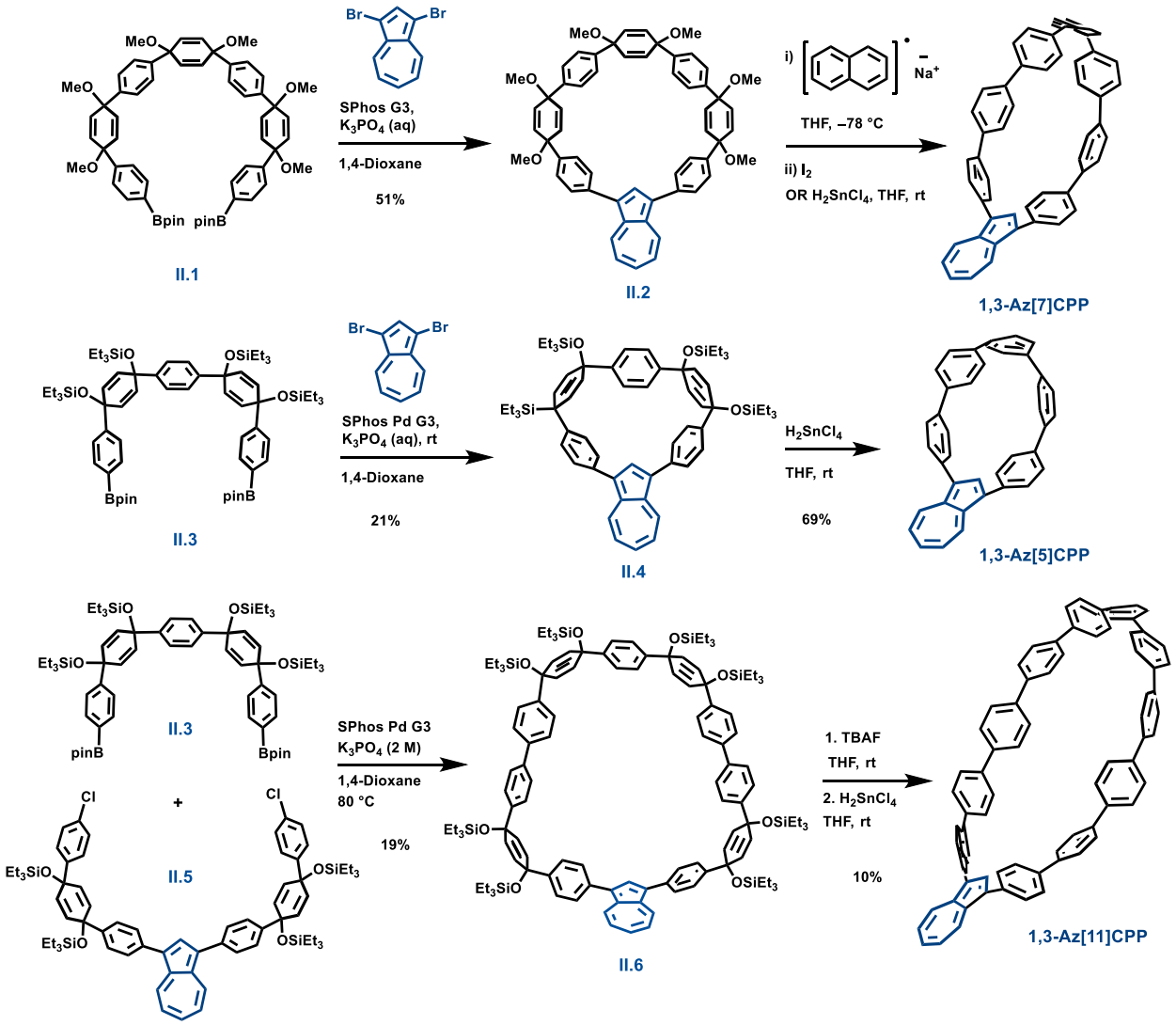
Figure II.2. A selection of previous CPP derivatives exhibiting anti-Kasha behavior (highlighted in blue), halochromic properties (highlighted in pink), both properties (displayed in a blue-pink gradient box) and [*n*]Cycloparaazulene (highlight in green, where *n* = 6, 8 and 10).

II.2. Results and Discussion

The synthetic procedures for **1,3-Az[*n*]CPPs** (*n* = 5, 7, and 11) are outlined in Scheme II.1. 1,3-Dibromoazulene was synthesized according to literature procedures via bromination of azulene in up to 87% yield.[68] Inspired by the work of Jiang *et al*. on 1,3-Az[9]CPP, a methoxy-protected macrocyclic precursor (**II.1**) was initially selected and prepared according to literature methods.[69] With both coupling partners in hand, a Suzuki cross-coupling reaction was performed to afford the macrocycle **II.2** in 65% yield. Subsequent reductive aromatization of this macrocycle with H_2SnCl_4 afforded **1,3-Az[7]CPP** in 25% yield as a green crystalline solid. The same macrocycle could also be aromatized under stronger reducing conditions using sodium naphthalenide, albeit in lower yield (11%).

However, due to the poor solubility of methoxy-protected **II.2** and the appreciable formation of rearranged side products during the aromatization step, macrocycles bearing triethylsilyl ether protecting groups were employed for the other ring sizes. **II.4** was synthesized via Suzuki cross-coupling between 1,3-Dibromoazulene and **II.3** under dilute conditions in 21% yield. To access **II.6**, macrocyclization under dilute conditions between **II.3** and **II.5**

furnished **II.6** in 22% yield. Finally, desilylation of **II.6** was carried out, and the resulting deprotected macrocycle, together with **II.4**, were separately subjected to Sn-mediated aromatization to afford **1,3-Az[5]CPP** as a dark yellow solid in 69% yield and **1,3-Az[11]CPP** as a deep blue solid in 10% yield.



Scheme II.1. Synthesis of **1,3-Az[*n*]CPPs** (where *n* = 5, 7 and 11).

The structures of **1,3-Az[*n*]CPPs** (where *n* = 5, 7 and 11) were characterized by ^{1}H NMR spectroscopy (Figure II.3), ^{13}C NMR spectroscopy, and mass spectrometry. As the ring size increases, the protons on the azulene unit become progressively deshielded, consistent with trends previously observed for ***meta*[*n*]CPPs**.[69] Notably, the proton at C(2) exhibits the largest chemical shift difference across the series, with a downfield shift of 0.73 ppm from the smallest to the largest

ring. These systematic chemical shift changes suggest that ring size significantly influences the electronic environment of the embedded azulene unit.

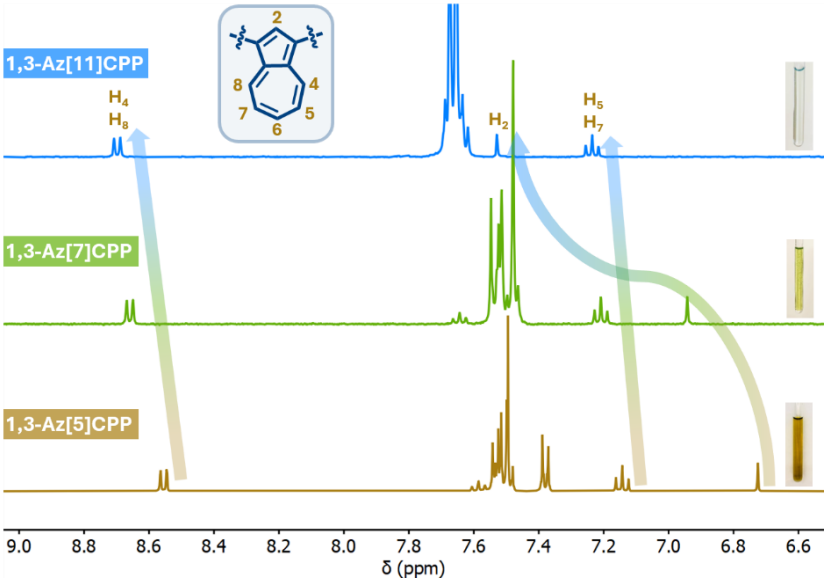


Figure II.3. Compilation of the ^{1}H NMR spectra of **1,3-Az[*n*]CPPs** (*n* = 5, 7 and 11) acquired in CD_2Cl_2.

Suitable single crystals for X-ray diffraction analysis were obtained for all three nanohoops via vapor diffusion of methanol into dichloromethane solution for **1,3-Az[5]CPP**, and hexanes into dichloromethane solutions for **1,3-Az[7]CPP** and **1,3-Az[11]CPP** at room temperature (Figure II.4). Structural analysis revealed distinct solid-state packing motifs across the series. **1,3-Az[5]CPP** adopts a herringbone packing arrangement stabilized primarily by C–H···π interactions between the phenylene C–H groups and the azulene π-system of neighboring molecules (Figure II.7). Similarly, **1,3-Az[7]CPP** forms a sandwich-like herringbone dimer packing motif featuring stronger C–H···π interactions (Figure II.8). In contrast, the largest nanohoop, **1,3-Az[11]CPP**, assembles into a slipped columnar stacking arrangement (Figure II.9). These results demonstrate that ring size significantly influences the intermolecular organization of azulene-containing CPPs in the solid state.

To investigate the electronic interplay between the azulene unit and the cycloparaphenylene backbone, the photophysical properties of **1,3-Az[*n*]CPPs** were studied using UV–Vis absorption and fluorescence spectroscopy, complemented by theoretical calculations. Time-dependent density functional theory (TD-DFT) calculations were performed using several functionals (CAM-B3LYP, ωB97XD, and PBE1PBE) at the 6-31G(d,p) level, with dichloromethane modeled using the

polarizable continuum model (PCM). Among these, the PBE1PBE functional predicted absorption energies in closest agreement with the experimental UV-Vis spectra and was therefore selected for further analysis (Figure II.14).

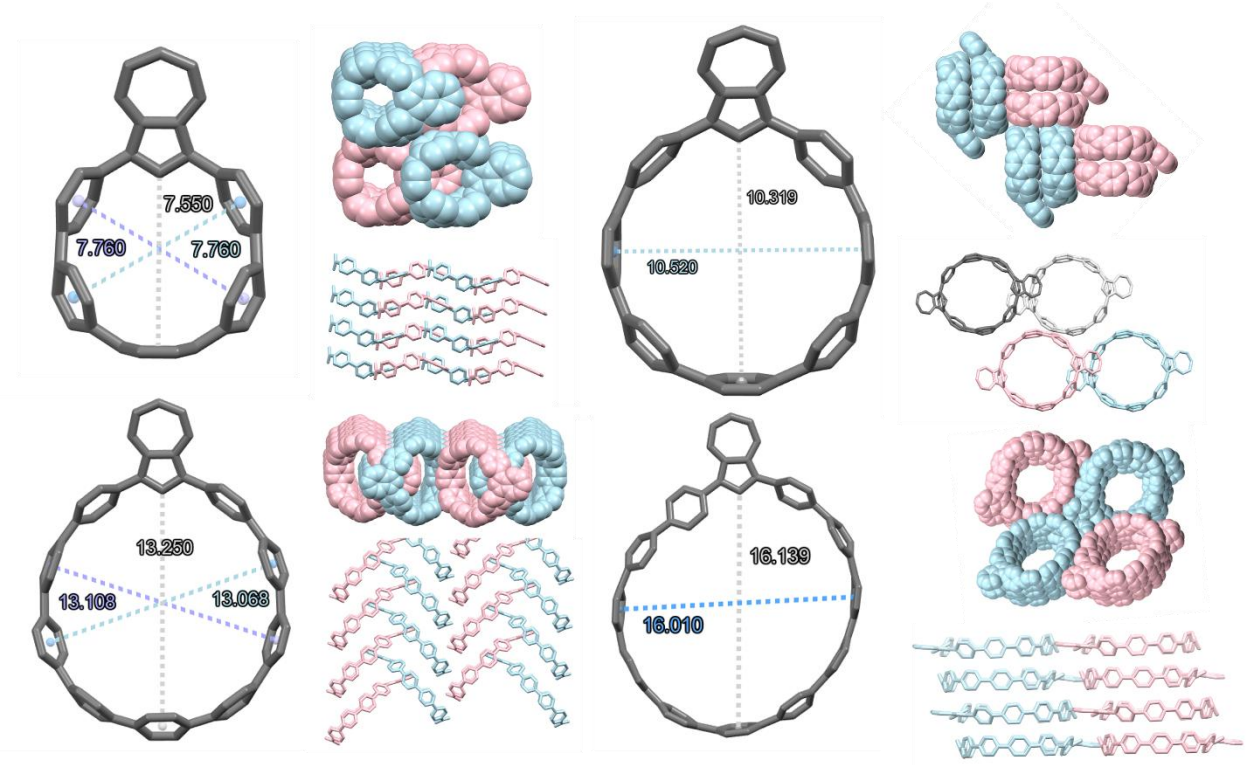


Figure II.4. X-ray crystallographic analysis of **1,3-Az[*n*]CPPs** (*n* = 5, 7 and 11), from left to right. The structure on the left side shows the size of the cavity in Å. The space-filling and capped stick models shown on the right side illustrate the crystal packing motif. Solvent molecules are omitted for clarity.

All three compounds exhibit a common absorption maximum near 330 nm (Figure II.5), similar to those observed for [*n*]CPPs and slightly red-shifted relative to ***meta*[*n*]CPPs**.[69] TD-DFT calculations suggest that this transition arises primarily from excitation to higher-energy excited states (S_n, $n \geq 7$, Table II.2–II.4). The lowest-energy apparent absorption feature, observed as a peak or shoulder in the case of **1,3-Az[11]CPP**, was assigned to the $S_0 \rightarrow S_2$ or $S_0 \rightarrow S_3$ transitions, with a major contribution from HOMO → LUMO+2 transition, consistent with the photophysical profile previously reported for 1,3-Az[9]CPP. A very weak broad band at 460–640 nm was assigned to the $S_0 \rightarrow S_1$ transition (HOMO → LUMO, $f < 0.006$). Compared to the planar model compound (**II.7**), **1,3-Az[*n*]CPPs** exhibit approximately twofold larger extinction coefficients,

suggesting enhanced transition intensity when the azulene unit is incorporated within a cyclic π-system.

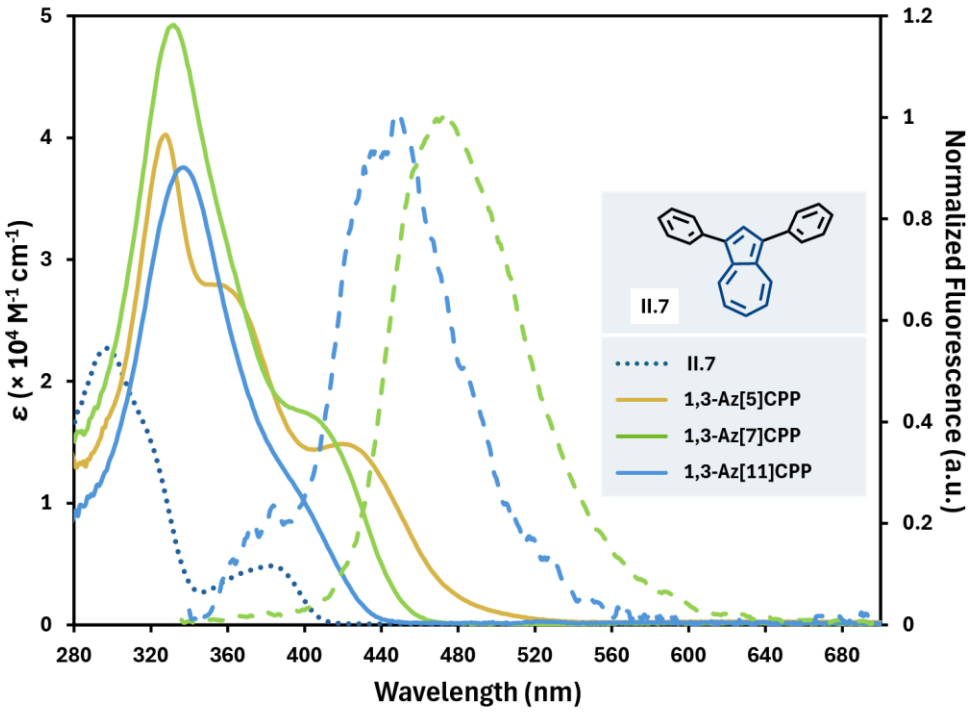


Figure II.5. UV-Vis absorption of **1,3-Az[*n*]CPPs** (solid lines) and model compound **II.7** (dotted line), and fluorescence spectra (dashed lines) in CH_2Cl_2 at room temperature.

In contrast to *meta*[6]CPP, **1,3-Az[5]CPP** was found to be non-emissive, while **1,3-Az[7]CPP** and **1,3-Az[11]CPP** display size-dependent emission behavior in which the smaller ring exhibits more bathochromically shifted fluorescence (Figure II.6). TD-DFT calculations indicate that the $S_1 \rightarrow S_0$ transition is forbidden ($f \leq 0.0004$) for all three sizes. Instead, intense transition from $S_5 \rightarrow S_0$ (**1,3-Az[7]CPP**: $\lambda_{em,\ calc} = 433$ nm, $f = 0.7707$; **1,3-Az[11]CPP**: $\lambda_{em,\ calc} = 423$ nm, $f = 0.6621$, Figures II.14–II.15) correlates to the experimental observed emission, supporting an anti-Kasha emission behavior. Overall, this series exhibits substantially weaker fluorescence than *meta*[*n*]CPPs, which may arise from the lesser orbital delocalization of the emissive excited state.

Next, we investigated the ring-size dependence of the halochromic behavior, **1,3-Az[7]CPP** were treated with *d*-TFA, resulting in the formation of dark red solutions (Figure II.11–Figure II.13). To better understand the electronic changes accompanying protonation and the origin of the pronounced bathochromic shift, computational studies were carried out on both the neutral

and protonated species. Ground-state calculations indicate that protonation leads to overall orbital stabilization through formation of a tropylium-like aromatic cation within the azulene moiety (Figure II.6a). As a result, the energies of the LUMO and LUMO+1 are lowered, together with a reduction in the HOMO–LUMO gap (Figure II.16), accounting for the observed, red-shifted absorption and deep-red coloration upon protonation.

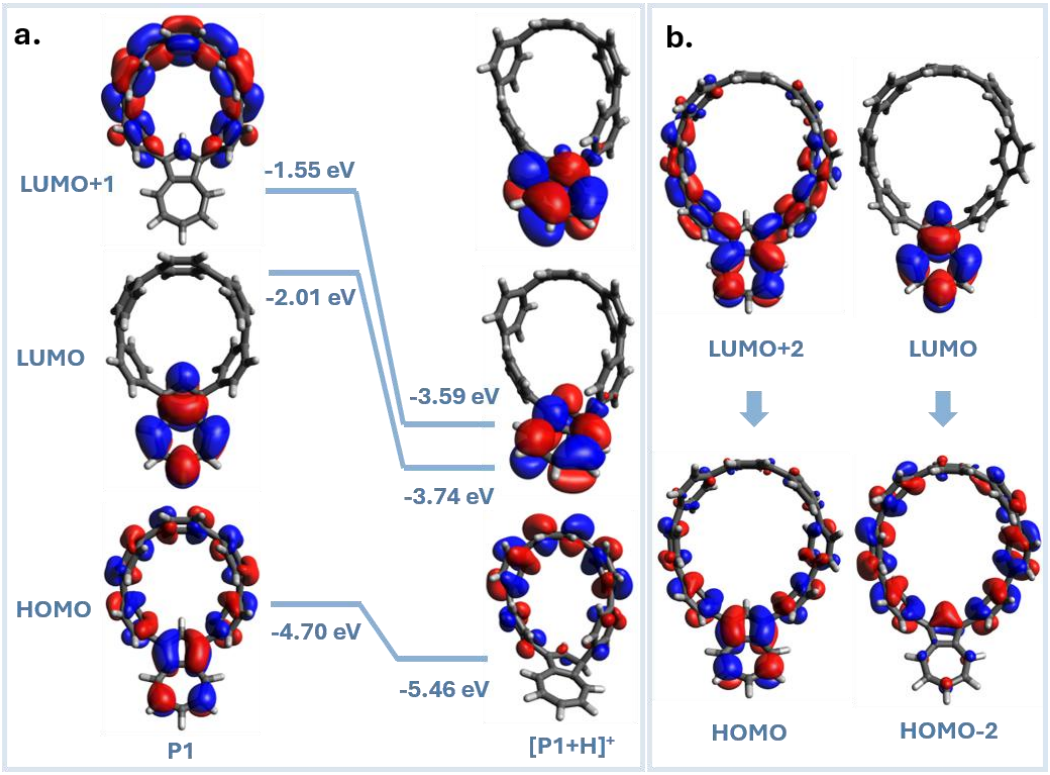
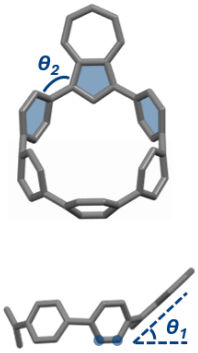


Figure II.6. a. The calculated ground state FMOs of 1,3-Az[5]CPP (a, left side) and after protonation, $[1,3\text{-Az[5]CPP+H}]^+$ (a, right side). b. Corresponding orbitals involved in the calculated $S_5 \rightarrow S_0$ fluorescence emission of 1,3-Az[7]CPP (LUMO+2 → HOMO and LUMO → HOMO-2).

Notably, protonation also induces intramolecular charge-transfer character (Figure II.6a, right). In the protonated species, the electron density in the LUMO remains localized primarily on the protonated azulene unit, which acts as an acceptor, whereas the electron density in the HOMO shifts predominantly over the CPP backbone, which acts as a donor. This interpretation is further supported by the increased tilt angle observed upon protonation (Table II.1), which favors enhanced electronic communication between the azulene moiety and the CPP backbone. Together, these results suggest that protonation transforms the system into a donor–acceptor architecture.

Table II.1. Tilt angle of the plane of azulene and plane defined by the two adjacent phenylene carbons (blue dots). Tilt angle for the neutral compounds is measured from their crystal structures, while those for the protonated structures are measured from optimized geometries. Reported dihedral angles represent average values.

	Neutral		Protonated
Compound	**Tilt angle, θ_1 (°)**	**Dihedral Angle, θ_2 (°)**	**Tilt angle, θ_1 (°)**
1,3-Az[5]CPP	40.34	38.36	58.83
1,3-Az[7]CPP	37.59	38.41	58.58
1,3-Az[9]CPP	23.90	45.87	57.23
1,3-Az[11]CPP	9.73	48.79	54.31



II.3. Conclusions

In summary, this work reports the synthesis of a series of **1,3-Az[*n*]CPPs** (*n* = 5, 7, and 11) and examines the influence of 1,3-azulene incorporation on the structural and photophysical properties of cycloparaphenylenes through spectroscopic, crystallographic, and computational studies. Members of this series exhibit both halochromic behavior and size-dependent anti-Kasha emission characteristics. Structural analysis further revealed distinct solid-state packing motifs across the series, with the largest nanohoop, **1,3-Az[11]CPP**, adopting a slipped columnar arrangement. Computational studies indicate that protonation induces donor–acceptor character through charge-transfer interactions between the azulene unit and CPP backbone. Together, these results demonstrate how incorporation of a non-alternant aromatic unit can modulate the electronic structure and optical properties of cyclic π-systems.

II.4. Methods and Materials

All reagents were purchased from commercial sources and used as received from commercial suppliers. 1,3-Dibromoazulene, **2**[69], **4**[69], **5**[70], and SPhos Pd G3[71] were prepared according to the literature methods and the obtained ^{1}H NMR spectra are consistent with literature. All reactions were carried out under a nitrogen atmosphere unless explicitly stated otherwise. Anhydrous tetrahydrofuran (THF), 1,4-Dioxane and Dichloromethane (DCM) were taken from solvent purification system (SPS) without further purification. For the stationary phase used in

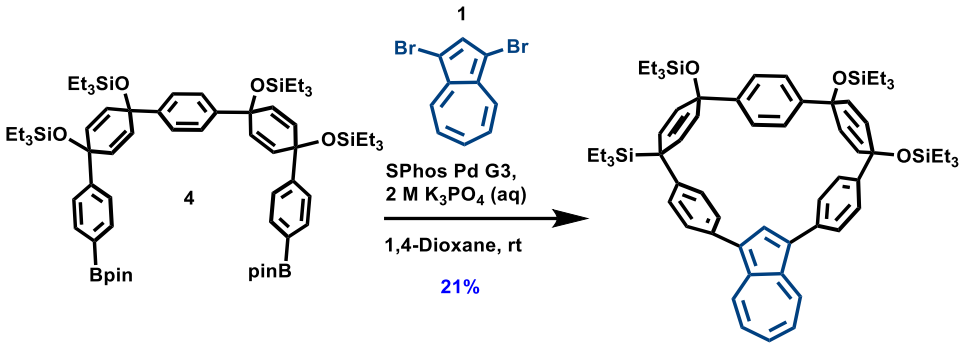
column chromatography, silica gel is purchased from ZEOCHEM® (ZEOprep Silicagel 60 HYD / 40-63 μm) and Alumina is purchased from Sorbtech (Alumina, Basic, Act. II-III). Proton (^{1}H) and carbon ($^{13}C\{^{1}H\}$) NMR spectra were recorded on the Bruker Avance-III HD 500 MHz NMR Spectrometer. $CDCl_3$ used for NMR experiment is 99.8% deuterated with 0.05% v/v tetramethylsilane (TMS). Chemical shifts were given in ppm relative to residue protons ($CHCl_3$: 7.26, s for ^{1}H, 77.16 for ^{13}C; CH_2Cl_2: 5.32, t for ^{1}H, 53.56 for ^{13}C). The abbreviations of s, d, t, q and m represent the multiplicities of singlet, doublet, triplet, quartet and multiplet, respectively. Mass spectrometric data were acquired by JMS-T2000GC AccuTOF™ GC-Alpha (EI), Waters Synapt G2-Si ESI/LC-MS (ESI) and Bruker Daltonics UltrafleXtreme MALDI TOFTOF (MALDI). UV-vis and fluorescence spectra were acquired in SPS-grade DCM using a 1 cm borosilicate cuvette on an Agilent Cary 60 UV-Vis and a HORIBA Jobin Yvon FluoroMax-4 spectrofluorometer, respectively.

The density functional theory (DFT) calculations were performed with the Gaussian 09 program (Revision E. 01)[72]. The ground state geometries of neutral species **1,3-Az[*n*]CPP** (*n* = 5,7 and 11) were optimized at B3LYP/6-31g(d,p) level of theory. For the protonated counterparts, the B3LYP-D3BJ/6-31g(d,p) level of theory was used[8], incorporating the polarizable continuum model (PCM) to account for the stabilization of the charged system. Time-dependent (TD)-DFT calculations were carried out for the first 12 excited states at PBE1PBE/6-31g(d,p) level of theory with the correction of PCM to consider the solvent effect of dichloromethane. Vibrational frequencies were calculated to ensure all optimized structures were true minima. Theoretical UV-Vis absorption spectra were generated using the GaussSum software package.

Suitable single crystals for X-ray diffraction analysis were obtained for all three nanohoops via layering methanol onto dichloromethane solutions of **1,3-Az[5]CPP**, and hexanes onto dichloromethane solutions of **1,3-Az[7]CPP** and **1,3-Az[11]CPP** at room temperature. Diffraction intensities for **1,3-Az[5]CPP** was collected at 170 K, and **1,3-Az[7]CPP** & **1,3-Az[11]CPP** were collected at 173 K on Bruker Apex2 diffractometer using CuKa radiation, 1.54178 Å. Space groups were determined based on systematic absences. Absorption correction was applied by SADABS[73]. Structures were solved by direct methods and Fourier techniques and refined on F2 using full matrix least-squares procedures. All non-H atoms were refined with anisotropic thermal parameters. H atoms in the structure were refined in calculated positions in a rigid group model. X-ray diffraction from crystals of **1,3-Az[7]CPP** & **1,3-Az[11]CPP** at high angles was very weak.

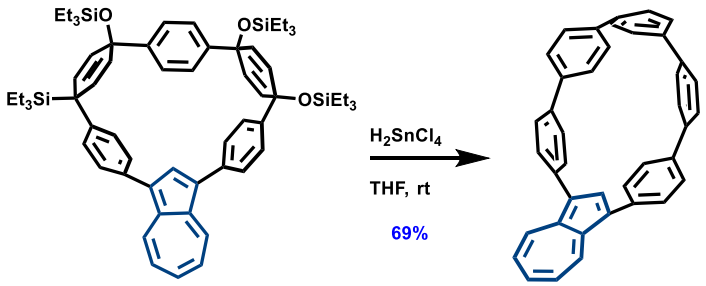
The crystals of **1,3-Az[7]CPP** are formed as very thin plates. In the crystal structure of **1,3-Az[11]CPP** there are a lot of highly disordered solvent molecules CH_2Cl_2. Even by using a strong X-ray micro focus source it was possible to collect diffraction data only up to $2\theta_{max} = 99.62°$ (**1,3-Az[7]CPP**) and 80.41° (**1,3-Az[11]CPP**). As a result the value of R_{int} is high: 0.2082 (**1,3-Az[7]CPP**) and 0.1979 (**1,3-Az[11]CPP**). However, the data collected provide appropriate number of measured reflections per refined parameters, 3842 per 510 (**1,3-Az[7]CPP**) and 8358 per 1447 (**1,3-Az[11]CPP**). The main molecules in **1,3-Az[11]CPP** form columns in the crystal structure. Solvent molecules, CH_2Cl_2 fill out a space inside and outside these columns. Three of these solvent molecules were found from the diffraction data and refined, other are highly disordered and were treated by SQUEEZE[74]. The structure of **1,3-Az[11]CPP** were determined in space group Cc. The Flack parameter is 0.51 indicating on a possible Centro symmetrical group C2/c. Our attempts to get the structure in group C2/c were failed. The arrangement of the main molecules in the crystal structure of **1,3-Az[11]CPP** seems to close to C2/c but positions of the solvent molecules seem to be out of the symmetry group C2/c. The RIGU option was used in the refinement of the **1,3-Az[11]CPP**. The structures of **1,3-Az[7]CPP** & **1,3-Az[11]CPP** are not precisely determined but they provide the clear chemical results. The structure of **1,3-Az[5]CPP** was determined on non-centrosymmetrical space group Cmc21; the Flack parameter is 0.00(3). All calculations were performed by the Bruker SHELXL-2014/7 package[75]. The detailed diffraction data collection and refinement parameters of all three sized macrocycles were listed in later section. Crystallographic data were deposited at the Cambridge Crystallographic Data Center (CCDC 2553105 for **1,3-Az[5]CPP**, CCDC 2553104 for **1,3-Az[7]CPP**, CCDC 2553103 for **1,3-Az[11]CPP**). Crystallographic data were visualized and analyzed using the Mercury software package.

II.4.1. Synthetic procedures



[5]macAz$_{1,3}$: To a 100 mL round bottom flask were added **1** (22 mg, 0.077 mmol, 1.0 equiv.), **4** (93.7 mg, 0.081 mmol, 1.05 equiv.) and SPhos Pd G3 (12 mg, 0.015 mmol, 20 mol%). The flask was evacuated and back-filled with N_2 three times before introducing 1,4-Dioxane (51 mL, 1.5 mM), followed by addition of aq. K_3PO_4 (2 M, 2.58 mL). After being stirred at room temperature for 19 h, the reaction mixture was passed through a silica gel plug (50% DCM in hexanes, a thin layer of Na_2SO_4 was added on top of the silica gel plug), and the collected dark green filtrate was concentrated in vacuo. The product was purified by flash column chromatography (silica gel, wet-loaded in 10% DCM in hexanes, gradient elution: 0–30% DCM in Hexanes). Fractions containing the product were concentrated and further purified by dissolving the residue in a minimal amount of DCM, followed by precipitation with MeOH. The precipitate was collected by vacuum filtration and washed with cold MeOH to afford **[5]macAz$_{1,3}$** as a blue crystalline solid (16.3 mg, 21%). R_f = 0.29 (20% DCM in Hexanes)

^{1}H NMR (500 MHz, $CDCl_3$) δ 8.64 (d, J = 9.4 Hz, 2H), 7.62 (t, J = 9.9 Hz, 1H), 7.48 (d, J = 8.5 Hz, 4H), 7.44 (d, J = 8.5 Hz, 4H), 7.20 (t, J = 9.8 Hz, 2H), 6.80 (s, 4 H), 6.73 (s, 1H), 6.27 (d, J = 10.2 Hz, 4H), 5.66 (d, J = 10.2 Hz, 4H), 0.96 (t, J = 8.0 Hz, 18H), 0.94 (t, J = 7.8 Hz, 18H), 0.68 (q, J = 7.8 Hz, 12H), 0.59 (q, J = 7.9 Hz, 12H). ^{13}C{^{1}H} NMR (126 MHz, $CDCl_3$) δ 154.2, 144.9, 143.9, 138.9, 138.8, 136.7, 134.6, 131.7, 131.6, 131.2, 129.0, 126.8, 125.4, 123.8, 71.2, 69.6, 7.3, 7.1, 6.8, 6.5. 20 carbon signals in total. HRMS (ESI-TOF) m/z calcd for $[M+H]^+$: $C_{64}H_{87}O_4Si_4$: 1031.5681, found 1031.5667, error -1.40 ppm.

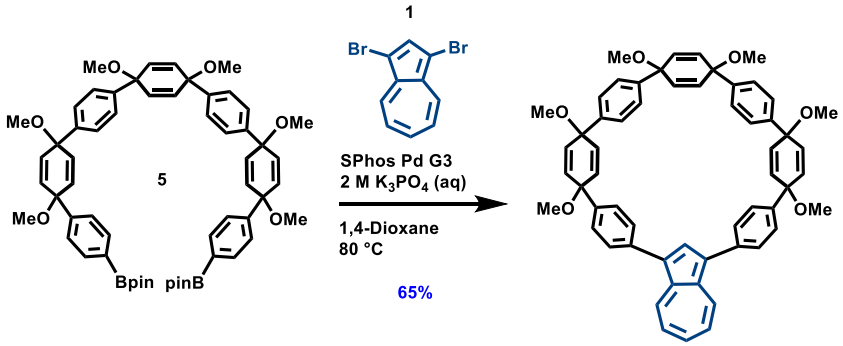


Preparation of 0.04 M H_2SnCl_4 in THF: To a flame-dried 25 mL flask was added $SnCl_2{\cdot}2H_2O$ (0.136 g, 0.603 mmol, 1.0 equiv). The flask was evacuated and back-filled with N_2 three times before introducing anhydrous THF (15 mL). To this solution, HCl (12 M, 0.10 mL, 2.0 equiv.) was added, and the mixture was stirred for at least 30 min prior to use. Unless otherwise stated, H_2SnCl_4 used for reductive aromatization was prepared freshly in the same manner as described above.

1,3-Az[5]CPP: To the scintillation vial containing **[5]macAz$_{1,3}$** (13.6 mg, 0.013 mmol, 1.0 equiv.), THF (3.3 mL) was added to dissolve the solid, giving a blue solution. Freshly prepared H_2SnCl_4 (0.4 M in THF, 1.47 mL, 4.4 equiv.) was added dropwise, and the resulting solution was stirred at room temperature under N_2 atmosphere, with time the reaction mixture turned from teal to dark yellow. The reaction progress was monitored by TLC after 40 min, which indicates the complete consumption of starting macrocycle. After being stirred at room temperature for 50 min, the reaction mixture was quenched with addition of NaOH (1 M, ca. 0.5 mL). The reaction mixture was diluted with DCM (10 mL) and transferred to a separatory funnel. The organic layer was separated, and the aqueous layer was further extracted with DCM (10 mL). The combined organic layers were washed with DI water (10 mL × 2), dried over Na_2SO_4, filtered and concentrated in vacuo. The crude was purified by flash column chromatography (silica gel, 20–40% DCM in Hexanes). Fractions containing the product were concentrated and further purified by triturated in MeOH. The solids were collected by vacuum filtration to afford **1,3-Az[5]CPP** as a dark brown solid (4.7 mg, 69%). R_f = 0.32 (30% DCM in hexanes).

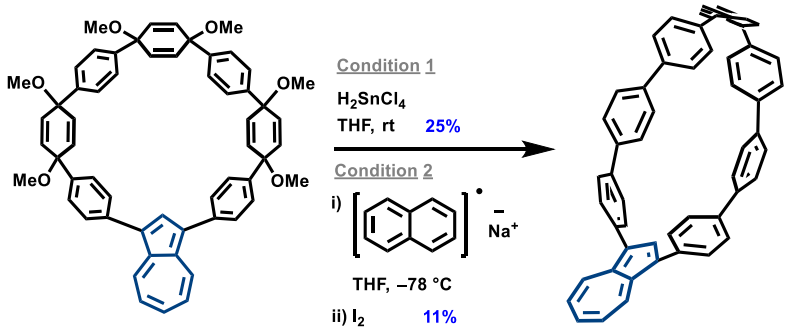
^{1}H NMR (500 MHz, CD_2Cl_2) δ 8.56 (d, J = 8.9 Hz, 2H), 7.59 (t, J = 9.9 Hz, 1H), 7.53 (m, 8H), 7.49 (m, 8H), 7.38 (d, J = 8.7 Hz, 4H), 7.14 (t, J = 9.9 Hz, 2H), 6.72 (s, 1H). ^{13}C {^{1}H} NMR (126 MHz, CD_2Cl_2) δ 150.6, 139.5, 138.6, 137.6, 136.9, 136.50, 136.47, 135.9, 134.8, 131.9, 129.3,

128.2, 128.0, 127.8, 127.4, 124.2. 16 carbon signals in total. HRMS (EI$^+$-TOF, AccuTOF) m/z calcd for $[M]^+$: $C_{40}H_{26}$: 506.20290, found 506.20267. Error -0.46 ppm.



[7]macAz$_{1,3}$: To a 250 mL round bottom flask were added **1** (30.0 mg, 0.105 mmol, 1.0 equiv.), **5** (110.2 mg, 0.113 mmol, 1.08 equiv.), SPhos Pd G3 (16.4 mg, 0.021 mmol, 20 mol%). The flask was evacuated and back-filled with N_2 three times before introducing 1,4-Dioxane (75 mL, 1.4 mM). The resulting mixture was stirred at 80 °C for 5 min, followed by addition of aq. K_3PO_4 (2 M, 1.76 mL). After being stirred at 80 °C for 12 h, the reaction mixture was passed through a short celite plug, flushed with DCM (60 mL) and concentrated in vacuo. The dark green crude was purified by flash column chromatography (silica gel, 0%–7% EtOAc in DCM) to yield the product as an emerald-green solid (57.6 mg, 65%). R_f = 0.39 (10% EtOAc in DCM).

^{1}H NMR (500 MHz, $CDCl_3$) δ 8.62 (d, J = 9.6 Hz, 2 H), 8.01 (s, 1 H), 7.62 (d, J = 8.5 Hz, 4 H), 7.60 (t, J = 9.8 Hz, 1 H), 7.53 (d, J = 8.4 Hz, 4 H), 7.47 (approx. s, 8 H), 7.15 (t, J = 9.8 Hz, 2 H), 6.21 (d, J = 8.9 Hz, 4 H), 6.20 (s, 4 H), 6.11 (d, J = 10.2 Hz, 4 H) 3.52 (s, 6 H), 3.44 (s, 6 H), 3.28 (s, 6 H). ^{13}C {^{1}H} NMR (126 MHz, $CDCl_3$) δ 143.4, 143.2, 141.5, 141.1, 139.1, 136.7, 136.2, 136.1, 134.1, 133.7, 133.0, 130.2, 129.6, 126.6, 126.45, 126.39, 123.9, 75.4, 74.7, 72.8, 52.5, 51.9, 51.5. 23 carbon signals in total. HRMS (MALDI–TOF) m/z calcd for $[M]^+$: $C_{58}H_{52}O_6$: 844.3758, found 844.3783. Error +2.96 ppm.

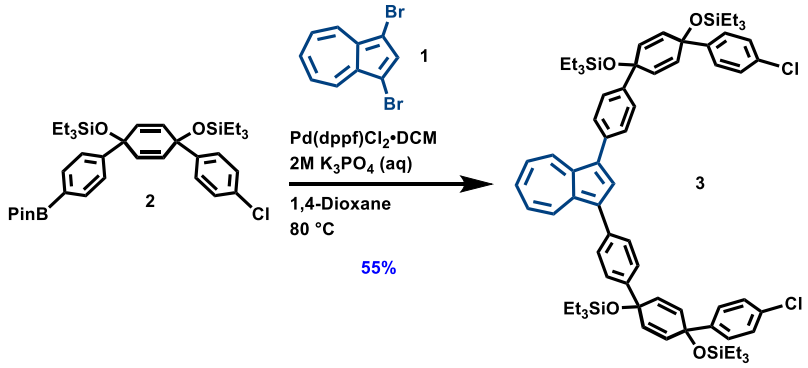


1,3-Az[7]CPP: *Condition 1*: A flame-dried 25 mL round bottom flask charged with **[7]macAz$_{1,3}$** (45.2 mg, 0.053 mmol, 1.0 equiv.) was evacuated and back-filled with N_2 three times, followed by addition of THF (8 mL). *The macrocycle remained partially insoluble in THF even after sonication, and H_2SnCl_4 was added directly to the resulting teal suspension.* Freshly prepared H_2SnCl_4 (8.83 mL, 6.6 equiv) was added dropwise, resulting in dissolution of additional solids and formation of a grass-green solution. The reaction progress was monitored by TLC after 2 h, which indicates the complete consumption of the starting macrocycle. After being stirred at room temperature for 20 h, the reaction was quenched with addition of NaOH (1 M, ca. 1 mL). The reaction mixture was diluted with DCM (30 mL) and transferred to a separatory funnel. The organic layer was separated, and the aqueous layer was further extracted with DCM (30 mL). The combined organic layers were washed with DI water (50 mL), dried over Na_2SO_4, filtered and concentrated in vacuo to afford the crude as a dark green solid. The crude was subjected to flash column chromatography (silica gel, wet loaded in 80% DCM in hexanes, gradient elution: 20–50% DCM in hexanes) to afford **1,3-Az[7]CPP** as a green solid (8.7 mg, 25%). R_f = 0.38 (40% DCM in hexanes). *A side product was also observed in the later-eluting fractions, showing three methoxy peaks characteristic of a rearranged product formed under acidic condition*.

Preparation of 0.25 M sodium naphthalenide in THF: To a pre-weighed, flame-dried 25 mL round-bottom flask was added hexanes-washed, sliced sodium metal (ca. 150 mg). The flask was evacuated and back-filled with N_2 three times, and the exact mass of sodium (131.4 mg, 5.71 mmol, 1.5 equiv.) was confirmed. Naphthalene (488 mg, 3.81 mmol, 1.0 equiv) was then added to the flask. The flask was again evacuated and back-filled with N_2 three times before anhydrous THF (15.2 mL) was introduced. The resulting mixture was sonicated for about 2 min and then stirred overnight to afford a dark green solution prior to use.

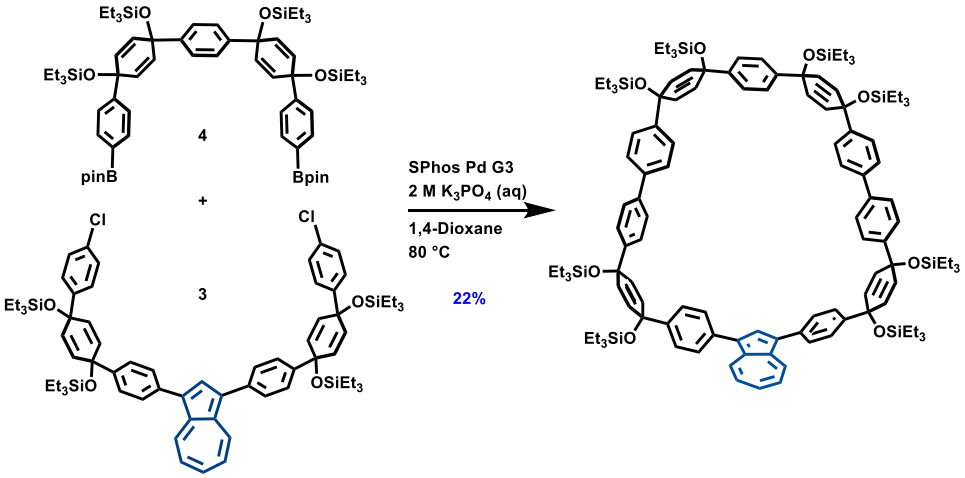
Condition 2: A flame-dried 25 mL round bottom flask charge with **[7]macAz$_{1,3}$** (20.2 mg, 0.024 mmol, 1.0 equiv.) was evacuated and back-filled with N_2 three times, followed by addition of THF (4.8 mL). The suspension was cooled to –78 °C for 5 min before dropwise addition of sodium naphthalenide solution (2.29 mL, 0.574 mmol, 24.0 equiv.). After being stirred at –78 °C for 4 h, the reaction was quenched by dropwise addition of I_2 in THF (1 M) until excess I_2 remained in solution. The reaction mixture was warmed to room temperature, and excess I_2 was quenched with addition of satd. aq. $Na_2S_2O_3$. The resulting mixture was diluted with DCM (20 mL). The organic layer was separated, and the aqueous layer was further extracted with DCM (20 mL). The

combined organic layers were washed with brine (50 mL), dried over Na_2SO_4, filtered and concentrated in vacuo. The crude was purified by flash column chromatography (silica gel, dry-loaded onto Celite, 30% DCM in hexanes) to afford **1,3-Az[7]CPP** as a green solid (1.8 mg, 11%). ^{1}H NMR (500 MHz, CD_2Cl_2) δ 8.66 (d, J = 9.5 Hz, 2H), 7.64 (t, J = 9.7 Hz, 1H), 7.56–7.45 (m, 28 H), 7.21 (t, J = 9.8 Hz, 2H), 6.94 (s, 1H). ^{13}C{^{1}H} NMR (126 MHz, $CDCl_3$) δ 147.5, 139.2, 138.7, 138.6, 138.2, 138.0, 138.0, 137.9, 136.9, 136.54, 135.46, 131.4, 129.6, 127.77, 127.75, 127.72, 127.66, 127.5, 123.9. 19 carbon signals were observed, with one signal likely obscured by overlap. HRMS (EI$^+$-TOF) m/z calcd for [M]$^+$: $C_{52}H_{34}$: 658.2661, found 658.2659. Error -0.30 ppm.



3: To a 25 mL round bottom flask were added **1** (40.0 mg, 0.140 mmol, 1.0 equiv.), **2** (191.9 mg, 0.294 mmol, 2.1 equiv.), Pd(dppf)Cl_2·DCM (11.4 mg, 0.014 mmol, 10 mol%). The flask was evacuated and back-filled with N_2 gas three times before introducing 1,4-Dioxane (3.5 mL, 40 mM). The resulting mixture was heated and stirred at 80 °C for 5 min, followed by addition of K_3PO_4 (2 M, 0.70 mL) was added. After being stirred at 80 °C for 17 h, the reaction mixture was concentrated in vacuo. The crude was subjected to flash column chromatography (1st column: silica gel, gradient elution: 5–16% DCM in hexanes; 2nd column, silica gel, 3–7% EtOAc in hexanes) to yield the product as a blue oil (91.0 mg, 55%). R_f = 0.63 (5% EtOAc in hexanes). ^{1}H NMR (500 MHz, $CDCl_3$) δ 8.52 (d, J = 9.4 Hz, 2H), 8.10 (s, 1H), 7.58 (t, J = 9.8 Hz, 1H), 7.56 (d, J = 8.4 Hz, 4H), 7.44 (d, J = 8.3 Hz, 4H), 7.33 (d, J = 8.5 Hz, 4H), 7.24 (d, J = 8.7 Hz, 4H), 7.12 (t, J = 9.8 Hz, 2H), 6.10 (d, J = 10.2 Hz, 4H), 6.00 (d, J = 10.0 Hz, 4H), 0.98 (t, J = 8.0 Hz, 18H), 0.96 (t, J = 7.8 Hz, 18H). 0.66 (q, J = 7.9 Hz, 12H), 0.63 (q, J = 8.1 Hz, 12H). ^{13}C{^{1}H} NMR (126 MHz, $CDCl_3$) δ 144.9, 144.1, 139.2, 137.3, 136.9, 136.4, 136.3, 133.1, 132.1, 131.3, 130.3, 129.7, 128.4, 127.6, 126.30, 123.7, 71.5, 71.4, 7.23, 7.19, 6.65, 6.60. 22 carbon signals in

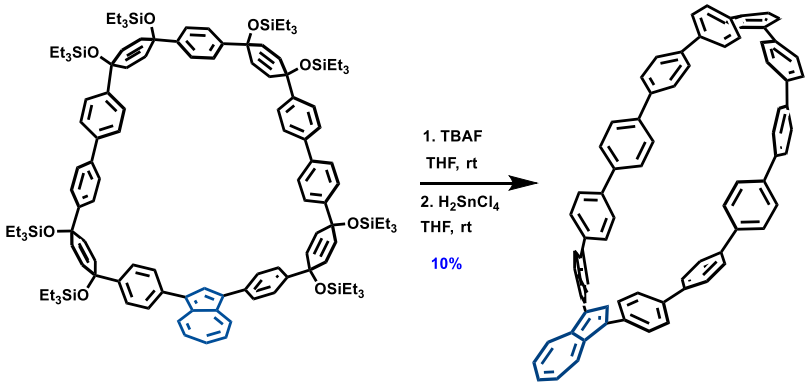
total. HRMS (MALDI–TOF) m/z calcd for $[M]^+$: $C_{70}H_{90}Cl_2O_4Si_4$: 1176.5288, found 1176.5268. Error -1.70 ppm.



[11]mazAz1,3: To a 100 mL round bottom flask were added **3** (60.0 mg, 0.051 mmol, 1.0 equiv.), **4** (64.9 mg, 0.056 mmol, 1.1 equiv.), SPhos Pd G3 (9.93 mg, 0.013 mmol, 25 mol%). The flask was evacuated and back-filled with N_2 gas three times before introducing 1,4-Dioxane (51 mL, 1 mM). The resulting mixture was heated and stirred at 80 °C for 5 min, followed by addition of K_3PO_4 (2 M, 1.7 mL). After being stirred at 80 °C for 22 h, the reaction mixture was concentrated and diluted with DCM (25 mL). The organic layer was separated, and the aqueous layer was further extracted with DCM (25 mL ×2). The combined organic layers were washed with DI water (50 mL), brine (50 mL), dried over Na_2SO_4, filtered and concentrated in vacuo to afford the crude as a dark green sticky oil. The crude was purified by flash column chromatography (silica gel, 0–30% DCM in Hexanes). Fractions containing the product were concentrated and further purified by dissolving in a minimum amount of residue in DCM, followed by precipitation with MeOH. The solids were collected by vacuum filtration and washed with MeOH to afford **[11]macAz$_{1,3}$** as a light blue solid (22.4 mg, 22%). R_f = 0.21 (20% DCM in hexanes).

^{1}H NMR (500 MHz, CD_2Cl_2) δ 8.52 (d, J = 9.7 Hz, 2H), 8.02 (s, 1H), 7.59 (t, J = 9.7 Hz, 1H), 7.50 (d, J = 8.3 Hz, 4H), 7.47 – 7.41 (m, 12H), 7.37 (d, J = 8.3 Hz, 4H), 7.29 (s, 4H), 7.24 (d, J = 8.3 Hz, 4H), 7.13 (t, J = 9.8 Hz, 2H), 6.09 (approx. s, 12H), 5.96 (d, J = 10.0 Hz, 4H), 1.00 (t, J = 8.0 Hz, 18H), 0.95 (t, J = 7.9 Hz, 18H), 0.94 (t, J = 7.9 Hz, 18H), 0.92 (t, J = 7.9 Hz ,18H), 0.70 (q, J = 7.9 Hz, 12H), 0.641 (q, J = 7.9 Hz, 12H), 0.637 (q, J = 8.0 Hz, 12H), 0.57 (q, J = 8.0 Hz,

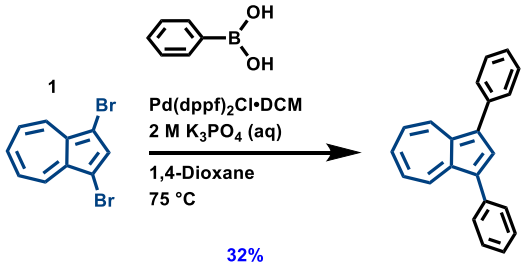
12 H). ^{13}C NMR (126 MHz, CD_2Cl_2) δ 145.6, 145.5, 145.3, 144.6, 140.2, 139.8, 139.5, 137.2, 137.1, 136.5, 136.3, 132.2, 131.9, 130.5, 129.8, 127.1, 127.0, 126.8, 126.6, 126.5, 126.4, 124.0, 72.0, 71.9, 71.8, 71.6, 7.3, 7.23, 7.20, 6.9, 6.84, 6.81, 6.77. 33 carbon signals in total, with 3 signals likely obscured by overlap. HRMS (MALDI–TOF) m/z calcd for $[M]^+$: $C_{124}H_{170}O_8Si_8$: 2011.1044, found 2011.0976. Error -3.38 ppm.



1,3-Az[11]CPP: Desilylation: To a flame-dried 25 mL round bottom flask was added **[11]mazAz$_{1,3}$** (29 mg, 0.014 mmol, 1.0 equiv.) and the flask was evacuated and back-filled with N_2 three times before introducing THF (1 mL, 14 mM). Tetrabutylammonium fluoride (1 M, 0.12 mL, 0.121 mmol, 8.4 equiv.) was added slowly to the reaction flask, during which the blue solution turned to dark green. Over time, the reaction mixture became a suspension containing teal-green solids. After being stirred at room temperature for 6 h, the reaction was quenched with addition of water and all the solids entered into the solution and gave a blue solution. THF was removed in vacuo, and the crude was sonicated for a few minutes to help crash out more products. The precipitate was collected by vacuum filtration, washed with water and dried overnight to afford desilylated product (ca. 10 mg). Aromatization: To a 25 mL round bottom flask was added desilylated product (ca. 10 mg, 0.009 mmol, 1.0 equiv.), followed by addition of THF (1.5 mL). To this solution, freshly prepared H_2SnCl_4 (0.04 M, 2.0 mL, 8.8 equiv.) was added dropwise and the reaction was stirred at room temperature under N_2 atmosphere. After being stirred at room temperature for 21 h, the reaction was quenched with addition of aq. NaOH (1 M). The reaction mixture was diluted with DCM (10 mL) and was transferred to a separatory funnel. The organic layer was separated, and the aqueous layer was further extracted with DCM (10 mL×2). The combined organic layers were washed with brine (40 mL), dried over Na_2SO_4, filtered and

concentrated in vacuo. The crude was purified by flash column chromatography (Alumina, dry loaded onto celite, gradient elution: 50–70 % DCM in hexanes) to afford the product as a blue solid. The solid was further recrystallized from DCM and hexanes to afford the **1,3-Az[11]CPP** as a dark blue crystalline solid (0.9 mg, 10%). R_f = 0.46 (50% DCM in hexanes).

^{1}H NMR (500 MHz, CD_2Cl_2) δ 8.70 (d, J = 9.4 Hz, 2H), 7.70–7.61 (m, 47H), 7.53 (s, 1H), 7.23 (t, J = 9.9 Hz, 2H). ^{13}C {^{1}H} NMR (126 MHz, CD_2Cl_2) δ 143.5, 139.7, 139.5, 139.1, 139.0, 138.93, 138.92, 138.90, 138.86, 138.81, 138.77, 137.1, 136.7, 136.4, 131.0, 130.2, 127.8, 127.73, 127.71, 127.6, 124.2. 28 signals in total, with 7 signals likely obscured by overlap. HRMS (MALDI-TOF) m/z calcd for $[M]^+$: $C_{76}H_{50}$: 962.3907, found 962.3919. Error +1.25 ppm.



II.7: To a 5 mL round bottom flask were added **1** (10 mg, 0.035 mmol, 1.0 equiv.), Phenylboronic acid (8.74 mg, 0.072 mmol, 2.05 equiv.) and Pd(dppf)Cl_2·DCM (2.86 mg, 0.003 mmol, 10 mol%). The flask was evacuated and back-filled with N_2 three times before introducing 1,4-Dioxane (1.17 mL). After being stirred at 75 °C for 19 h, the reaction was cooled to room temperature and concentrated in vacuo. The crude was purified by flash column chromatography (100% hexanes) and the solid was further washed with pentane to afford **II.7** as green solids (3.1 mg, 32%). R_f = 0.47 (100% hexanes).The ^{1}H NMR spectrum was consistent with literature data.[68]

II.4.2. Single crystal X-ray diffraction information

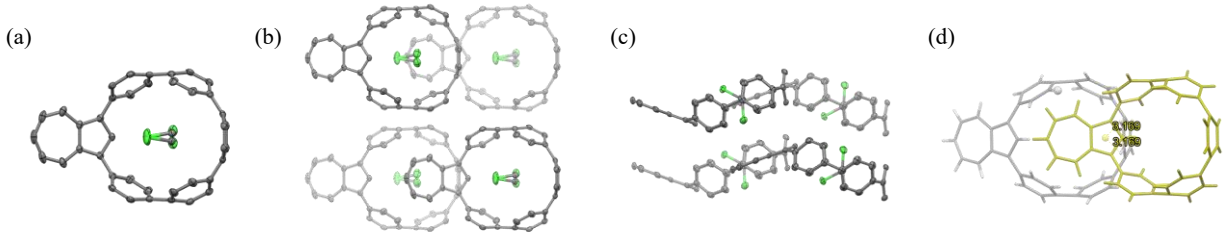


Figure II.7. Crystal structure of 1,3-Az[5]CPP: (a) 1,3-Az[5]CPP with solvent molecule inside; (b) top view. (c) side view. H atoms have been omitted for clarity. Thermal ellipsoids at the 50%

probability level. (d) C-H···π interaction (distances are reported in Å). Disordered atoms in the cavity are shown with all resolved orientations.

Crystallographic Data for **1,3-Az[5]CPP** (CCDC 2553105): $C_{41}H_{28}Cl_2$, M = 591.53, 0.19 × 0.22 × 0.23 mm, T = 170(2) K, Orthorhombic, space group *PCmc2*$_1$, *a* = 18.995(2) Å, *b* = 10.1434(12) Å, *c* = 15.589(2) Å, *V* = 3003.6(6) Å^3, *Z* = 4, Z' = 1, *D*c = 1.308 Mg/m^3, μ(Mo) = 0.246 mm^{-1}, F(000) = 1232, $2\theta_{max}$ = 56.58°, 12342 reflections, 3426 independent reflections [R_{int} = 0.0363], R_1 = 0.0337, wR_2 = 0.0870 and GOF = 1.026 for 3426 reflections (265 parameters) with I>2σ(I), R_1 = 0.0370, wR_2 = 0.0898 and GOF = 1.026 for all reflections, the Flack = 0.00(3), max/min residual electron density +0.189/-0.225 eÅ^{-3}.

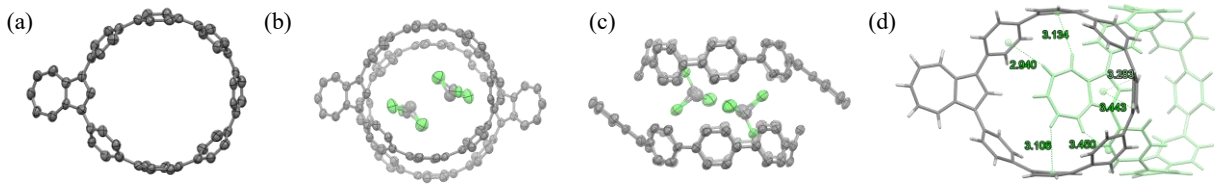


Figure II.8. Crystal structure of 1,3-Az[7]CPP: (a) 1,3-Az[7]CPP with solvent molecule inside; (b) top view. (c) side view. H atoms have been omitted for clarity. Thermal ellipsoids at the 50% probability level. (d) C-H···π interaction (distances are reported in Å).

Crystallographic Data for **1,3-Az[7]CPP** (CCDC 2553104): $C_{53}H_{35.77}Cl_{2.23}$, M = 751.72, 0.005 × 0.19 × 0.22 mm, T = 173(2) K, Monoclinic, space group *P2*$_1$/*n*, *a* = 13.8514(13) Å, *b* = 16.4825(14) Å, *c* = 17.7977(16) Å, β = 111.494(5)°, *V* = 3780.7(6) Å^3, *Z* = 4, Z' = 1, *D*c = 1.321 Mg/m^3, μ(Cu) = 1.980 mm^{-1}, F(000) = 1567, $2\theta_{max}$ = 99.62°, 24589 reflections, 3842 independent reflections [R_{int} = 0.2082], R_1 = 0.0703, wR_2 = 0.1623 and GOF = 1.000 for 3842 reflections (510 parameters) with I>2σ(I), R_1 = 0.1564, wR_2 = 0.2106 and GOF = 1.000 for all reflections, max/min residual electron density +0.356/-0.367 eÅ^{-3}.

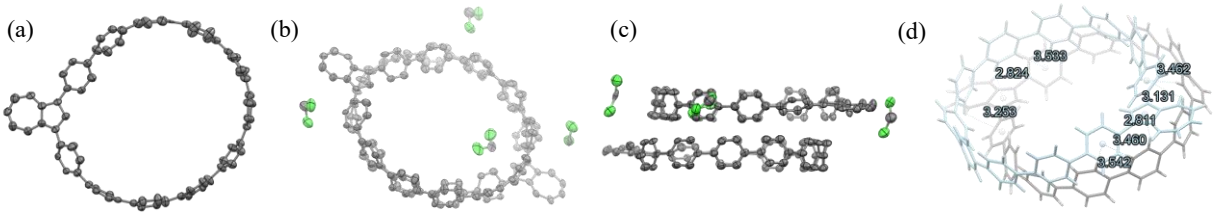


Figure II.9. Crystal structure of 1,3-Az[11]CPP: (a) 1,3-Az[11]CPP with solvent molecule inside; (b) top view. (c) side view. H atoms have been omitted for clarity. Thermal ellipsoids at the 50% probability level. (d) C-H···π interaction (distances are reported in Å).

Crystallographic Data for **1,3-Az[11]CPP** (CCDC 2553103): $C_{77.16}H_{52.32}Cl_{2.32}$, M = 1061.78, 0.06 × 0.04 × 0.03 mm, T = 173(2) K, Monoclinic, space group *Cc*, *a* = 37.419(3) Å, *b* = 11.2130(14) Å, *c* = 34.197(3) Å, β = 96.946(5)°, *V* = 14243(3) Å^3, *Z* = 8, Z' = 2, *D*c = 0.990 Mg/m^3, μ(Cu) = 1.206 mm^{-1}, F(000) = 4438, $2\theta_{max}$ = 80.41°, 35372 reflections, 8358 independent reflections [R_{int} = 0.1979], R_1 = 0.0822, wR_2 = 0.1946 and GOF = 1.033 for 8358 reflections (1447 parameters) with I>2σ(I), R_1 = 0.1496, wR_2 = 0.2394 and GOF = 0.968 for all reflections, the Flack = 0.51(4), max/min residual electron density +0.273/-0.244 eÅ^{-3}.

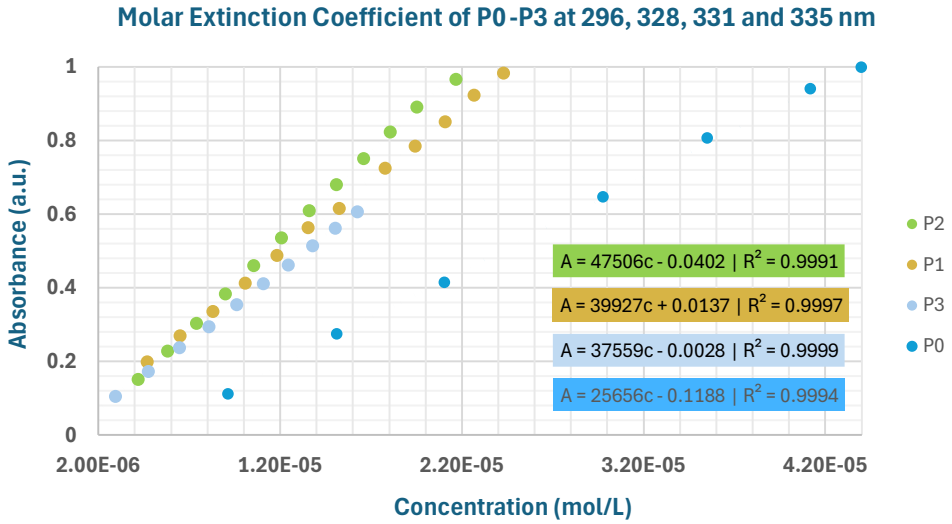


Figure II.10. Molar extinction coefficient measurements of **1,3-Az[*n*]CPPs** and model compound **II.7**. **II.7** (P0), **1,3-Az[5]CPP** (P1), **1,3-Az[7]CPP** (P2), **1,3-Az[11]CPP** (P3).

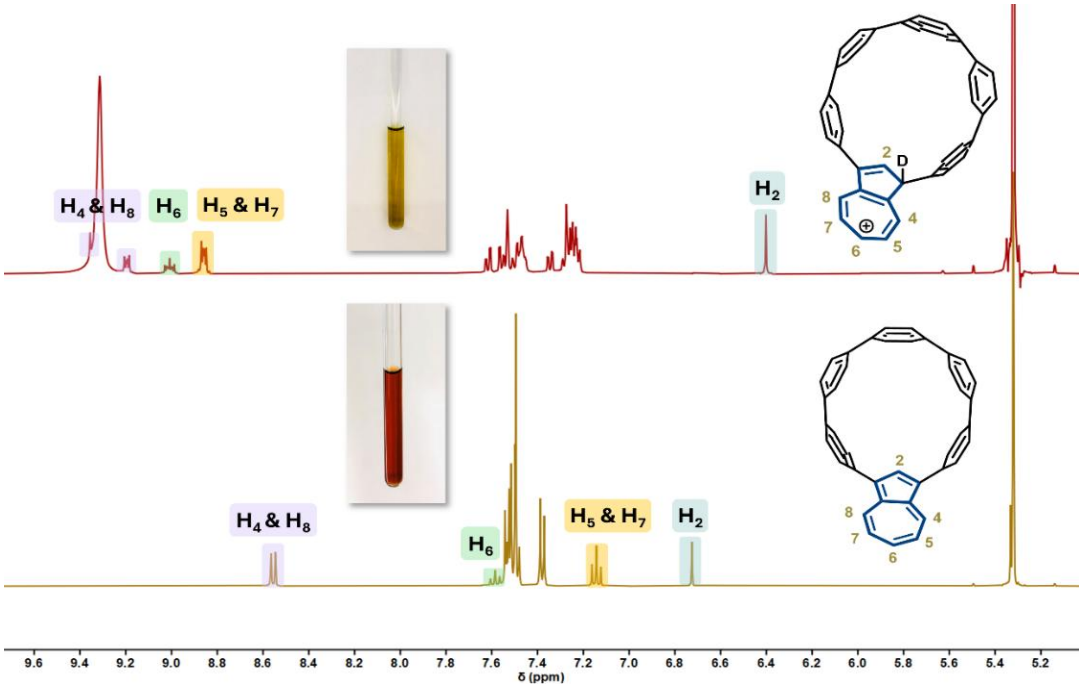


Figure II.11. pH-responsiveness experiment of 1,3-Az[5]CPP conducted using excess *d*-TFA in CD_2Cl_2. A detailed analysis of the signal H_4–H_8 were not attempted but the assignment for H_2 is certain.

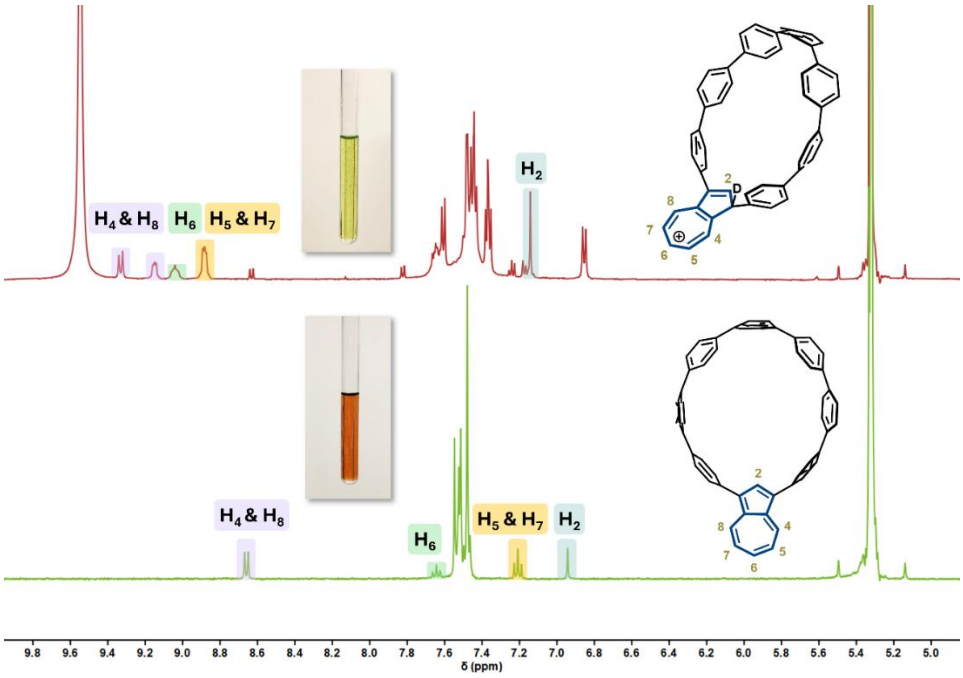


Figure II.12. pH-responsiveness experiment of 1,3-Az[7]CPP conducted using excess *d*-TFA in CD_2Cl_2. A detailed analysis of the signal H_4–H_8 were not attempted but the assignment for H_2 is certain.

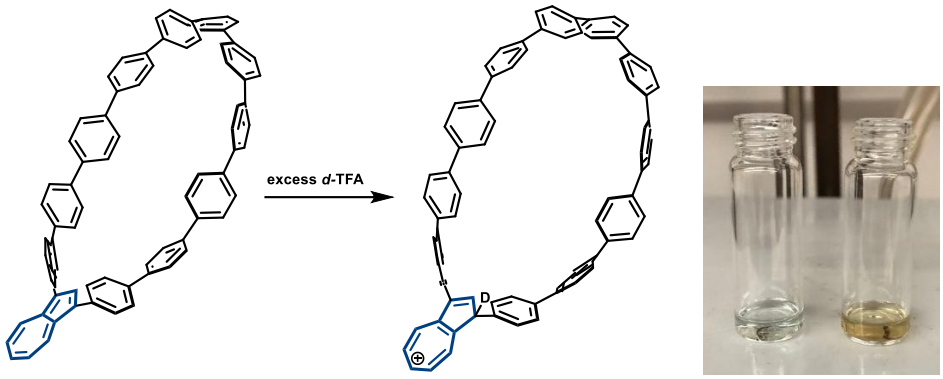


Figure II.13. pH-responsiveness experiment of 1,3-Az[11]CPP conducted using excess *d*-TFA in DCM (left: P3, right: *d*-TFA added)

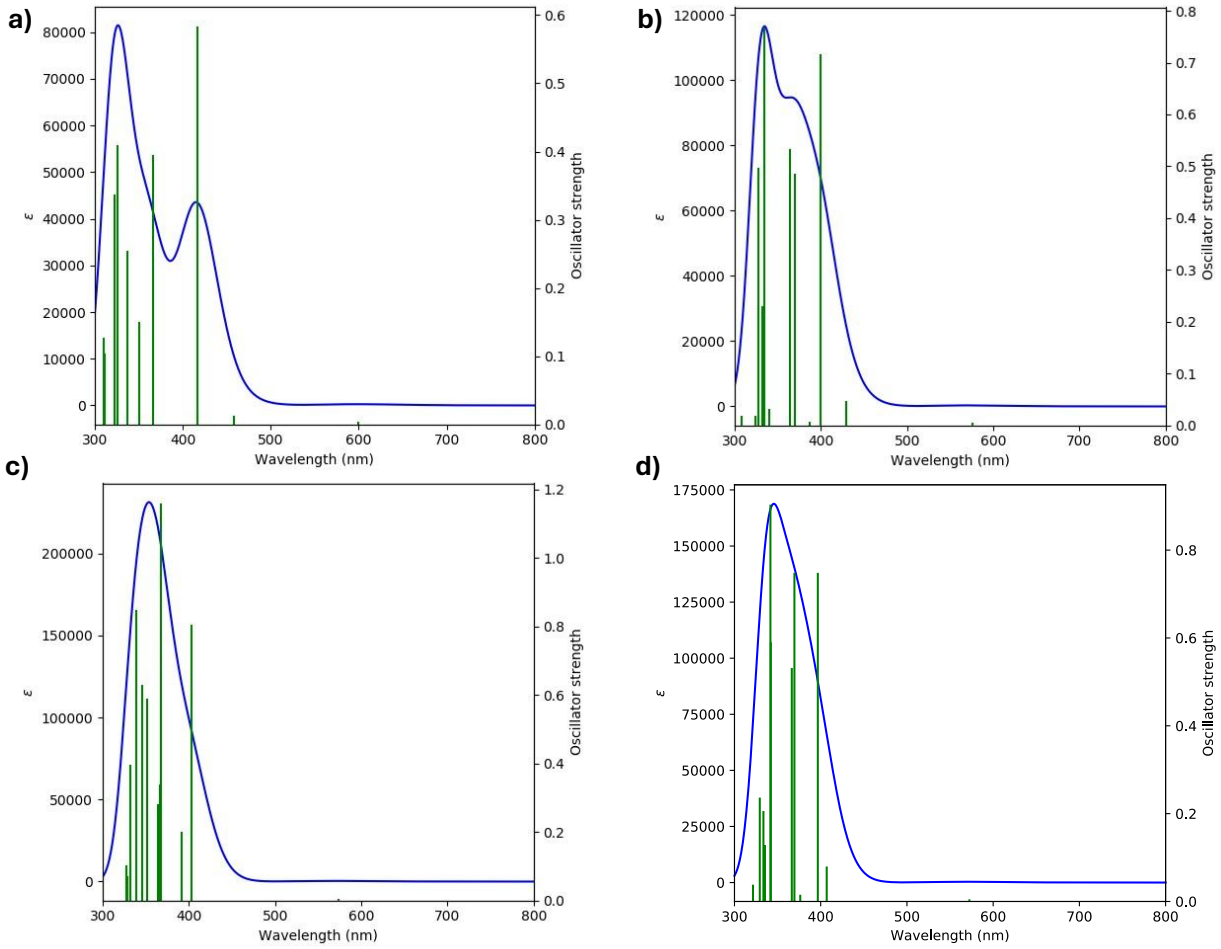


Figure II.14. TD-DFT calculated UV-Vis absorption spectra of (a) 1,3-Az[5]CPP, (b) 1,3-Az[7]CPP, (c) 1,3-Az[11]CPP, and (d) 1,3-Az[9]CPP.

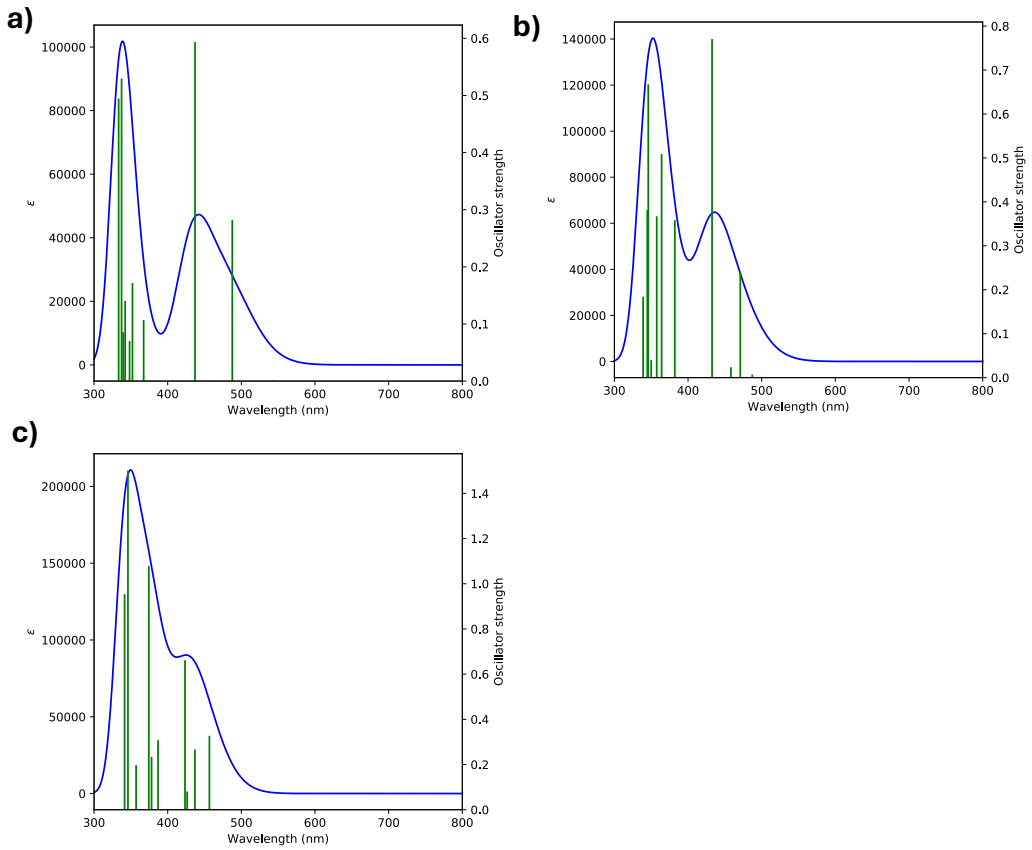


Figure II.15. TD-DFT calculated fluorescence spectra of (a) 1,3-Az[5]CPP, (b) 1,3-Az[7]CPP, (c) 1,3-Az[11]CPP.

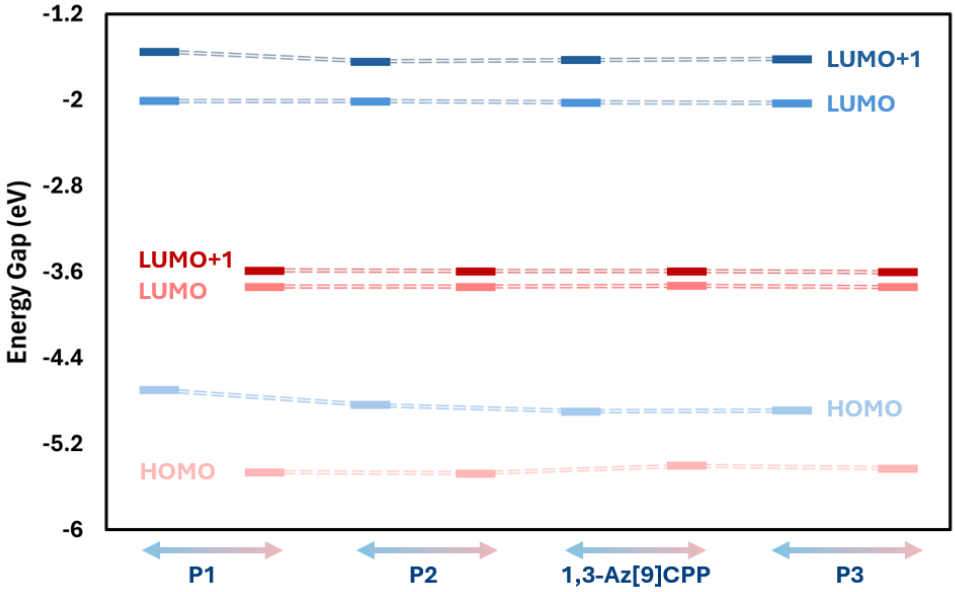


Figure II.16. Computed energy gaps (HOMO, LUMO, LUMO+1) of 1,3-Az[*n*]CPP (*n* = 5, 7 and 11) and 1,3-Az[9]CPP (blue trend) and protonated species (red trend).

II.4.3. Computational results of 1,3-Az[*n*]CPPs

Table II.2. Major electronic transitions of **1,3-Az[5]CPP** calculated by TD-DFT method

No.	Energy (eV)	Wavelength (nm)	Osc. Strength	Major Contributions
1	2.0689	599.28	0.0036	H->L (90%)
2	2.7045	458.44	0.0128	H->L+1 (96%)
3	2.9785	416.26	0.5837	H->L+2 (88%)
4	3.1893	388.75	0	H-1->L (87%)
5	3.3895	365.79	0.3953	H-2->L (83%)
6	3.5384	350.40	0.1501	H-1->L+1 (76%) H-2->L+2 (20%)
7	3.6838	336.57	0.2542	H-1->L+2 (53%) H-2->L+1 (42%)
8	3.8032	326.00	0.0346	H->L+3 (50%) H-2->L+1 (27%) H-1->L+2 (19%)
9	3.8048	325.86	0.4098	H-2->L+2 (75%) H-1->L+1 (22%)
10	3.8473	322.26	0.3375	H->L+3 (31%) H-2->L+1 (27%) H-3->L (14%) H-1->L+2 (14%)
11	3.9798	311.53	0.1039	H->L+5 (73%) H-3->L (10%)
12	3.9998	309.98	0.1275	H->L+4 (82%)

Table II.3. Major electronic transitions of **1,3-Az[7]CPP** calculated by TD-DFT method

No.	Energy (eV)	Wavelength (nm)	Osc. Strength	Major Contributions
1	2.1536	575.71	0.0045	H->L (88%) H-1->L (10%)
2	2.8853	429.71	0.0477	H->L+1 (87%)
3	3.1025	399.63	0.7169	H->L+2 (84%)
4	3.2001	387.44	0.0071	H-1->L (85%) H->L (11%)
5	3.3541	369.65	0.4853	H-1->L+1 (85%)
6	3.3999	364.67	0.5337	H-2->L (80%) H->L+2 (10%)
7	3.6502	339.66	0.0325	H-1->L+2 (71%) H-2->L+1 (21%)
8	3.7027	334.85	0.7684	H-2->L+1 (54%) H->L+3 (18%) H-1->L+2 (11%)
9	3.7389	331.61	0.2299	H->L+3 (56%) H-2->L+1 (19%)
10	3.7796	328.04	0.4963	H-2->L+2 (47%) H->L+4 (28%)
11	3.8268	323.99	0.0183	H->L+4 (52%) H-2->L+2 (34%)
12	4.0277	307.83	0.0182	H-3->L (70%) H-4->L (15%)

Table II.4. Major electronic transitions of **1,3-Az[11]CPP** calculated by TD-DFT method

No.	Energy (eV)	Wavelength (nm)	Osc. Strength	Major Contributions
1	2.1602	573.95	0.0055	H->L (94%)
2	3.0757	403.11	0.8045	H->L+2 (43%) H->L+1 (40%)
3	3.1640	391.86	0.1998	H->L+2 (38%) H->L+1 (29%) H-1->L+1 (11%)
4	3.3769	367.15	1.1599	H-1->L+1 (61%) H->L+1 (11%)
5	3.3796	366.86	0.3396	H-1->L (42%) H-2->L (32%)
6	3.4007	364.58	0.2817	H-1->L (50%) H-2->L (29%)
7	3.5233	351.90	0.5901	H->L+3 (51%) H->L+4 (20%) H->L+1 (17%)
8	3.5819	346.14	0.6287	H->L+4 (33%) H-2->L (16%) H->L+3 (16%) H-2->L+1 (15%)
9	3.6623	338.54	0.8471	H-2->L+1 (32%) H-1->L+2 (26%) H->L+4 (18%)
10	3.7311	332.30	0.3961	H-2->L+2 (55%)
11	3.7717	328.72	0.0713	H-1->L+2 (46%) H-2->L+1 (39%)
12	3.7836	327.69	0.1024	H-3->L (71%) H-2->L+2 (12%)

Table II.5. Major electronic transitions of **1,3-Az[9]CPP** calculated by TD-DFT method

No.	Energy (eV)	Wavelength (nm)	Osc. Strength	Major Contributions
1	2.1659	572.4373	0.0049	H->L (92%)
2	3.0467	406.9459	0.0797	H-1->L+1 (15%) H->L+1 (73%)
3	3.1257	396.6606	0.7482	H->L+2 (82%)
4	3.2949	376.2912	0.0153	H-1->L (88%)
5	3.3553	369.5175	0.7482	H-1->L+1 (75%) H->L+1 (16%)
6	3.3832	366.4702	0.5317	H-2->L (77%) H->L+2 (10%)
7	3.6235	342.1669	0.5902	H->L+4 (67%)
8	3.6284	341.7049	0.9035	H-2->L+1 (25%) H-1->L+2 (21%) H->L+3 (24%)
9	3.6974	335.328	0.1286	H-1->L+2 (47%) H->L+3 (37%)
10	3.7168	333.5778	0.206	H-2->L+1 (64%) H-1->L+2 (22%)
11	3.7646	329.3423	0.2366	H-2->L+2 (68%)
12	3.8568	321.4691	0.0383	H-3->L (80%)

Table II.6. Major electronic transitions (emission) of 1,3-Az[5]CPP calculated by TD-DFT method

No.	Energy (eV)	Wavelength (nm)	Osc. Strength	Major Contributions
1	1.1829	1048.1376	0.0004	H->L (96%)
2	2.2850	542.5767	0	H->L+1 (97%)
3	2.5421	487.7043	0.2823	H-2->L (33%) H->L+2 (65%)
4	2.6603	466.0359	0.0002	H-1->L (94%)
5	2.8363	437.1182	0.5935	H-2->L (65%) H->L+2 (33%)
6	3.3751	367.3388	0.1068	H-2->L+2 (31%) H-1->L+1 (66%)
7	3.5205	352.1678	0.1717	H-2->L+1 (54%) H-1->L+2 (40%)
8	3.5603	348.2311	0.07	H->L+3 (80%)
9	3.6228	342.2236	0.1402	H-2->L+2 (53%) H-1->L+1 (24%) H->L+5 (20%)
10	3.6507	339.6083	0.0855	H-2->L+1 (24%) H-1->L+2 (28%) H->L+4 (42%)
11	3.6750	337.3628	0.5297	H-3->L (23%) H-2->L+1 (16%) H-1->L+2 (12%) H->L+4 (41%)
12	3.7189	333.3805	0.4945	H->L+5 (67%) H->L+6 (12%)

Table II.7. Major electronic transitions (emission) of 1,3-Az[7]CPP calculated by TD-DFT method

No.	Energy (eV)	Wavelength (nm)	Osc. Strength	Major Contributions
1	1.2857	964.3322	0.0004	H->L (96%)
2	2.5450	487.1486	0.0071	H->L+1 (92%)
3	2.6324	470.9751	0.2405	H-2->L (41%) H->L+2 (51%)
4	2.7061	458.1487	0.0238	H-1->L (90%)
5	2.8658	432.6187	0.7707	H-2->L (55%) H->L+2 (43%)
6	3.2453	382.0305	0.3585	H-2->L+2 (10%) H-1->L+1 (83%)
7	3.4049	364.1239	0.509	H->L+3 (87%)
8	3.4679	357.5092	0.3674	H-3->L (15%) H->L+4 (70%)
9	3.5424	349.9907	0.0399	H-2->L+1 (21%) H-1->L+2 (71%)
10	3.5836	345.9670	0.6676	H-2->L+1 (60%) H-2->L+2 (15%)
11	3.5972	344.6590	0.3815	H-4->L (10%) H-2->L+1 (12%) H-2->L+2 (46%) H-1->L+2 (12%)
12	3.6575	338.9769	0.1841	H-4->L (63%) H-2->L+2 (21%)

Table II.8. Major electronic transitions (emission) of 1,3-Az[11]CPP calculated by TD-DFT method

No.	Energy (eV)	Wavelength (nm)	Osc. Strength	Major Contributions
1	1.3710	904.3340	0.0003	H->L (98%)
2	2.7152	456.6132	0.3274	H-2->L (34%) H->L+1 (13%) H->L+2 (40%)
3	2.8374	436.9487	0.2668	H-2->L (13%) H->L+1 (65%) H->L+3 (12%)
4	2.9078	426.3702	0.0808	H-1->L (83%)
5	2.9278	423.4577	0.6621	H-2->L (41%) H-1->L (10%) H->L+2 (43%)
6	3.2046	386.8824	0.3079	H>L+1 (17%) H->L+3 (66%)
7	3.2791	378.0928	0.2339	H-4->L (16%) H->L+4 (58%)
8	3.3119	374.3484	1.0779	H-1->L+1 (75%)
9	3.3299	372.3249	0.0003	H-3->L (88%)
10	3.4720	357.0870	0.1974	H-4->L (66%) H->L+4 (25%)
11	3.5831	346.0153	1.5002	H-2->L+1 (55%) H-1->L+2 (23%)
12	3.6309	341.4602	0.954	H-2->L+2 (71%)

Table II.9. FMOs of neutral compounds, **1,3-Az[*n*]CPPs**, where *n* = 5,7,9 and 11.

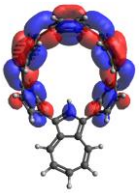
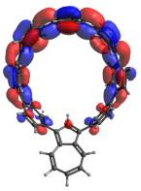
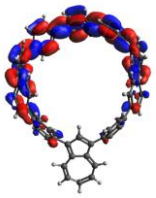
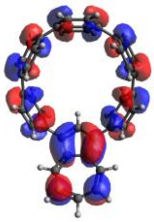
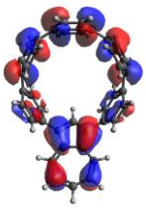
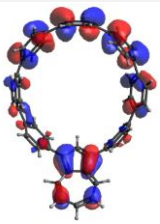
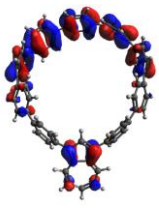
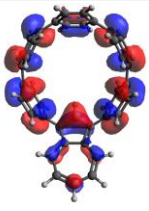
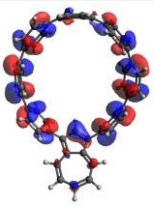
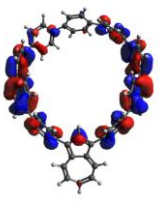
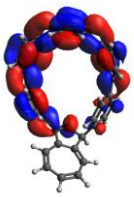
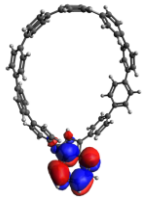
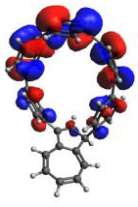
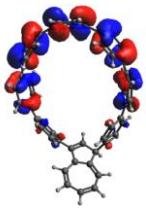
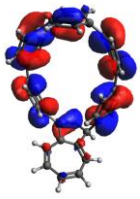
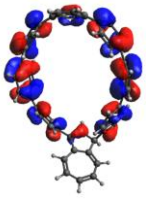
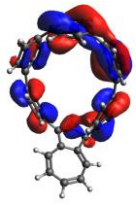
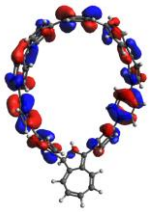
Energy Level	P1	P2	1,3-Az[9]CPP	P3
LUMO+2				
	-1.522 eV	-1.511 eV	-1.535 eV	-1.564 eV
LUMO+1				
	-1.549 eV	-1.640 eV	-1.628 eV	-1.619 eV
LUMO				
	-2.008 eV	-2.012 eV	-2.022 eV	-2.029 eV
HOMO				
	-4.696 eV	-4.836 eV	-4.895 eV	-4.888 eV
HOMO-1				
	-5.421 eV	-5.253 eV	-5.254 eV	-5.288 eV
HOMO-2				
	-5.569 eV	-5.522 eV	-5.462 eV	-5.436 eV

Table II.10. FMOs of protonated **1,3-Az[n]CPPs**, where *n* = 5,7,9 and 11.

Energy Level	$[P1+H]^+$	$[P2+H]^+$	$[1,3\text{-Az}[9]\text{CPP}+H]^+$	$[P3+H]^+$
LUMO+2				
	-1.973 eV	-1.909 eV	-1.950 eV	-1.880 eV
LUMO+1				
	-3.585 eV	-3.592 eV	-3.591 eV	-3.602 eV
LUMO				
	-3.737 eV	-3.735 eV	-3.728 eV	-3.739 eV
HOMO				
	-5.463 eV	-5.473 eV	-5.402 eV	-5.428 eV
HOMO-1				
	-6.153 eV	-5.950 eV	-5.810 eV	-5.742 eV
HOMO-2				
	-6.977 eV	-6.501 eV	-6.201 eV	-6.002 eV

II.4.3. Mass spectrometric data of 1,3-Az[*n*]CPPs

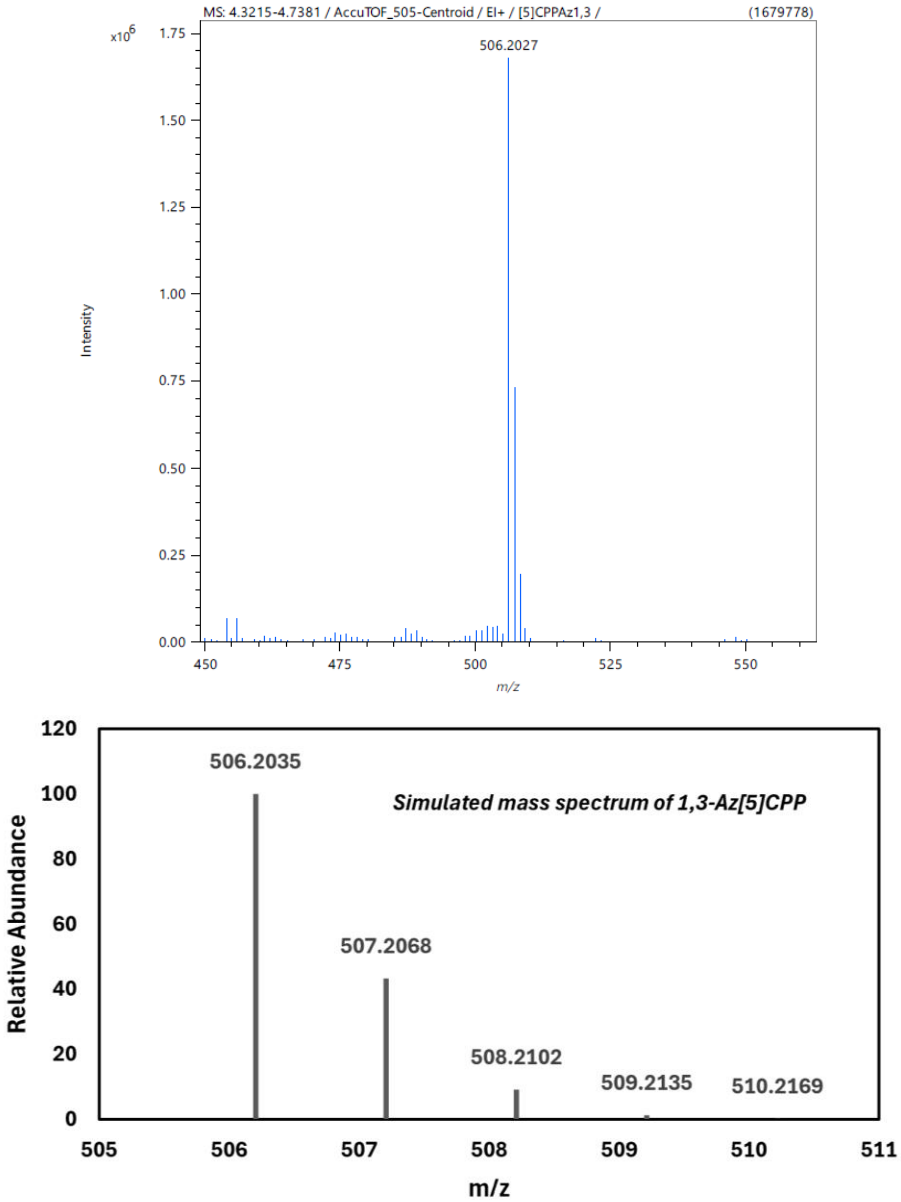
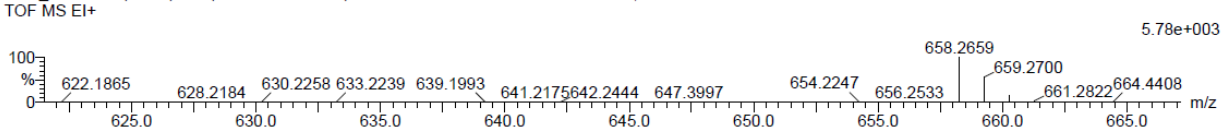


Figure II.17. HRMS (EI^+-TOF, AccuTOF) chart of **1,3-Az[5]CPP** and its calculated isotopic distribution (calcd. for $C_{40}H_{26}$; $[M]^+$).

Monoisotopic Mass, Odd and Even Electron Ions
504 formula(e) evaluated with 5 results within limits (all results (up to 1000) for each mass)
Elements Used:
C: 0-60 H: 0-100 N: 0-5 O: 0-10
GCT_10746 51 (1.870) Cm (46:51-9:21x2.000) Order ;
TOF MS EI+



Minimum:				-1.5		
Maximum:		5.0	5.0	150.0		
Mass	Calc. Mass	mDa	PPM	DBE	i-FIT	Formula
658.2659	658.2661	-0.2	-0.3	36.0	4.2	C52 H34
	658.2679	-2.0	-3.0	23.0	51.2	C40 H38 N2 O7
	658.2666	-0.7	-1.1	23.5	69.1	C38 H36 N5 O6
	658.2652	0.7	1.1	18.5	94.7	C37 H40 N O10
	658.2639	2.0	3.0	19.0	119.2	C35 H38 N4 O9

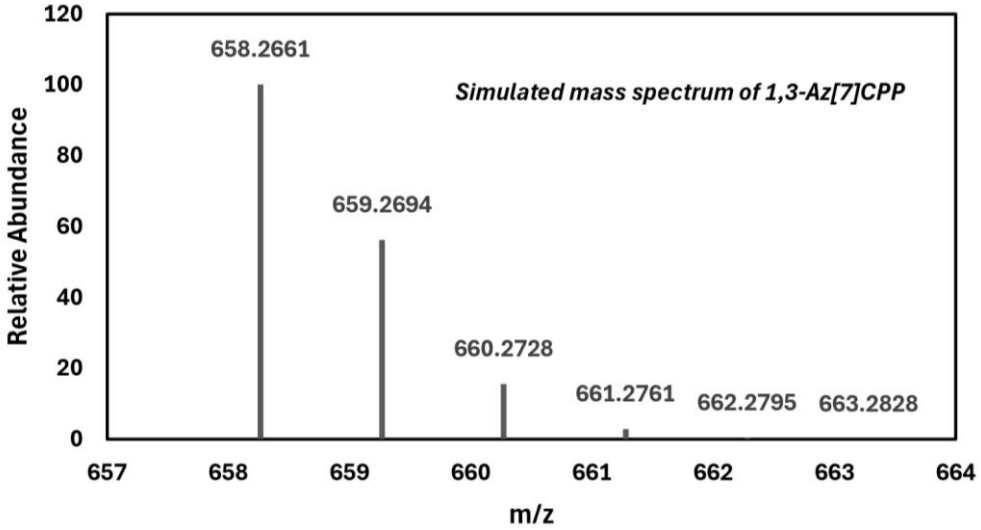


Figure II.18. HRMS (EI^+-TOF) chart of **1,3-Az[7]CPP** and its calculated isotopic distribution (calcd. for $C_{52}H_{34}$; $[M]^+$).

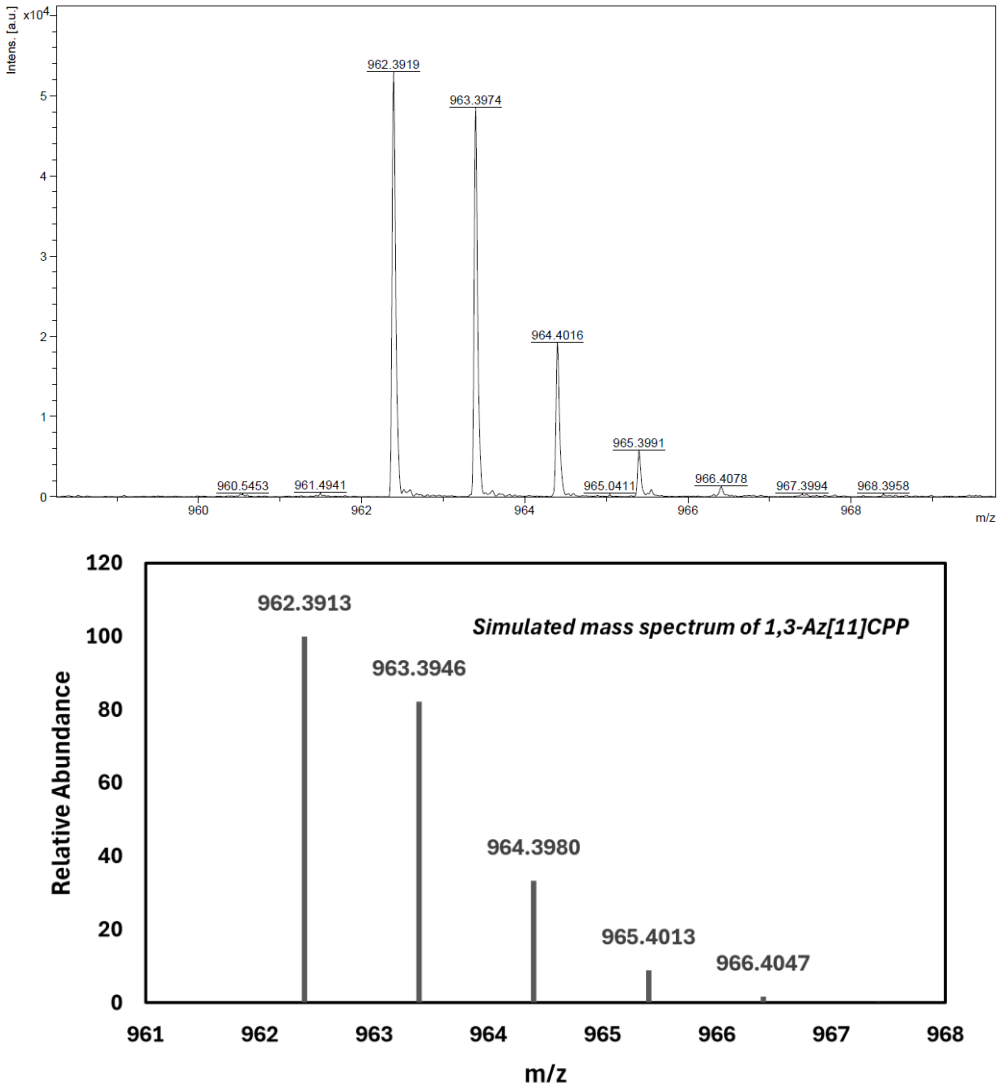


Figure II.19. HRMS (MALDI-TOF) chart of **1,3-Az[11]CPP** and its calculated isotopic distribution (calcd. for $C_{76}H_{50}$; $[M]^+$).

II.5. Bridge to Chapter II

This chapter describes the synthesis of 1,3-Az[*n*]CPPs (*n* = 5, 7, 11) and their characterization using spectroscopic methods and single crystal X-ray diffraction. Photophysical studies indicate that incorporating azulene via 1,3-position results in the retention of both the anti-Kasha emission and halochromic behaviors characteristic of azulene. In the next chapter, another non-alternant PAH-embedded nanohoop is discussed, focusing on the synthesis of cyclopenta[*hi*]aceanthrylene-containing CPP.

CHAPTER III SYNTHESIS OF CYCLOPENTA[*HI*]ACEANTHRYLENE-CONTAINING CYCLOPARAPHENYLENES

This chapter was written by myself with editorial assistance from Professor Ramesh Jasti. This work discusses the early efforts in incorporating cyclopenta[*hi*]aceanthrylene into the CPP system.

III.1. Introduction

Cyclopenta-fused polycyclic aromatic hydrocarbons (CP-PAH) captures a lot attention due to their great electronic accepting ability. Within this family, cyclopenta[*hi*]aceanthrylene (CPA), an anthracene fused with two five-membered rings, as a subsegment of C_{70}, is a good electronic acceptor (Figure III.1a).[76,77] Although CPA has a total of 18 π electrons, fulfilling the criteria for Hückel aromaticity, crystallographic analysis reveals electronic localization, where the electronic character resembles a delocalized anthracene core and two virtually isolated double bonds, with more localized electrons.[77] However, CPA can readily undergo a two-electron reduction to achieve aromatic stabilization by forming two benzocylopentadienyl anions, a phenomenon supported by computational study[78] and experimentally by cyclic voltammetry[77] (Figure III.1b).

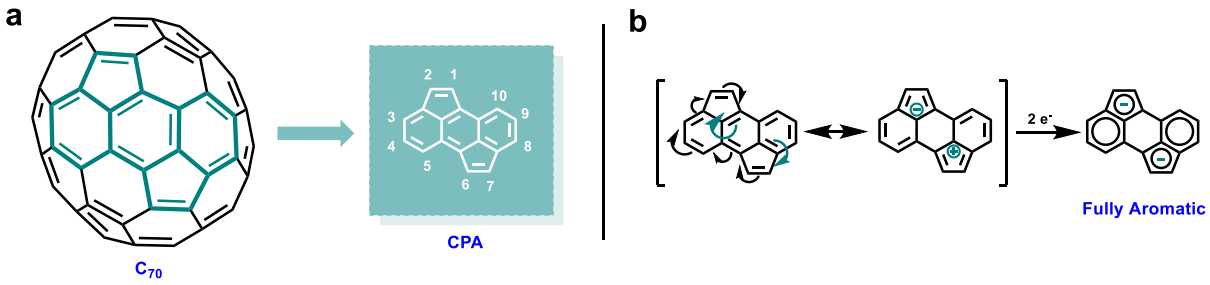


Figure III.1. (a) Cyclopenta[*hi*]aceanthrylene (CPA) is a subsegment of C_{70}. (b) The resonance structure of CPA. Upon accepting two electrons, the resulting dianion is fully aromatic.

A primary advantage of CPA over fullerenes is the increased feasibility of structural functionalization. Fullerene derivatives are typically limited to addition reactions[79], while CPA scaffolds can be synthesized in good yields and provide functionalization handle for precise electronic tuning. Historically, the synthesis of PAHs relied on high temperature flash vacuum pyrolysis (FVP). However, more efficient synthetic methods have been established since the early 2000s (Figure III.2). In 2001, Garcia-Garibay and co-workers pioneered the synthesis of the anthracene fused with one five membered ring, known as aceanthrylene **III.2**, by subjecting 9-bromoanthracene **III.1** to a condition similar to Sonogashira coupling reaction in the absence of

Cu(I) catalyst, achieving 93% selectivity over the side product **III.3**. By 2002, this group extended the methodology to append a second five-membered ring, yielding the CPA derivative **III.5**. These seminal works simplified access to CPA-based scaffolds. The field was further advanced in 2012 by the Plunkett group, who established a robust, multigram synthesis of BisTMS-CPA **III.7**. Subsequent bromination with *N*-bromosuccinimide yielded DiBr-CPA (**III.8**), while Ir-catalyzed C-H activation enabled the installation of boronic ester groups at the 4,9-positions (**III.9**) in great yield.

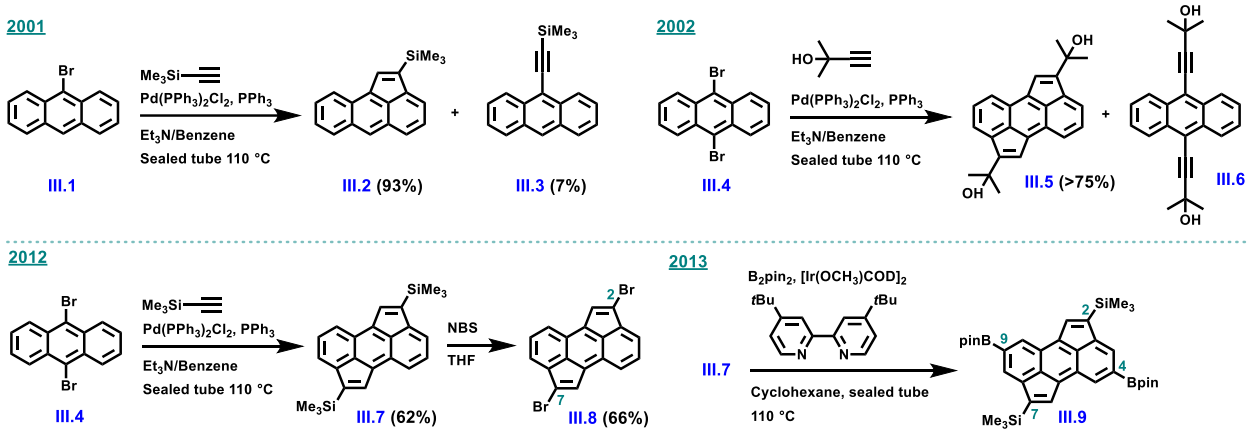


Figure III.2. The synthetic evolution of aceanthrylene derivative III.2 and CPA derivatives (**III.5, III.7– III.9**).

With these CPA building blocks (**III.8** and **III.9**) in hand, researchers have successfully functionalized the CPA core via cross coupling reactions, such as Suzuki and Sonogashira reactions to systematically decorate the periphery a the 2,7-positions (**III.11** and **III.12**) and tune its frontier molecular orbital energy levels (Figure III.3).[80–82] Furthermore, **III.8** has been utilized to construct conjugated ladder polymers (**III.17**) containing nonbenzenoid moieties through on-surface chemistry.[83] It is noteworthy that external fusion of five-membered rings onto the PAH scaffold lowers the LUMO more effectively than internal fusion[78,84], rendering CPA a good electron acceptor for *n*-type materials and an active component for donor-acceptor (D-A) or D-A-D systems (**III.10**, **III.14** and **III.15**).[82,85,86] Beyond cross coupling reactions, the bromine groups on **III.8** can be substituted with cyano groups, which significantly lowers the LUMO and reduces the antiaromatic character of the fused five membered ring.[87] In a similar vein, the diradicaloid character of the five-membered ring of CPA (Figure III.3b) has been shown to promote the conversion of polyynes into cumulene when CPA is used as the end-capping groups.[88] Finally, by taking advantage of the large π-surface area of the CPA unit, researchers designed **III.13**, in which

CPA is appended with phenylene with dodecyl hydrophilic side chains to facilitate the debundling of single-walled carbon nanotubes (SWCNTs).[89] Collectively, these examples highlight the significance of this moiety as a modular and highly tunable building blocks for materials applications.

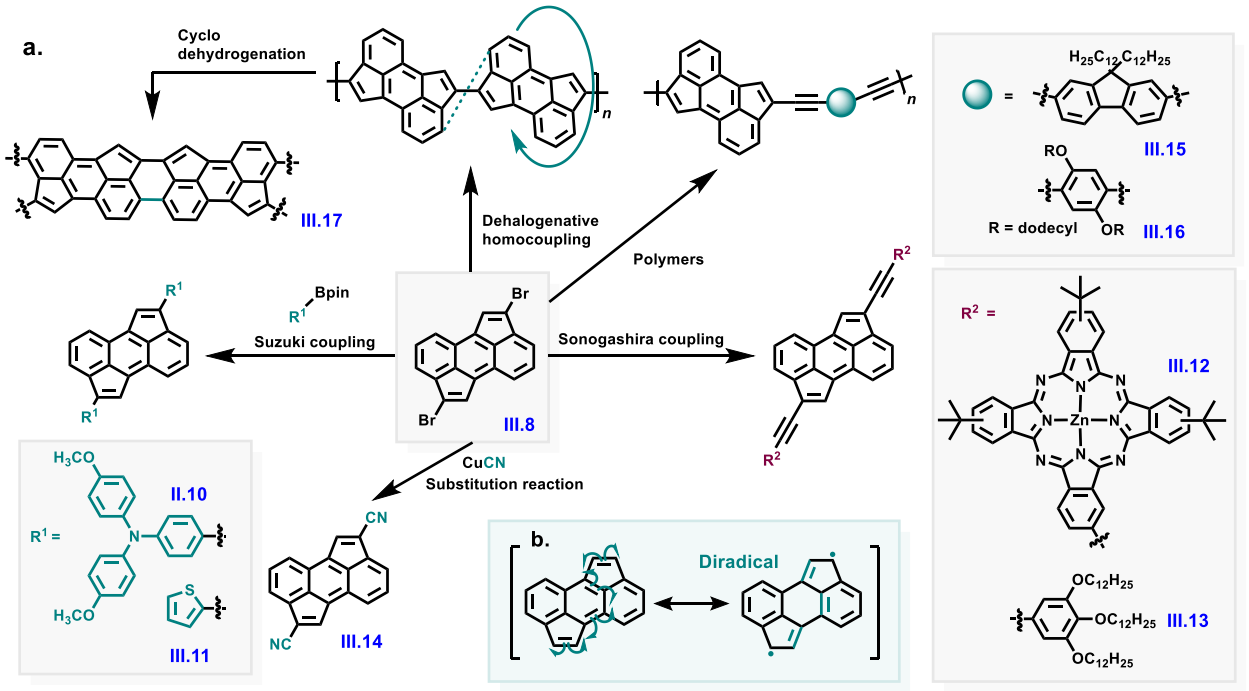
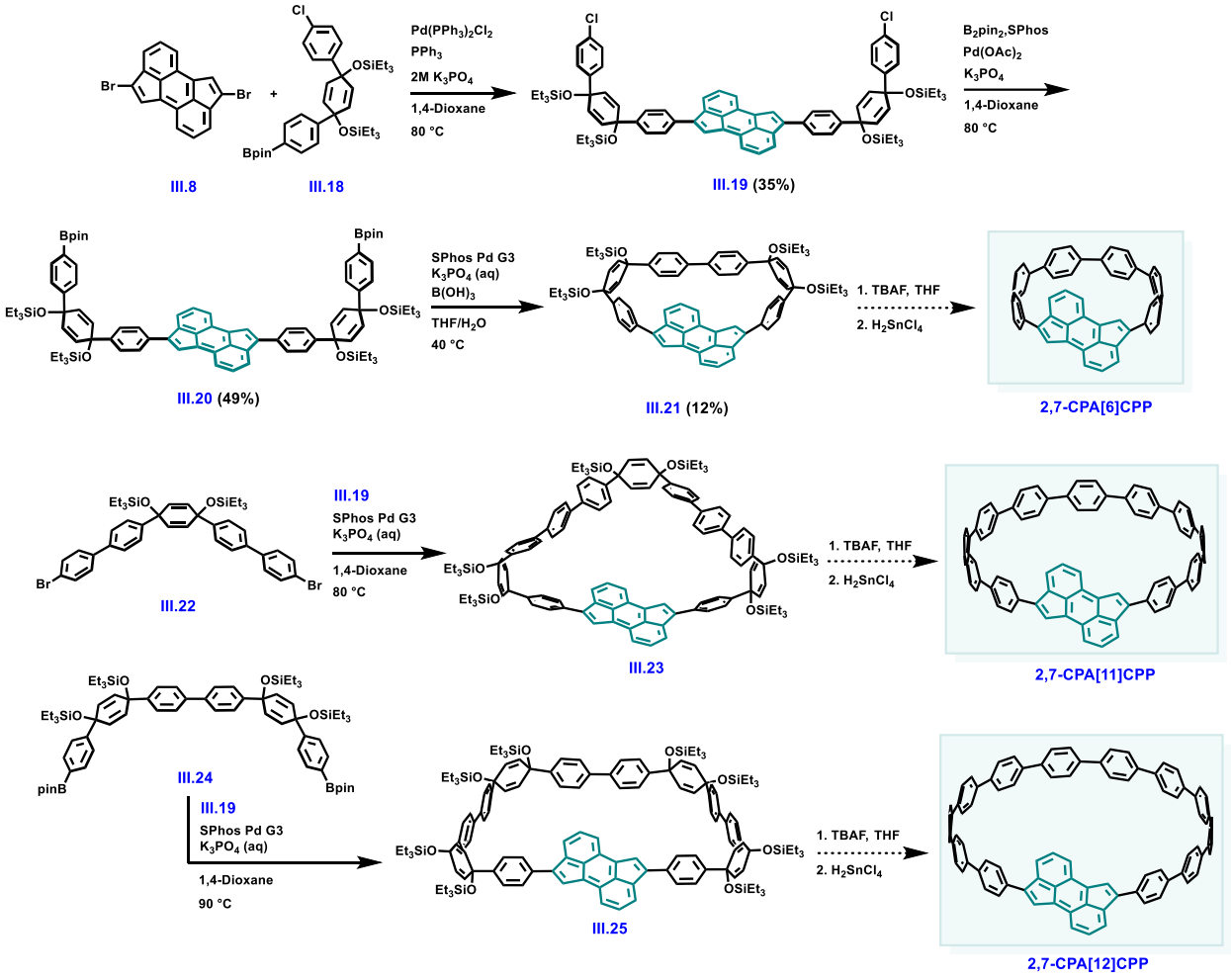


Figure III.3. (a) Selective examples of CPA-based structures demonstrating the tunability of the CPA core upon appending different functional groups, highlighting their applications in materials and polymer applications. (b) Resonance structures illustrating the diradical character of CPA.

III.2. Results and Discussions

We envisioned that by incorporating CPA units into the CPP backbone, a donor-acceptor system could be realized, and the site of CPA incorporation would lead to distinct photophyscai properties. This section presents the preliminary results regarding the synthesis of macrocyclic precursor for **2,7-CPA[*n*]CPP** (*n* = 6, 7, 11 and 12) and **4,9-CPA[7]CPP**, where the numerical prefix denotes the site of substitution on the CPA and *n* specifies the number of phenylene units in the nanohoop (Scheme III.1). DiBr-CPA (**III.8**) was synthesized according to the literature procedure.[81] Suzuki cross coupling of **III.8** with the three-ring, cyclohexadiene-containing building block **III.18** afforded the intermediate **III.19** in 38% yield, followed by Miyaura borylation to yield the bisboronic esters **III.20**. With both **III.19** and **III.20** in hand, we targeted the large macrocyclic precursor for **2,7-BisCPA[12]CPP**. However, this reaction failed to yield

the target and instead, the oxidative homocoupled product **III.21** was isolated in 12% yield, as confirmed by mass spectrometry and ^{1}H NMR spectroscopy. To favor this homocoupling pathway, we replaced $Pd(PPh_3)_2Cl_2$ with the more active SPhos Pd G3 catalyst, employing the standard oxidative homocoupling conditions[90] to reproduce these results. With a small amount of **III.21** on hand, deprotection and aromatization was attempted to obtain **2,7-CPA[6]CPP**. However, analysis of the crude ^{1}H NMR spectrum revealed no characteristic signals corresponding to the protons on the CPA unit. We hypothesize that the target compound decomposed under the reaction conditions. This is supported by the fact that its less-strained macrocyclic precursor **III.21** can undergo slow degradation at ambient temperature over time. Consequently, the exploration of alternative aromatization methods and careful storage of **III.21** are necessary for future studies.



Scheme III.1. Synthetic schemes for **2,7-CPA[*n*]CPP** (*n* = 6,11 and 12).

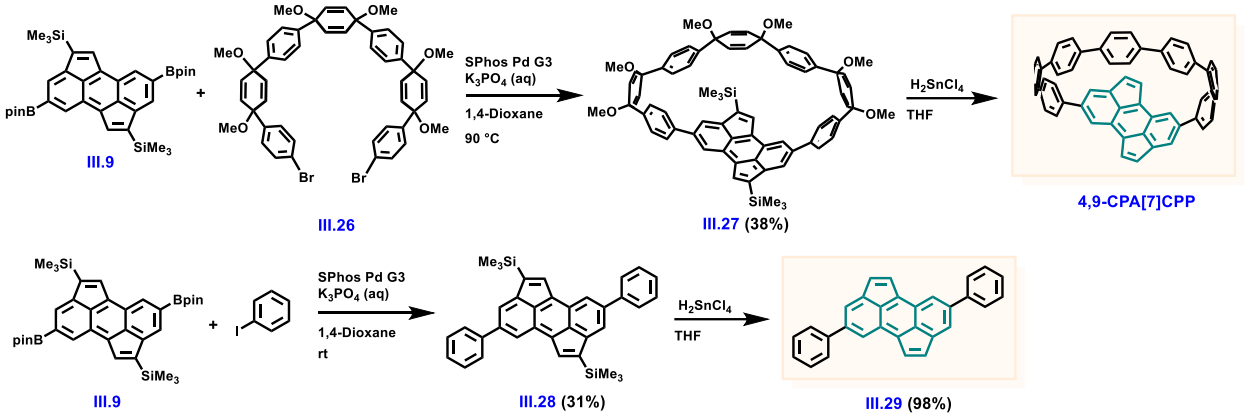
Synthesis of larger sized 2,7-CPA[*n*]CPPs were also attempted. The macrocyclic precursors **III.23** for 2,7-CPA[11]CPP was obtained by subjecting V-shaped building block **III.22** to Suzuki cross-coupling conditions with **III.20**. Similarly, the C-shaped 6-ring building block **III.24** reacted with **III.19** to afford the macrocycle **III.25** in near quantitative yield and high purity as confirmed by ^{1}H NMR spectroscopy. However, the deprotection and aromatization also failed to afford the fully aromatized **2,7-CPA[12]CPP** target.

With these results, we shifted our focus to the synthesis of **4,9-CPA[7]CPP**, in which the anthracene core is incorporated into the nanohoop backbone. We hypothesized that incorporation at the 4,9-position would result in greater structural stability because modification at these sites has a less pronounced impact on the HOMO-LUMO gap compared to the 2,7-postion. Furthermore, the choice of this specific size is also inspired by the work of Du and coworkers, who reported **[7]CPPRu$_{2,9}$**, a structurally similar target featuring an intercalated rubicene units.[9] As shown in **Figure III.5**, by utilizing the Suzuki macrocyclization, the 4,9-bisboronic ester substituted CPA (**III.9**) was reacted with C-shaped, methoxy protected seven-ring intermediate (**III.26**) to afford the desired macrocyclic precursor (**III.27**) in 38% yield. Excitingly, treatment of **III.27** with H_2SnCl_4 (6.3 equivalents) afforded the fully aromatized **4,9-CPA[7]CPP** as an orange solid. It is noteworthy that the trimethyl silyl groups (TMSs) were cleaved during the reductive aromatization step.

Subsequently, with the target CPP on hand, we synthesized a model compound (**III.28**) to evaluate the influence of the CPA unit on the photophysical properties of the parent CPP system. The model compound was prepared by reacting **III.9** with iodobenzene under Suzuki cross-coupling conditions to afford **III.28**. Subsequent deprotection of TMS groups using excess of H_2SnCl_4 (13 equivalents) afforded **III.29** as a red solid. It is noteworthy that this desilylation step requires a larger excess of the reductant compared to the macrocyclic precursor (**III.27**). We attributed this to the fact that during macrocyclic aromatization, the in-situ generation of methanol facilitates TMS cleavage, a process that is absent in the synthesis of the model compound.

The photophysical properties of **III.29** and **4,7-CPA[7]CPP** were probed by UV-Vis spectroscopy in CH_2Cl_2 solution. Neither compound exhibits observable fluorescence under UV lamp. As shown in Figure III.4, the macrocycle exhibits the characteristic CPP absorption peak at 335 nm, attributed to HOMO to LUMO+1 transition (λ_{calc}= 344 nm), while the peak centered around 500 nm is attributed to the HOMO-1 to LUMO transition (λ_{calc}= 505 nm). The UV-Vis

spectrum of the model compound resembles that of **III.30**, in which two thiophenes are appended at the 4,9-position.[81]



Scheme III.2. Synthetic schemes of 4,9-CPA[7]CPP and the planar model compound **III.29**.

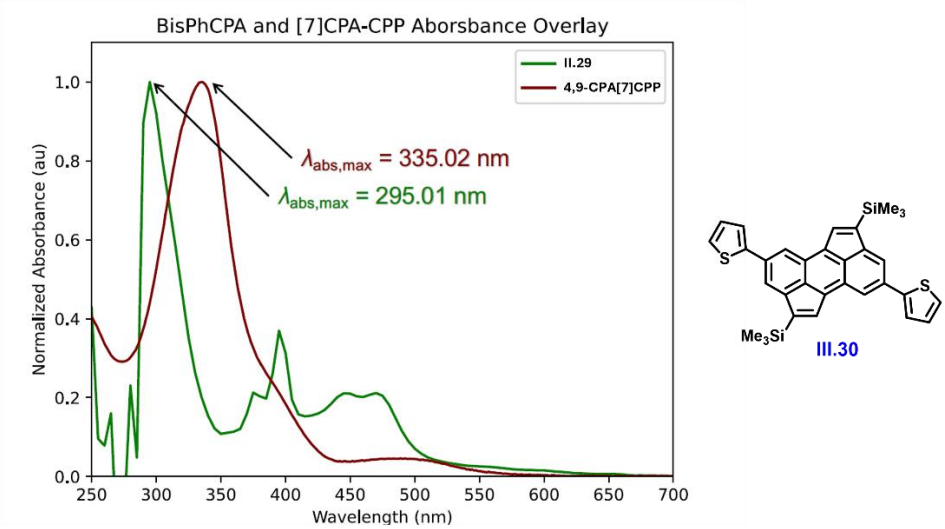


Figure III.4 UV-Vis spectra of 4,9-CPA[7]CPP & III.29 in CH_2Cl_2 and the literature reported compound III.30 (The UV-Vis figure is plotted by Brandon).

To evaluate the effect of connectivity on the photophysical properties of CPA-containing nanohoops, we subsequently explored the synthesis of the 2,7-CPA[7]CPP isomer. This was attempted by subjecting building block **III.8** to a Suzuki cross-coupling reaction with the dibromo, methoxy-protected seven-ring intermediate (**III.31**). However, the major product observed was the seven-ring methoxy-protected macrocycle (**III.33**), with only a minor amount of the target compound formed, as evidenced by the characteristic peaks in ^{1}H NMR spectrum (Figure III.5). Alternative synthetic pathways must be identified, as the isolation of the target compound from the major side product (**III.33**) proved challenging due to similar polarities and limited solubility.

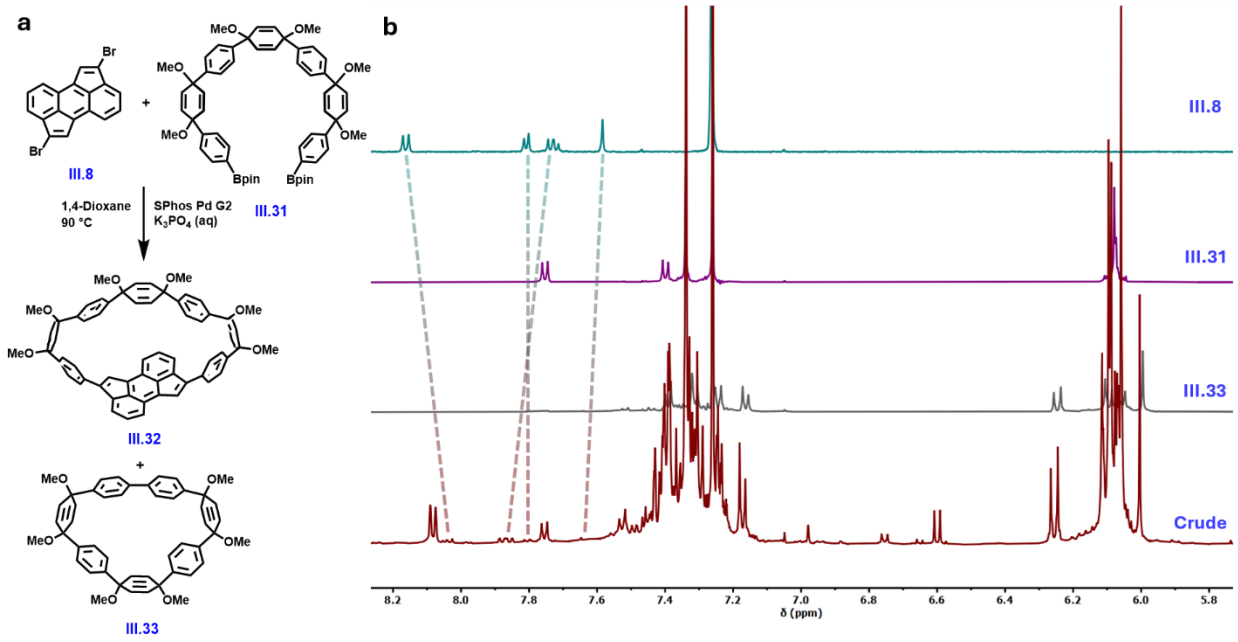


Figure III.5. (a) Synthesis schemes of **2,7-CPA[7]CPP**. (b) ^{1}H NMR spectra of the starting materials and the crude reaction mixture. The gradient lines track the chemical shift changes of the characteristic peaks on the CPA unit before and after the macrocyclization.

III.3. Conclusions

In conclusion, this chapter has detailed our research progress toward the synthesis of CPA-containing CPPs. Although only 4,9-CPA[7]CPP was successfully isolated, the groundwork has been established for further development. If the aromatization conditions for the 2,7-CPA[*n*]CPP (*n* = 6, 7, 11 and 12) can be further optimized, a library of CPA-CPP derivatives could be obtained. Subsequent cyclic voltammetry studies would then allow for a systematic evaluation of their electronic accepting abilities and the impact of the CPA unit on their redox properties. Additionally, the good electronic-accepting behavior of CPA may serve as an interesting motif for the construction of rotaxanes (Figure III.6), where the formation of the rotaxane may induce fluorescence quenching of the macrocycle while providing increased protection for the π-conjugated thread.[91,92]

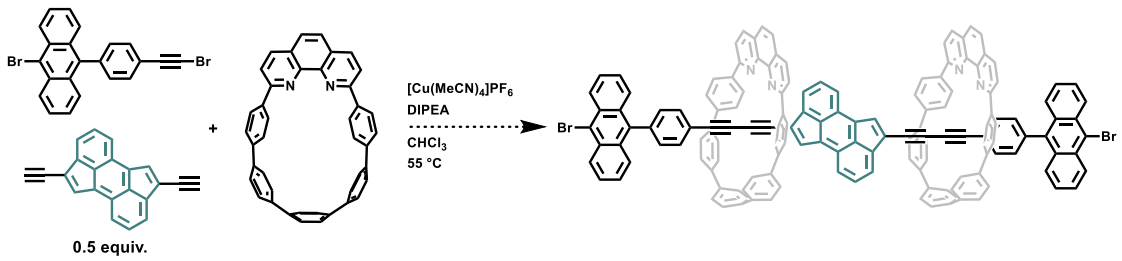
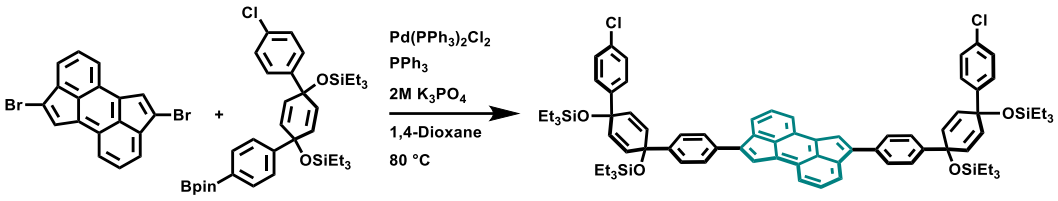


Figure III.6. Proposed synthetic strategy for the [3]rotaxane with a CPA-containing thread.

III.4. Methods and Materials

All reagents were purchased from commercial sources and used as received from commercial suppliers. **III.18**[69], **III.22**[69], **III.24**[93], **III.26**[94], **III.31**[94], SPhos Pd G3[95] were prepared according to the literature methods and the obtained ^{1}H NMR spectra are consistent with literature. Anhydrous tetrahydrofuran (THF) and 1,4-Dioxane were taken from solvent purification system (SPS) without further purification. For the stationary phase used in column chromatography, silica gel is purchased from ZEOCHEM® (ZEOprep Silicagel 60 HYD / 40–63 µm). Proton (^{1}H) and carbon (^{13}C{^{1}H}) NMR spectra were recorded on the Bruker Avance-III HD 500 MHz NMR Spectrometer. $CDCl_3$ used for NMR experiment is 99.8% deuterated with 0.05% v/v tetramethylsilane (TMS). Chemical shifts were given in ppm relative to residue protons ($CHCl_3$: 7.26, s for ^{1}H, 77.16, t for ^{13}C, CH_2Cl_2: quintet for ^{1}H: δ = 5.32 and quintet for ^{13}C: δ = 53.84). The abbreviations of s, d, t, q and m represent the multiplicities of singlet, doublet, triplet, quartet and multiplet, respectively. Mass spectrometric data were acquired by Waters Synapt G2-Si ESI/LC-MS (ESI) and Bruker Daltonics UltrafleXtreme MALDI TOFTOF (MALDI). UV-vis spectra were acquired in SPS-grade DCM using a 1 cm quartz cuvette on an Agilent Cary 60 UV-Vis Spectrometer. Preparation of fresh H_2SnCl_4 solution: To a solution of $SnCl_2$•$2H_2O$ (140 mg, 0.620 mmol) in 13 mL THF was added conc. HCl (0.10 mL, 1.241 mmol). The resulting solution was then stirred for 30 minutes prior to use. The density functional theory (DFT) calculations were performed with the Gaussian 09 program (Revision E. 01). The ground state geometries of 4,9-CPA[7]CPP was optimized at B3LYP/6-31G(d) level of theory incorporating GD3BJ dispersion. Time-dependent (TD)-DFT calculations were carried out for the first 12 excited states at CAM-B3LYP/6-31G(d,p) level of theory with the correction of PCM to consider the solvent effect of dichloromethane.

III.4.1. Synthetic procedures

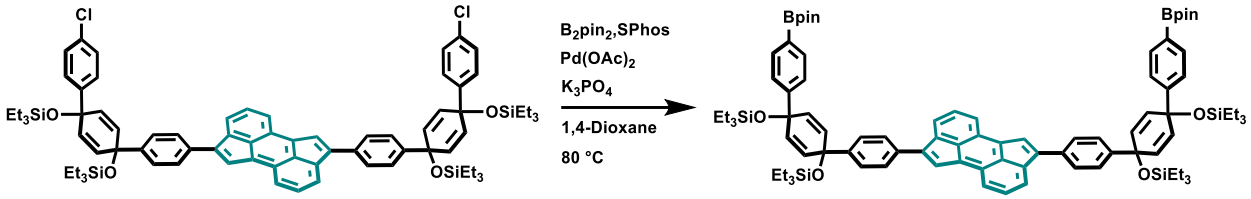


III.8 III.18 III.19 (35%)

Synthesis of III.19: To 25 mL round bottom flask were added **III.8** (100 mg, 0.260 mmol, 1 equiv.), **III.18** (340.2 mg, 0.520 mmol, 2 equiv.), $Pd(PPh_3)_2Cl_2$ (18.3 mg, 0.026 mmol, 10 mol%) and PPh_3 (13.7 mg, 0.052 mmol, 20 mol%). The flask was evacuated and back-filled with N_2 three times before introduction of 1,4-dioxane (10 mL). The reaction mixture was sparged for 10 min before heating in the oil bath to 80 ºC. An aqueous solution of K_3PO_4 (2 M, 6.5 mL) was added. After stirring at 80 ºC for 5.5 h, the mixture was cooled to room temperature and filtered through a silica plug (eluting with DCM). The concentrated filtrate was dissolved in minimal amount of DCM and layered over methanol. The resulting precipitate was collected by vacuum filtration and further purified by flash column chromatography (crude was dissolved in hexanes and loaded onto silica gel, gradient elution: 10–25% DCM in hexanes). The fractions containing the product were concentrated and triturated in methanol to afford **III.19** as a green solid (116 mg, 35%). $R_f = 0.26$ (25% DCM in hexanes).

^{1}H NMR (500 MHz, $CDCl_3$) δ 8.27 (d, J = 8.4 Hz, 2H), 8.06 (d, J = 6.6 Hz, 2H), 7.78 (d, J = 9.6 Hz, 4H), 7.73 (dd, J = 8.4, 6.7 Hz, 2H), 7.66 (s, 2H), 7.46 (d, J = 8.5 Hz, 4H), 7.33 (d, J = 8.7 Hz, 4H), 7.27 (d, J = 8.3 Hz, 4H), 6.09 (d, J = 10.1 Hz, 4H), 6.01 (d, J = 10.2 Hz, 4H), 0.98 (t, J = 8.0 Hz, 18H), 0.96 (t, J = 7.9 Hz, 18H), 0.66 (q, J = 7.9 Hz, 12H), 0.63 (q, J = 7.9 Hz, 12H).

^{13}C {^{1}H} NMR (126 MHz, $CDCl_3$) δ 145.30, 144.85, 142.27, 139.87, 137.50, 135.48, 133.17, 131.94, 131.39, 129.09, 128.84, 128.43, 127.96, 127.55, 126.76, 126.49, 126.10, 124.58, 123.68, 71.34, 7.24, 7.20, 6.65, 6.60.

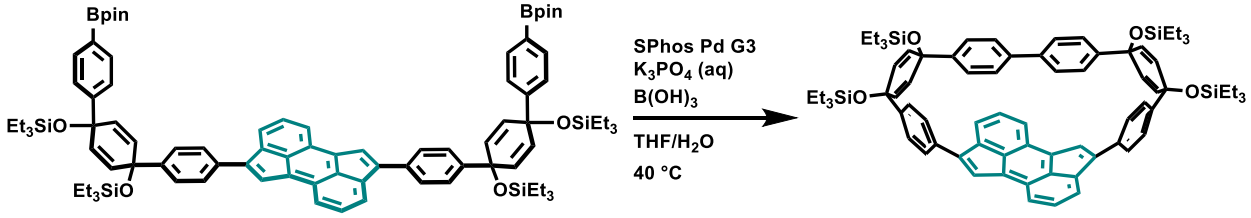


III.19 III.20 (49%)

Synthesis of III.20: To a flamed-dried flask were charged with **III.19** (467 mg, 0.366 mmol), B_2Pin_2 (372 mg, 1.46 mmol, 4 equiv.), $Pd(OAc)_2$ (8 mg, 0.037 mmol, 10 mol%), SPhos (30.0 mg, 0.073 mmol, 20 mol%) and K_3PO_4 (466 mg, 2.19 mmol, 6 equiv.). The flask was subjected to evacuation and back-filled with N_2 five times before introduction of 1,4-Dioxane (2 mL). After being stirred at 80 ºC for 1 d, the reaction was cooled to room temperature and passed through a celite plug (DCM, 150 ml). The filtrate was concentrated and dissolved in minimal amount of DCM and layered over methanol. The recrystallized solids were collected by vacuum filtration to afford the product as a dark green solid (261 mg, 49%) with decent purity and can be used without further purification.

^{1}H NMR (500 MHz, $CDCl_3$) δ 8.30 (d, J = 8.4 Hz, 2H), 8.10 (d, J = 6.7 Hz, 2H), 7.79 (d, J = 8.1 Hz, 8H), 7.76 (dd, J = 8.4, 6.9 Hz, 2H), 7.69 (s, 2 H), 7.51 (d, J = 8.3 Hz, 4H), 7.47 (d, J = 8.1 Hz, 4H), 6.08 (s, 8H), 1.02 (t, J = 8 Hz, 18H), 0.97 (t, J = 8 Hz, 18H), 0.71 (q, J = 7.9 Hz, 12H), 0.63 (q, J = 7.9 Hz, 12H).

^{13}C {^{1}H} NMR (126 MHz, $CDCl_3$) δ 149.38, 145.52, 142.37, 139.92, 137.51, 135.34, 134.91, 131.77, 131.55, 129.08, 128.81, 127.93, 126.80, 126.50, 126.06, 125.46, 124.57, 123.64, 83.92, 71.70, 71.65, 25.04, 7.26, 7.21, 6.65, 6.64.



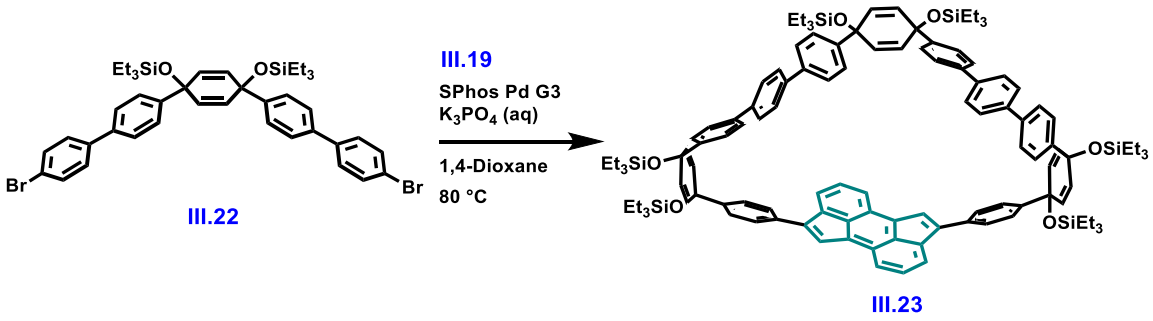
III.20 III.21 (12%)

Synthesis of III.21: To a 25 mL round bottom flask were added **II.20** (14.6 mg, 0.010 mmol), SPhos Pd G3 (4.68 mg, 0.006 mmol, 60 mol%), $B(OH)_3$ (3.09 mg, 0.05 mmol, 5 equiv). THF (10 mL) and DI water (1 mL) were added, and the reaction mixture was stirred vigorously at 40 ºC in

an open flask before the addition of an aqueous solution of K_3PO_4 (2 M, 0.005 mL, 1 equiv.). After being stirred at 40 ºC for 24 h, the reaction mixture was cooled to room temperature and diluted with DCM (15 mL). The mixture was transferred to a separatory funnel, together with DI water (30 mL). The organic layer was separated, and the aqueous layer was extracted with additional DCM (30 mL). The combined organic layers were washed with brine (50 mL), dried over Na_2SO_4, filtered and concentrated in vacuo. The crude product was purified via a pipette column chromatography (gradient elution: 25–50% DCM in hexanes) to afford the target compound as a green solid (0.8 mg, 12%). R_f = 0.55 (50% DCM in hexanes).

^{1}H NMR (500 MHz, $CDCl_3$) δ 8.25 (d, J = 8.4 Hz, 2H), 8.05 (d, J = 6.6 Hz, 2H), 7.76 (d, J = 8.4 Hz, 4H), 7.72 (dd, J = 8.4, 6.7 Hz, 2H), 7.64 (s, 2H), 7.49 (d, J = 8.4 Hz, 4H), 7.42 (d, J = 7.0 Hz, 4H), 7.31 (approx. t, J = 7.1 Hz, 4H), 6.06 (s, 8H), 0.99 (t, J = 8 Hz, 18H), 0.93 (t, J = 8.0 Hz, 18H), 0.68 (q, J = 7.9 Hz, 12H), 0.62 (q, J = 7.9 Hz, 12H).

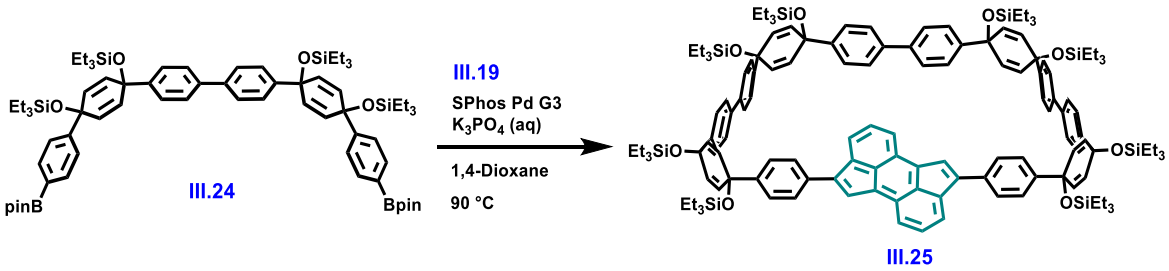
HRMS (TOF MS AP$^+$) calcd for $[M]^+$ $C_{78}H_{94}O_4Si_4$: 1206.6229, found: 1206.5542. error -57.0 ppm



Synthesis of III.23: To a 25 mL round bottom flask were added **III.22** (11.0 mg, 0.0137 mmol, 1 equiv.), **III.19** (20 mg, 0.0137 mmol, 1 equiv.), SPhos Pd G3 (2.67 mg, 0.0034 mmol, 25 mol%). The flask was evacuated and back-filled with N_2 three times, followed by addition of 1,4-Dioxane (10 mL). The reaction mixture was heated in an oil bath at 80 ºC for 3 min before addition of an aqueous solution of K_3PO_4 (2 M, 0.07 mL). After being stirred at 80 ºC for 1 day, the reaction was cooled to room temperature. The reaction mixture was concentrated in vacuo and purified via flash column chromatography (1st column: gradient: 25–40% DCM in hexanes, 2nd column: 6% EtOAc in hexanes) to afford the target compound in good purity. R_f = 0.46 (6.25% DCM in hexanes).

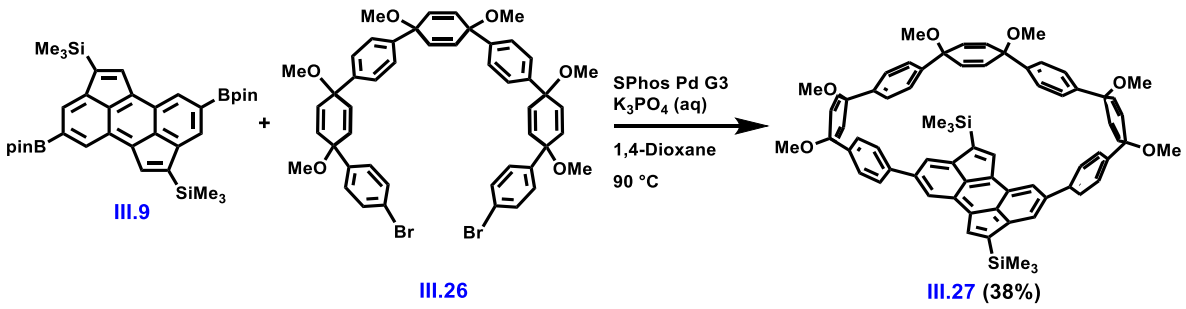
^{1}H NMR (500 MHz, $CDCl_3$) δ 8.26 (d, J = 8.3 Hz, 2H), 8.06 (d, J = 6.7 Hz, 2H), 7.77 (d, J = 8.3 Hz, 4H), 7.71 (dd, J = 8.4, 6.7 Hz, 2H), 7.68–7.64 (m, 10H), 7.60 (d, J = 8.4 Hz, 4H), 7.57 (d, J = 8.4 Hz, 4H), 7.51 (d, J = 8.3 Hz, 4H), 7.49 (d, J = 8.3 Hz, 4H), 7.42 (d, J = 8.5 Hz, 4H), 6.10 (d, J

= 10.4 Hz, 4H), 6.09 (d, *J* = 10.3 Hz, 4H), 6.04 (s, 4H), 1.01 (t, *J* = 8.0 Hz, 12H), 0.99 (t, *J* = 8.0 Hz, 12H), 0.94 (t, *J* = 8.0 Hz, 12H), 0.70 (q, *J* = 7.8 Hz, 12 H), 0.68 (q, *J* = 7.9 Hz, 12H), 0.62 (q, *J* = 7.9 Hz, 12H).



Synthesis of III.25: To a 100 mL round bottom flask were added **II.19** (50 mg, 0.039 mmol, 1 equiv.), **II.24** (50.8 mg, 0.041 mmol, 1.05 equiv.), SPhos Pd G3 (7.64 mg, 0.098 mmol, 25 mol%). The flask was evacuated and back-filled with N_2 three times before introduction of 1,4-dioxane (39 mL, 1 mM). The reaction was heated to 90 ºC for 5 min before an aqueous solution of K_3PO_4 (2 M, 0.39 mL) was added. After stirring at 90 ºC for 15 h, the mixture was cooled to room temperature, filtered through a silica plug (eluting with 100% Hexanes) and concentrated in vacuo. The concentrated crude was triturated in methanol to afford the target compound **II.25** as a green solid in decent purity. R_f = 0.43 (5% EtOAc in hexanes).

^{1}H NMR (500 MHz, $CDCl_3$) δ 8.26 (d, *J* = 8.4 Hz, 2H), 8.05 (d, *J* = 6.7 Hz, 2H), 7.77 (d, *J* = 8.4 Hz, 4H), 7.72 (dd, *J* = 8.5, 6.8 Hz, 2H), 7.65 (s, 2H), 7.47 (approx.t, J = 8.8 Hz, 8H), 7.37 (approx. t, *J* = 8.2 Hz, 8H), 7.33 (d, *J* = 8.7 Hz, 4H), 7.26 (d, *J* = 8.7 Hz, 4H), 7.27–7.25 (m, 4H), 6.08 (d, *J* = 10.1 Hz, 4H), 6.03–5.99 (m, 12H) 1.00–0.92 (m, 72H), 0.68–0.57 (m, 48H).



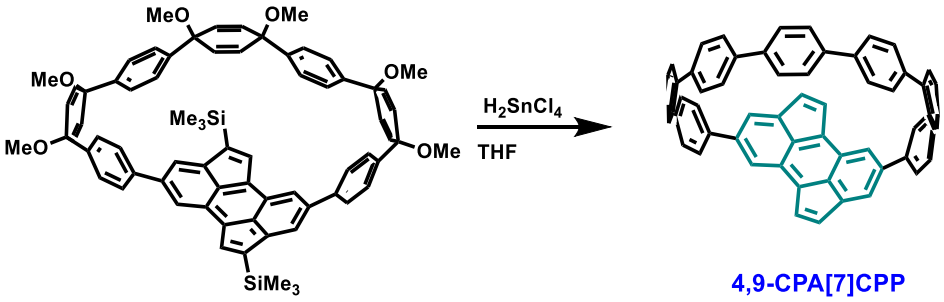
Synthesis of III.27: To a 50 mL round bottom flask were added **III.9** (15 mg, 0.0171 mmol, 1 equiv.), **III.26** (11.2 mg, 0.018 mmol, 1.05 equiv.), SPhos Pd G3 (2.70 mg, 0.003 mmol, 20 mol%). The flask was evacuated and back-filled with N_2 three times before introduction of 1,4-dioxane

(17 mL, 1 mM). The reaction was heated to 80 ºC for 5 min before an aqueous solution of K_3PO_4 (2 M, 0.45 mL) was added. After stirring at 80 ºC for 1 day, the mixture was cooled to room temperature, filtered through a celite plug (eluting with 100% DCM) and concentrated in vacuo. The crude product was purified via flash column chromatography (20% EtOAc in hexanes), concentrated, dissolved in minimal amount of DCM, and recrystallized from methanol. The solids were collected via vacuum filtration to afford **III.27** as a red solid (7.1 mg, 38%). R_f = 0.55 (20% DCM in hexanes).

^{1}H NMR (500 MHz, $CDCl_3$) δ 8.24 (d, J = 0.9 Hz, 2H), 7.98 (d, J = 0.8 Hz, 2H), 7.84 (s, 2H), 7.50 (d, J = 8.5 Hz, 4H), 7.36 (d, J = 8.5 Hz, 4H) 7.26 (d, J = 8.5 Hz, 4H), 7.11 (d, J = 8.5 Hz, 4H), 6.14–6.05 (m, 8H), 5.98–5.93 (m, 4H), 3.51 (s, 6H), 3.36 (s, 6H), 3.18 (s, 6H), 0.48 (s, 18H).

^{13}C {^{1}H} NMR (126 MHz, $CDCl_3$) δ 146.05, 143.71, 143.33, 142.57, 142.37, 142.12, 141.38, 139.83, 135.86, 134.20, 133.94, 133.85, 133.80, 133.18, 132.78, 131.44, 128.03, 127.37, 126.80, 126.54, 126.16, 126.11, 123.98, 75.73, 74.86, 72.47, 52.56, 51.83, 51.43, 51.06.

HRMS (ESI-TOF) m/z calcd for $[M+Na]^+$: $C_{72}H_{70}O_6Si_2Na$: 1109.4609, found 1109.4625. Error +1.44 ppm.



III.27 4,9-CPA[7]CPP

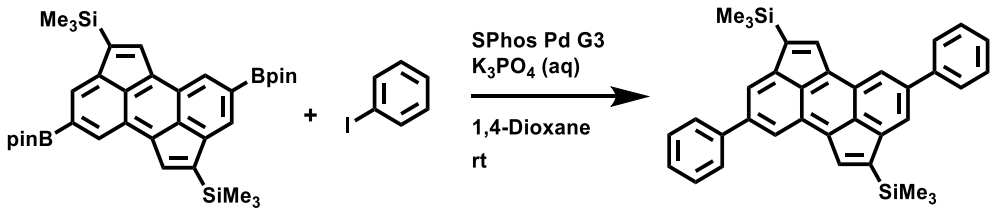
Synthesis of 4,9-CPA[7]CPP: To a 25 mL vial containing **III.27** (7.1 mg, 0.0065 mmol, 1 equiv.) was added THF (1 mL). Freshly prepared H_2SnCl_4 (0.68 mL, 0.041 mmol, 6.3 equiv.) was added to the vial. Upon addition of the reductant, the solution color changed from orange-red to vibrant red. After stirring at room temperature for 20 h, the reaction was quenched by the addition of aqueous $NaHCO_3$ (10 mL). The mixture was diluted with DCM (10 mL) and transferred to a separatory funnel. The organic layer was collected, and the aqueous layer was extracted with additional DCM (10 mL × 2). The combined organic layers were dried over Na_2SO_4, filtered and concentrated in vacuo. The crude product was purified by flash column chromatography (silica

gel, 20% EtOAc in hexanes) to afford the target compound as an orange solid. R_f = 0.49 (20% EtOAc in hexanes).

Note: The product is not stable under concentrated acidic condition. This reactivity may be attributed to halochromism behavior, or alternatively, it may reflect rapid decomposition of the fully aromatized system if the reaction was not properly quenched prior to solvent removal.

^{1}H NMR (500 MHz, $CDCl_3$) δ 8.14 (d, J = 0.9 Hz, 2H), 7.94 (d, J = 0.9 Hz, 2H), 7.62 (d, J = 8.8 Hz, 4H), 7.53–7.45 (m, 26H), 7.10 (d, J = 5.2 Hz, 2H).

HRMS (MALDI) calcd for $[M]^+$ $C_{60}H_{36}$: 756.2812, found: 756.279. Error: -2.90 ppm.

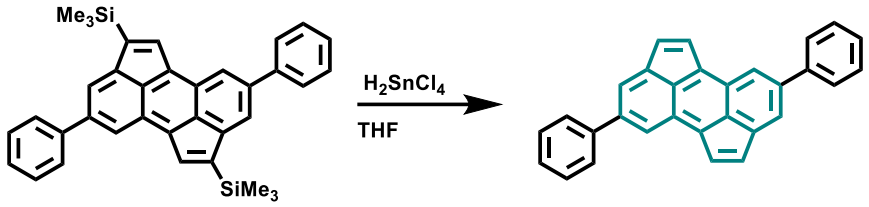


III.9 III.28 (31%)

Synthesis of III.28: To a 5 mL round bottom flask were added **III.9** (11.7 mg, 0.0189 mmol, 1.1 equiv.), iodobenzene (2 µL, 0.0172 mmol, 1.0 equiv.), $Pd(dppf)Cl_2$·DCM (2.1 mg, 0.0026 mmol, 15 mol%). The flask was evacuated and back-filled with N_2 three times before the introduction of 1,4-dioxane (1.72 mL, 10 mM) and an aqueous solution of K_3PO_4 (2 M, 0.172 mL). The reaction proceeds slowly at room temperature. Due to the slow reaction progress, the mixture was subsequently heated to 40 ºC. After stirring at 40 ºC for 20 h, the reaction was cooled to room temperature, filtered through a celite plug (eluting with hexanes), and concentrated in vacuo. The crude product was purified by a silica gel plug (eluting with 10% DCM in hexanes), concentrated and triturated in methanol afforded **III.28** as a red solid (2.8 mg, 31%). R_f = 0.53 (20% DCM in hexanes).

^{1}H NMR (500 MHz, CDCl3) δ 8.34 (d, J = 1.2 Hz, 2H), 8.08 (d, J = 1.1 Hz, 2H), 7.84 – 7.83 (m, 4H), 7.82 (s, 2H), 7.56 (dd, J = 7.7 Hz, 4H),7.46 (t, J = 7.4 Hz, 2H), 0.49 (s,18H).

^{13}C{^{1}H} NMR (126 MHz, CDCl3) δ 145.17, 142.91, 142.65, 142.10, 138.57, 136.56, 130.69, 129.14, 127.89, 127.88, 126.99, 124.26, 123.06, 29.86.



III.28 **III.29** **(10%)**

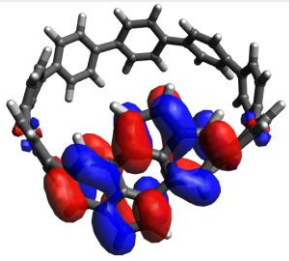
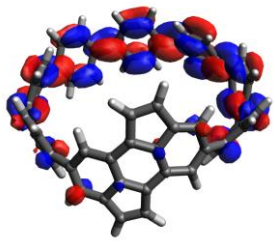
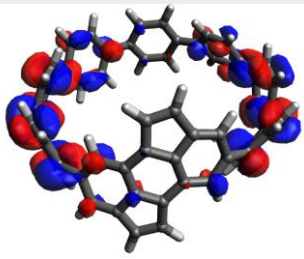
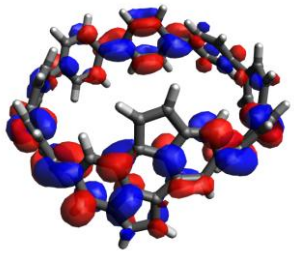
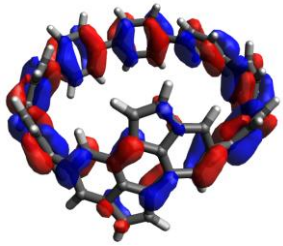
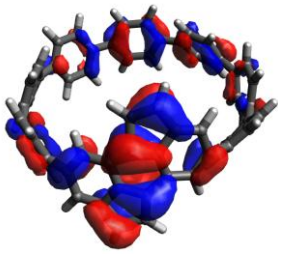
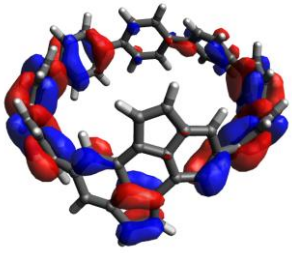
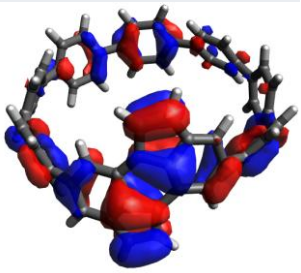
Synthesis of III.29: To a 25 mL vial containing **III.28** (7.1 mg, 0.0136 mmol, 1.0 equiv.) was added THF (2 mL). Freshly prepared H_2SnCl_4 (1.67 mL, 0.101 mmol, 7.4 equiv.) was added to the vial. Upon addition of the reductant, the solution color changed from orange-red to vibrant red. After stirring at room temperature for 21 h, the reaction was quenched by the addition of aqueous $NaHCO_3$ (5 mL). The mixture was diluted with DCM (10 mL) and transferred to a separatory funnel. The organic layer was collected, and the aqueous layer was extracted with additional DCM (15 mL × 2). The combined organic layers were dried over Na_2SO_4, filtered and concentrated in vacuo. The crude product was purified by flash column chromatography (silica gel, 20% DCM in hexanes) to afford the target compound as an orange-red solid. R_f = 0.32 (20% DCM in hexanes). ^{1}H NMR (500 MHz, CD_2Cl_2) δ 8.40 (d, J = 1.2 Hz, 2H), 8.12 (d, J = 1.2 Hz, 2H), 7.86 (dd, J = 8.2, 1.3 Hz, 4H), 7.68 (d, J = 5.2 Hz, 2H), 7.57 (t, J = 7.7 Hz, 4H), 7.46 (t, J = 7.5 Hz, 2H), 7.25 (d, J = 5.2 Hz, 2H).

III.4.2. Computational results of FMOs of 4,9-CPA[7]CPP

Table III.1. Major electronic transitions (absorption) of 4,9-CPA[7]CPP calculated by TD-DFT method

No.	Energy (eV)	Wavelength (nm)	Osc. Strength	Major Contributions
1	2.4556	504.90	0.0338	H-3->L (63%), H-1->L (26%)
2	2.7337	453.54	0.2839	H-1->L (31%), H->L (52%)
3	2.8976	427.89	0.0266	H-4->L (54%), H-2->L (36%)
4	3.4149	363.07	0.0444	H-5->L (43%) H-1->L (10%) H->L+1 (18%)
5	3.6032	344.09	0.779	H-6->L (10%) H-5->L (25%) H->L+1 (39%)
6	3.7944	326.76	0.7049	H-7->L (10%) H-4->L (15%) H-2->L (29%)
7	3.8505	322.00	0.2213	H-2->L (13%) H-1->L (16%) H->L (33%)
8	4.1089	301.75	1.2436	H-2->L (10%) H-2->L+1 (26%) H->L+2 (34%)
9	4.1805	296.58	1.5467	H-1->L+1 (18%) H->L+3 (30%)
10	4.4366	279.46	0.0049	H-3->L+4 (23%) H-1->L+4 (49%)
11	4.5901	270.11	0.0340	H-6->L (23%)
12	4.5981	269.64	0.0096	H-8->L+1 (10%), H->L+5 (26%)

Table III.2. Major electronic transitions (absorption) of 4,9-CPA[7]CPP calculated by TD-DFT method

LUMO	L+1	L+2	L+3
			
-1.878 eV	-0.650 eV	-0.207 eV	0.065 eV
HOMO	H-1	H-2	H-3
			
-6.399 eV	-6.783 eV	-6.891 eV	-7.086 eV

III.5. Bridge to chapter IV

This chapter provides a brief overview of the discovery, synthesis, and functionalization of cyclopenta[*hi*]aceanthrylene (CPA), emphasizing its role as an electron acceptor in optoelectronic applications. To expand upon these properties, subsequent efforts were directed toward incorporating CPA into cyclic systems via its 2,7- and 4,9-positions. The successful synthesis of 4,9-CPA[7]CPP was demonstrated and its instability under strongly acidic conditions mirrors the reactivity observed in azulene analogues. Chapters II and III conclude the exploration of non-alternant PAH-containing CPPs. The following chapter investigates the use of CPP-based macrocycles as templates for constructing mechanically interlocked systems, with a focus on π-conjugated rotaxanes.

CHAPTER IV SYNTHESIS AND DESIGN OF [2]ROTAXANE FEATURING PHEN[*N*]CPP MACROCYCLE AND ANTHRACENE BASED THREAD

IV.1. Introduction

To date, a library of mechanically interlocked polymers (MIPs) have been synthetically realized, such as polyrotaxanes and polycatenanes.[96] Importantly, several MIPs have been successfully utilized in practical applications, such as drug-delivery vehicles[97] and stimuli-responsive materials[16]. Inspired by this, the goal of this project is to develop a method to synthesize fully π-conjugated CPP-based rotaxane monomer with functionalizable handles, probe the electronic communication between the radial π-conjugation of the macrocycle and the linear π-system of the thread, and ultimately, optimize the polymerization methods to attain fully conjugated polyrotaxane systems.

At present, there are three methods that are employed and established to construct CPP-based rotaxanes. The first method leverages host-guest chemistry, reminiscent of the classic "capping" approach in rotaxane synthesis, wherein a partial axle component is coordinated within the macrocycle prior to appending bulkier stopper groups. In 2018, von Delius group, inspired by the strong concave-convex π-π interaction between C_{60} and [10]CPP (Figure IV.1a) with a high association constant of 1.8×10^6 M^{-1}, they strategically designed a fullerene based [2]rotaxane with [10]CPP **IV.4**.[98] This was accomplished by the approach shown in **Figure IV.1**. First, a pseudo-rotaxane **IV.2** was obtained by the host-guest interaction between **IV**.**1** and [10]CPP. Subsequently, Bingel reaction between fullerene guest and the half-axle component, bromomalonic ester **IV.3**, afforded the target rotaxane with several different regioisomers. To prevent the dethreading of [10]CPP, bulky fullerene hexakis-adducts were selected as the stoppers, which were obtained through cyclopropanation of fullerene via Bingel reaction. Serving as the workhorse for the synthesis, Bingel reaction offers a distinct advantage as it operates at or below room temperature, preventing potential dethreading or decomposition at the final step. Additionally, it is noteworthy the supramolecular interaction between [10]CPP and central fullerene improves the regioselectivity of the second Bingel reaction during the capping of the pseudo rotaxane **IV.2** with the second stopper **IV.3**. This work showcases the first example of

synthesis of [2]rotaxane with parent CPP without heteroatoms and shed light on the advancing the regioselective bis-functionalization of fullerene for potential device applications.

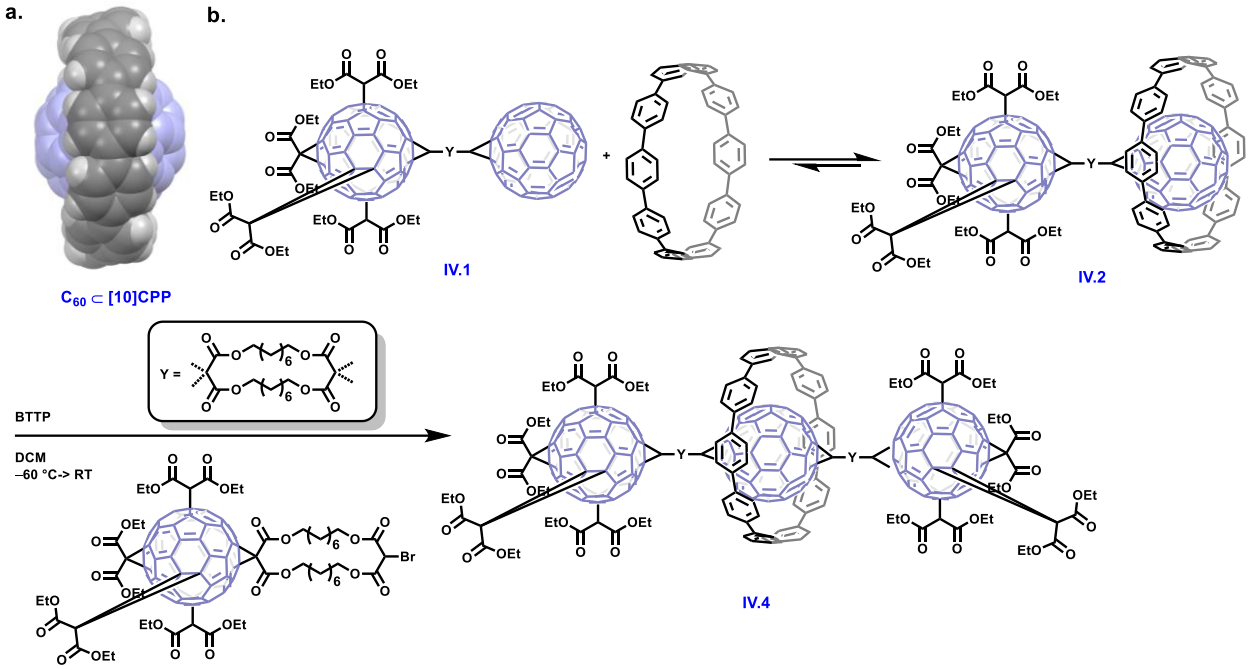


Figure IV.1. (a) Host-guest chemistry of C_{60} and [10]CPP. (b) Concave-convex π-π template method toward Fullerene-CPP rotaxane developed by the von Delius group.

Similarly, in 2023, Kawai and Tsuchido group synthesized **[6]CPP-12OMe**, a highly electron rich nanohoop, using the Au-template method.[99] Owing to the strong electron donating character of the twelve methoxy groups, this CPP derivative possesses a significantly higher HOMO level than the pristine parent [6]CPP. Capitalizing on the electron-rich nature of the cavity, the authors explored its potential as a supramolecular host. After screening various guest molecules in $CDCl_3$, a good binding affinity for electron-deficient alkyl chains, such as adiponitrile, was observed **IV.5** (Figure IV.2). Subsequently, to lock this interaction mechanically, they first synthesized an inclusion complex of [6]CPP-12OMe with hexamethylene diisocyanate **IV.6** and the subsequent introduction a bulky 1-adamantanemethylamine stoppers via urea bond formation successfully afford the corresponding [2]rotaxanes **IV.7**. This work presented the first example of CPP capable of encapsulating a guest molecule with a flexible alkyl structure. However, it is worth noting that while the host-guest complexation successfully leads to the mechanically interlocked architecture, the thermodynamic binding affinity of [6]CPP-12OMe for these linear aliphatic guests remains low (K_a = 186 M^{-1} in $CDCl_3$), compared to the exceptionally high association

constants between [10]CPP and C_{60}. This low binding affinity likely accounts for both the low yield and the necessity of utilizing a large excess number of guests to push the formation of inclusion complex **IV.6**, as well as a substantial loading of the nucleophile for the final stoppering step.

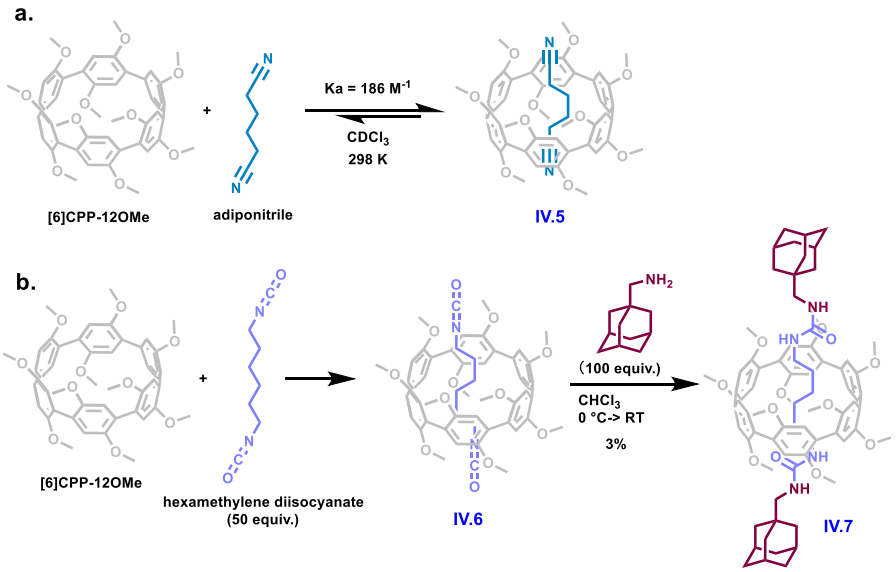


Figure IV.2. (a) Host-guest interaction between [6]CPP-12OMe and adiponitrile (b) [2]rotaxane synthesis featuring [6]CPP-12OMe macrocycle and bulky adamantyl stoppers.

The second method utilizes a covalent template approach to tether the partial axle and macrocycle together, followed by the subsequent traceless removal of the covalent linker to afford the desired interlocked structures. This approach allows access to improbable rotaxanes that naturally lack any direct, thermodynamically favored recognition site between the axle and macrocycle. In 2024, the Cong group introduced a covalent azo-group template method and successfully synthesized a series of rotaxanes featuring *meta*-[8]CPP (Figure IV.3).[100] The key intermediate is an azobenzene containing pre-rotaxane **IV.8**, which enables the strategic incorporation of bulky stoppers before the cleavage of the azo bond. Taking [2]rotaxane **IV.10** as an example, the authors chose *meta*-[8]CPP, because it places the azo group perfectly inside the cavity and the selection of the *meta*-terphenylene-featured axle component introduces a structural kink that prevents the macrocycle from escaping. Beyond using *meta*-terphenylene units as capping groups, the authors also successfully appended [10]CPP at both ends of the axle component to afford rotaxane **IV.12**. Furthermore, a more sophisticated [3]rotaxane **IV.11** was

also synthesized via cross coupling of two equivalents of **IV.8** to a bisfunctionalized spacer, followed by capping the axle component using the *meta*-terphenylene.

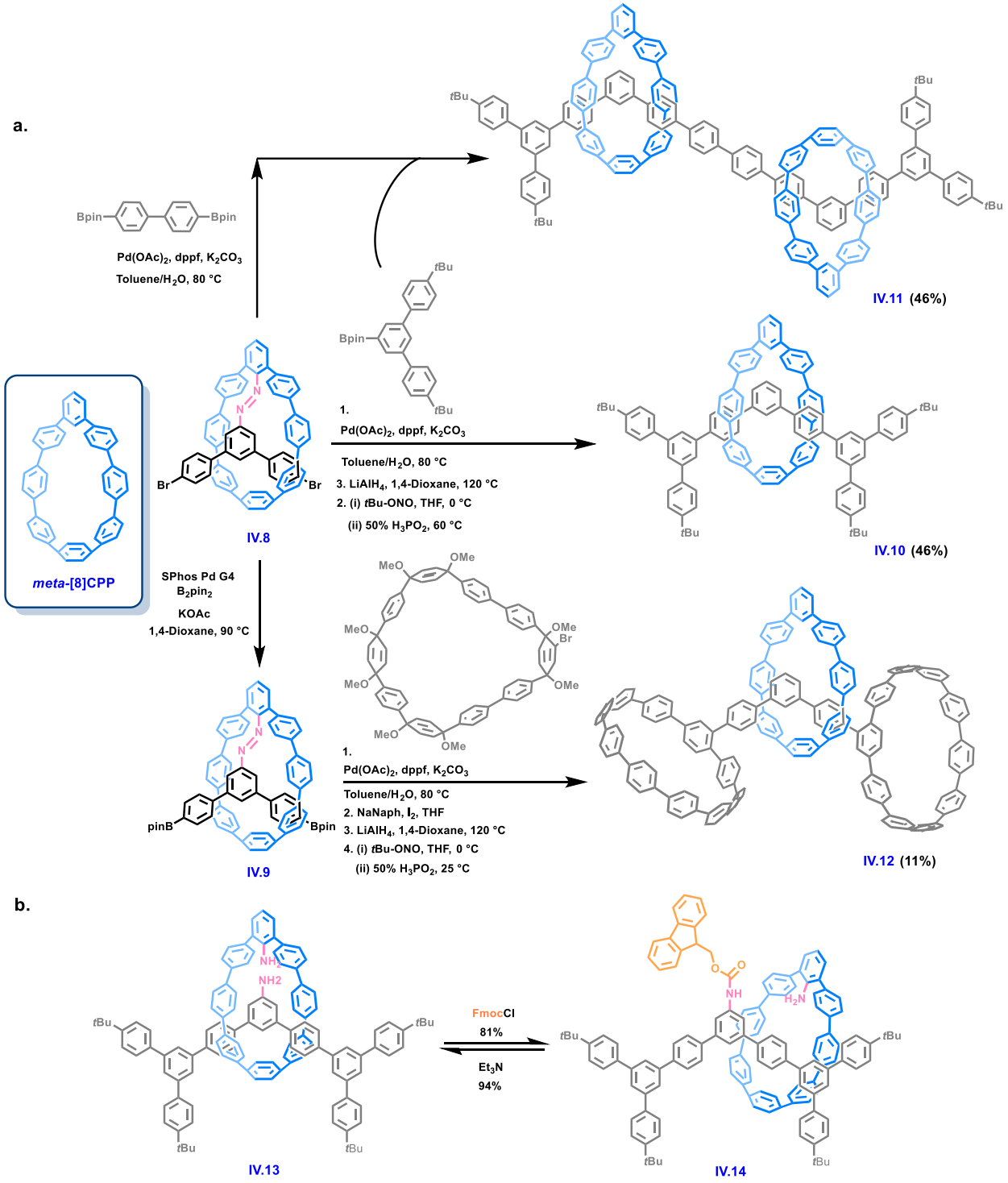
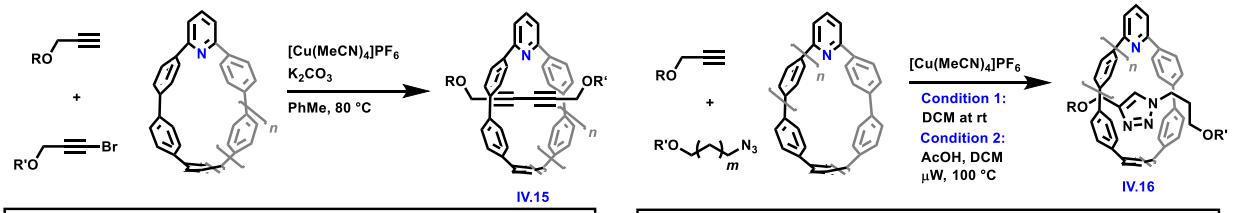
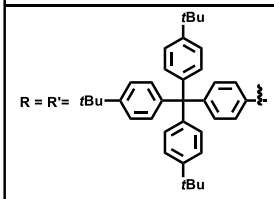


Figure IV.3. (a) Covalent azo-group template for the synthesis of improbable rotaxanes with all benzene scaffolds. (b) Chemical stimuli experiment of aniline derived rotaxane **IV.13**.

The authors also evaluated the chemical stimuli responsiveness of the aniline-derived rotaxane **IV.13** prior to hydrodeamination. They discovered that the amino group on the axle component selectively reacts with 9-fluorenylmethoxycarbonyl chloride (Fmoc-Cl) to form **IV.14**, while the amino appended to the ***meta*[8]CPP** remains untouched, cleanly shuttling the macrocycle to one side of axle. It is noteworthy that the shuttling process is fully reversible upon addition of triethylamine. This work elegantly demonstrates the power of the azo-template methodology, the versatility of the post-functionalization of the key rotaxane precursor **IV.8** and its potential application in molecular machinery and motion control.

The third method is known as the active template (AT) strategy, pioneered by the Leigh group.[101,102] In this approach, the macrocycle features internal coordination sites that selectively bind a catalytic metal within its cavity. This supramolecular pre-organization facilitates the coupling reaction to take place inside the cavity, ultimately affording the interlocked structures. The Jasti lab has published several seminal works pioneering this specific methodology within the field of CPP-based rotaxanes. Starting in 2019, van Raden *et al* reported the successful synthesis of a series of [2]rotaxane via active template Cadiot-Chodkiewicz (AT-CC) reaction and active template azide-alkyne cycloaddition (AT-CuAAC) via the use of *meta*-aza[6]CPP and *meta*-aza[8]CPP, in which a single pyridyl unit is incorporated into the CPP backbone via its 2,6-positions (Figure IV.4). Both methods yield [2]rotaxanes IV.15 and IV.16 in moderate to high yields.[91]



Alkyne & Bromoalkyne	Macrocycle	Rotaxane
R = R'= 	*n* = 1 or 3	54% | 51%
R = R'= 	*n* = 1	52%

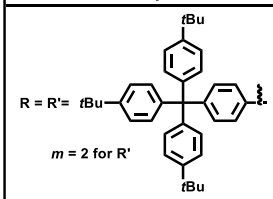
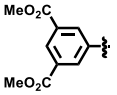
Alkyne & Azide	Macrocycle	Rotaxane
R = R'=  *m* = 2 for R'	*n* = 3	70%
R = R'= 	*n* = 1	45%

Figure IV.4. Synthesis of [2]rotaxanes via AT-CC and AT-CuAAC methods through *meta*-aza[6] and *meta*-aza[8]CPP

Notably, the choice of the stoppers was successfully shifted from traditional bulky trityl groups to relatively smaller 3,5-substitued benzene units. In addition, the authors explored the molecular machine behavior of these systems to determine if the interlocked nanohoops could participate in further metal coordination. Excitingly, the addition of $[Cu(MeCN)_4]PF_6$ or $[Pd(MeCN)_4](BF_4)_2$ quenches the fluorescence of the macrocycle and the process is reversible with addition of EDTA. Furthermore, they also synthesized a new [2]rotaxane IV.17 via AT-CC method, featuring stoppers equipped with electronic-accepting 3,5-dinitrobenzene units and a fluoride cleavable TIPS group (Figure IV.5). Upon treatment with TBAF, the bulky TIPS group is cleaved, allowing the thread to escape the macrocycle cavity, resulting in drastic enhancement in emission intensity. In summary, this work paved the way for the development of [2]rotaxane utilizing CPP-based macrocycles, expanding the boundaries of how functionalized nanohoops can be manipulated to build complex machinery and advancing their utility in the field of molecular sensing field. Later in 2021, the Jasti group, in collaboration with the Pluth group, reported the utilization of *meta*-aza[6]CPP based rotaxane as a fluorescent sensor toward reactive sulfur species, in particular, H_2S, which predominantly exists as HS^- under physiological conditions (Figure IV.5).[92]

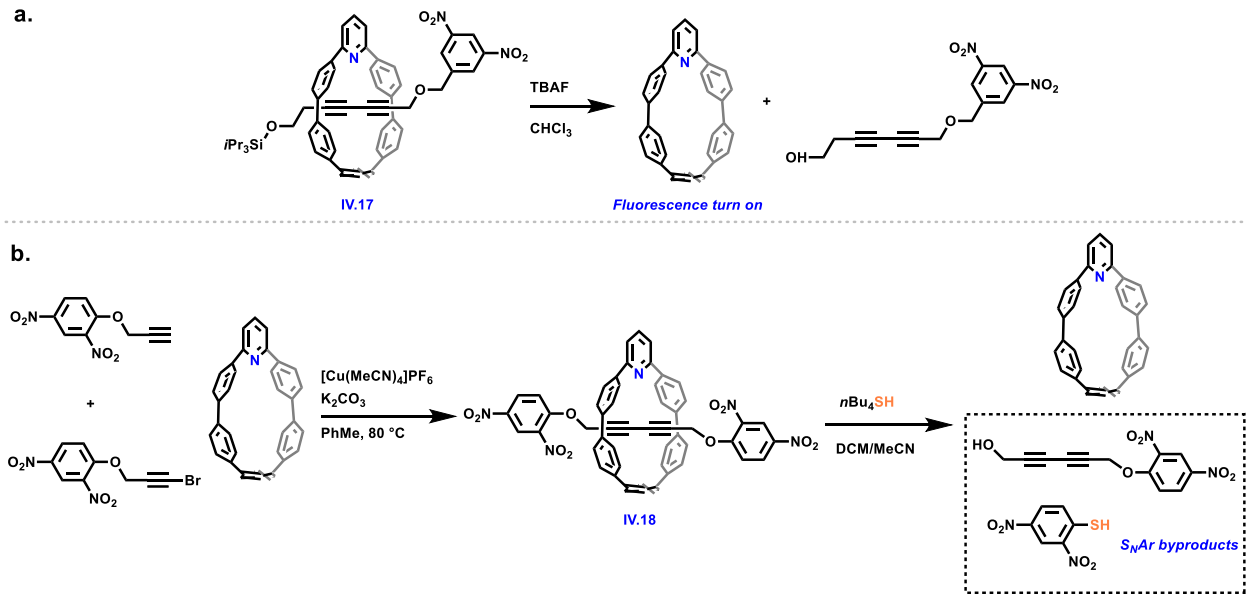


Figure IV.5. (a) Rotaxane **IV.17** shows a turn-on fluorescence property upon treatment with TBAF. (b) Rotaxane fluorescent sensor toward RSS, H_2S, which exists at SH^- at physiological condition.

The synthesized [2]rotaxane IV.18 featured stoppers functionalized with 2,4-dinitrophenyl ethers, showing high selectivity for small thiolates like *n*BuSH over the more sterically encumbered NBu_4S*t*Bu and NBu_4SBn, as proven through time-course fluorescence studies. This proof-of-principle work corroborates the feasibility of using mechanically interlocked nanohoop architectures as size-selective sensors for RSS, benefiting from the highly sterically hindered environment imposed by the dense interlocked structure.

In addition to chemical sensing, *meta*-aza[6]CPP has also been successfully utilized as a protecting sheath to insulate linear polyynes. It is known that while bulky terminal groups can effectively stabilize polyynes containing up to 24 contiguous alkyne units, this stabilization effect diminishes with increasing chain length. This limitation necessitates the development of suitable macrocycles capable of shielding longer polyynes, potentially threading multiple macrocycles to push the envelope toward longer polyyne entities. In 2022, the Anderson group, in collaboration with the Jasti lab, reported the synthesis of a polyyne [3]rotaxane **IV.21** insulated by *meta*-aza[6]CPP nanohoop, as well as by phenathroline-based macrocycle **IV.20**.[103]

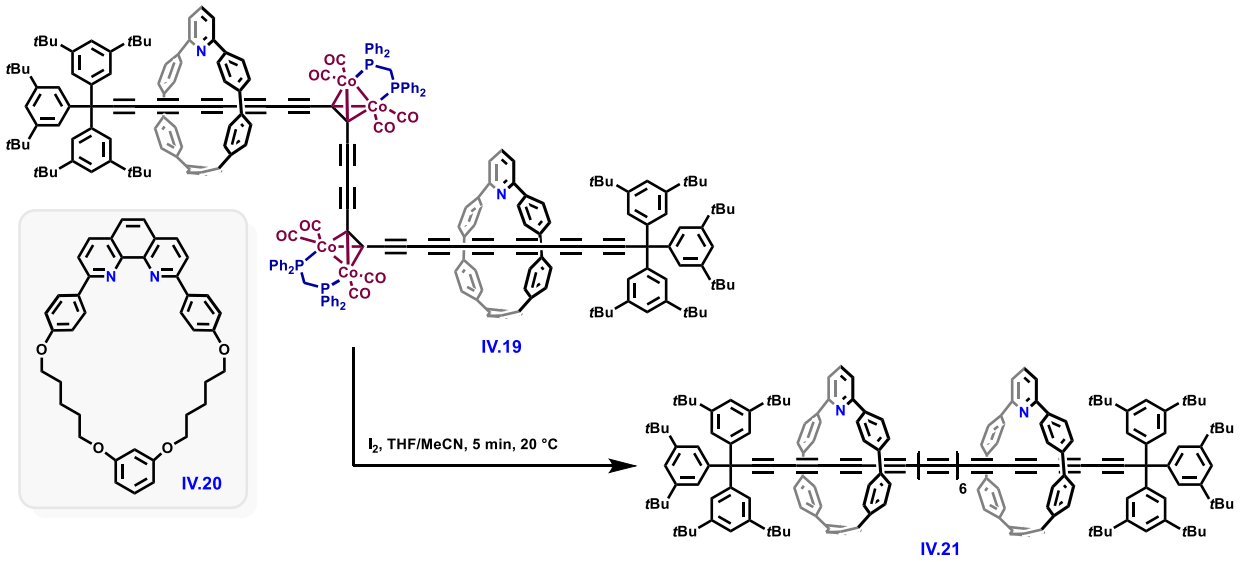


Figure IV.6. (a) Enhanced solution-phase stability of a polyyne [3]rotaxane insulated by *meta*-aza[6]CPP compared to phenanthroline-based macrocycle **IV.20**.

Taking the synthesis of rotaxane **IV.21** as an example, the group utilized the dicobalt carbonyl complexes as masked alkyne equivalents (MAEs) to temporarily stabilize the reactive polyyne intermediates. Through an AT-CC reaction followed by oxidative homocoupling, they successfully formed the masked precursor **IV.19**, and subsequent oxidative decomplexation removed the MAE to afford the targeted [3]rotaxane **IV.21** with 14 consecutive alkyne units. Remarkably, solution-phase stability studies in decalin revealed that *meta*-aza[6]CPP, compared to the phenanthroline containing macrocycle **IV.20**, offers strong protection to the polyyne core by a factor of 4.5, highlighting the great protective capacity and thermal stability provided by its rigid and compact cavity.

In 2023, James May *et al.* from the Jasti lab further advanced the field of nanohoop-based mechanically interlocked molecules (MIMs).[104] In their work, they expanded the library of CPP

architectures to include complex rotaxanes (Figure IV.7) and catenanes with diverse topologies.

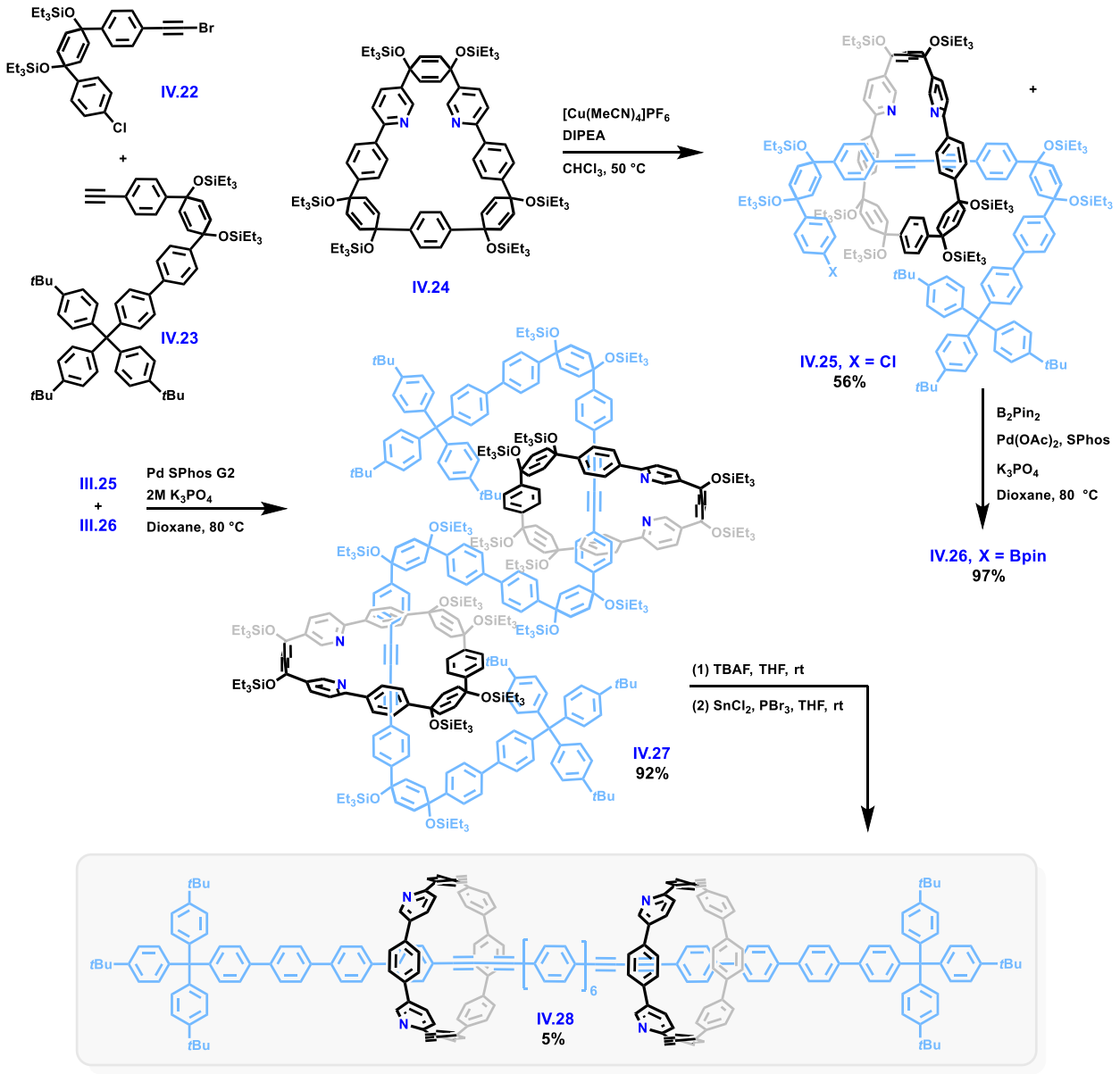


Figure IV.7. Synthesis of [3]rotaxane **IV.28** via AT-CC utilizing diaza[8]macrocycle **IV.24**.

They mentioned that while fully aromatized pyridine-containing nanohoops tend to coordinate metal exotopically, the unaromatized macrocyclic precursors, diaza[8]CPP macrocycle intermediate **IV.24** can bind Cu(I) inside the cavity as shown by the successful synthesis. In this work, a partial unaromatized three-ring precursor **IV.22** featuring an internal cyclohexadiene unit was selected due to its comparable size to the diaza macrocycle **IV.24**. The synthesis starts with a Cu-catalyzed AT-CC reaction between the terminal alkyne **IV.23** and bromo alkyne **IV.22** within

the cavity of the macrocycle, affording the [2]rotaxane **IV.25** in good yield. Subsequently, the terminal aryl chloride of the rotaxane thread was borylated to yield the corresponding boronic ester **IV.26**. With the complementary coupling partners on hand, compounds **IV.25** and **IV.26** underwent a Suzuki cross coupling reaction to yield the [3]rotaxane **IV.27** and lastly, a deprotection and aromatization afforded the rotaxane **IV.28**. Beyond the established methodology, the authors investigated how the position of the pyridyl nitrogen atoms within the macrocycle affects active-template efficiency (Figure IV.8). Interestingly, a macrocycle containing only a single pyridyl units failed to yield any interlocked product under the ideal active-template conditions. Conversely, separating the two pyridyl nitrogen units within the hoop provided [2]rotaxane **IV.30** with an improved yield compared to **IV.29**. This study implies that copper(I) coordination within these macrocycles is far more structurally nuanced than initially hypothesized, pointing toward the value of exploring alternative heteroatom-doped macrocyclic scaffolds for advanced active-template applications.

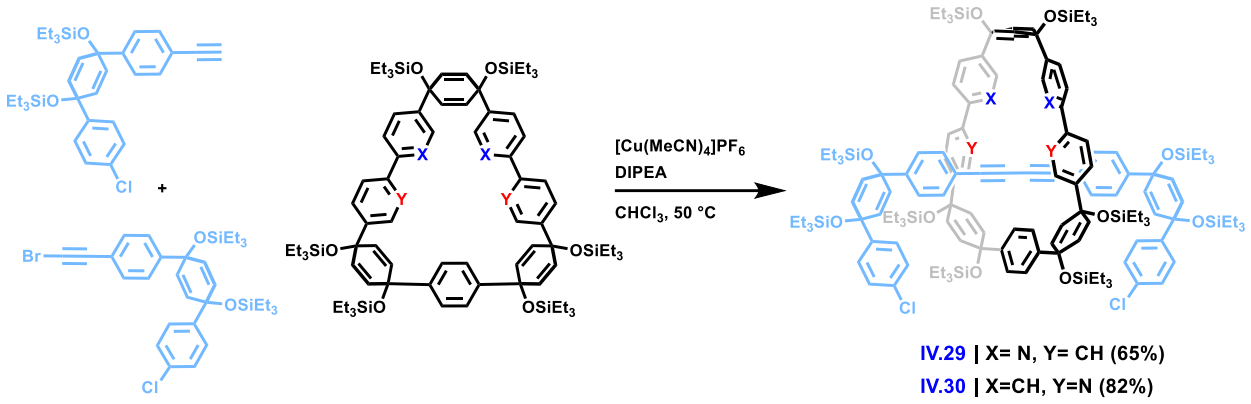


Figure IV.8. Evaluation of the nitrogen-atom positioning on the macrocycles during the AT-CC reaction, highlighting the requirement of multiple heteroatom coordination sites.

Moving forward from their success in advancing the active template method via Cadiot-Chodkiewicz reaction, in 2024, May *et al*. further explored the scope of AT-CuAAC using a macrocyclic precursor of 2,2'-bipyridyl embedded [9]CPP (**IV.31**, Figure IV.9).[105] Notably, compared to the diyne formed through AT-CC method, the rotaxane synthesized through this method is more robust and can better survive through the relative harsh condition during the aromatization. They found that by replacing the bulky triethylsilyl protecting groups used in prior designs with more compact butyl groups, the macrocyclic precursor significantly outperformed previous iterations. This modification resulted in a yield increase of nearly 40%, while requiring

only 1.5 equivalents loading for half-axle coupling partners. Furthermore, the reduced steric profile of the butyl groups allowed for the subsequent derivatization to access more compact catenane structures via the Suzuki macrocyclization of the dichlorinated [2]rotaxane **IV.32** with bisboronic esters.

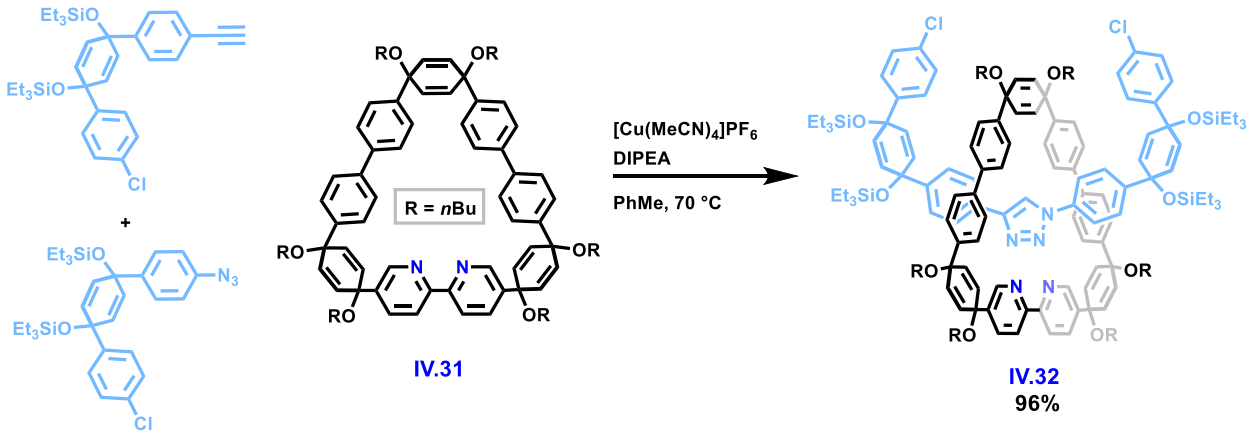


Figure IV.9. Near-quantitative yield from the AT-CuAAC synthesis using the prearomatized macrocycle **IV.31** with butyl protecting groups.

IV.2. Results and Discussion

IV.2.1. Method Design

In light of the burgeoning development of these diverse synthetic methodologies, we sought to leverage these foundational strategies to expand the scope of mechanically interlocked nanohoop based structures toward fully π-conjugated rotaxanes capable of subsequent polymerization. We envisioned that the encapsulating nanohoop could serve not only as a protective steric shield for the conjugated inner thread but also significantly enhance the overall solubility of the system, thereby ensuring the solution processibility for future material fabrication.

Inspired by the AT-CC coupling synthesis of nanohoop rotaxanes and the Cong group's work on phenanthroline-containing catenanes, we conceived that incorporating the 1,10-pheanthroline via 2,9-position into the nanohoop scaffold could facilitate the efficient synthesis of targeted rotaxanes. Due to the superior chelating ability and structural rigidity of 1,10-phenanthroline compared to the bipyridyl units, this substitution pattern allows for more robust metal coordination, potentially suppressing the formation of non-interlocked free threads often observed with weaker binding motifs. For our stopper design, anthracene-based derivatives **IV.33** and **IV.34** were chosen as their spatial dimensions are comparable to those of nanohoops

previously shown to support rotaxane formation. Moreover, they exhibit greater chemical stability than longer acenes. This choice renders an ideal testbed to investigate the synthetic feasibility before attempting the use of more air-sensitive acenes, such as tetracene and pentacene, which are prone to photooxidation and require more meticulous handling. Furthermore, we synthesized tetramethyl-substituted anthracene stoppers **IV.35** and **IV.36** to accommodate studies involving larger-sized nanohoops.

Regarding our initial macrocycle screening, both *meta*-aza[6]CPP and diaza[8]macrocycle precursor **IV.24** failed to give the desired rotaxane, resulting only in the recovery of the starting macrocycle and the formation of free thread (Figure IV.10). These outcomes suggested that transitioning to a smaller, more rigid nanohoop containing a more potent binding site (1,10-phenanthroline) was indeed necessary to drive the desired rotaxane formation. Excitingly, by switching the macrocycle to **Phen[5]CPP** (5 denoting the number of phenylenes), the corresponding [2]rotaxane was successfully synthesized in near-quantitative yield.

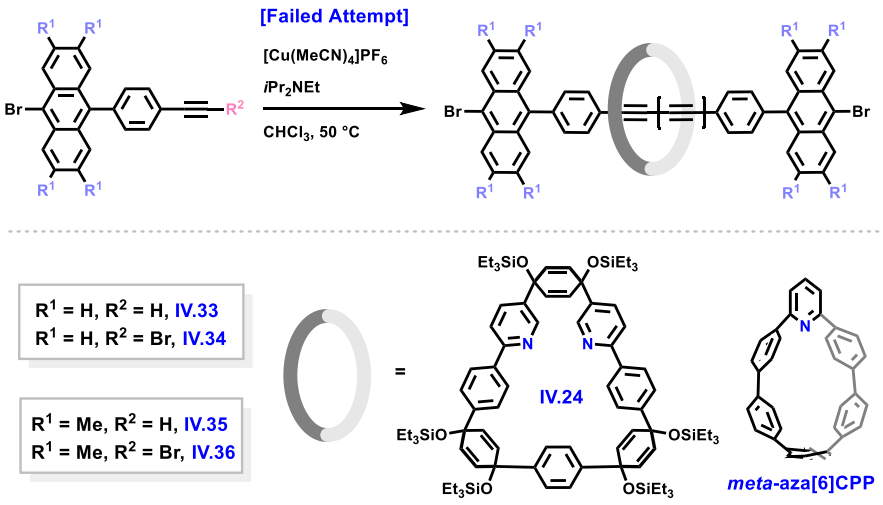


Figure IV.10. Selected failed attempts toward [2]rotaxane formation using macrocycle IV.24 and *meta*-aza[6]CPP using the AT-CuAAC synthesis.

Herein, we first discuss the synthesis of **Phen[*n*]CPPs** (n = 5–7) and a series of fully π-conjugated, CPP-based rotaxanes bearing a functionalizable handle, followed by an initial exploration into their viability for subsequent cross-coupling reactions to extend the conjugated backbones (Figure IV.11).

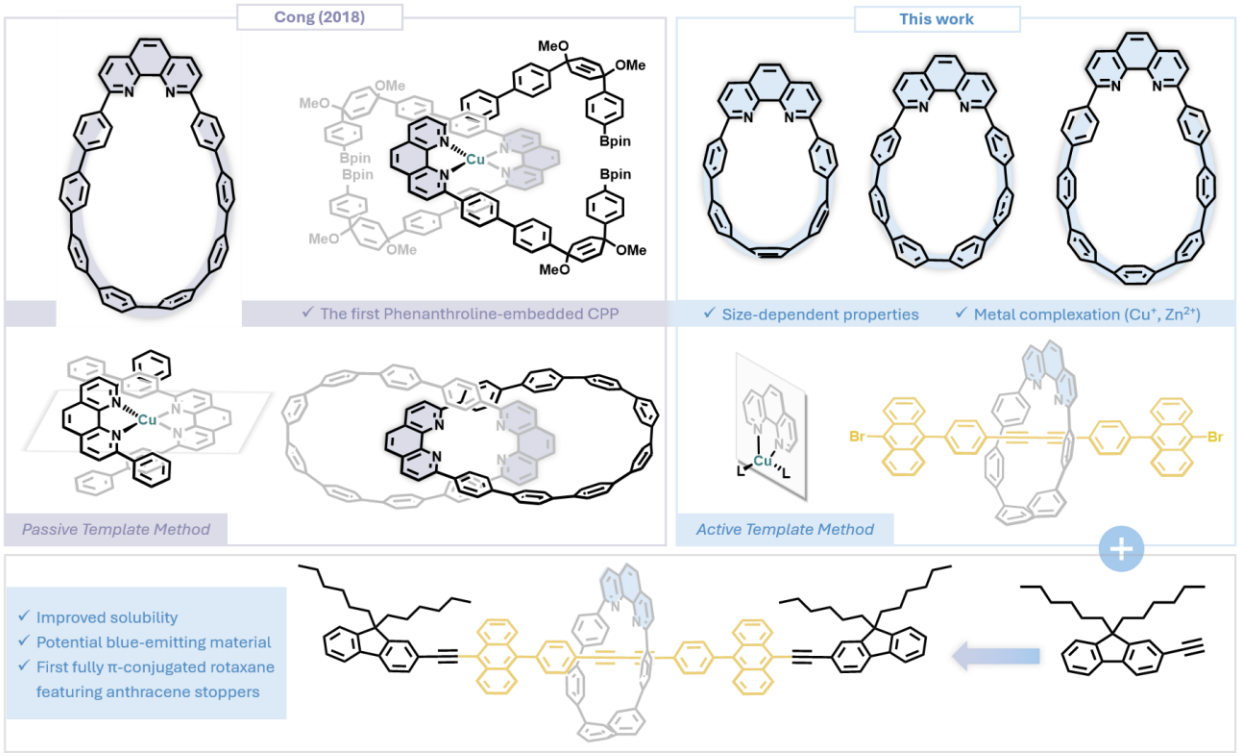
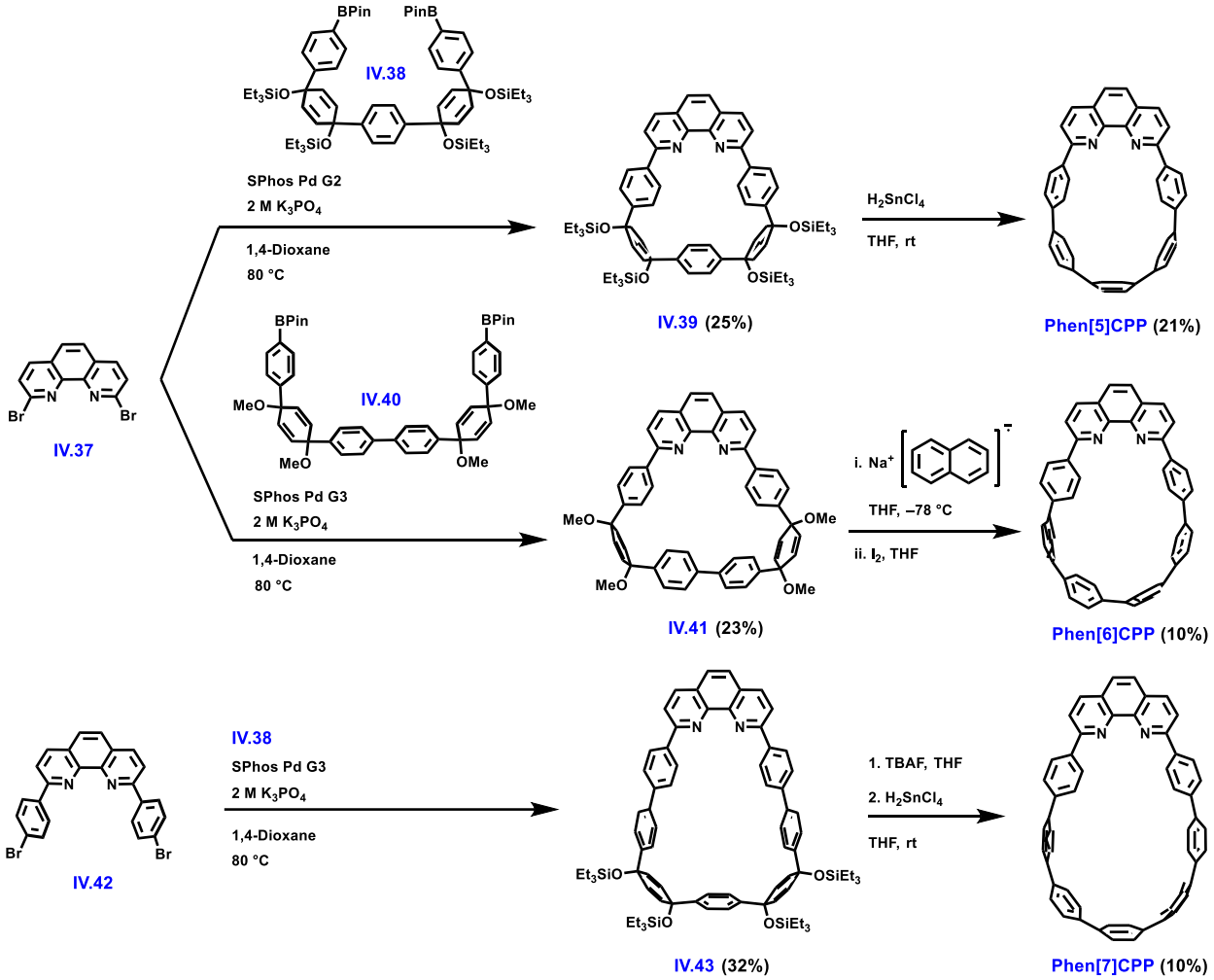


Figure IV.11. Overview of the synthetic library of Phen[*n*]CPP-based rotaxanes and their potential for downstream cross-coupling applications toward conjugated polymers.

IV.2.2. Synthesis of Phen[*n*]CPPs (*n* = 5–7)

The synthesis of Phen[*n*]CPPs follows the established methodology pioneered by the Bertozzi and Jasti groups. As shown in scheme IV.1, all macrocyclic precursors were synthesized by Suzuki-Miyaura macrocyclization under dilute conditions using appropriate coupling partners. To incorporate the phenanthroline unit, commercially available 2,9-dibromo-1,10-phenanthroline (**IV.37**) and 2,9-bis(4-bromophenyl)-1,10-phenathroline (**IV.42**) which were prepared in high yield following Sauvage's method was employed. For the synthesis of Phen[5]CPP and Phen[7]CPP, the C-shaped, cyclohexadiene-containing unit **IV.38** was coupled with **IV.37** and **IV.42**, respectively, to afford the macrocycle precursor **IV.39**[106] and **IV.43** in 25% and 32% yields. The higher yield observed for the larger macrocycle is attributed to a more favorable size match between the coupling partners. Subsequently, deprotection and aromatization using H_2SnCl_4 according to the procedure reported by Yamago *et al.*[107] afforded the target **Phen[5]CPP** and **Phen[7]CPP** in 21% and 10% yields, respectively. Similarly, subjecting **IV.40** to analogous Suzuki macrocyclization conditions yielded the macrocycle precursor **IV.41** in 23% yield. Given that the methoxy protecting group is prone to rearrangement under acidic aromatization condition,

sodium naphthalenide, a strong basic reductant was utilized to aromatize **IV.41**, yielding **Phen[6]CPP** in 10% yield. It is noteworthy that the solubility of these nanohoops decreases as the macrocycle size increases.



Scheme IV.1. Synthetic scheme to **Phen[*n*]CPPs** (where *n* = 5–7).

While ^{1}H NMR spectrum, mass spectrometry and single-crystal X-ray diffraction confirmed the structural identity of three macrocycles, the poor solubility of **Phen[7]CPP** hindered the acquisition of high-resolution of $^{13}C\{^{1}H\}$ NMR spectrum. This trend is consistent with reports by Cong *et al*., who noted that **Phen[8]CPP**, in contrast to the catenated structure (Figure IV.11, structure on the middle left), has very poor solubility, precluding the acquisition of a meaningful carbon spectrum.[108] However, by coordinating **Phen[7]CPP** with a 1 M $ZnCl_2$ solution in Et_2O (Figure IV.12a), its solubility in CH_2Cl_2 and $CHCl_3$ is effectively improved, affording the complex

in 63% yield. The resulting complex, isolated as a bright orange solid, exhibits an 85 nm (approx. 1765 cm^{-1}) red-shift in emission (Figure IV.12b).

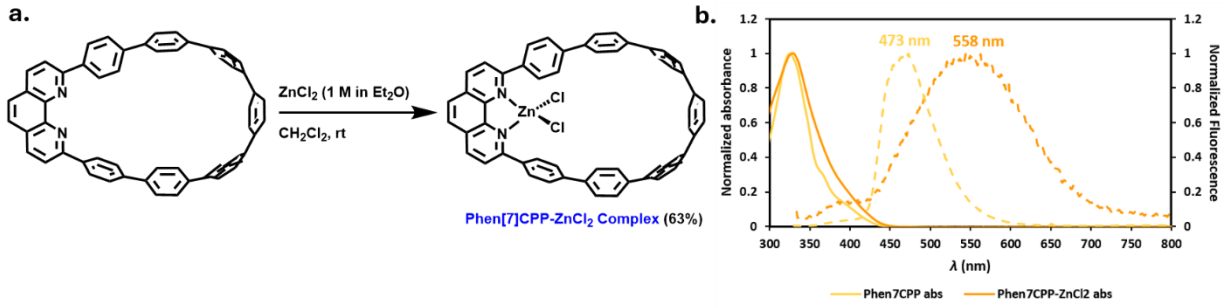
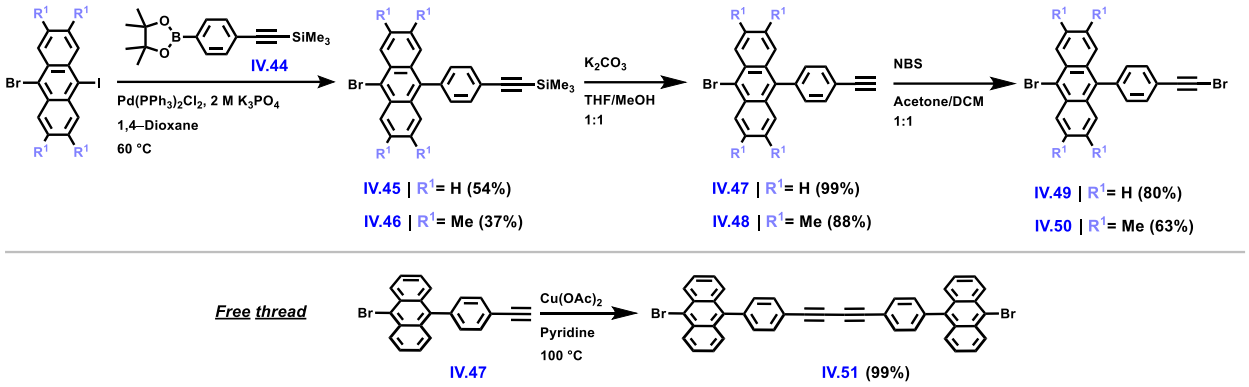


Figure IV.12. (a) Synthesis of Phen[7]CPP-$ZnCl_2$ complex. (b) Photophysical property measured in CH_2Cl_2 (absorbance traces are shown as solid lines and emission trace as dashed line: light yellow: Phen[7]CPP, orange line: Phen[7]CPP-$ZnCl_2$).

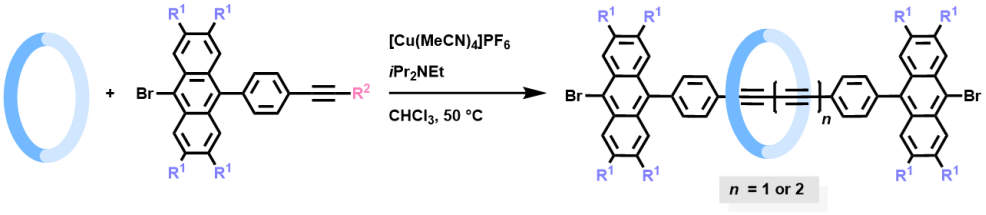
IV.2.3. Synthesis of anthracene-based half-axle, free thread and [2]rotaxanes

The synthesis of half-axle components incorporating anthracene units commenced from 9-bromo-10-iodoanthracene and its methylated analog, 2,3,6,7-tetramethyl-9-bromo-10-iodoanthracene (Scheme IV.2). Subjecting these materials to Suzuki-Miyaura cross coupling with boronic ester **IV.44** afforded the extended anthracene intermediate **IV.45** and **IV.46** in 54% and 37% yield, respectively. We envision that the phenylene between the anthracene and alkyne could act as an spacer to prevent steric clash between the anthracene unit and the macrocycle that could impedes the effective coupling between the half-axle components during the AT-CC reaction. With the trimethylsilyl-protected alkynes in hand, deprotection afforded the terminal alkyne **IV.47** and **IV.48** in 99% and 88% yields, respectively. Subsequent bromination using *N*-Bromosuccinimide afforded the bromo alkyne **IV.49** and **IV.50** in 80% and 63% yields. The free thread was also prepared from terminal alkyne **IV.47** using the Eglinton oxidative coupling condition, which gives the symmetrical diyne **IV.51** with 99% yield.

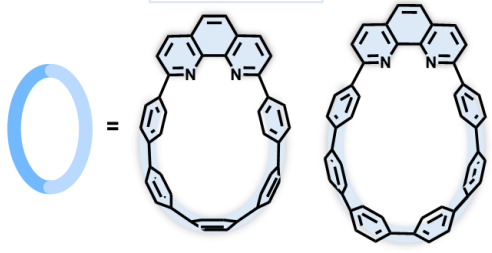


Scheme IV.2. Synthetic approach to anthracene-based half-axle components and the free thread IV.51 for comparison.

With the synthetic methods established for coupling partners and macrocycles, the synthesis of [2]rotaxane was investigated (Figure IV.13). Excitingly, [2]rotaxane **IV.52** was synthesized in near-quantitative yield when **IV.47** and **IV.49** were treated with diisopropylethylamine, $[Cu(MeCN)_4]PF_6$ in the presence of macrocyclic ligand Phen[5]CPP. The reaction reached completion in an hour, and the complete dissolution of the reaction mixture served as a strong indication of the successful formation of the interlocked structure. This result corroborates our hypothesis that encapsulating the π-conjugated thread **IV.51** indeed improves its solubility. In a similar fashion, [2]rotaxane **IV.54**, featuring tetramethyl-derivatized anthracene stoppers, was obtained under the same condition, albeit in a lower 30% yield, which is attributed to unoptimized purification techniques and reduced solubility compared to **IV.52**.



Macrocycle



Reactions

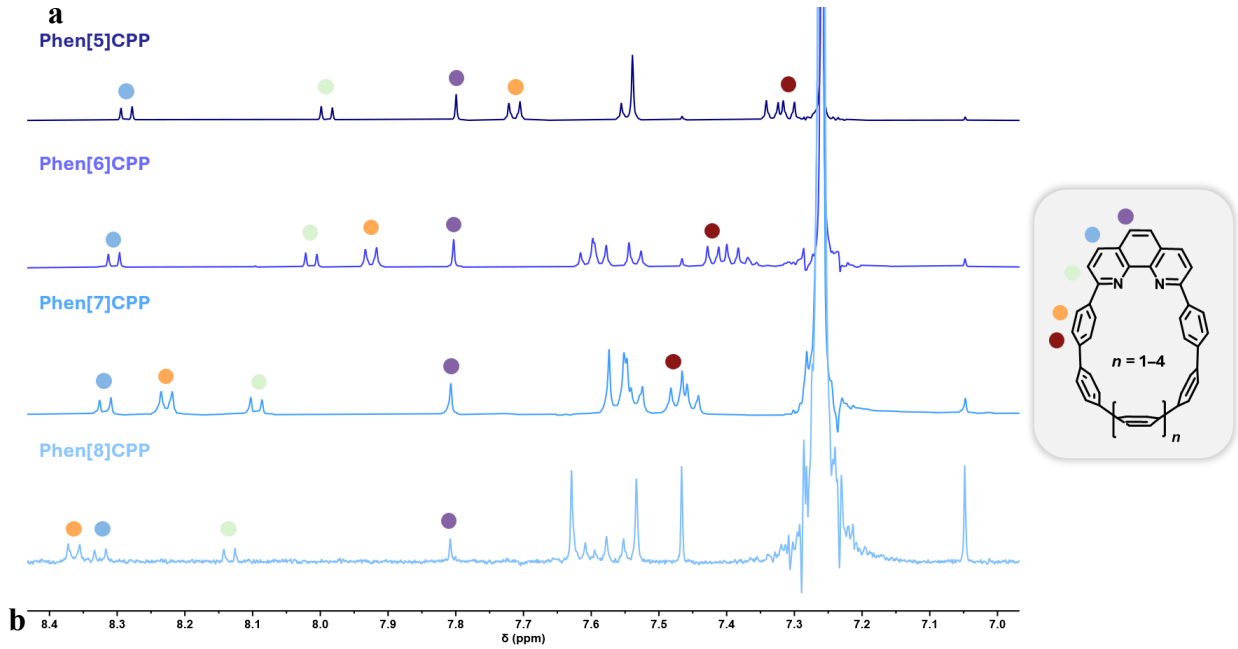
Rotaxane	R^1	R^2 | Equiv.		Macrocycle	% Yield
1 | IV.52	H	H | 2.5	Br | 2.5	Phen[5]CPP	Quantitative
2 | IV.53		CC-H | 2.5			92%
3 | IV.54	Me	H | 2.0	Br | 2.0		30%
4 | IV.55				Phen[6]CPP	23%

Figure IV.13. Synthesis of [2]rotaxanes (**IV.52–IV.55**) via AT-CC coupling reaction.

Furthermore, the synthesis of a longer triyne-based [2]rotaxane IV.53 was attempted, which proceeded with a high yield of 92%. In contrast, when the Phen[6]CPP macrocycle was subjected to the same AT-CC coupling condition with tetramethyl substituted coupling partners, the yield plummeted to 23%. This outcome is unsurprising, as the diminished solubility of the larger macrocycle likely hinders effective Cu(I) coordination, thereby compromising coupling efficacy. Finally, Phen[7]CPP was utilized to explore the potential of accessing larger rotaxane structures. However, its lowest solubility and largest cavity among the Phen[*n*]CPP series precluded the formation of any desired interlocked structures.

IV.2.4. ^{1}H NMR spectrum, crystal structure and photophysical properties of Phen[*n*]CPPs

For the Phen[*n*]CPP series, the protons on the phenylene unit adjacent to the phenanthroline moiety, as indicated by the orange dot, exhibit the most pronounced downfield chemical shift (Figure IV.14a). To elucidate this behavior, the single-crystal x-ray diffraction results were analyzed. As summarized in Figure IV.14b, increasing the macrocycle size correlates with a decrease in both the dihedral angle between the phenanthroline and the adjacent phenylene unit and the N···H-C distance. This observation suggests the observed downfield shift is driven by increased proximity of the protons to the electronegative nitrogen atom, and more importantly, the improved effective π-conjugation resulting from the reduced dihedral angle. Furthermore, we evaluated the contribution of the quinoidal form via bond length alternation (BLA) analysis, following the methodology reported by Yamago and coworkers (Figure IV.14b).[109] Given that the magnitude of the BLA is directly proportional to the quinoidal character of the phenylene rings, the high BLA values (>0.03 Å) at specific positions for all three macrocycles indicate a significant contribution of the quinoidal resonance form. This distortion correlates with the dihedral angle change between neighboring phenylene units, where a sign change indicates the site of Möbius backbone inversion (Figure IV.14b). While these structural and electronic features suggest a Möbius topology for all three macrocycles, further computation analysis, such as Anisotropy of the Induced Current Density (AICD) and Nucleus-Independent Chemical Shift (NICS) is required to definitely support this conclusion.



Compound	Average N···H-C distance *d* (Å)	Dihedral Angle *θ* (°)							
		1	2	3	4	5	6	7	8
Phen[5]CPP	2.649	50.72	37.85	-25.56	16.26	34.24	48.26		
Phen[6]CPP	2.478	-30.75	-43.98	-10.92	26.45	-22.12	-50.5	148.11	
Phen[7]CPP	2.448	9.74	57.45	23.85	-23.59	24.67	-24.01	-43.11	-24.37

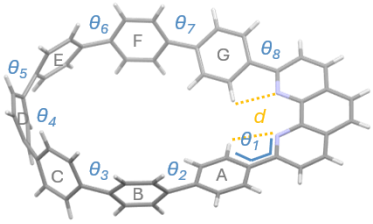
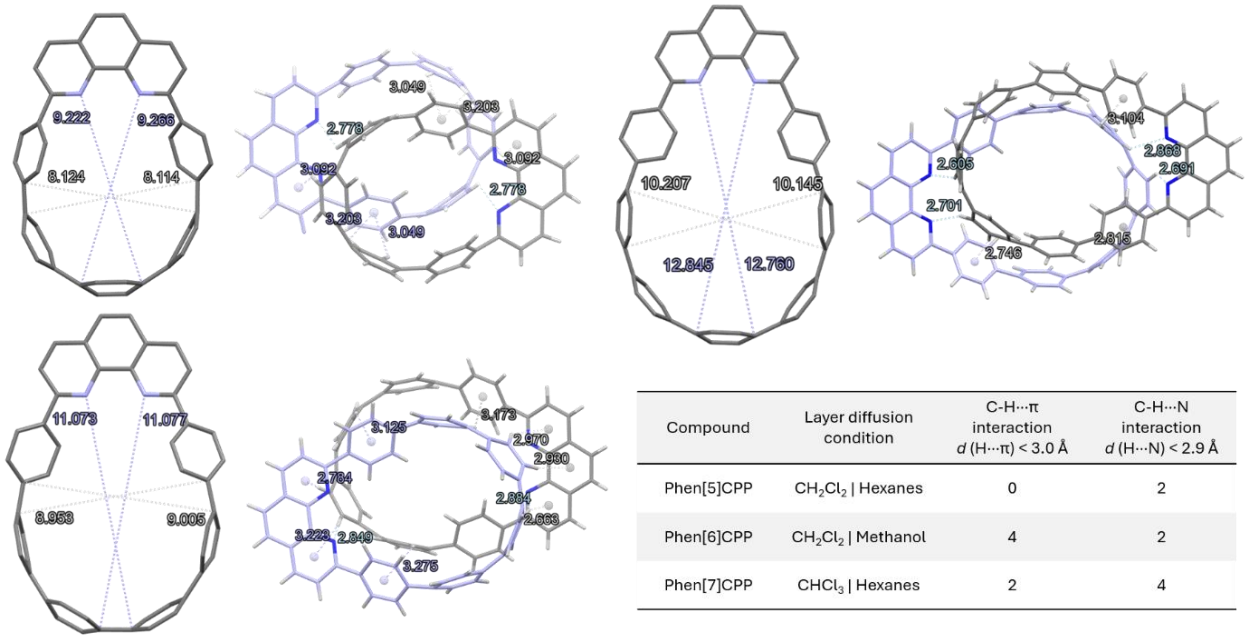


Figure IV.14. (a) ^{1}H NMR compilation of **Phen[*n*]CPPs** (*n* = 5–8). (b) dihedral angles measured from the single-crystal X-ray structure.

Lastly, single crystals for all three macrocycles were obtained via layer diffusion, using the condition summarized in Figure IV.15. The measured cavity dimensions and the distances for the preferred intermolecular C-H···π and N···C-H interactions are also reported. Based on the data, larger sized macrocycles exhibit a higher number of favored and stronger intermolecular contacts, which accounts for the observed decrease in solubility for the larger Phen[*n*]CPPs.

The photophysical properties of Phen[*n*]CPP series were subsequently measured (Figure IV.16). The UV-Vis absorption spectra exhibit an intense band (λ_{max} = 314, 320 and 324 nm, for *n* = 5 to 7), alongside a lower energy shoulder that is attributed to the HOMO-LUMO transition, which becomes electronically allowed due to breaking of central symmetry. Furthermore, the fluorescence emission spectra exhibit a hyposochromic shift as the macrocycle size increases, from **Phen[5]CPP** (486 nm), **Phen[6]CPP** (476 nm) and **Phen[7]CPP** (470 nm). This is consistent with the emission behavior for [*n*]CPPs.[2]



Compound	Layer diffusion condition	C-H···π interaction d (H···π) < 3.0 Å	C-H···N interaction d (H···N) < 2.9 Å
Phen[5]CPP	CH_2Cl_2 | Hexanes	0	2
Phen[6]CPP	CH_2Cl_2 | Methanol	4	2
Phen[7]CPP	$CHCl_3$ | Hexanes	2	4

Figure IV.15. Single-crystal structure of Phen[*n*]CPPs. Cavity dimensions and intermolecular C-H···π and N···C-H interaction distances are reported in Å. The table summarizes the number of the favored intermolecular contacts and the specific crystallization conditions for each macrocycle.

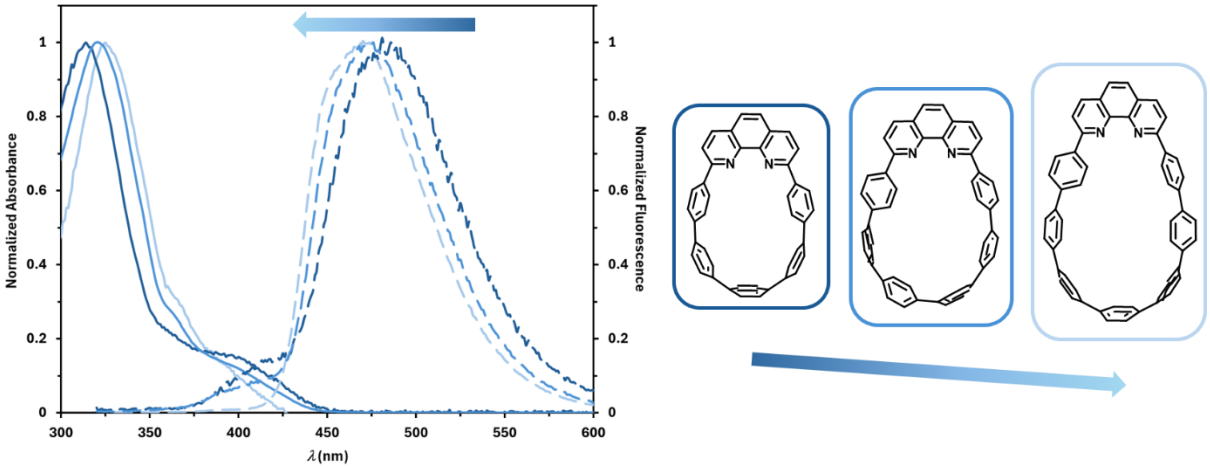


Figure IV.16. UV-Vis absorption and fluorescence data of Phen[*n*]CPP measured in CH_2Cl_2 solutions.

IV.2.5. ^{1}H NMR spectrum, crystal structure and photophysical properties of [2]rotaxanes

A characteristic feature of [2]rotaxane formation is the pronounced upfield shift of the thread component protons situated within the aromatic cavity of the macrocycle. In this case, the shielding effect is observed for the protons on the phenylene between the anthracene and alkyne

units, designated as A (A') and B (B'), as shown in Figure IV.19a. Additionally, single crystals of the [2]rotaxane were obtained via vapor diffusion of hexanes into a dichloromethane solution of the rotaxane (Figure IV.17b).

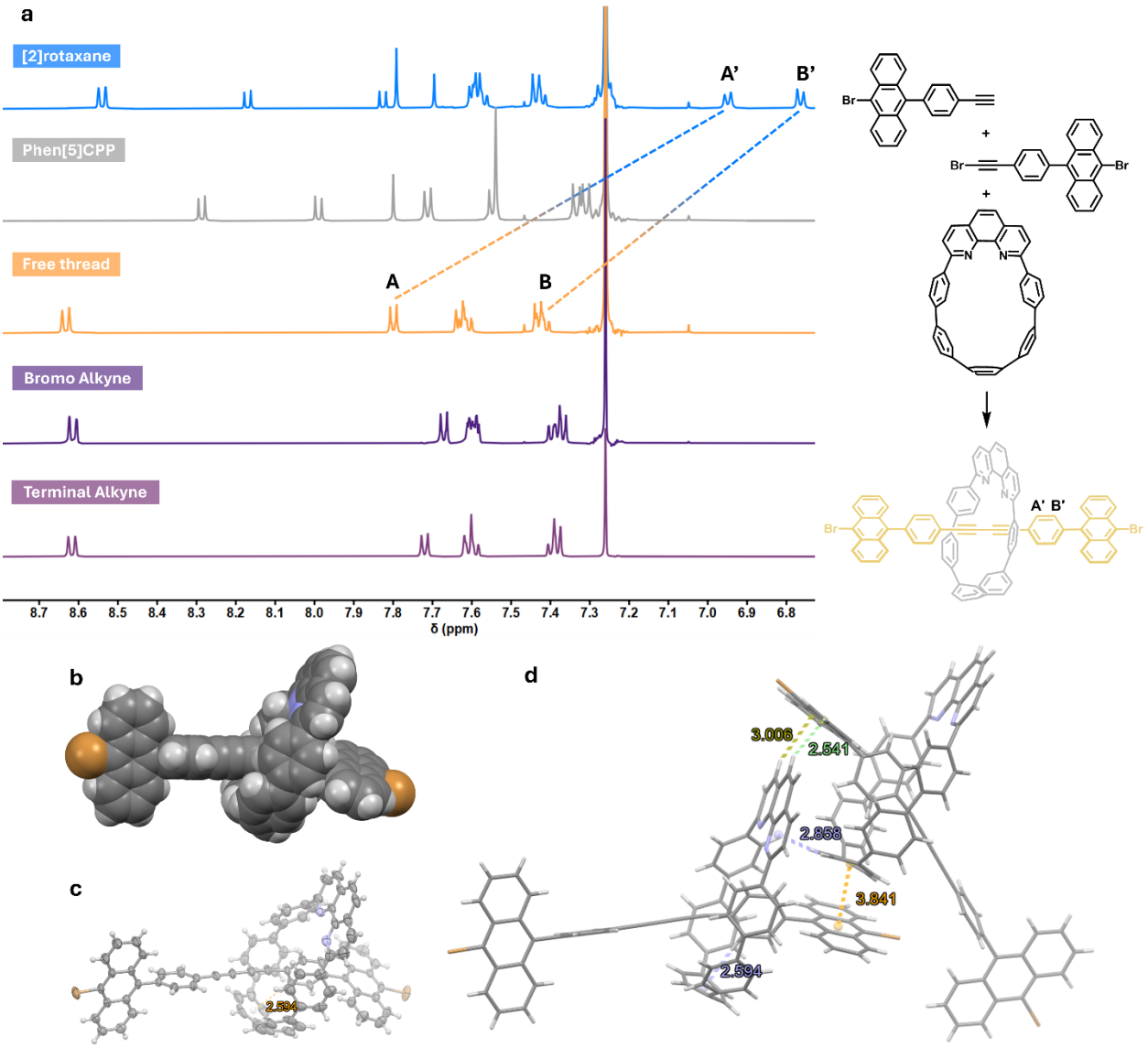


Figure IV.17. (a) ^{1}H NMR spectra compilation of [2]rotaxane **IV.52** and its individual components measured in $CDCl_3$. Upon formation of the interlocked structure, H_A and H_B undergo an upfield shift to $H_{A'}$ and $H_{B'}$, attributed to the shielding effect of the **Phen[5]CPP**. (b) Single crystal structure of **IV.52** shown in space-filling model. (c) The intramolecular C-H···π interaction between the axle component and macrocycle. (d) The intermolecular C-H···π and π-π interaction between [2]rotaxane.

The crystal structure unambiguously confirms the interlocked nature and reveals strong C-H···π interaction between the phenylene unit on the thread and **Phen[5]CPP**, which further

confirms that H_A' and H_B' reside within the shielding zone of the macrocycle in the solid state (Figure IV.17c). Furthermore, analysis of the crystal packing shows three distinct intermolecular C-H···π contacts (<3.1 Å) and π-π interaction (3.84 Å) between the Phen[5]CPP unit and anthracene core of the adjacent rotaxanes (Figure IV. 17d). As suggested by the crystal packing motif, the presence of the macrocycle effectively blocks intermolecular anthracene C-H···π interactions, which supports our hypothesis that the interlocked architecture indeed provide a fully π-conjugated thread with enhanced solution processibility.

To examine the impact of the mechanical bond on the photophysical properties of the individual component, the UV-Vis and fluorescence spectra of the [2]rotaxane **IV.52** were compared to those of free thread **IV.51** and Phen[5]CPP. As shown in Figure IV.18, the emission of the interlocked structure is nearly identical (λ_{em} = 489 nm) to that of macrocycle (λ_{em} = 486 nm), with no discernible feature originating from the free thread **IV.51** (λ_{em} = 428 nm).

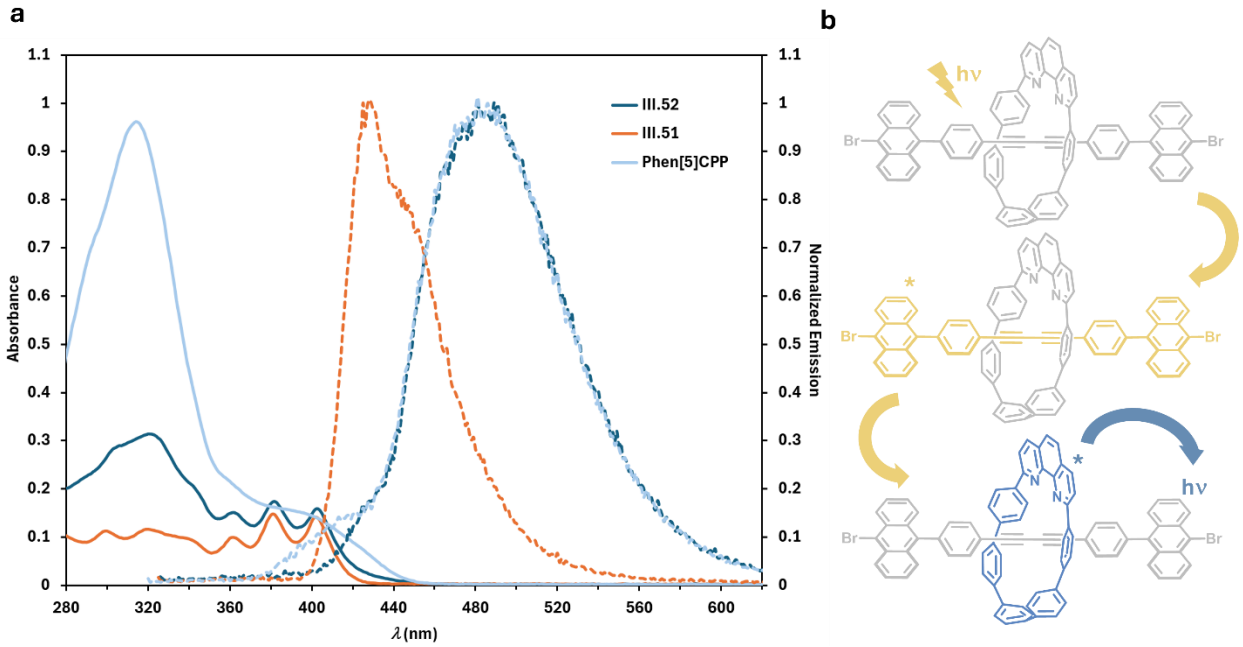


Figure IV.18. (a) Qualitative UV-Vis absorption (solid lines) and fluorescence (dashed lines) of the dichloromethane solution of [2]rotaxane **IV.52**, free thread **IV.51** and **Phen[5]CPP**. The fluorescence spectra of **Phen[5]CPP** were measured upon excitation at 315 nm, and the spectra of **IV.51** and **IV.52** were measured upon excitation at 320 nm. (b) The proposed fluorescence mechanism with asterisk (*) represents the component in the excited state.

These observations are consistent with reports by the Itami and Jasti groups, which demonstrate that the red-emitting fluorophore dominates the fluorescence behavior in CPP-based

interlocked structures. TD-DFT calculations using the B3LYP/6-31G(d,p) functional and basis set were performed to analyze the excited state of the [2]rotaxane. The preliminary results indicate the lowest energy emission is anthracene centered, which contradicts experimentally observed dominance of the macrocycle-centered emission. This discrepancy underscores the necessity of future computational studies on excited geometry optimization to better model the photophysical behavior. The fluorescence quantum yield of [2]rotaxane (Φ_F = 0.09) is more closely aligned with that of **Phen[5]CPP** (Φ_F = 0.06), compared to the free thread **IV.51** (Φ_F = 0.17). The brightness will be reported upon determination of the molar extinction coefficient. Finally, the observed lower quantum yield relative to other reported interlocked CPP-based systems is attributed to the presence of bromine, which facilitates non-radiative decay via intersystem crossing due to the heavy-atom effect.

IV.2.6. Functionalization of the [2]rotaxane with fluorenyl derivatives

Having successfully synthesized the [2]rotaxane, we sought to explore its potential as a monomer for the construction of fully π-conjugated polyrotaxanes. To evaluate the feasibility of post-functionalization, cross-coupling reactions were initially conducted on the free thread **IV.51** to establish a robust synthetic protocol. Anthracene derivatives, such as 9,10-bis(2-naphthyl)anthracene (**IV.56**), represent some of the most widely adopted blue emitting host materials in display manufacturing (Figure IV.19).

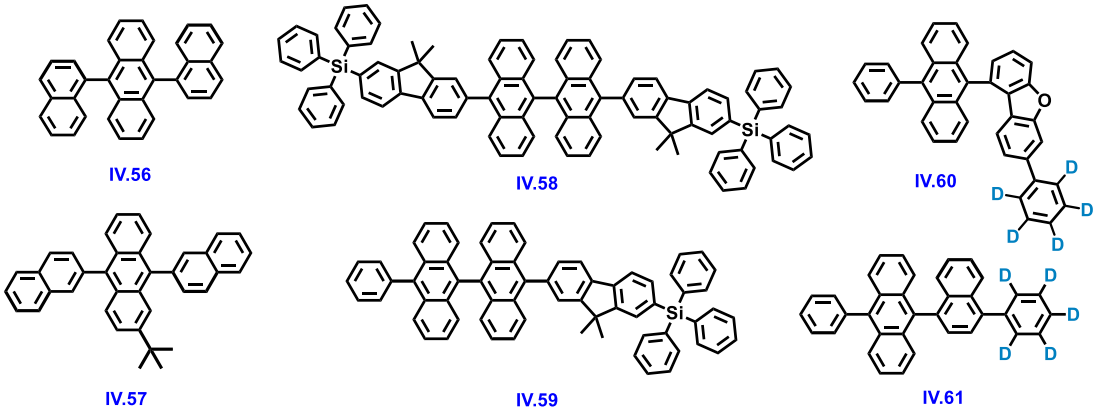


Figure IV.19. Representative anthracene-based derivatives (IV.56–IV.61) used in display technology.

The inclusion of napththyl units effectively suppresses the molecular aggregation. Similarly, in 2-*tert*-butyl-9,10-di-2-naphthylanthracene (**IV.57**), the addition of bulky *tert*-butyl group to the

anthracene core further inhibits intermolecular interactions in the solid state, thereby enhancing the fluorescence quantum yield. Other structural modification such as appending triphenylsilyl and fluorenyl groups (**IV.58** and **IV.59**), also serve to mitigate aggregation.[110,111] Furthermore, deuterated anthracene derivatives (**IV.60** and **IV.61**) have been explored as active hosts, leveraging the lower vibrational energy of C-D bonds compared to C-H bonds to enhance the lifetime.[112] To date, these first-generation anthracene-based fluorescent emitter remain industry standards for blue organic light-emitting diodes (OLEDs) due to their excellent thermal stability, narrow emission bandwidth, minimal difference of emission maximum between solution and solid states, and superior operational lifetimes.

Fluorene derivatives, another class of blue emitting materials, also exhibit excellent thermal stability. Furthermore, the solubility of these systems can be enhanced by appending alky chains at the 9-position. Therefore, 2-bromo-9,9-dihexyl-9H-fluorene (**IV.62**) was selected as a precursor to evaluate the feasibility of the post-functionalization of the rotaxane (Figure IV.20a). Starting from **IV.62**, a Sonogashira coupling reaction with trimethylsilyl acetylene, followed by desilylation afforded the terminal alkyne containing unit **IV.64** in 89% yield. Subsequently, subjecting **IV.64** and **IV.65** to Sonogashira conditions successfully afforded the coupled product **IV.65** as a bright yellow solid, which exhibited bright blue emission in solution and improved solubility compared to the parent thread. Due to time constraints, the unoptimized conditions were directly applied to the [2]rotaxane **IV.52**. After column purification, the ^{1}H NMR spectrum of the isolated fractions, despite showing the presence of the alkyne homocoupled side product **IV.67**, clearly suggests the formation of the desired extended rotaxane structure **IV.66** as shown in Figure IV.20b, where the protons on the phenanthroline moiety and the two most shielded protons on the axle components all shift downfield. Next, preliminary UV–vis and fluorescence spectra were measured to study the impact of fluorenyl moiety on the photophysical properties of the free thread and interlocked structure (Figure IV.21). Interestingly, the fluorenyl-appended free thread (**IV.65**) exhibits a bathochromic shift in emission compared to the free thread (**IV.51**, Figure IV.18), resembling that of the [2]rotaxane (**IV.52**). In contrast, appending the fluorenyl moiety to the [2]rotaxane does not impact the emission profile compared to that of [2]rotaxane **IV.52**. Future studies, including measurements of fluorescence quantum yield, brightness and lifetime will be conducted to fully rationalize the influence of the fluorenyl units on the photophysical performance of the rotaxanes and evaluate their potential as good blue emitters.

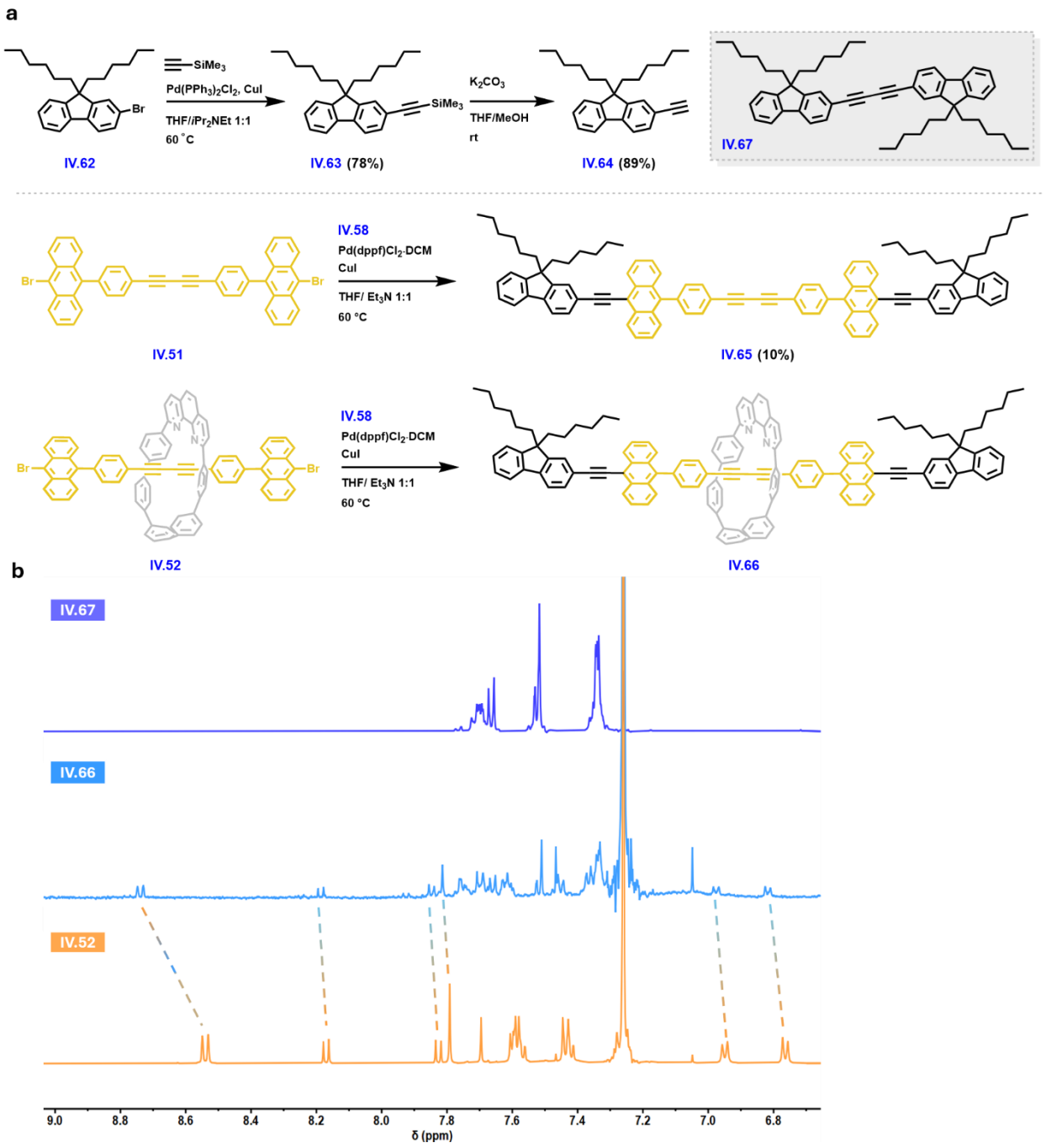


Figure IV.20. (a) Synthetic route of fluorenyl with terminal alkyne **IV.64** and the subsequent Sonogashira cross coupling reaction with free thread **IV.51** to yield the model compound **IV.65**, and with the rotaxane **IV.52** to afford the monomer analog **IV.66**. (b) ^{1}H NMR spectra comparison confirms the targeted fluorenyl-functionalized [2]rotaxane **IV.66** was obtained.

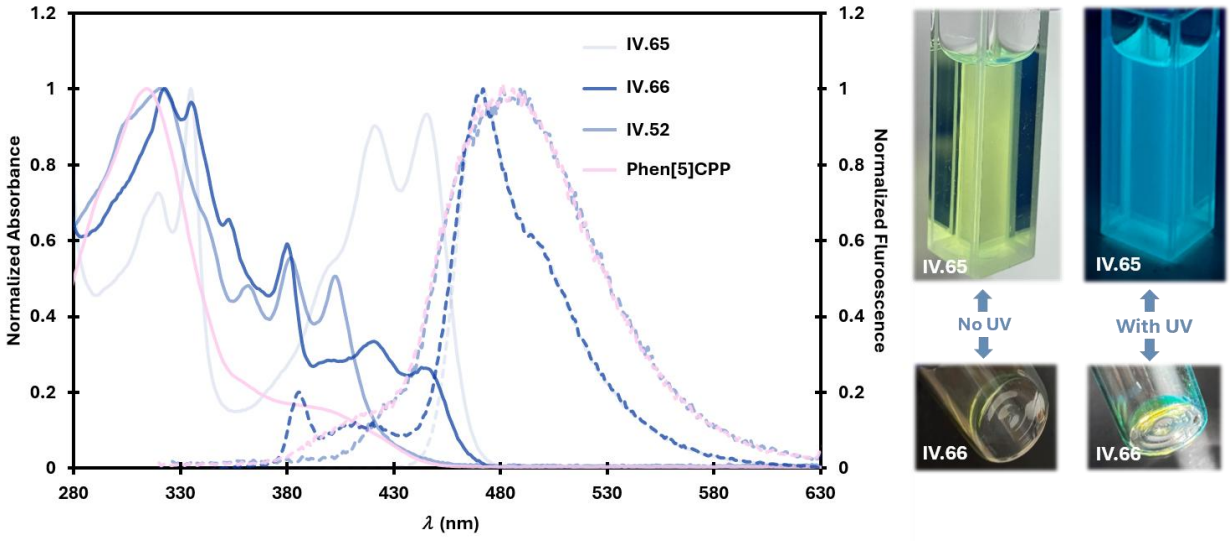


Figure IV.21. UV–Vis and fluorescence spectra of [2]rotaxane **IV.52**, fluorenyl-functionalized free thread **IV.65** and that of [2]rotaxane **IV.66** measured in CH_2Cl_2. The product shows bright blue emission under UV irradiation or direct sunlight.

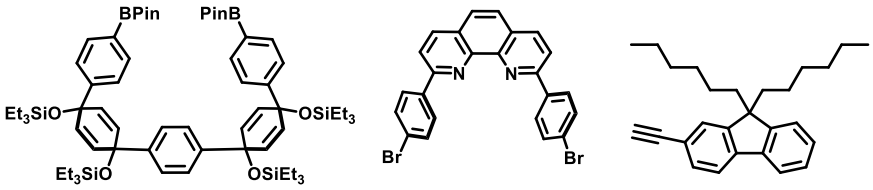
IV.3. Conclusions

These rotaxane examples represent an exciting avenue toward topological molecular nanocarbons. To the best of our knowledge, this is the first series of fully π-conjugated rotaxane featuring PAH molecules amenable to post functionalization. Polymerization using fluorenyl derivatives are under study, which renders these rotaxanes promising candidates for use in organic light emitting diodes.

IV.4. Methods and Materials

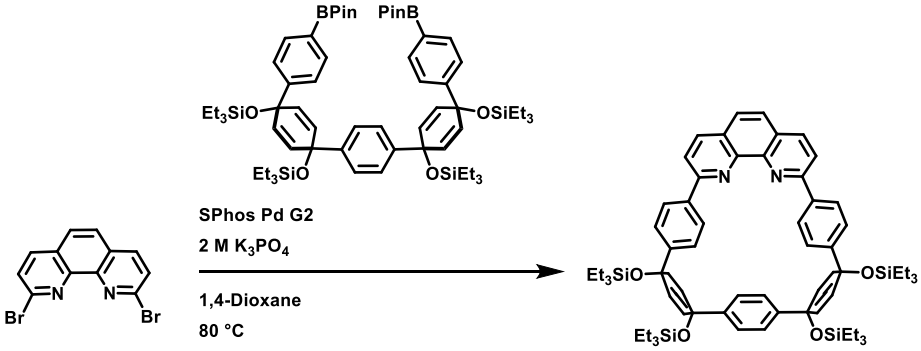
All reagents were purchased from commercial sources and used as received from commercial suppliers. **IV.38**,[69] **IV.42**[113] and **IV.64**[114] were prepared according to the literature methods and the obtained ^{1}H NMR spectra are consistent with literature. All reactions were carried out under a nitrogen atmosphere unless explicitly stated otherwise. Anhydrous tetrahydrofuran (THF), 1,4-Dioxane and Dichloromethane (DCM) were taken from solvent purification system (SPS) without further purification. For the stationary phase used in column chromatography, silica gel is purchased from ZEOCHEM® (ZEOprep Silicagel 60 HYD / 40-63 µm) and Alumina is purchased from Sorbtech (Alumina, Basic, Act. II-IV). Proton (^{1}H) and carbon (^{13}C{^{1}H}) NMR spectra were recorded on the Bruker Avance-IV HD 500 MHz NMR Spectrometer. $CDCl_3$ used

for NMR experiment is 99.8% deuterated with 0.05% v/v tetramethylsilane (TMS). Chemical shifts were given in ppm relative to residue protons ($CHCl_3$: 7.26, s for ^1H, 77.16 for ^{13}C; CH_2Cl_2: 5.32, t for ^1H, 53.56 for ^{13}C). The abbreviations of s, d, t, q and m represent the multiplicities of singlet, doublet, triplet, quartet and multiplet, respectively. Mass spectrometric data were acquired by JMS-T2000GC AccuTOF™ GC-Alpha (EI), Waters Synapt G2-Si ESI/LC-MS (ESI) and Bruker Daltonics UltrafleXtreme MALDI TOFTOF (MALDI). UV-vis and fluorescence spectra were acquired in SPS-grade DCM using a 1 cm borosilicate cuvette on an Agilent Cary 60 UV-Vis and a HORIBA Jobin Yvon FluoroMax-4 spectrofluorometer, respectively. Preparation of fresh H_2SnCl_4 solution: To a solution of $SnCl_2 \cdot 2H_2O$ (140 mg, 0.620 mmol) in 13 mL THF was added conc. HCl (0.10 mL, 1.241 mmol). The resulting solution was then stirred for 30 minutes prior to use.



IV.38 IV.42 IV.64

IV.4.1. Synthetic procedures



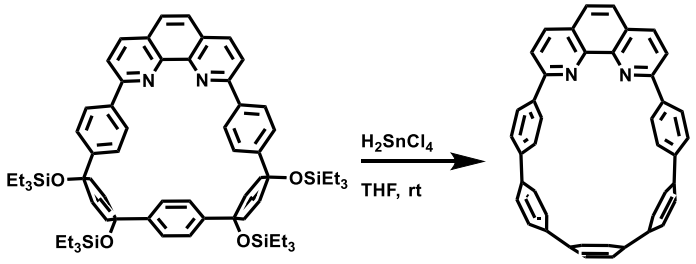
Phen[5]mac-OTES: To a 100 mL round bottom flask were added 2,9-Dibromo-1,10-phenanthroline (55.4 mg, 0.164 mmol, 0.95 equiv.), **IV.38** (200 mg, 0.172 mmol, 1 equiv.) and SPhos Pd G2 (18.6 mg, 0.0129 mmol, 15 mol%). The flask was evacuated and backfilled with N_2 three times before introducing 1,4-Dioxane (~86 mL, 1.5 mM). The reaction mixture was heated to 80 °C and stirred for 3 min prior to the addition of aqueous solution of K_3PO_4 (2 M, 8.62 mL,

100 equiv.). After being stirred at 80 °C for 18 h, the reaction mixture was cooled to room temperature and concentrated in vacuo. The crude was diluted with DI water (10 mL) and DCM (20 mL). The organic layer was collected, and the aqueous layer was further extracted with DCM (30 mL × 2). The combined organic layers were washed with DI water (50 mL), brine (50 mL), dried over Na_2SO_4, filtered and concentrated in vacuo. The crude was subjected to column chromatography (SiO_2, wet loaded, 50–80% DCM in Hexanes) to give the title compound as an off-white solid (64.4 mg, 36%). R_f = 0.25 (SiO_2, 50% DCM in Hexanes).

^{1}H NMR (500 MHz, $CDCl_3$) δ 8.51 (d, J = 8.6 Hz, 4H), 8.26 (d, J = 8.4 Hz, 2H), 8.14 (d, J = 8.5 Hz, 2H), 7.75 (s, 2H), 7.53 (s, 2H), 7.52 (d, J = 2.8 Hz, 6H), 6.12 (d, J = 10.1 Hz, 4H), 5.92 (d, J = 10.0 Hz, 4H), 1.05 (t, J = 7.9 Hz, 18H), 0.92 (t, J = 7.9 Hz, 18H), 0.77 (q, J = 8.0 Hz, 12H), 0.52 (q, J = 8.0 Hz, 12H).

^{13}C{^{1}H} NMR (126 MHz, $CDCl_3$) δ 155.53, 147.72, 146.21, 145.88, 137.79, 136.57, 132.28, 130.92, 127.51, 127.28, 126.31, 126.11, 125.67, 118.74, 77.41, 77.16, 76.90, 72.04, 70.98, 7.31, 7.28, 6.71, 6.55, 0.14.

HRMS (ESI-TOF) m/z: $[M+H]^+$ calcd for $C_{66}H_{87}N_2O_4Si_4$: 1083.5743, found 1083.5726. Error -1.57 ppm.



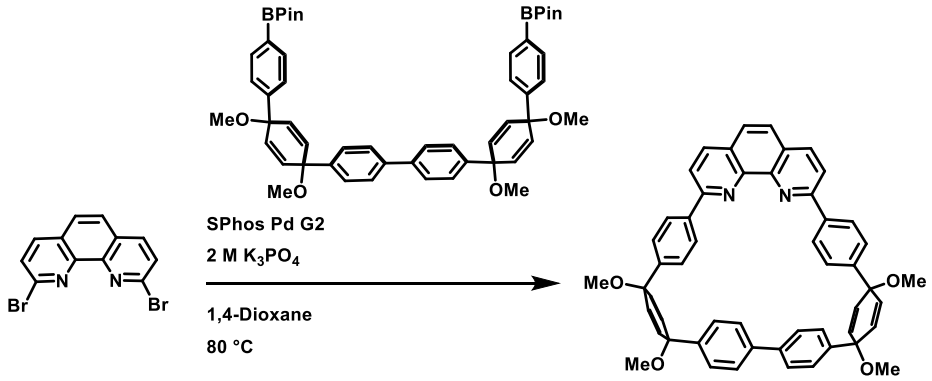
Phen[5]CPP: To a flask charged with Phen[5]mac-OTES (44 mg, 0.040 mmol) was evacuated and backfilled with N_2 three times before introducing THF (5 mL). Freshly prepared H_2SnCl_4 (4.40 mL, 0.176 mmol, 0.04 M in THF, 4.4 equiv.) was added dropwise and the reaction turned to light yellow rapidly. The reaction was stirred at rt for 6 h before quenching with NaOH (1 M, ~ 3 mL). The reaction mixture was diluted with DCM (30 mL) and DI water (30 mL). The organic layer was separated, and the aqueous layer was further extracted with DCM (40 mL × 2). The combined organic layers were washed with DI water (50 mL), dried over Na2SO4, filtered and concentrated in vacuo to afford crude as a yellow solid. The crude was fully dissolved in DCM, and dried loaded onto alumina and subjected to column chromatography (Al_2O_3, 20–50% DCM in Hexanes) to

afford the title compound as a yellow solid (6.2 mg, 28%). Further purification by recrystallization from dichloromethane/hexanes could afford a highly pure sample. R_f = 0.30 (Alumina, 50% DCM in Hexanes).

^{1}H NMR (500 MHz, $CDCl_3$) δ 8.29 (d, J = 8.2 Hz, 2H), 7.99 (d, J = 8.2 Hz, 2H), 7.80 (s, 2H), 7.71 (d, J = 8.0 Hz, 4H), 7.55 (d, J = 8.1 Hz, 8H), 7.32 (dd, J = 11.8, 8.5 Hz, 8H).

^{13}C{^{1}H} NMR (126 MHz, $CDCl_3$) δ 159.25, 146.61, 142.52, 140.41, 138.96, 138.75, 136.95, 136.62, 129.38, 128.91, 128.76, 127.85, 127.84, 127.53, 125.97, 120.73.

HRMS (ESI-TOF) m/z: $[M+H]^+$ calcd for $C_{42}H_{27}N_2$ 559.2174, found 559.2173. Error -0.01 ppm.

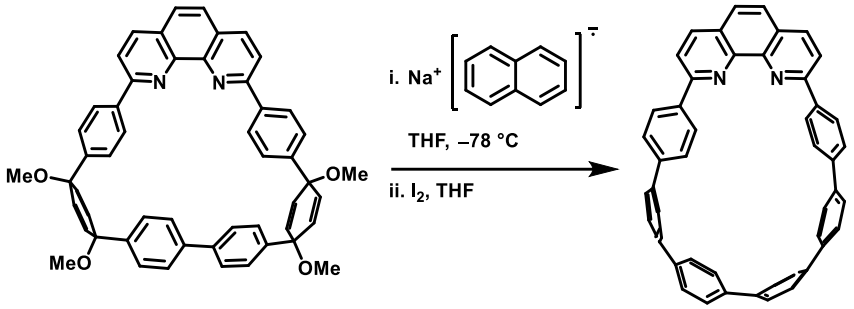


Phen[6]OMe: To a 250 mL round bottom flask were charged with 2,9-Dibromo-1,10-phenthroline (47.0 mg, 0.139 mmol, 0.95 equiv.), BisBpin[6]OMe (122.2 mg, 0.146 mmol, 1 equiv.) and SPhos Pd G2 (15.8 mg, 0.022 mmol, 15 mol%). The flask was evacuated and back-filled with N_2 three times, followed by introduction of 1,4-Dioxane (ca. 130 mL, 1.1 mM). The reaction mixture was heated to 80 °C and stirred for 5 min prior to the addition of aqueous solution of K_3PO_4 (2 M, 7.32 mL, 100 equiv.). After being stirred at 80 °C for 20 h, the reaction mixture was cooled to room temperature and concentrated in vacuo. The crude was diluted with DI water (10 mL) and DCM (20 mL). The organic layer was collected, and the aqueous layer was further extracted with DCM (30 mL × 2). The combined organic layers were washed with DI water (50 mL), brine (50 mL), dried over Na_2SO_4, filtered and concentrated in vacuo. The crude was triturated in 1:1 EtOAc/DCM, filtered to afford product as a light yellow with good purity.

^{1}H NMR (500 MHz, $CDCl_3$) δ 8.32 (d, J = 8.4 Hz, 2H), 8.16 (d, J = 8.4 Hz, 4H), 8.02 (d, J = 8.4 Hz, 2H), 7.81 (s, 2H), 7.64 (d, J = 8.4 Hz, 4H), 7.54 (d, J = 8.4 Hz, 4H), 7.41 (d, J = 8.4 Hz, 4H), 6.20 (s, 8H), 3.53 (s, 6H), 3.45 (s, 6H).

$^{13}C\{^{1}H\}$ NMR (126 MHz, $CDCl_3$) δ 158.55, 146.76, 144.38, 141.99, 140.01, 139.14, 137.46, 134.84, 132.27, 128.70, 128.61, 126.96, 126.77, 126.73, 126.34, 122.95, 75.93, 75.12, 52.55, 51.87.

HRMS (ESI-TOF) m/z: $[M+H]^+$ calcd for $C_{52}H_{43}N_2O_4$: 759.3223, found 759.3220. Error: -0.40 ppm.

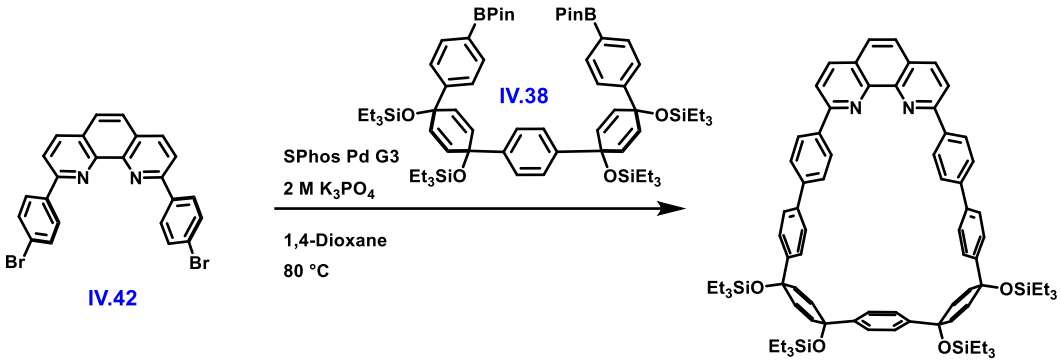


Phen[6]CPP: A flame-dried flask charged with Phen[6]mac-OMe (22.2 mg, 0.029 mmol, 1.0 equiv.) was evacuated and back-filled with N_2 three times, followed by addition of THF (5.85 mL). The suspension was cooled to –78 ºC for 5 min before dropwise addition of sodium naphthalenide solution (1 M in THF) was added dropwise. After being stirred at –78 ºC for 4 h, the reaction was quenched with addition of I_2 in THF (1 M) until excess I_2 remained in solution. The reaction mixture was warmed at room temperature, and excess I_2 was quenched with addition of satd. aq. $Na_2S_2O_3$. The resulting mixture was diluted with DCM (20 mL). The organic layer was separated, and the aqueous layer was further extracted with DCM (20 mL × 2). The combined organic layers were washed water (50 mL), dried over Na2SO4, filtered and concentrated in vacuo. The crude material was dissolved in DCM, dry-loaded onto alumina, and purified via flash column chromatography (alumina, gradient elution: 50–60% DCM in hexanes). The product-containing fractions were concentrated and triturated with pentane to afford the title compound as a yellow solid (2.7 mg, 10%). R_f = 0.57 (80% DCM in hexanes).

^{1}H NMR (500 MHz, $CDCl_3$) δ 8.31 (d, J = 8.3 Hz, 2H), 8.01 (d, J = 8.3 Hz, 2H), 7.93 (d, J = 8.2 Hz, 4H), 7.80 (s, 2H), 7.60 (approx. t , J = 9.3 Hz, 8H), 7.53 (d, J = 8.8 Hz, 4H), 7.41 (d, J = 14.8, 8.2 Hz, 4H), 7.39 (d, J = 8.4 Hz, 4H).

$^{13}C\{^{1}H\}$ NMR (126 MHz, $CDCl_3$) δ 158.75, 146.59, 142.20, 140.15, 139.70, 138.55, 138.22, 136.82, 136.74, 128.99, 128.62, 128.54, 128.36, 127.73, 127.58, 127.42, 126.10, 120.95. 18 carbon signals in total.

HRMS (ESI-TOF) m/z: $[M+H]^+$ calcd for $C_{48}H_{31}N_2$: 635.2487, found 635.2491. Error: -0.40 ppm.

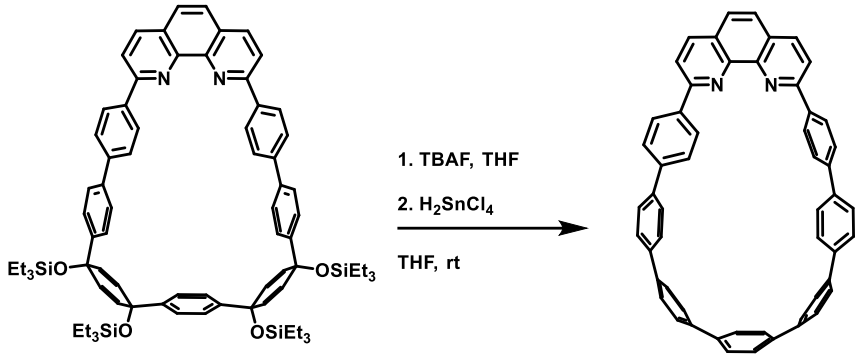


Phen[7]mac-OTES: To a 100 mL round bottom flask were added **IV.42** (20.1 mg, 0.041 mmol, 0.95 equiv.), **IV.38** (50 mg, 0.043 mmol, 1 equiv.) and SPhos Pd G3 (5.05 mg, 0.006 mmol, 15 mol%). The flask was evacuated and backfilled with N_2 three times before introducing 1,4-Dioxane (~22 mL, 2 mM). The reaction mixture was heated to 80 °C and stirred for 3 min prior to the addition of aqueous solution of K_3PO_4 (2 M, 0.91 mL, 42 equiv.). After being stirred at 80 °C for 1 day, the reaction mixture was cooled to room temperature and concentrated in vacuo. The crude was diluted with DI water (10 mL) and DCM (20 mL). The organic layer was collected, and the aqueous layer was further extracted with DCM (20 mL × 2). The combined organic layers were washed with DI water (30 mL), brine (30 mL), dried over Na_2SO_4, filtered and concentrated in vacuo. The crude was purified by flash column chromatography (SiO_2, wet loaded, 10–30% EtOAc in hexanes) to afford the target product as a white solid (12.8 mg, 24%). Alternatively, the crude post workup can also subjected to trituration in EtOAc and hexanes mixture to afford target product. R_f = 0.47 (20% EtOAc in hexanes).

^{1}H NMR (500 MHz, $CDCl_3$) δ 8.55 (d, J = 8.2 Hz, 4H), 8.31 (d, J = 8.3 Hz, 2H), 8.12 (d, J = 8.3 Hz, 2H), 7.80 (d, J = 8.3 Hz, 4H), 7.80 (s, 2H) 7.65 (d, J = 8.2 Hz, 4H), 7.54 (s, 4H), 7.51 (d, J = 8.2 Hz, 4H), 6.14 (d, J = 10.0 Hz, 4H), 5.99 (d, J = 10.0 Hz, 4H), 1.01 (t, J = 7.9 Hz, 18H), 0.93 (t, J = 7.9 Hz, 18H), 0.73 (q, J = 7.9 Hz, 12H), 0.53 (q, J = 7.9 Hz, 12H).

^{13}C {^{1}H} NMR (126 MHz, $CDCl_3$) δ 156.23, 146.32, 145.95, 145.78, 141.78, 139.59, 139.43, 136.43, 132.49, 131.28, 128.69, 127.56, 127.16, 127.15, 126.26, 126.24, 125.67, 119.05, 71.29, 70.39, 7.31, 7.28, 6.67, 6.60.

HRMS (ESI) m/z: $[M+H]^+$ calcd for $C_{78}H_{95}N_2O_4Si_4$ 1235.6369, found 1235.6378. Error 0.73 ppm.

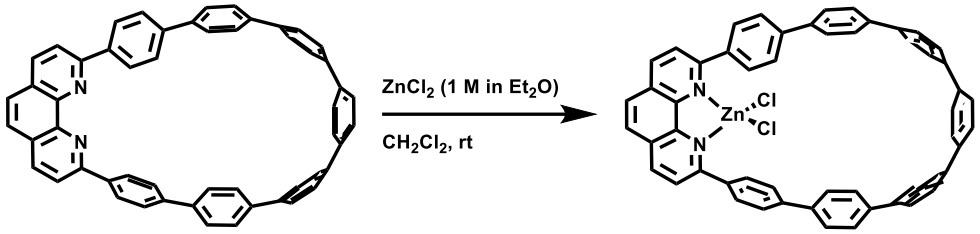


Phen[7]CPP: To a 25 mL round bottom flask was added **Phen[7]mac-OTES** (31.1 mg, 0.025 mmol), which was subjected to evacuation and back-filled with N_2 three times before dissolved in THF (3.5 mL). To this solution was then added freshly prepared H_2SnCl_4 (2.21 mL, 0.111 mmol, 0.05 M) dropwise, which turned the colorless reaction mixture to bright yellow immediately (fluorescence turned off). After stirring for 16 h, satd. aq. $NaHCO_3$ was added to the reaction mixture to quench the residual acid along with addition of some water (ca. 3 mL). The reaction mixture was diluted with DCM (20 mL) and DI water (20 mL). The organic layer was separated and the aqueous layer was extracted with additional DCM (50 mL × 2). The organic layers were combined, washed with water (30 mL), brine (30 mL), dried over Na_2SO_4, filtered and concentrated in vacuo to afford the crude as a light-yellow solid. The crude was purified via plug (alumina, 50% DCM in hexanes) and first eluted blue band was collected, concentrated, and triturated in pentane to afford target product with decent purity (1.7 mg, 10%).

^{1}H NMR (500 MHz, $CDCl_3$) δ 8.32 (d, J = 8.1 Hz, 2H), 8.23 (d, J = 7.7 Hz, 4H), 8.10 (d, J = 8.1 Hz, 2H), 7.81 (s, 2H), 7.57 –7.53 (m, 16H), 7.48 (d, J = 8.5 Hz, 4H), 7.45 (d, J = 7.6 Hz, 4H).

Notes: *^{13}C NMR spectrum cannot be acquired due to poor solubility.*

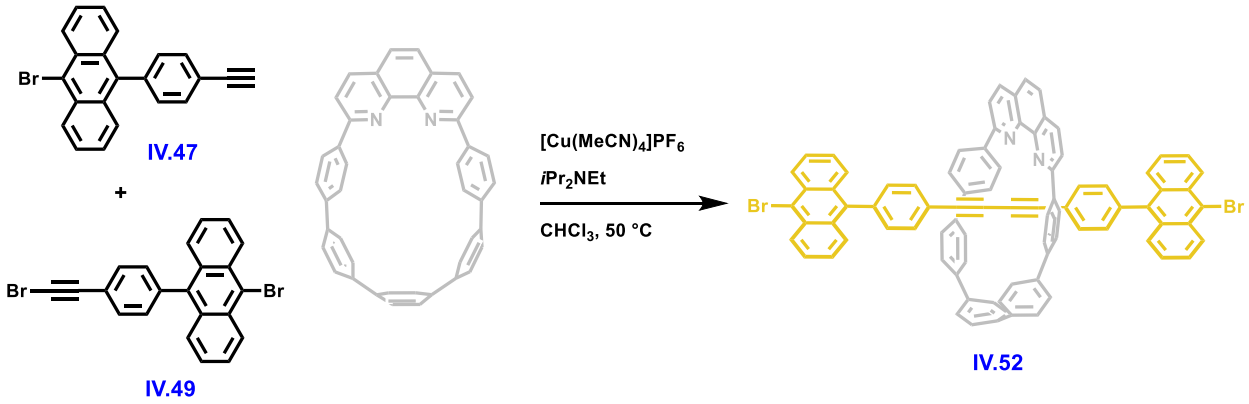
HRMS (ESI-TOF) m/z: $[M+H]^+$ calcd for $C_{54}H_{35}N_2$: 711.2800, found 711.2801. Error +0.14 ppm.



Phen[7]CPP-$ZnCl_2$ complex: To a flame-dried flask was added Phen[7]CPP (2 mg, 0.003 mmol), which was subjected to evacuation and back-filled with Nitrogen three times before addition of DCM (2.6 mL). To this suspension was then added $ZnCl_2$ (1 M in Et_2O, 0.028 mL, 10 equiv.) Upon addition of $ZnCl_2$ solution, the reaction turned from cloudy suspension (poor solubility) to bright yellow solution, suggesting successful formation of complex. After stirring at room temperature for 5.5 h, the reaction was concentrated in vacuo. The crude was dissolved in DCM and triturated with Et_2O to remove access $ZnCl_2$. The precipitate was collected by vacuum filtration to afford the target product as an orange solid (1.5 mg, 63%).

^{1}H NMR (500 MHz, $CDCl_3$) δ 8.62 (d, J = 8.4 Hz, 2H), 8.16 (d, J = 8.4 Hz, 2H), 8.04 (s, 2H), 8.01 (d, J = 8.4 Hz, 4H), 7.65 (d, J = 8.4 Hz, 4H), 7.59–7.48 (m, 20H).

HRMS (MALDI) m/z: [M^+]: calcd for $C_{54}H_{34}N_2ZnCl_2$: 844.1385, found 844.1399. Error 1.61 ppm.



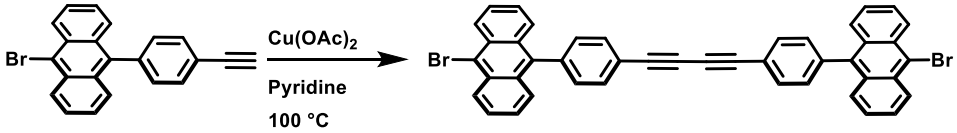
IV.52: To a flame-dried 5 mL round bottom flask were added, **IV.47** (1.56 mg, 0.004 mmol, 2.5 equiv.), **IV.49** (1.9 mg, 0.004 mmol, 2.5 equiv.), Phen[5]CPP (1.03 mg, 0.002 mmol, 1 equiv), and $[Cu(MeCN)_4]PF_6$ (0.65 mg, 0.002 mmol). The flask was evacuated and backfilled with N_2 gas five times before adding N_2-sparged $CHCl_3$ (~2 mL). The mixture was sonicated for 4–5 minutes before start heating to 50 °C and DIPEA (1 uL, 0.001 mmol) was then quickly added. After stirring at 50 C for 2.5 h, the reaction was quenched with addition of NH_3-EDTA with vigorous stirring. The

reaction mixture was diluted with DCM (5 mL). The organic layer was separated, and the aqueous layer was further extracted with DCM (5 mL × 2). The combined organic layers were washed with DI water (10 mL), dried over Na_2SO_4, filtered and concentrated in vacuo to afford crude as off-white solids. The crude was dried loaded onto alumina and then subjected to flash column chromatography (Alumina, 30–35% DCM in hexanes) to afford the target rotaxane as a light-yellow solid. (2.4 mg, quantitative). R_f = 0.16 (Alumina, 30% DCM in hexanes).

^{1}H NMR (500 MHz, CD_2Cl_2) δ 8.53 (d, J = 8.9 Hz, 4H), 8.21 (d, J = 8.3 Hz, 2H), 7.86 (d, J = 8.3 Hz, 2H), 7.82 (s, 4H), 7.72 (s, 2H), 7.63 (d, J = 8.8 Hz, 4H), 7.61–7.59 (m, 4H) 7.59 (d, J = 8.4 Hz, 4H), 7.50 – 7.41 (m, 4H), 7.44 (d, J = 8.3 Hz, 4H), 7.31 (d, J = 8.8 Hz, 4H), 7.28 (d, J = 8.8 Hz, 4H), 7.01 (d, J = 8.1 Hz, 4H), 6.80 (d, J = 8.2 Hz, 4H).

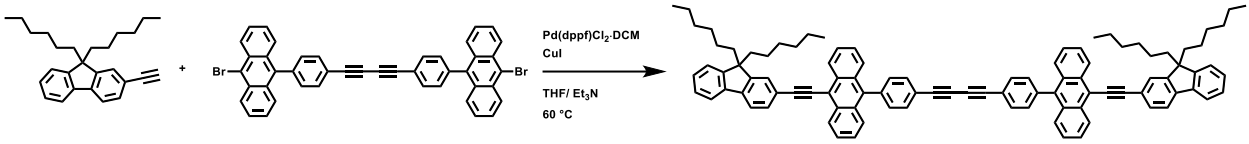
^{13}C {^{1}H} NMR (151 MHz, CD_2Cl_2) δ 159.94, 147.02, 141.59, 140.75, 138.77, 138.63, 138.30, 137.89, 137.47, 136.64, 133.82, 131.00, 130.41, 130.25, 129.62, 128.80, 128.58, 128.38, 128.00, 127.75, 127.72, 127.42, 126.15, 125.78, 122.69, 121.24, 120.44, 82.21, 74.61.

HRMS (ESI-TOF) m/z: $[M+H]^+$ calcd for $C_{86}H_{51}Br_2N_2$: 1269.2414, found 1269.2443. Error 2.28 ppm.



Anthracene-butadiyne: To a 25 mL round bottom flask were added, $Cu(OAc)_2 \cdot H_2O$, to which pyridine (3 mL) was added, afforded a blue suspension. The terminal alkyne was fully dissolved in pyridine (2 mL) and the solution was transferred to the flask containing the Cu(II) catalyst. The reaction was then heated to 100 ºC and stirred for 2 h before heat stopped. *TLC suggested the reaction has gone completion after 2 h.* The reaction was worked up 2 days after, to which water was added, and DCM (15 mL) was added to dilute the reaction mixture. The reaction mixture was transferred to the separatory funnel, and the organic layer was collected. The aqueous layer was further extracted with DCM (25 mL x 2). The combined organic layers were dried over Na_2SO_4, filtered, concentrated in vacuo and washed with methanol to afford the target compound as a yellow-orange solid (51.9 mg, 92%). R_f = 0.45 (SiO_2, 20% DCM in Hexanes).

^{1}H NMR (500 MHz, $CDCl_3$) δ 8.63 (d, J = 8.9 Hz, 4H), 7.80 (d, J = 8.0 Hz, 4H), 7.65–7.59 (m, 8H), 7.45–7.38 (m, 8H). ^{13}C{^{1}H} NMR (126 MHz, $CDCl_3$) δ 139.91, 136.70, 132.79, 131.59, 130.89, 130.38, 128.16, 127.20, 127.13, 126.05, 123.46, 121.50, 81.84, 74.81. 14 carbons in total. HRMS (



Fluorenyl-anthracene dyad: To a 5 mL round bottom flask were added diyne (30 mg, 0.042 mmol, 1.0 equiv), terminal alkyne (60.39 mg, 0.168 mmol, 4.3 equiv), Pd(dppf)Cl_2·DCM (3.85 mg, 0.004 mmol, 11 mol%) and CuI (1.6 mg, 0.008 mmol, 20 mol%). The flask was subjected to evacuation and back-filled with N_2 three times before introducing THF (1 mL) and Et3N (1 mL). The reaction mixture was sparged with N_2 for 5 min and the reaction mixture was heated to 60 C. After being stirred at 60 ºC for 2 days, the reaction mixture was diluted with DCM (30 mL) and was transferred to a separatory funnel. 10% NH_4Cl was added (30 mL). The organic layer was separated and the aqueous layer was further extracted with DCM (30 mL x 2). The combined organic layers were washed with DI water (50 mL), brine (50 mL), dried over Na_2SO_4, filtered and concentrated in vacuo to afford the crude as a dark brown solid. The crude was purified by flash column chromatography (SiO_2, gradient elution:10–20% DCM in Hexanes) and washed with pentane to afford the desired product as a bright yellow solid. R_f = 0.45 (silica gel, 25% DCM in Hexanes).

^{1}H NMR (500 MHz, $CDCl_3$) δ 8.83 (d, J = 8.8 Hz, 4H), 7.82 (d, J = 8.1 Hz, 4H), 7.79 (s, 4H), 7.76 (d, J = 7.5 Hz, 4H), 7.73 (s, 2H), 7.68 (d, J = 8.9 Hz, 4H), 7.67–7.63 (m, 4H), 7.48 (d, J = 8.2 Hz, 4H), 7.47 – 7.42 (m, 4H), 7.41–7.34 (m, 4H), 2.06 (m, 8H), 1.30–1.26 (m, 12H), 1.12 (m, 24H), 0.78 (t, J = 7.1 Hz, 8H).

^{13}C{^{1}H} NMR (126 MHz, $CDCl_3$) δ 151.57, 142.36, 140.86, 140.41, 137.49, 133.04, 132.57, 131.99, 131.13, 130.17, 128.10, 127.45, 127.36, 126.92, 126.41, 126.39, 123.46, 122.07, 121.52, 120.45, 120.23, 118.48, 103.05, 86.66, 82.14, 74.74, 55.74, 40.78, 31.98, 30.10, 24.24, 22.99, 14.18. HRMS (MALDI-TOF) m/z calcd for $[M]^+$: $C_{98}H_{90}$: 1266.7037, found 1266.6991, error 3.65 ppm.

IV.5. Bridge to chapter V

In this chapter, the synthesis of **Phen[*n*]CPPs** and the solid-state analysis of their Möbius character are discussed. Furthermore, **Phen[*n*]CPPs** (n = 5, 6) were successfully employed as active templates for Cadiot-Chodkiewicz (AT-CC) reactions to afford π-conjugated [2]rotaxanes featuring an anthracene-terminated axle component. Specifically, the smaller **Phen[5]CPP** facilitates the formation of a [2]rotaxane with high efficiency. The following chapter describes the synthesis of a [2]catenane precursor featuring 1,10-phenanthroline-embedded nanohoops using the passive template (PT) method.

CHAPTER V SYNTHESIS AND DESIGN OF [2]CATENANE FEATURING 1,10-PHENANTHROLINE AND ALKYNE FUNCTIONAL HANDLE

This chapter was written by myself with editorial assistance from Professor Ramesh Jasti. Building on the previous discussion of rotaxanes, this chapter focuses on the CPP-derived catenane family.

V.1. Introduction

The development of CPP-based catenanes represents an important advancement in accessing mechanically interlocked structures with unique topologies. Unlike the axle-ring interface of rotaxanes, where translational motion is often a defining feature of their dynamic properties, the catenane architecture provides an extended interfacial contact area between the entwined macrocycles. These distinct structural characteristics motivate us to investigate how the properties of CPP-derived fully π-conjugated catenane polymers diverge from their rotaxane counterparts, particularly concerning their dynamic behavior, the electronic communication between the macrocycles, and ultimately, how the mechanical properties of these polycatenanes differ from traditional, covalently linked polymer systems.

The development of the synthetic methodology of CPP-based rotaxanes and catenanes has been synergistic, as the successful synthesis of one topological motif often has provided critical methodologies for the other. The first two [2]catenanes made up of CPPs were reported by the

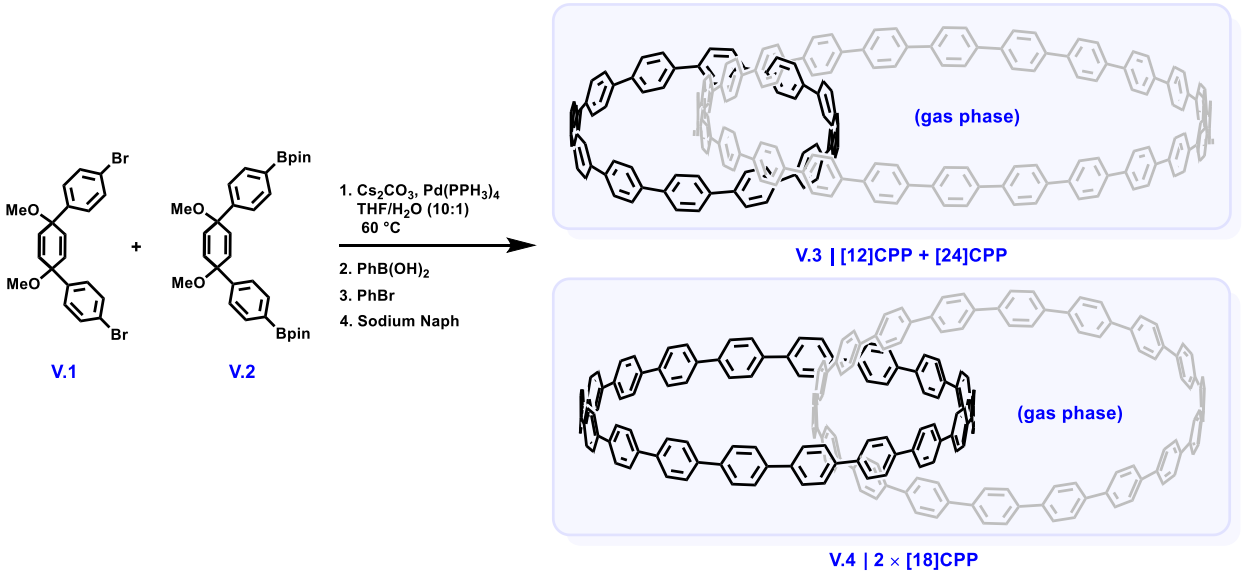


Figure V.1. The first reported identification of [2]catenanes consists of CPPs.

Müllen group in 2017.[115] They employed the Jasti method[3] to synthesize macrocyclic precursors from C-shaped building blocks (**V.1** and **V.2**). Subsequent end-capping with phenyl groups facilitated the conversion of these precursors into discrete linear and cyclic species, which improved the efficiency of the following separation (Figure V.1). By using ion-mobility mass spectrometry (IMMS) that separates the mixture based on molecular size, they successfully identified CPPs and the co-exsistent of catenated CPPs (**V.3** and **V.4**) that are challenging to elucidate using traditional mass spectrometric methods. Although only trace amounts were identified, this discovery revealed the potential for constructing CPP-based catenanes, thereby motivating researchers to pursue more directional and selective synthetic strategies.

Starting in 2018, several research groups demonstrated the successful synthesis of topologically distinct CPP-based catenanes, with a subset of these studies further expanding the scope to polycatenane architectures. Regarding synthetic methodology, four main strategies have been used for the construction of fully π-conjugated, CPP-derived catenanes. The first method utilizes passive template (PT) method established by Sauvage and coworkers,[116,113] in which the installation of a phenanthroline-containing macrocyclization precursor enables the formation of a stable tetrahedral intermediate with Cu(I). This process preorganizes the two components into an intertwined geometry favorable for subsequent ring closure, and the final demetallation affords the desired catenane.

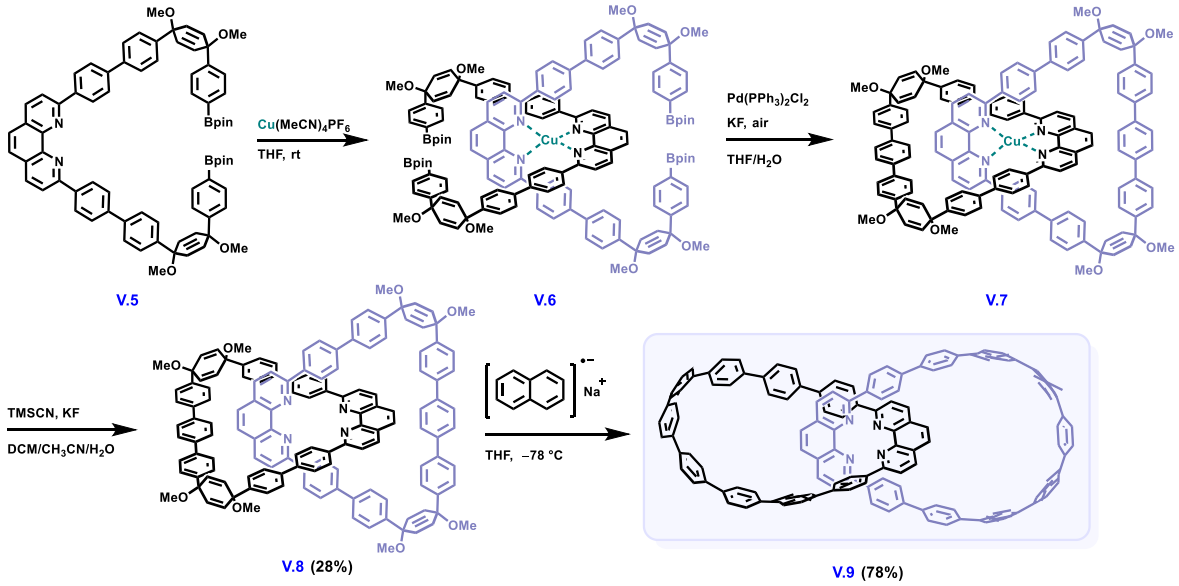


Figure V.2. [2]catenane consists of two Mobiüs conjugated nanohoops.

In 2008, the Cong group applied this concept and demonstrated the first example of a fully π-conjugated catenane incorporating a 1,10-phenathroline moiety at the 2,9-position (Figure V.2).[108] By mixing the phenanthroline-containing precursor **V.5** with $Cu(MeCN)_4PF_6$, the tetrahedral intermediate **V.6** readily forms, which was evidenced by the color change from colorless to bright red. This thermodynamically stable intermediate was then subjected to the oxidative homocoupling to effect ring closure, and subsequent demetallation and aromatization afforded the target [2]catenane **V.9** in good yield.

The second approach leverages a covalent template strategy, which operates on principles similar to the passive template approach. Rather than linking macrocyclic precursors through metal coordination, this method employs stable, yet labile, covalent linkages that can be cleaved selectively to yield the target catenated compounds. Two types of labile linkages have been employed for this purpose: spirosilane-based tethers and azo-based linkers, pioneered by the Itami and Cong groups, respectively. In 2019, Itami and coworkers utilized the first covalent linker to obtain two catenanes (**V.12** and **V.15**) and a trefoil knot **V.18** (Figure V.3).[117]

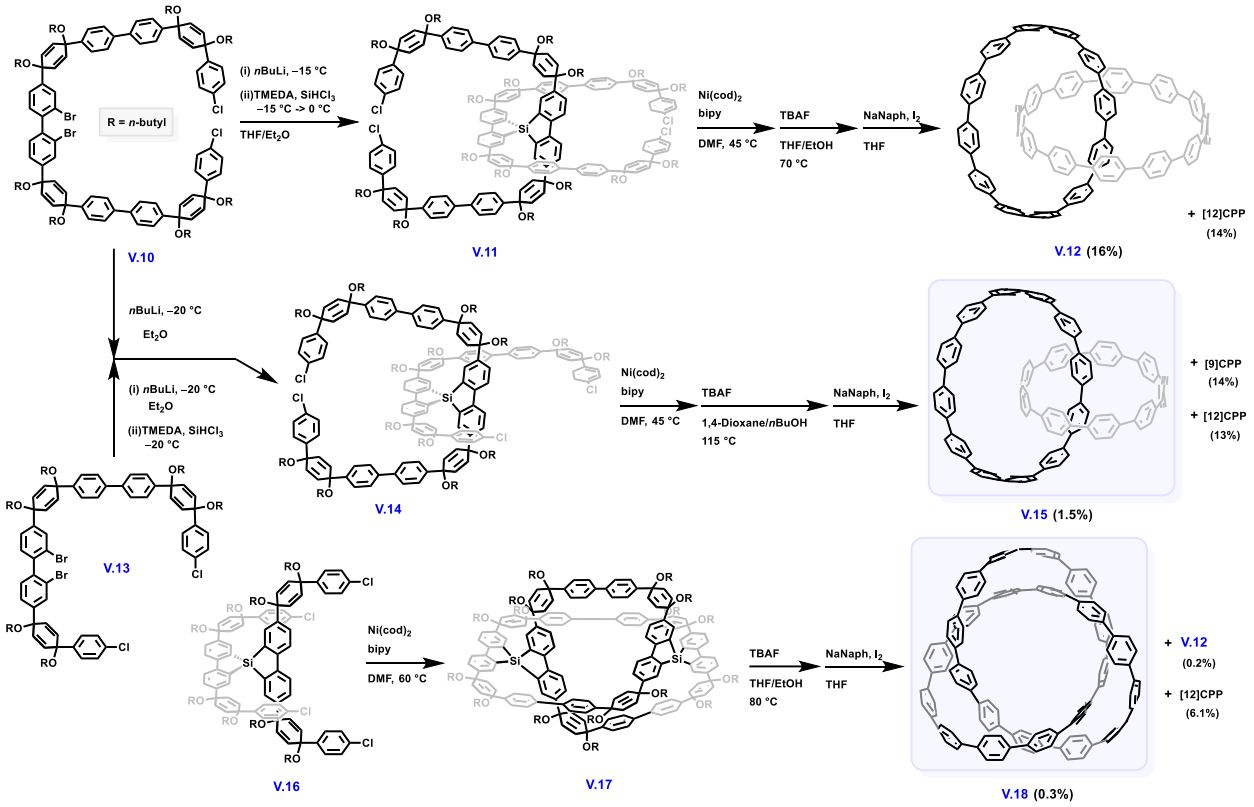


Figure V.3. Synthesis of [2]catenanes and trefoil knot using covalent template method via spirosilane motif.

Starting with a dibrominated U-shaped component (**V.10**), dilithiation, followed by spirosilylation afforded the key intermediate **V.11**. Subsequent ring closure using Yamamoto coupling, cleavage of the spriosilane using a fluoride source, and reductive aromatization afforded the [2]catenane **V.12**, which consists of two interlocked [12]CPPs. Similarly, by employing two different dibrominated U-shaped components (**V.10** and **V.13**), a heteroleptic [2]catenane **V.15,** consisting of [9]CPP and [12]CPP was obtained. Finally, a more challenging trefoil structure was also accessed using the appropriate U-shaped unit (**V.16**). Dimerization of **V.16** provided the trefoil precursor **V.17**, which upon desilylation and aromatization, yielded the trefoil knot **V.18** in low yield. This example underscores the potential of covalent template strategy, often referred to as a traceless template method, which generates interlocked structures with no heteroatoms remaining in the final structures.

Subsequently, in 2022, the Cong group demonstrated the feasibility of an azo-linker as a second traceless template methodology to access a [2]catenane consisting of two *meta*-[9]CPPs (Figure V.4).[118] Suzuki cross coupling with three-ring intermediates **V.21**, followed by Miyaura borylation provided intertwined unit **V.21**. Appending an additional phenylene unit with Suzuki cross coupling afforded **V.22**, which finalized the backbone construction of the *meta*-[9]CPP. Yamamoto coupling then yielded precatenane with azolinker (**V.23**). Subsequent aromatization, reduction of azo linker and deamination afforded the final [2]catenane **V.25**.

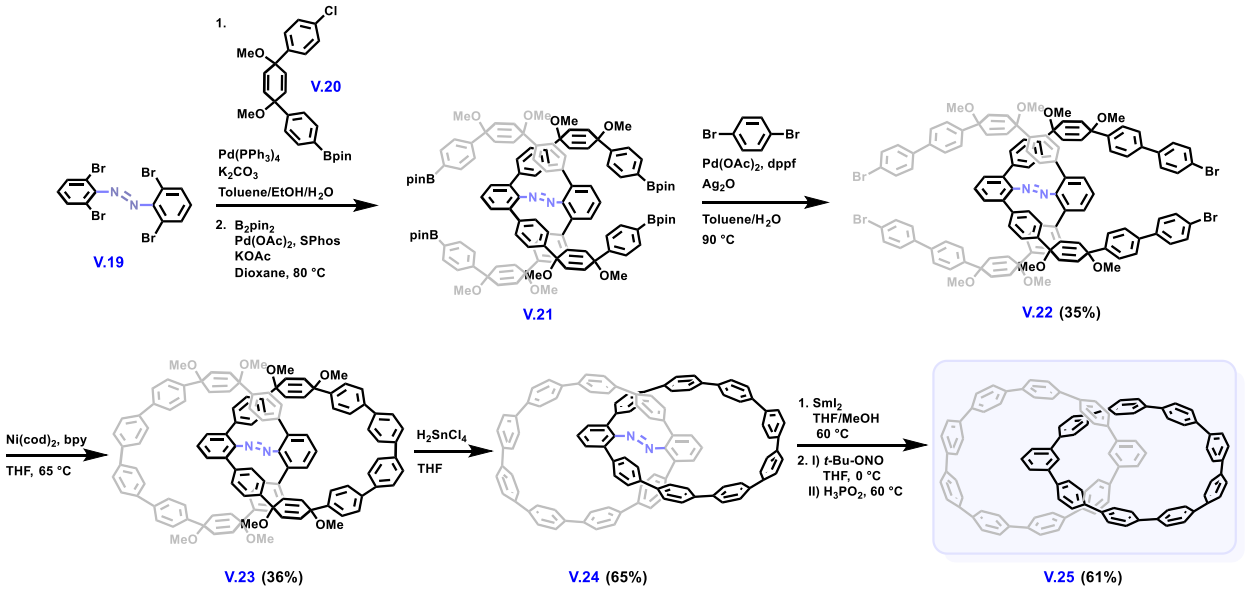


Figure V.4. Synthesis of [2]catenane consists of two *meta*-[9]CPPs using covalent template method via azo linker.

The third synthetic approach utilizes a host-guest template strategy, which relies on non-covalent interactions to preorient individual components into the geometry favorable for the subsequent catenation step. In 2023, building on their successful synthesis of a C_{60}/[10]CPP-based rotaxane reported in 2018, the von Delius group reported a C_{60}/[10]CPP-based catenane (Figure V.5).[119] In this work, they employed a tetragonal prismatic Pd-nanocapsule (**V.28**) that is formed through self-assembly between macrocycle **V.26** and porphyrin derivative **V.27** as a host to encapsulate C_{60} and [10]CPP.[120] This provided a three-shell matryoshka-like supramolecular structure, which significantly enhanced the regioselectivity of the bis-Bingel cyclopropanation reaction with **V.30** to provide the *trans*-3 C_{60}/[10]CPP-based [2]catenane (**V.31**) with >97% selectivity.

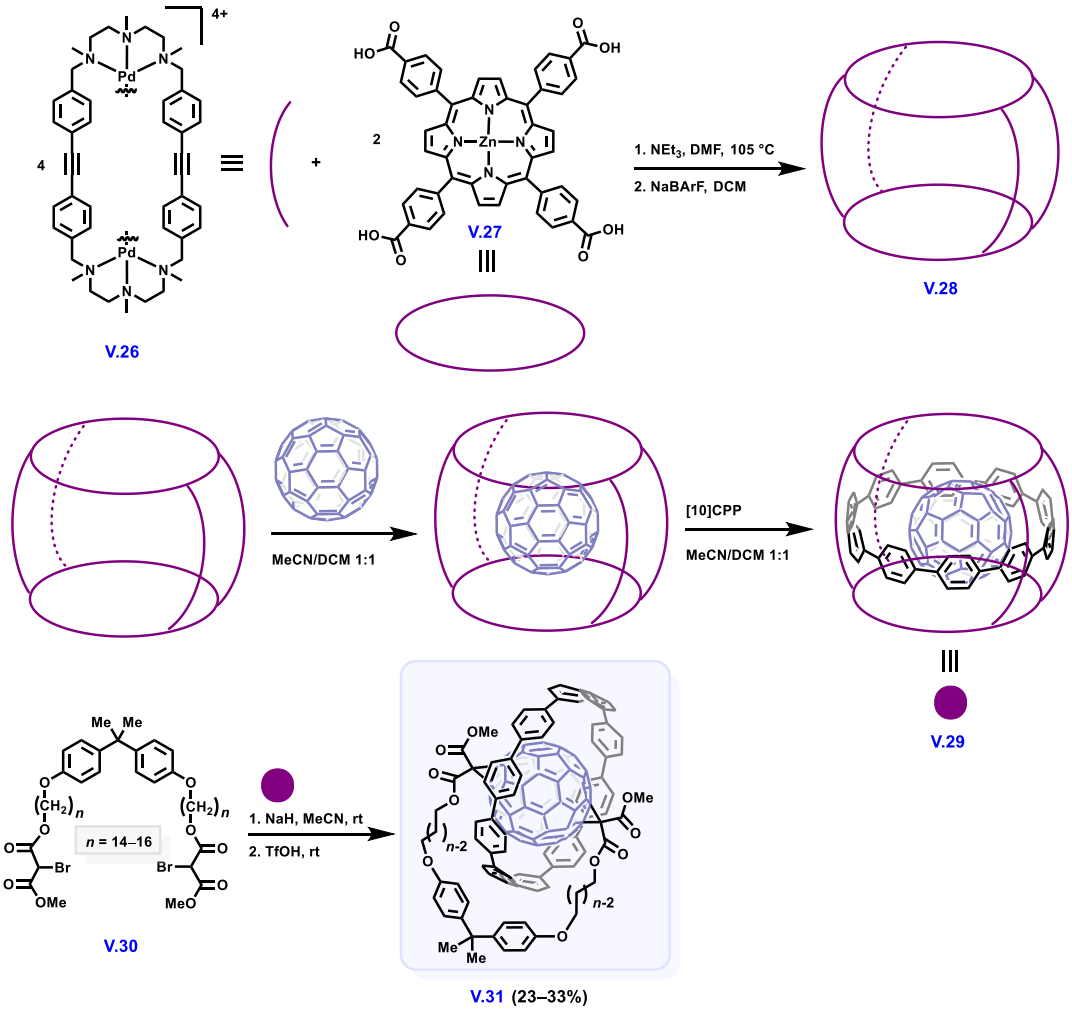


Figure V.5. Synthesis of C60/[10]CPP-based catenanes using Pd-nanocapsule as a mask to enhance regioselectivity.

In 2025, the group further collaborated with the Du and Xu group, reported the first [12]CPP-containing [3]catenane (Figure V.6).[121]

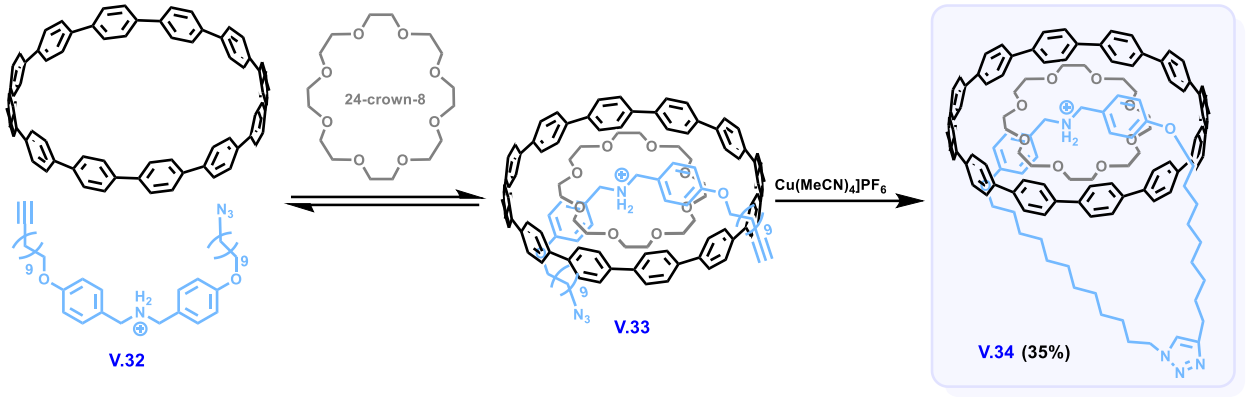


Figure V.6. Synthesis of a [3]catenane **V.34** via a ring-in-ring strategy using a ternary template to promote intramolecular CuAAC.

In this work, inspired by the favorable interaction between a chiral [12]CPP derivative and 18-crown-6 reported by the Jiang group, the authors employed a ring-in-ring strategy to promote the [3]catenane formation. To accommodate an axle component with phenylene units, 24-crown-8 was chosen for its larger cavity. Importantly, an investigation into the non-covalent association between [12]CPP, a dibenzylammonium axle unit bearing two terminal iodide groups, and 24-crown-8 revealed that the presence of axle component enhances the interaction between [12]CPP and 24-crown-8. This suggests a thermodynamically favorable ternary complex (**V.33**) is formed, which serves as a pre-organized intermediate for the catenation step. Consequently, by mixing [12]CPP, 24-crown-8, and axle component **V.32** for one day, followed by the addition of a Cu(I) catalyst for an intramolecular alkyne-azide cycloaddition (CuAAC), the desired [3]catenane **V.34** was isolated in 35% yield. While this host-guest template method provides access to structurally unique catenanes, it necessitates a more careful selection of substrates to assure strong non-covalent interactions, which limits the ability to generalize the method to diverse structural motifs.

The fourth method is the active template (AT) strategy, which serves as a 'Goldilocks' methodology, bridging the gap between traceless and PT methods. In this approach, the

macrocyclic template possesses a recognition site that endotopically coordinates a catalytic metal center inside the cavity, which facilitates the bond-forming reaction to establish the interlocked structure. This fundamentally distinguishes the AT method from the PT method, where the metal merely functions to preorganize the precursors into the required geometry without actively catalyzing the ring-closure step. Furthermore, the AT strategy enables access to kinetically controlled products that are often inaccessible using the PT methods, which are primarily driven by thermodynamic stability. In 2023, the Itami group utilized the AT method to report the first [9]CPP-bipyridine catenane (Figure V.7).[122] By subjecting a bipyridine-containing macrocycle **V.35** and a three-ring intermediate **V.36** to nickel-mediated homocoupling conditions, they accessed the interlocked structure **V.37**. Subsequent deprotection and aromatization yielded the [2]catenane consisting of [9]CPP and the bipyridine macrocycle (**V.38**) in 38% yield.

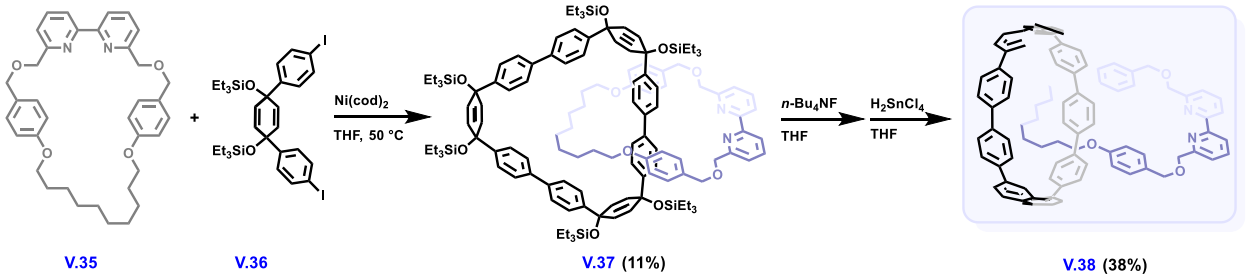


Figure V.7. Synthetic scheme of CPP-bipyridine **V.38** via AT method via Ni-mediated homocoupling condition.

In addition to Ni-mediated homocoupling, active template methods based on Cu(I)-catalyzed Cadiot-Chodkiewicz (AT-CC) coupling and alkyne-azide cycloaddition (AT-AAC) are also employed in the construction of CPP-derived catenanes. In these instances, however, the AT method is first utilized to synthesize a [2]rotaxane featuring a C-shaped axle component. This rotaxane intermediate is then subjected to macrocyclization with suitable CPP-buliding blocks to afford the target catenane. This represents an indirect AT-based method for accessing [2]catenanes, which differs from the direct approach demonstrated in the aforementioned work by Itami. In 2023, May *et al*. demonstrated the synthesis of three novel [2]rotaxanes using the AT-CC method.[104] These were subsequently subjected to macrocyclization with suitable CPP building blocks to afford two [2]catenanes and one [3]catenane, all featuring diaza-containing CPP

macrocycles. Starting from the bisboronic ester-containing [2]rotaxane (**V.39a** and **V.39b**), which incorporated diaza[8]CPP and diaza[9]CPP precursors, Suzuki macrocyclization with V-shaped five-ring building block (**V.40**) afforded the precatenanes (**V.41a** and **V.41b**).

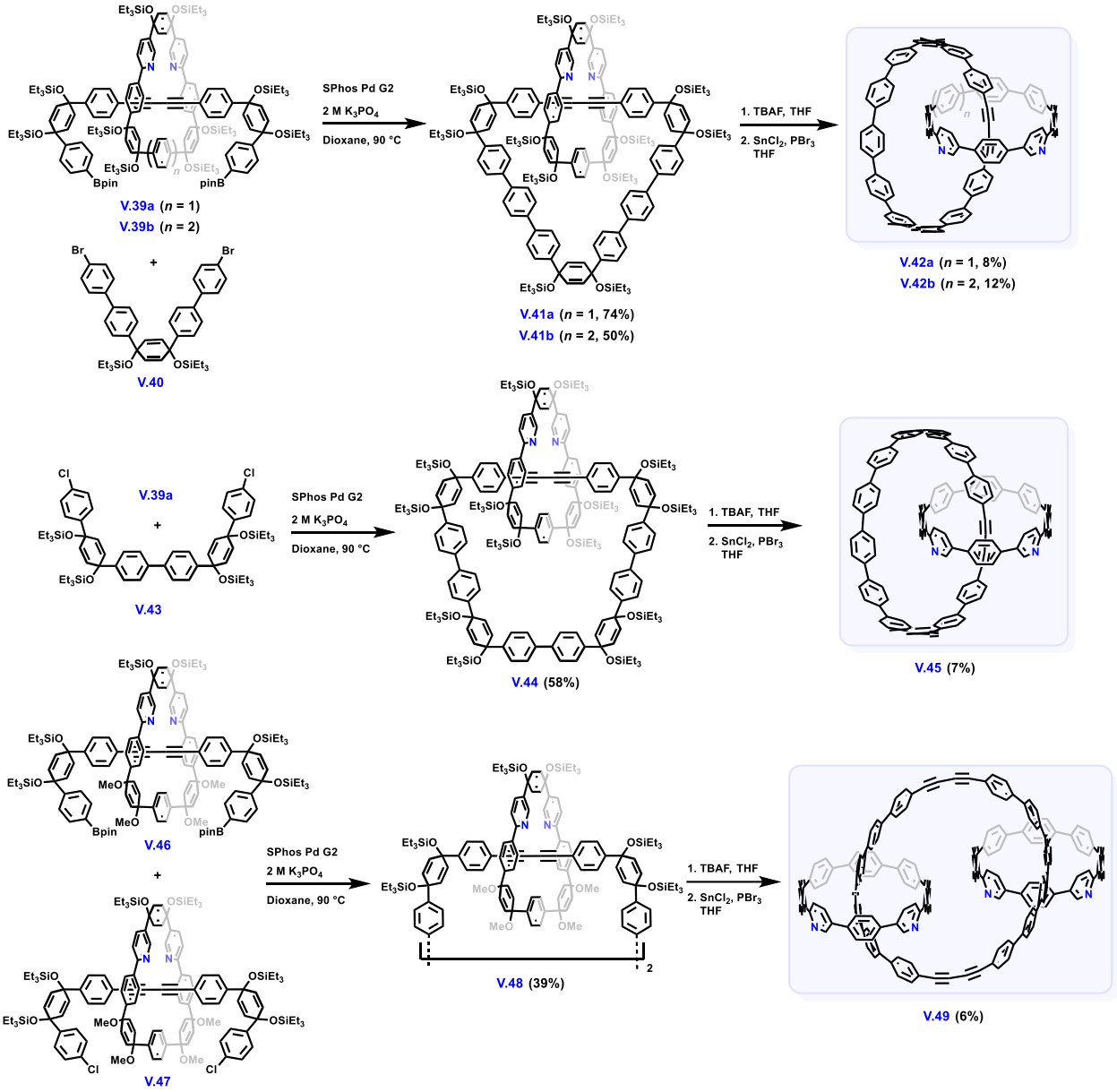


Figure V.8. [2]rotaxane synthesized via the AT-CC method for the construction of fully π-conjugated [2]catenanes (**V.42(a-b), V.45**) and [3]catenane (**V.49**).

Subsequent desilylation and aromatization yielded [2]catenane (**V.42a** and **V.42b**) in 8% and 12% yields, respectively. Furthermore, by substituting the CPP building block **V.40** with **V.43**,

macrocyclization with **V.39a** afforded [2]catenane (**V.45**) consisting of a larger [12+2]CPP and diaza[8]CPP. Lastly, the rotaxane (**V.46**) featuring bisboronic esters reacted with the dichloro counterpart (**V.47**) under Suzuki macrocyclization conditions to afford the precatenane (**V.48**), which upon desilylation and aromatization, afforded the [3]catenane featuring two diaza[8]CPP and a [12+4]CPP.

The Jasti group achieved further success by subjecting [2]rotaxanes featuring bipyridine-containing macrocyclic precursor, obtained via AT-AAC method, to macrocyclization to access [2]catenanes featuring Triazole containing CPPs (Figure V.9).[105]

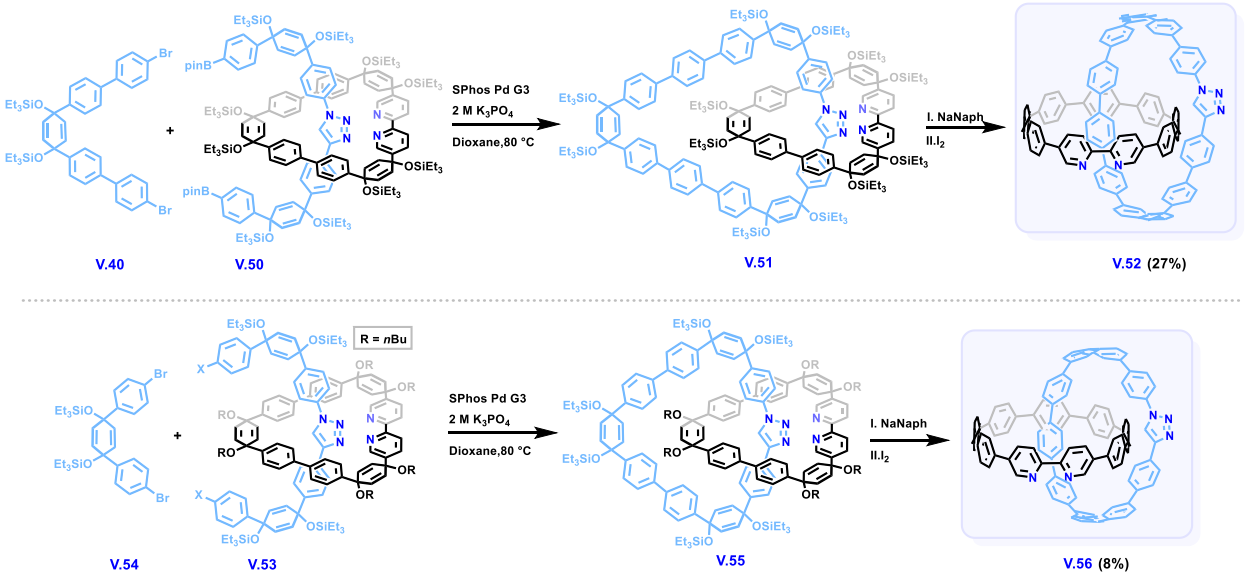


Figure V.9. [2]rotaxane synthesized via AT-AAC for the construction of fully π-conjugated [2]catenanes (**V.52** and **V.56**).

Starting from rotaxane **V.50**, Suzuki coupling with **V.40** afforded the catenane **V.51**, followed by aromatization with sodium naphthalenide to yield the [2]catenane **V.52**, featuring bipy[9]CPP and Tz[12]CPP (where Tz denotes a triazole moiety). Similarly, replacing the silyl ethyl group with less bulky butyl groups facilitated the Suzuki macrocyclization with three-ring building block **V.54**, allowing access to the more compact catenane **V.55**. Subsequent aromatization yielded [2]catenane **V.56**, featuring a smaller Tz[10]CPP. These two examples, based on AT-CC and AT-AAC methods, demonstrate a broad substrate scope, as various combinations of [2]rotaxane and

CPP building blocks with matched size conducive to cyclization enable the synthesis of a diverse library of fully π-conjugated diverse [2] and [3]catenanes.

Notwithstanding the established synthetic routes to CPP-based [2]catenanes, only two reported examples have been shown to be amenable to post-functionalization. In both cases, Ir-catalyzed C-H borylation is employed to functionalize the catenanes, as shown in Figure V.10.

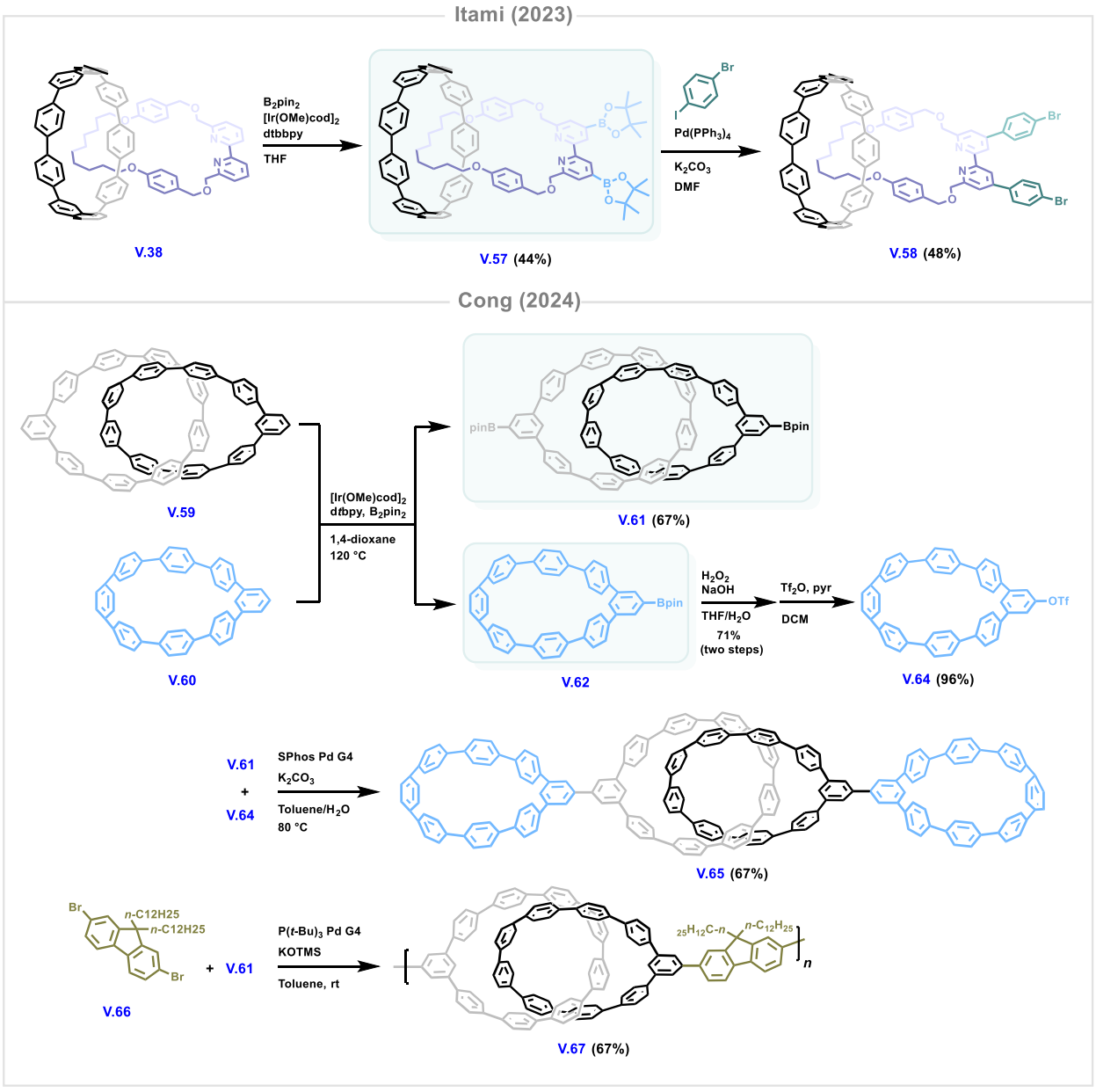


Figure V.10. Literature examples of CPP-based catenanes capable of post-synthetic modification.

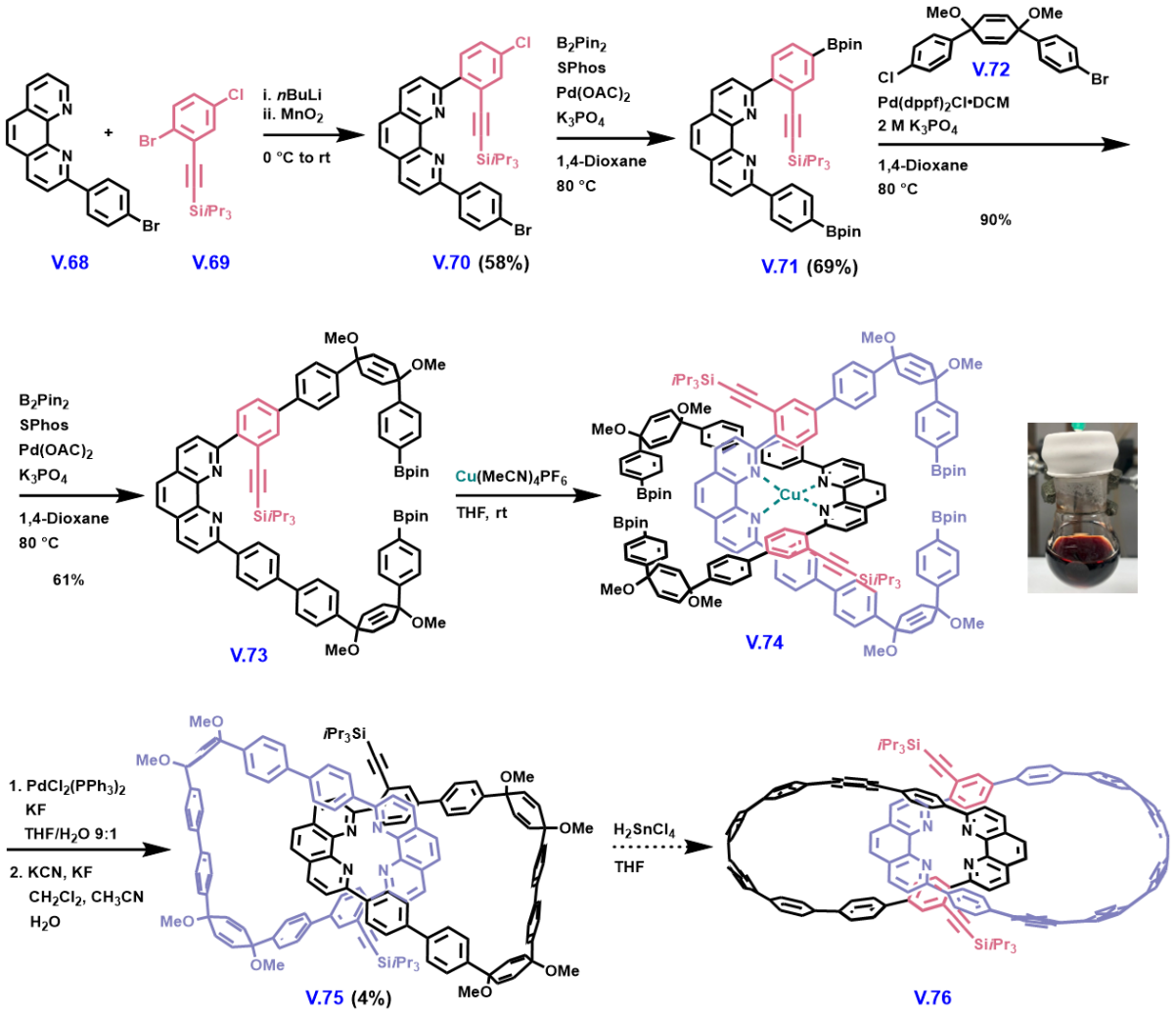
The CPP-bipyridine catenane **V.38** was treated with B_2pin_2 and 4,4'-di-*tert*-butyl-2,2'-bipyridine (d*t*bpy) in the presence of $[Ir(OMe)cod]_2$ to afford the borylated catenane **V.57** in 44% yield.[122] Subsequent Suzuki cross coupling with 1-Bromo-4-iodobenzene afforded the aryl-bromide functionalized catenane **V.58**, which serves as a versatile handle for further cross coupling condition. The second reported example involves catenanes consisting of *meta*[10]CPP.[23] Subjecting *meta*[*n*]CPP (where $n = 7–9$) to the Ir-catalyzed C-H borylation installed the Bpin group on *meta* phenylene unit that on the least sterically hindered position, as shown by the conversion from **V.60** to **V.62**. These conditions were also successfully applied to the [2]catenane **V.59**, yielding the borylated [2]catenane **V.61** in good yield. Furthermore, the Ar-Bpin moiety can be converted to Ar-OH by oxidative hydroxylation using H_2O_2. And subsequent treatment with Tf_2O afforded the aryl triflate containing **V.64**. This two-step sequence effectively converts a nucleophile to electrophile, which facilitates access to more complex structures using Suzuki cross coupling, such as the formation of **V.65**.

Most importantly, a proof-of-concept for the synthesis of polycatenanes has been demonstrated. Suzuki coupling of **V.61** with dibromofluorene derivative **V.66** yield the first fully π-conjugated polycatenane in 67% yield. As this represents the only example of a CPP-based [2]catenane capable of polymerization, we sought to explore other opportunities for the access of functionalized [2]catenanes suitable for copolymerization. Herein, preliminary results regarding the synthetic efforts toward [2]catenane featuring alkyne handles, via the PT method, are discussed.

V.2. Results and Discussions

As illustrated in Scheme V.1, an alternative strategy to the aforementioned post-functionalization approach is to install the functional handles at an early stage, masked by suitable protecting groups, which can be subsequently removed to reveal the desired functionality amenable for polymerization. Therefore, inspired by the PT method reported by the Cong group in 2018 and given the synthetic feasibility to asymmetrically substituting the 1,10-Phenanthroline at the 2,9-positions, we hypothesized that the [2]catenane **V.75** would be attainable. Subsequent desilylation would then afford the terminal alkyne, providing a versatile handle for cross coupling via Sonogashira or oxidative homocoupling conditions. Starting from monosubstituted phenanthroline **V.68**, lithium-halogen exchange of **V.69**, followed by nucleophilic attack to **V.68**

and subsequent oxidation afforded the asymmetric phenanthroline building block **V.70**. Miyaura borylation of **V.70** then provided the corresponding bisboronate **V.71** in 69% yield. To extend the backbone, the bisboronate ester **V.71** was reacted with the methoxy-protected three-ring building block **V.72** under Suzuki conditions and a second Miyaura borylation provided the key intermediate **V.73** for PT method. The methoxy-protected three-ring building block **V.72** rather than the triethylsily- protected three-ring building block was used, to prevent premature desilylation of the masked alkyne unit. Mixing **V.73** with Cu(I) indeed induced color change immediately, indicative of the formation of metal complex **V.74**.



Scheme V.1. Synthetic scheme toward a [2]catenane (V.76) featuring a phenanthroline-containing macrocycle and tri*iso*propylsilyl-protected alkyne handle

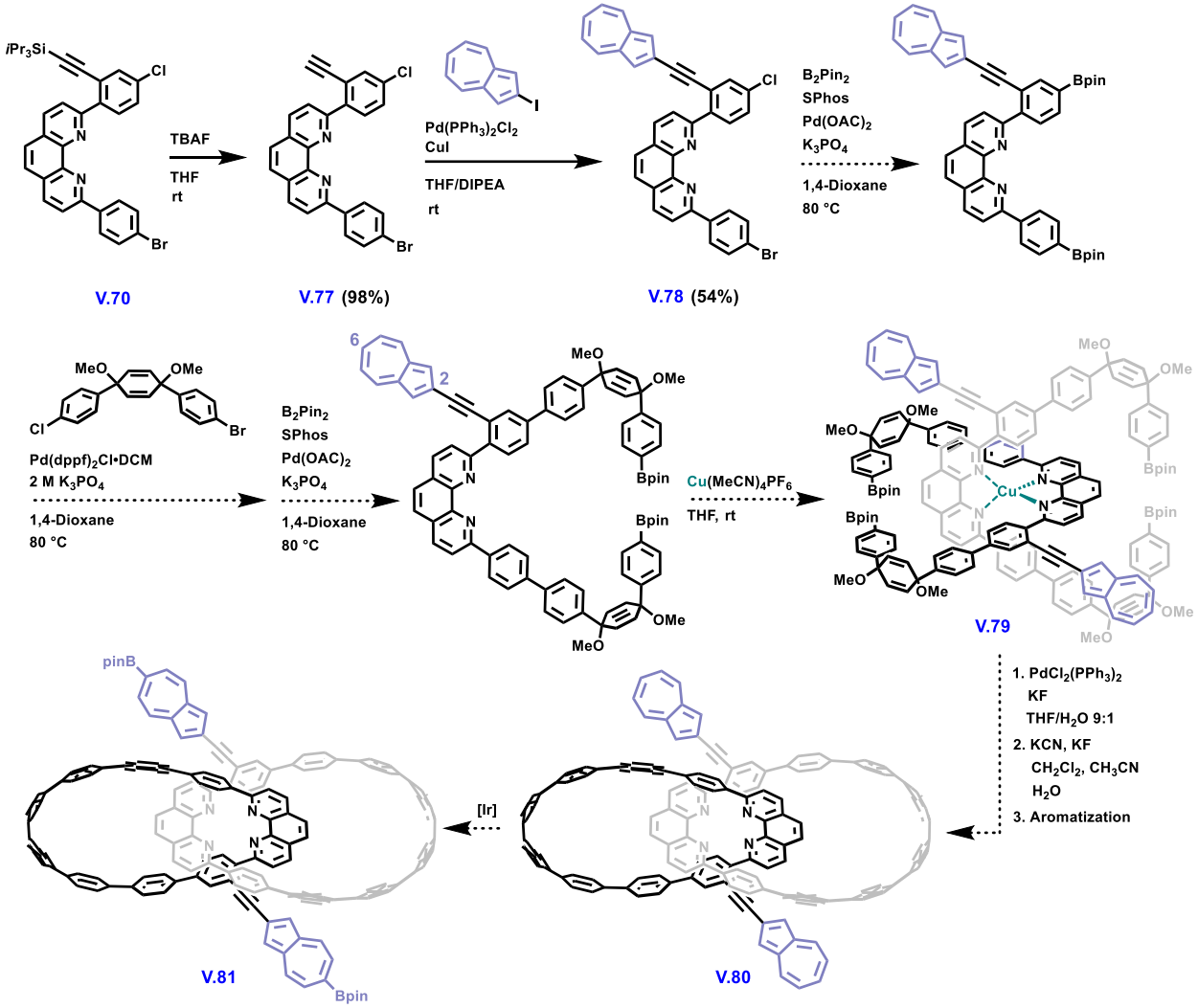
Excitingly, application of the oxidative homocoupling conditions previously demonstrated by the Cong group successfully afford **V.74** in 4% yield, as confirmed by ^{1}H NMR spectroscopy

and mass spectrometry. Attempts to aromatize the intermediate use H_2SnCl_4 were subsequently performed. However, clean isolation of the product proved challenging under the tested conditions. Future work will focus on two aspects. First, the efficiency of the Cu(I)-templated [2]catenane synthesis requires optimization, particularly the demetallation step. Currently, large excess of KCN (over 20 equivalents) and prolonged reaction time are used, however, the persistence of the red color characteristic of the Cu(I)-phenanthroline complex suggests the incomplete decomplexation, which partly contributes to the low isolated yield. Second, efforts should be directed toward scaling up the synthesis and screening alternative aromatization conditions to achieve target [2]catenane **V.76**.

Another different [2]catenane (**V.80**) suitable for post-functionalization was proposed, leveraging the incorporation of an azulene moiety at the 2-position of the asymmetric building block, as shown in compound **V.78** (Scheme V.2). This design is inspired by the established regioselective borylation of azulene, where the 2-position is borylated preferentially, followed by the 6-position.[123] We hypothesized that this azulene unit could serve as a versatile functional handle and upon aromatization, a regioselective Ir-catalyzed C-H borylation could install a Bpin group at the 6-position (**V.81**), thereby providing an effective site for subsequent polymerization. Starting from **V.70**, desilylation afforded the terminal alkyne containing unit **V.77**, subsequent Sonogashira cross coupling with 2-iodoazulene afforded **V.78** in 54% yield. Given the constraints of the project timeline and limited amount of 2-iodoazulene, study into this route was concluded at this stage.

V.3. Conclusions

In conclusion, this chapter reviewed the state of the art regarding the synthetic methodologies of CPP-based catenanes and discussed the initial efforts toward the synthesis of fully π-conjugated [2]catenane with functional handle amenable for post-functionalization. Furthermore, this work discussed a few bottlenecks that must be addressed to successfully realize the ultimate goal of accessing CPP-derived polycatenanes.



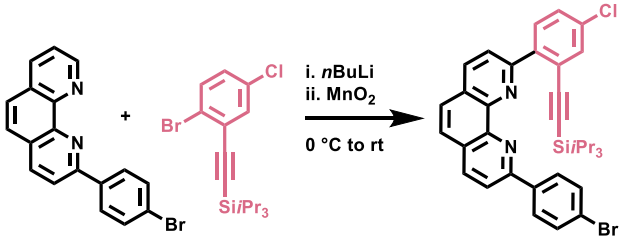
Scheme V.2. Proposed synthetic pathway toward a [2]catenane (V.80) featuring a phenanthroline-containing macrocycle and azulene-appended alkyne handle.

V.4. Methods and Materials

All reagents were purchased from commercial sources and used as received from commercial suppliers. **V.68**,[113] **V.72**,[40] 2-iodoazulene[124] and SPhos Pd G3[95] were prepared according to the literature methods and the obtained ^{1}H NMR spectra are consistent with literature. **V.69** was prepared using the general Sonogashira cross coupling condition. All reactions were carried out under a nitrogen atmosphere unless explicitly stated otherwise. Anhydrous tetrahydrofuran (THF), 1,4-Dioxane and Dichloromethane (DCM) were taken from solvent purification system (SPS) without further purification. For the stationary phase used in column chromatography, silica gel is purchased from ZEOCHEM® (ZEOprep Silicagel 60 HYD / 40-63 μm) and Alumina is purchased

from Sorbtech (Alumina, Basic, Act. II-III). Proton (^{1}H) and carbon ($^{13}C\{^{1}H\}$) NMR spectra were recorded on the Bruker Avance-III HD 500 MHz NMR Spectrometer. $CDCl_3$ used for NMR experiment is 99.8% deuterated with 0.05% v/v tetramethylsilane (TMS). Chemical shifts were given in ppm relative to residue protons ($CHCl_3$: 7.26, s for ^{1}H, 77.16 for ^{13}C). The abbreviations of s, d and m represent the multiplicities of singlet, doublet, and multiplet, respectively. Mass spectrometric data were acquired by Waters Synapt G2-Si ESI/LC-MS (ESI).

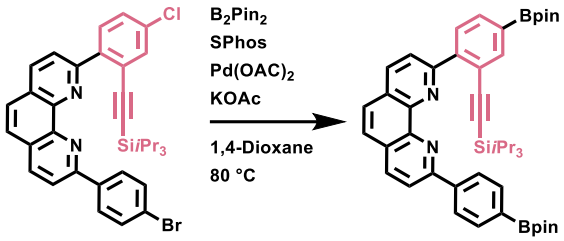
V.4.1. Synthetic Procedures



V.68 V.69 V.70 (58%)

Synthesis of V.70: A flame-dried 100 mL three-necked round bottom flask charged with **V.69** (2.02 g, 5.43 mmol, 2 equiv) was subjected to evacuation and back-filled with N_2 5 times, followed by addition of anhydrous Et_2O (60 mL). The solution cooled down to 0 °C for 10 min before dropwise addition of *n*BuLi (1.6 M, 3.40 mL, 5.43 mmol, 2 equV.), during which a colorless solution turned brown with concomitant formation of precipitate. To this suspension, **V.68** was added as solids (0.91 g, 2.71 mmol, 1 equV.) under a positive nitrogen flow. The reaction turned dark purple/black rapidly. After stirring at 0 °C for 2 h, the reaction was quenched with addition of DI water (10 mL), during which the color of the mixture changes immediately from dark purple to bright yellow. The organic layer was decanted, and the aqueous layer was extracted with DCM (50 mL × 3). The combined organic layers were transferred to a 500 mL round bottom flask, to which MnO_2 (2 g) was added. After stirring overnight, the mixture was passed through a silica gel plug (100% EtOAc) and the resulting filtrate was concentrated in vacuo to afford a yellow-orange oil. Trituration of the oil in hexanes under sonication afforded **V.70** as an off-white solid (1.05 g, 58%). R_f = 0.23 (SiO_2, 10% EtOAc in hexanes)

^{1}H NMR (500 MHz, $CDCl_3$) δ 8.50 (d, J = 8.3 Hz, 1H), 8.33 (d, J = 8.4 Hz, 1H), 8.28 (d, J = 8.6 Hz, 2H), 8.25 (d, J = 8.4 Hz, 1H), 8.23 (d, J = 8.4 Hz, 1H), 8.11 (d, J = 8.4 Hz, 1H), 7.83 (s, 2H), 7.68 (d, J = 8.5 Hz, 2H), 7.64 (d, J = 2.2 Hz, 1H), 7.55 (dd, J = 8.4, 2.2 Hz, 1H), 1.02 (m, 21H).

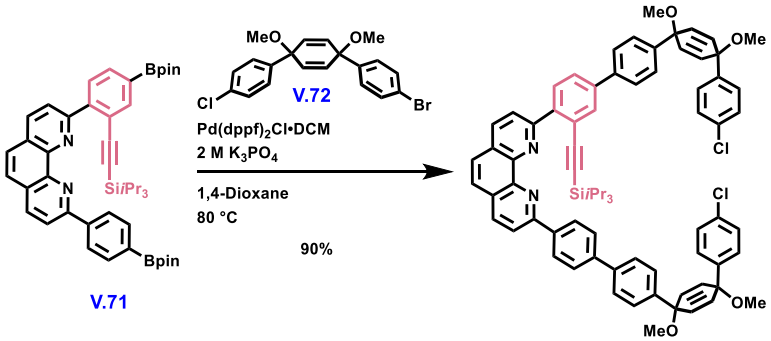


V.70 V.71 (69%)

Synthesis of V.71: A flame-dried flask charge with **V.70** (0.78 g, 1.25 mmol, 1 equV.), B_2pin_2 (1.27 g, 4.98 mmol, 4 equV.), $Pd(OAc)_2$ (27.9 mg, 0.12 mmol, 10 mol%), SPhos (102 mg, 0.25 mmol, 20 mol%), oven-dried KOAc (733.6 mg, 7.47 mmol, 6 equV.) were subjected to evacuation and back-filled with N_2 five times, followed by introduction of 1,4-Dioxane (11 mL). The reaction was lowered to oil bath at heated to 80 °C. After stirring at 80 °C for 2.5 h, the reaction was cooled to room temperature and passed through a celite plug (eluting with DCM). The resulting filtrate was concentrated in vacuo, dissolved in minimal amount of EtOAc and layered with hexanes for recrystallization. The solid was collected by vacuum filtration to afford **V.71** as an off-white solid. (655.6 mg, 69%).

^{1}H NMR (500 MHz, $CDCl_3$) δ 8.57 (d, J = 8.3 Hz, 1H), 8.44 (d, J = 8.0 Hz, 2H), 8.37 (d, J = 7.8 Hz, 1H), 8.32 (d, J = 8.4 Hz, 1H), 8.21 (d, J = 8.3 Hz, 1H), 8.18 (d, J = 8.4 Hz, 1H), 8.09 (approx. s, 1H), 8.02 (dd, J = 7.7 Hz, 0.9 Hz, 1H), 7.99 (d, J = 8.0 Hz, 2H), 7.82 (s, 2H), 1.41 (s, 12H), 1.38 (s, 12 H), 1.03 (m, 21H).

^{13}C {^{1}H} NMR (126 MHz, $CDCl_3$) δ 157.68, 156.74, 146.35, 146.34, 145.15, 141.89, 140.38, 136.96, 135.40, 135.38, 135.21, 130.43, 128.08, 128.01, 126.96, 126.37, 126.33, 124.77, 121.54, 120.20, 106.69, 94.71, 84.23, 83.99, 25.10, 25.08, 18.80, 11.49.

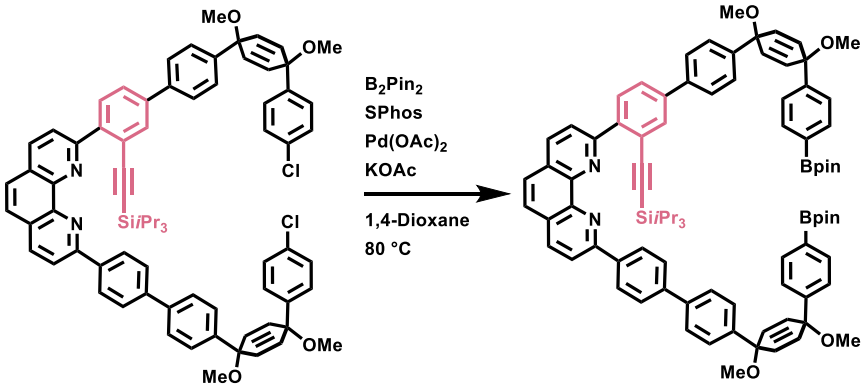


V.71

Synthesis of the DiCl-V.73: A 15 mL round bottom flask charged with **V.71** (100 mg, 0.131 mmol, 1 equV.), **V.72** (106 mg, 0.262 mmol, 2 equV.) and $Pd(dppf)Cl_2$·DCM (10.7 mg, 0.013 mmol, 10 mol%) were subjected to evacuation and back filled with N_2 five times followed by

addition of 1,4-Dioxane (4 mL). The reaction mixture was heated to 80 ºC for 2 min before addition of aqueous K_3PO_4 (2 M, 0.65 mL). After stirring overnight for 20 h, the reaction mixture was concentrated in vacuo, and the concentrated reaction mixture was passed through a celite plug (flushing with EtOAc). The filtrate was extracted with EtOAc (30 mL × 3), washed with brine (60 mL), dried over Na_2SO_4 and concentrated in vacuo. The crude was dried loaded onto celite and subjected to flash column chromatography (silica gel, 20% EtOAc in hexanes) afforded the target product as a light-yellow oil (136.78 mg, 90%). R_f = 0.12 (20% EtOAc in hexanes).

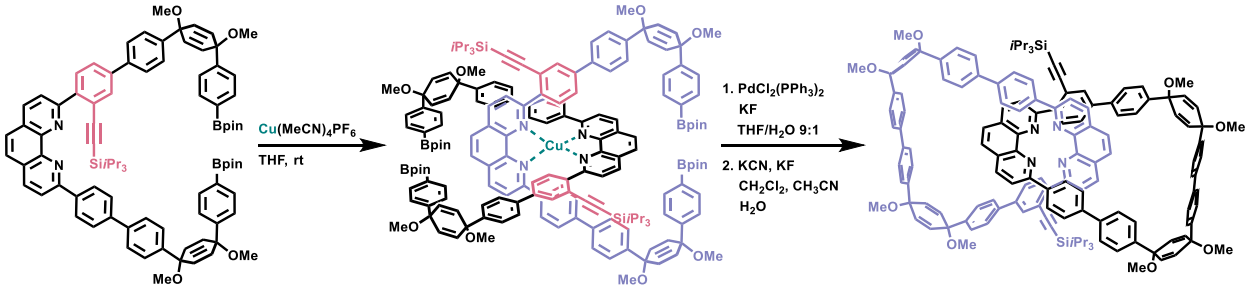
^{1}H NMR (500 MHz, $CDCl_3$) δ 8.60 (d, J = 8.3 Hz, 1H), 8.51 (d, J = 8.3 Hz, 2H), 8.45 (d, J = 8.1 Hz, 1H), 8.34 (d, J = 8.4 Hz, 1H), 8.24 (d, J = 8.4 Hz, 1H), 8.19 (d, J = 8.4 Hz, 1H), 7.87 (dd, J = 1.8 Hz, 1H), 7.83 (s, 2H), 7.81 (dd, J = 8.2, 2.1 Hz, 1H), 7.79 (d, J = 8.5 Hz, 2H), 7.68 (d, J = 6.4 Hz, 2H), 7.66 (d, J = 6.4 Hz, 2H), 7.50 (d, J = 8.4 Hz, 2H), 7.48 (d, J = 8.5 Hz, 2H), 7.39–7.36 (m, 4H), 7.32–7.29 (m, 4H), 6.21–6.18 (m, 4H), 6.12–6.09 (m, 4H), 3.474 (s, 3 H), 3.465 (s, 3H), 3.455 (s, 3H), 3.449 (s, 3H), 1.05–1.04 (m, 21H).



V.73 (61%)

Synthesis of V.73: A flame-dried flask charge with **DiCl-V.73** (314 mg, 0.270 mmol, 1 equV.), B_2pin_2 (274 mg, 1.08 mmol, 4 equV.), $Pd(OAc)_2$ (6.06 mg, 0.027 mmol, 10 mol%), SPhos (22.2 mg, 0.054 mmol, 20 mol%), oven-dried KOAc (733.6 mg, 7.47 mmol, 6 equV.) were subjected to evacuation and back-filled with N_2 five times, followed by introduction of 1,4-Dioxane (9 mL). After stirring at 80 ºC for 20 h, solvent was removed in vacuo, and the crude was subjected directly to silica plug (eluting with EtOAc). The resulting filtrate was concentrated in vacuo and dissolved in minimal amount of EtOAc and layered with excess of hexane for recrystallization. The crystallized product was collected by vacuum filtration to afford **V.73** as an off-white solid (220 mg, 61%).

^{1}H NMR (500 MHz, $CDCl_3$) δ 8.61 (d, J = 8.4 Hz, 1H), 8.52 (d, J = 8.4 Hz, 2H), 8.46 (d, J = 8.2 Hz, 1H), 8.34 (d, J = 8.4 Hz, 1H), 8.23 (d, J = 8.4 Hz, 1H), 8.21 (d, J = 8.5 Hz, 1H), 7.87 (d, J = 1.9 Hz, 1H), 7.83 (s, 2H), 7.82–7.76 (m, 7fH), 7.67 (d, J = 6.7 Hz, 2H), 7.65 (d, J = 6.7 Hz, 2H), 7.52 (d, J = 8.4 Hz, 2H), 7.49 (d, J = 8.3 Hz, 2H), 7.47–7.44 (m, 4H), 6.17–6.11 (m, 8H), 3.473 (s, 3H), 3.465 (s, 3H), 3.460 (s, 3H), 3.465 (s, 3H), 1.31 (approx. s, 24H), 1.05–1.04 (m, 21H).

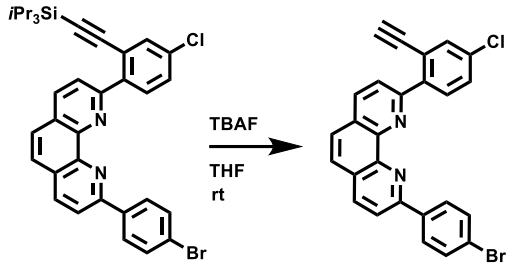


V.73 V.74 V.75 (4%)

Synthesis of V.75: A flame-dried 25 mL round bottom flask charged with **V.73** (40 mg, 0.030 mmol, 1 equV.), $Cu(MeCN)_4PF_6$ (5.54 mg, 0.015 mmol, 0.5 equV.) was subjected to evacuation and back-filled with N_2 three times. THF (ca. 2 mL) was added, which turned the reaction mixture to bright red immediately. After stirring for 20 min, the reaction mixture was diluted using THF (90 mL) and transferred into a 250 mL round bottom flask. To this flask, $Pd(PPh)_3Cl_2$ (20.9 mg, 0.030 mmol, 1 equV.), KF (34.5 mg, 0.595 mmol, 20 equV.) and DI water (10 mL) were added. The flask was fitted with an air balloon through a needle that is inserted into the septum. After stirring for one day, THF was removed in vacuo. The crude was dissolved in DCM (3 mL) and CH_3CN (3 mL), followed by addition of KCN (38.8 mg, 0.594 mmol, 20 equV.), KF (25.9 mg, 0.446 mmol, 15 equV.) and DI water (3 mL). After stirring for one week, the reaction was diluted with DCM (30 mL) and transferred to a separatory funnel. The organic layer was separated, and the aqueous layer was extracted with additional DCM (30 mL × 2). The combined organic layers were washed with diluted bleach (50 mL × 2), DI water (50 mL), brine (50 mL), dried over Na_2SO_4, filtered and concentrated in vacuo. The crude was firstly purified by subjecting to alumina plug (eluting with 50% EtOAc in Hexanes) and the concentrated filtrated was dissolved in minimum of DCM and purified secondly via flash column chromatography (Alumina, 20–25% EtOAc in hexanes) to afford **V.75** as an off white solid (2.6 mg, 4%). R_f = 0.22 (Alumina, 25% EtOAc in hexanes).

^{1}H NMR (500 MHz, $CDCl_3$) δ 8.55 (t, J = 8.2 Hz, 6H), 8.36 (d, J = 8.0 Hz, 2H), 8.31 (d, J = 8.4 Hz, 2H), 8.23 (dd, J = 8.4, 3.1 Hz, 4H), 7.77 (s, 4H), 7.72 (d, J = 1.9 Hz, 2H), 7.64 (dd, J = 8.4, 3.5 Hz, 8H), 7.48 (dd, J = 8.4, 2.8 Hz, 8H), 7.38–7.30 (m, 12H), 7.23–7.17 (m, 10H), 6.14–5.96 (m, 16H), 3.43 (s, 6H), 3.41 (s, 6H), 3.38 (s, 6H), 3.37 (s, 6H). 1.04–1.03 (m, 42H).

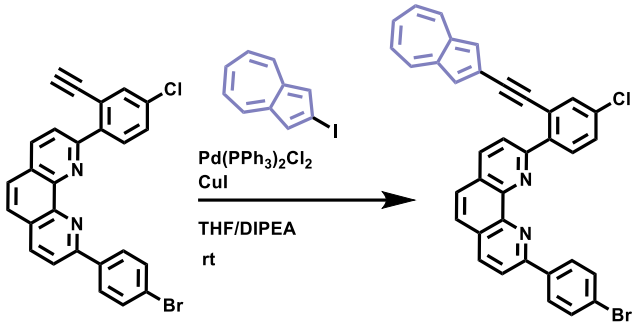
HRMS (ESI-TOF) m/z calcd for $[M+2H]^{2+}$: $C_{150}H_{142}N_4O_8Si_2$: 1091.5183, found 1091.5170. Error 1.19 ppm.



V.70 V.77 (98%)

Synthesis of V.77: A flame-dried 25 mL round bottom flask charged with **V.70** (100 mg, 0.160 mmol, 1 equV.) was subjected to evacuation and back-filled with N_2 three times, followed by addition of THF (2 mL). TBAF was added dropwise (1 M in THF, 0.16 mL, 1 equV.) and the reaction was stirred at room temperature, during which the mixture deepened in yellow color, with concomitant formation of white precipitate. After stirring for 2 hours, the reaction was quenched with addition of DI water (10 mL). The precipitate was dissolved in DCM (15 mL). The organic layer was separated, and the aqueous layer was extracted with additional DCM (50 mL). The combined organic layers were washed with DI water (50 mL), dried over Na_2SO_4, filtered and concentrated in vacuo. The solid crude was triturated in hexanes and the solid was collected by vacuum filtration to afford **V.77** as an off-white solid (73 mg, 97%). R_f = 0.10 (10% EtOAc in Hexanes).

^{1}H NMR (500 MHz, $CDCl_3$) δ 8.39 (d, J = 8.3 Hz, 1H), 8.36 (d, J = 8.4 Hz, 1H), 8.33 (d, J = 8.4 Hz, 1H), 8.31 (d, J = 8.6 Hz, 2H), 8.24 (d, J = 8.4 Hz, 1H), 8.14 (d, J = 8.4 Hz, 1H), 7.87 (s, 2H), 7.75–7.68 (m, 3H), 7.60 (dd, J = 8.4, 2.2 Hz, 1H), 3.21 (s, 1H).



V.77 V.78 (54%)

Synthesis of V.78: A flask charged with 2-Iodoazulene (8.1 mg, 0.0319 mmol, 1 equV.), **V.77** (0.015 mg, 0.0319 mmol, 1 equV.), $Pd(PPh_3)_2Cl_2$ (3.4 mg, 0.0048 mmol, 15 mol%) and CuI (6.2 mg, 0.0326 mmol, 1.05 equV.) were subjected to evacuation and back filled with N_2 three times, followed by addition of THF (1.6 mL) and DIPEA (1.60 mL). After stirring for 23 h, the reaction was quenched with addition of NH_3-EDTA solution (5 mL) and diluted with DI water (5 mL). The reaction mixture was diluted with DCM (20 mL) and transferred to a separatory funnel. The organic layer was separated, and the aqueous layer was extracted with additional DCM (30 mL), washed with NH_3-EDTA (5 mL), water (30 mL), brine (30 mL), dried over Na_2SO_4, filtered and concentrated in vacuo to afford brownish/greenish solid. The crude was dry loaded onto celite and purified via flash column chromatography (10–30% EtOAc in hexanes, followed by 5% EtOAc in DCM as the product has limited solubility in EtOAc/hexanes mixture) to afford **V.78** as a greenish solid (10.2 mg, 54%). $R_f = 0.52$ (40% EtOAc in Hexanes)

^{1}H NMR (500 MHz, $CDCl_3$) δ 8.53 (d, J = 8.3 Hz, 1H), 8.35 (t, J = 8.6 Hz, 2H), 8.29 (d, J = 8.4 Hz, 1H), 8.25 (d, J = 8.6 Hz, 2H), 8.18 (d, J = 9.3 Hz, 2H), 8.11 (d, J = 8.4 Hz, 1H), 7.88 (d, J = 8.7 Hz, 1H), 7.86 (d, J = 8.7 Hz, 1H), 7.79 (d, J = 2.1 Hz, 1H), 7.64 (d, J = 8.6 Hz, 2H), 7.58 (dd, J = 8.4, 2.2 Hz, 1H), 7.53 (t, J = 9.9 Hz, 1H), 7.30 (s, 2H), 7.16 (t, J = 9.8 Hz, 2H).

HRMS (ESI-TOF) m/z calcd for $[M+H]^+$: $C_{35}H_{21}N_2ClBr$: 595.0577, found 595.0568. Error -1.5 ppm.

CHAPTER VI CONCLUDING REMARKS

Fascinated by the unique topology of mechanically interlocked systems and the elegant, radially π-conjugated architecture of cycloparaphenylenes (CPPs) that have great solubility in common organic solvents compared to their linear π-conjugated counterparts, we envisioned the synthesis of fully π-conjugated CPP-derived mechanically interlocked polymers. In this dissertation, we demonstrated that Phen[*n*]CPP (*n* = 5) serves as an efficient macrocyclic template for active template Cadiot-Chodkiewicz (AT-CC) reaction and reported the first example of a fully π-conjugated rotaxanes featuring anthracene stoppers. Post-functionalization of this rotaxane with fluorenyl derivatives with solubilizing groups resulted in further improved solubility and enhanced fluorescence intensity, suggesting its potential utility in optoelectronic applications as a blue-emitting material. Furthermore, preliminary synthetic efforts toward [2]catenane with alkyne-based handles proved promising, though future studies are required to optimize the aromatization conditions. Beyond these interlocked structures, we investigated the incorporation of non-alternant azulene into the nanohoop, which demonstrated a retention of anti-Kasha properties and halochromic behavior of azulene. Finally, our early success with cyclopenta[*hi*]aceanthrylene (CPA)-containing nanohoops show the potential for expanding the library of non-alternant PAH-embedded CPPs to access systems with narrow energy gaps and redox-active properties.

CITED REFERENCES

(1) Tobe, Y. Non-Alternant Non-Benzenoid Aromatic Compounds: Past, Present, and Future. *The Chemical Record* **2015**, *15*, 86–96.

(2) Darzi, E. R.; Jasti, R. The Dynamic, Size-Dependent Properties of [5]–[12]Cycloparaphenylenes. *Chem. Soc. Rev.* **2015**, *44*, 6401–6410.

(3) Jasti, R.; Bhattacharjee, J.; Neaton, J. B.; Bertozzi, C. R. Synthesis, Characterization, and Theory of [9]-, [12]-, and [18]Cycloparaphenylene: Carbon Nanohoop Structures. *J. Am. Chem. Soc.* **2008**, *130*, 17646–17647.

(4) Li, Y.; Segawa, Y.; Yagi, A.; Itami, K. A Nonalternant Aromatic Belt: Methylene-Bridged [6]Cycloparaphenylene Synthesized from Pillar[6]Arene. *J. Am. Chem. Soc.* **2020**, *142*, 12850–12856.

(5) Du, P.; Huang, Q.; Wu, Y.; Zhou, Y.; Et., A. Synthesis, Photophysical and Supramolecular Properties of a π-Conjugated Molecular Crown Containing a Pentagonal Unit: A Model Compound for Fullerene C240. *Synthesis* **2020**.

(6) Wassy, D.; Pfeifer, M.; Esser, B. Synthesis and Properties of Conjugated Nanohoops Incorporating Dibenzo[a,e]Pentalenes: [2]DBP[12]CPPs. *J. Org. Chem.* **2020**, *85*, 34–43.

(7) Wössner, J. S.; Wassy, D.; Weber, A.; Bovenkerk, M.; Hermann, M.; Schmidt, M.; Esser, B. [N]Cyclodibenzopentalenes as Antiaromatic Curved Nanocarbons with High Strain and Strong Fullerene Binding. *J. Am. Chem. Soc.* **2021**, *143*, 12244–12252.

(8) Li, X.; Jia, L.; Wang, W.; Wang, Y.; Sun, D.; Jiang, H. A Nonalternant Azulene-Embedded Carbon Nanohoop Featuring Anti-Kasha Emission and Tunable Properties upon pH Stimuli-Responsiveness. *J. Mater. Chem. C* **2023**, *11*, 1429–1434.

(9) Kong, X.; Zhang, X.; Yuan, B.; Zhang, W.; Lu, D.; Du, P. Synthesis and Photophysical Properties of a Chiral Carbon Nanoring Containing Rubicene. *J. Org. Chem.* **2024**, *89*, 8255–8261.

(10) Schuldt, M. P.; Rominger, F.; Mastalerz, M. Synthesis of Enantiopure [3]Cyclorubicenes. *Angew Chem Int Ed* **2025**, e20880.

(11) Stoddart, J. F. Mechanically Interlocked Molecules (MIMs)—Molecular Shuttles, Switches, and Machines (Nobel Lecture). *Angew Chem Int Ed* **2017**, *56*, 11094–11125.

(12) Sauvage, J.-P. From Chemical Topology to Molecular Machines (Nobel Lecture). *Angew Chem Int Ed* **2017**, *56*, 11080–11093.

(13) Feringa, B. L. The Art of Building Small: From Molecular Switches to Motors (Nobel Lecture). *Angew Chem Int Ed* **2017**, *56*, 11060–11078.

(14) Sluysmans, D.; Stoddart, J. F. The Burgeoning of Mechanically Interlocked Molecules in Chemistry. *Trends in Chemistry* **2019**, *1*, 185–197.

(15) Zhang, J.; Ma, P. X. Cyclodextrin-Based Supramolecular Systems for Drug Delivery: Recent Progress and Future Perspective. *Adv Drug Deliv Rev* **2013**, *65*, 10.1016/j.addr.2013.05.001.

(16) Zhang, Y.-M.; Liu, Y.-H.; Liu, Y. Cyclodextrin-Based Multistimuli-Responsive Supramolecular Assemblies and Their Biological Functions. *Advanced Materials* **2020**, *32*, 1806158.

(17) Chen, L.; Sheng, X.; Li, G.; Huang, F. Mechanically Interlocked Polymers Based on Rotaxanes. *Chem. Soc. Rev.* **2022**, *51*, 7046–7065.

(18) Hart, L. F.; Hertzog, J. E.; Rauscher, P. M.; Rawe, B. W.; Tranquilli, M. M.; Rowan, S. J. Material Properties and Applications of Mechanically Interlocked Polymers. *Nat Rev Mater* **2021**, *6*, 508–530.

(19) Takata, T.; Kihara, N.; Furusho, Y. Polyrotaxanes and Polycatenanes: Recent Advances in Syntheses and Applications of Polymers Comprising of Interlocked Structures. In *Polymer Synthesis*; Advances in Polymer Science; Springer Berlin Heidelberg: Berlin, Heidelberg, 2004; Vol. 171, pp 1–75.

(20) Fleury, G.; Brochon, C.; Schlatter, G.; Bonnet, G.; Lapp, A.; Hadziioannou, G. Synthesis and Characterization of High Molecular Weight Polyrotaxanes: Towards the Control over a Wide Range of Threaded α-Cyclodextrins. *Soft Matter* **2005**, *1*, 378.

(21) Bai, R.; Zhang, Z.; Di, W.; Yang, X.; Zhao, J.; Ouyang, H.; Liu, G.; Zhang, X.; Cheng, L.; Cao, Y.; Yu, W.; Yan, X. Oligo[2]Catenane That Is Robust at Both the Microscopic and Macroscopic Scales. *J. Am. Chem. Soc.* **2023**, jacs.3c00221.

(22) Bu, A.; Cong, H. Mechanically Interlocked Molecules Consisting of Radially Conjugated Macrocycles. *Nano Research* **2025**, *18*, 94907549.

(23) Gao, J.-N.; Bu, A.; Chen, Y.; Huang, M.; Chen, Z.; Li, X.; Tung, C.-H.; Wu, L.-Z.; Cong, H. Synthesis of All-Benzene Multi-Macrocyclic Nanocarbons via Post-Functionalization of meta-Cycloparaphenylenes. *Angew Chem Int Ed* **2024**, e202408016.

(24) Fan, Y.; He, J.; Guo, S.; Jiang, H. Host-Guest Chemistry in Binary and Ternary Complexes Utilizing π-Conjugated Carbon Nanorings. *ChemPlusChem* **2024**, *89*, e202300536.

(25) Peters, G. M.; Grover, G.; Maust, R. L.; Colwell, C. E.; Bates, H.; Edgell, W. A.; Jasti, R.; Kertesz, M.; Tovar, J. D. Linear and Radial Conjugation in Extended π-Electron Systems. *J. Am. Chem. Soc.* **2020**, *142*, 2293–2300.

(26) Maust, R. L.; Li, P.; Shao, B.; Zeitler, S. M.; Sun, P. B.; Reid, H. W.; Zakharov, L. N.; Golder, M. R.; Jasti, R. Controlled Polymerization of Norbornene Cycloparaphenylenes Expands Carbon Nanomaterials Design Space. *ACS Cent. Sci.* **2021**, *7*, 1056–1065.

(27) Wang, S.; Li, X.; Zhang, X.; Huang, P.; Fang, P.; Wang, J.; Yang, S.; Wu, K.; Du, P. A Supramolecular Polymeric Heterojunction Composed of an All-Carbon Conjugated Polymer and Fullerenes. *Chem. Sci.* **2021**, *12*, 10506–10513.

(28) Peterson, E.; Maust, R. L.; Jasti, R.; Kertesz, M.; Tovar, J. D. Splitting the Ring: Impact of Ortho and Meta Pi Conjugation Pathways through Disjointed [8]Cycloparaphenylene Electronic Materials. *J. Am. Chem. Soc.* **2022**, *144*, 4611–4622.

(29) Seitz, P.; Bhosale, M.; Rzesny, L.; Uhlmann, A.; Wössner, J. S.; Wessling, R.; Esser, B. Conjugated Nanohoop Polymers Based on Antiaromatic Dibenzopentalenes for Charge Storage in Organic Batteries. *Angew Chem Int Ed* **2023**, *62*, e202306184.

(30) Reid, H. W.; Bhattacharjee, R.; Sun, P. B.; Skala, M. E.; Serck, N. P.; Kertesz, M.; Golder, M. R.; Jasti, R. High Molar Mass [n]Cycloparaphenylene Conjugated Polymers and Copolymers with Improved Electronic Delocalization. *Macromolecules* **2026**, *59*, 6963–6972.

(31) Nadeem, R. Y.; Fang, P.; Shi, Y.; Wang, J.; Yuan, B.; Zhang, X.; Kong, X.; Wang, C.; Du, P. A Radial-Linear π-Conjugated Polymer by Integrating Poly(Para-phenylene Vinylene) and Cycloparaphenylene for Enhanced Optoelectronic and Electrochemical Performance. *Angew Chem Int Ed* **2026**, e6921317.

(32) Omachi, H.; Segawa, Y.; Itami, K. Synthesis and Racemization Process of Chiral Carbon Nanorings: A Step toward the Chemical Synthesis of Chiral Carbon Nanotubes. *Org. Lett.* **2011**, *13*, 2480–2483.

(33) Sun, Z.; Suenaga, T.; Sarkar, P.; Sato, S.; Kotani, M.; Isobe, H. Stereoisomerism, Crystal Structures, and Dynamics of Belt-Shaped Cyclonaphthylenes. *Proceedings of the National Academy of Sciences* **2016**, *113*, 8109–8114.

(34) Okada, K.; Yagi, A.; Segawa, Y.; Itami, K. Synthesis and Properties of [8]-, [10]-, [12]-, and [16]Cyclo-1,4-Naphthylenes. *Chem. Sci.* **2016**, *8*, 661–667.

(35) Farajidizaji, B.; Huang, C.; Thakellapalli, H.; Li, S.; Akhmedov, N. G.; Popp, B. V.; Petersen, J. L.; Wang, K. K. Synthesis and Characterization of Functionalized [12]Cycloparaphenylenes Containing Four Alternating Biphenyl and Naphthyl Units. *J. Org. Chem.* **2017**, *82*, 4458–4464.

(36) Wang, J.; Zhuang, G.; Huang, Q.; Xiao, Y.; Zhou, Y.; Liu, H.; Du, P. Precise Synthesis and Photophysical Properties of a Small Chiral Carbon Nanotube Segment: Cyclo[7]Paraphenylene-2,6-Naphthylene. *Chem. Commun.* **2019**, *55*, 9456–9459.

(37) Li, P.; Wong, B. M.; Zakharov, L. N.; Jasti, R. Investigating the Reactivity of 1,4-Anthracene-Incorporated Cycloparaphenylene. *Org. Lett.* **2016**, *18*, 1574–1577.

(38) Della Sala, P.; Capobianco, A.; Caruso, T.; Talotta, C.; De Rosa, M.; Neri, P.; Peluso, A.; Gaeta, C. An Anthracene-Incorporated [8]Cycloparaphenylene Derivative as an Emitter in Photon Upconversion. *J. Org. Chem.* **2018**, *83*, 220–227.

(39) Wang, J.; Zhuang, G.; Chen, M.; Lu, D.; Li, Z.; Huang, Q.; Jia, H.; Cui, S.; Shao, X.; Yang, S.; Du, P. Selective Synthesis of Conjugated Chiral Macrocycles: Sidewall Segments of (−)/(+)-(12,4) Carbon Nanotubes with Strong Circularly Polarized Luminescence. *Angew Chem Int Ed* **2020**, *132*, 1636–1643.

(40) Wang, J.; Shi, H.; Wang, S.; Zhang, X.; Fang, P.; Zhou, Y.; Zhuang, G.; Shao, X.; Du, P. Tuning the (Chir)Optical Properties and Squeezing out the Inherent Chirality in Polyphenylene-Locked Helical Carbon Nanorings. *Chemistry A European J* **2022**, *28*.

(41) Nishiuchi, T.; Makihara, Y.; Kubo, T. Strain-Induced Quinoidal Character in a Carbon Nanoring Embedding Anthracene Units. *J Am Chem Soc* **2025**, *147*, 37488–37496.

(42) Yagi, A.; Venkataramana, G.; Segawa, Y.; Itami, K. Synthesis and Properties of Cycloparaphenylene-2,7-Pyrenylene: A Pyrene-Containing Carbon Nanoring. *Chem. Commun.* **2014**, *50*, 957–959.

(43) Iwamoto, T.; Kayahara, E.; Yasuda, N.; Suzuki, T.; Yamago, S. Synthesis, Characterization, and Properties of [4]Cyclo-2,7-Pyrenylene: Effects of Cyclic Structure on the Electronic Properties of Pyrene Oligomers. *Angewandte Chemie International Edition* **2014**, *53*, 6430–6434.

(44) Li, J.; Zhuang, G.; Huang, Q.; Wang, J.; Wu, Y.; Du, P. A Conjugated Molecular Crown Containing a Single Pyrenyl Unit: Synthesis, Characterization, and Photophysical Properties. *Chinese Journal of Organic Chemistry* **2021**, *41*, 2401.

(45) Beer, M.; Longuet-Higgins, H. C. Anomalous Light Emission of Azulene. *J. Chem. Phys.* **1955**, *23*, 1390–1391.

(46) Michl, J.; Thulstrup, E. W. Why Is Azulene Blue and Anthracene White? A Simple Mo Picture. *Tetrahedron* **1976**, *32*, 205–209.

(47) Itoh, T. Fluorescence and Phosphorescence from Higher Excited States of Organic Molecules. *Chem. Rev.* **2012**, *112*, 4541–4568.

(48) Veys, K.; Escudero, D. Anti-Kasha Fluorescence in Molecular Entities: Central Role of Electron–Vibrational Coupling. *Acc. Chem. Res.* **2022**, *55*, 2698–2707.

(49) Dunlop, D.; Ludvíková, L.; Banerjee, A.; Ottosson, H.; Slanina, T. Excited-State (Anti)Aromaticity Explains Why Azulene Disobeys Kasha's Rule. *J. Am. Chem. Soc.* **2023**, *145*, 21569–21575.

(50) S. S. Danyluk; W. G. Schneider. THE PROTON RESONANCE SPECTRA AND STRUCTURES OF SUBSTITUTED AZULENES IN TRIFLUOROACETIC ACID. *Canadian Journal of Chemistry* **1962**, *40*, 1777–1785.

(51) Murfin, L. C.; Lewis, S. E. Azulene—A Bright Core for Sensing and Imaging. *Molecules* **2021**, *26*, 353.

(52) Lvov, A. G.; Bredihhin, A. Azulene as an Ingredient for Visible-Light- and Stimuli-Responsive Photoswitches. *Org. Biomol. Chem.* **2021**, *19*, 4460–4468.

(53) Xin, H.; Hou, B.; Gao, X. Azulene-Based π-Functional Materials: Design, Synthesis, and Applications. *Acc. Chem. Res.* **2021**, *54*, 1737–1753.

(54) Wang, X.; Ng, J. K.-P.; Jia, P.; Lin, T.; Cho, C. M.; Xu, J.; Lu, X.; He, C. Synthesis, Electronic, and Emission Spectroscopy, and Electrochromic Characterization of Azulene−Fluorene Conjugated Oligomers and Polymers. *Macromolecules* **2009**, *42*, 5534–5544.

(55) Lim, S. Z. H.; Neo, W. T.; Cho, C. M.; Wang, X.; Tan, A. Y. X.; Chan, H. S. O.; Xu, J. Electrochromic P-Conjugated Copolymers Derived from Azulene, Fluorene, and Dialkyloxybenzothiadiazole. *Aust J Chem* **2013**, *66*, 1048–1056.

(56) Huang, J.; Huang, S.; Zhao, Y.; Feng, B.; Jiang, K.; Sun, S.; Ke, C.; Kymakis, E.; Zhuang, X. Azulene-Based Molecules, Polymers, and Frameworks for Optoelectronic and Energy Applications. *Small Methods* **2020**, *4*, 2000628.

(57) Salman, H.; Abraham, Y.; Tal, S.; Meltzman, S.; Kapon, M.; Tessler, N.; Speiser, S.; Eichen, Y. 1,3-Di(2-Pyrrolyl)Azulene: An Efficient Luminescent Probe for Fluoride. *European Journal of Organic Chemistry* **2005**, *2005*, 2207–2212.

(58) Xin, H.; Gao, X. Application of Azulene in Constructing Organic Optoelectronic Materials: New Tricks for an Old Dog. *ChemPlusChem* **2017**, *82*, 945–956.

(59) Dong, J.-X.; Zhang, H.-L. Azulene-Based Organic Functional Molecules for Optoelectronics. *Chinese Chemical Letters* **2016**, *27*, 1097–1104.

(60) Zhang, X.; Chen, C.; Zhang, W.; Yin, N.; Yuan, B.; Zhuang, G.; Wang, X.-Y.; Du, P. Anomalous Anti-Kasha Excited-State Luminescence from Symmetry-Breaking Heterogeneous Carbon Bisnanohoops. *Nat Commun* **2024**, *15*, 2684.

(61) Wu, S.; Jie, J.; Liu, L.; Liu, L.; Guo, S.; Li, X.; He, J.; Lian, Z.; Wang, Y.; Xu, X.; Su, H.; Chen, X.; Jiang, H. A Redox-Active π-Extended Tetrathiafulvalene-Based Carbon Nanohoop Featuring Unique Kasha/Anti-Kasha Dual Emissions: Structure, Photophysical Properties, and Photoconductivity. *Angew Chem Int Ed* **2025**, *64*, e202512167.

(62) Liang, J.; Zhu, L.; Li, Y.; Xu, G.; Han, H.; Li, Y.; Zhou, Z. Abnormal Anti-Kasha Emission and TADF in Anionic Cycloarylenes. *Angew Chem Int Ed* **2025**, *137*, e202512344.

(63) Xu, Z.; Liu, X.; Ge, C.; Tian, X.; Ma, X.; Sun, Z. Controlling the Flipping Motion of Cycloparaphenylene Dimers. *J. Org. Chem.* **2025**, *90*, 11564–11571.

(64) Hines, D. A.; Darzi, E. R.; Hirst, E. S.; Jasti, R.; Kamat, P. V. Carbon Nanohoops: Excited Singlet and Triplet Behavior of Aza[8]CPP and 1,15-Diaza[8]CPP. *J. Phys. Chem. A* **2015**, *119*, 8083–8089.

(65) Matsui, K.; Segawa, Y.; Itami, K. Synthesis and Properties of Cycloparaphenylene-2,5-Pyridylidene: A Nitrogen-Containing Carbon Nanoring. *Org. Lett.* **2012**, *14*, 1888–1891.

(66) Douglas, C.; Sprachmann, J.; Dunlop, D.; Schlecht, J.; Neudörfl, J.; Wachsmuth, T.; Frost, J.; Slanina, T.; Dumele, O. Cycloazulenylene. *ChemRxiv 2026* (0227).

(67) Wang, Y.; Sun, J.; Miao, X.; Liu, J. Cyclo-Para-Azulenes: Segments of Metallic Nonalternant Carbon Nanotubes. *J. Am. Chem. Soc.* **2026**, *148* (21), 21238–21245.

(68) Dubovik, J.; Bredihhin, A. A Convenient Synthesis of Functionalized Azulenes via Negishi Cross-Coupling. *Synthesis* **2014**, *47*, 538–548.

(69) Lovell, T. C.; Colwell, C. E.; Zakharov, L. N.; Jasti, R. Symmetry Breaking and the Turn-on Fluorescence of Small, Highly Strained Carbon Nanohoops. *Chem. Sci.* **2019**, *10*, 3786–3790.

(70) Seitz, P.; Bhosale, M.; Rzesny, L.; Uhlmann, A.; Wössner, J. S.; Wessling, R.; Esser, B. Conjugated Nanohoop Polymers Based on Antiaromatic Dibenzopentalenes for Charge Storage in Organic Batteries. *Angew Chem Int Ed* **2023**, *62*, e202306184.

(71) Bruno, N. C.; Tudge, M. T.; Buchwald, S. L. Design and Preparation of New Palladium Precatalysts for C–C and C–N Cross-Coupling Reactions. *Chem. Sci.* **2013**, *4*, 916–920.

(72) *Gaussian 09, Revision A.1 – ScienceOpen*. https://www.scienceopen.com/document?vid=45e9a2b5-64f1-4e2c-8a2e-0e0bec409f69 (accessed 2026-05-14).

(73) *Sheldrick, G.M. (1996) SADABS, Program for Area Detector Adsorption Correction. Institute for Inorganic Chemistry, University of Gottingen, Germany. - References - Scientific Research Publishing*. https://www.scirp.org/reference/referencespapers?referenceid=2266422 (accessed 2026-05-11).

(74) van der Sluis, P.; Spek, A. L. BYPASS: An Effective Method for the Refinement of Crystal Structures Containing Disordered Solvent Regions. *Acta Cryst A* **1990**, *46*, 194–201.

(75) Sheldrick, G. M. Crystal Structure Refinement with SHELXL. *Acta Cryst C* **2015**, *7*, 3–8.

(76) Dang, H.; Garcia-Garibay, M. A. Palladium-Catalyzed Formation of Aceanthrylenes: A Simple Method for Peri-Cyclopentenelation of Aromatic Compounds. *J. Am. Chem. Soc.* **2001**, *123*, 355–356.

(77) Dang, H.; Levitus, M.; Garcia-Garibay, M. A. One Step Pd(0)-Catalyzed Synthesis, X-Ray Analysis, and Photophysical Properties of Cyclopent[*Hi*]Aceanthrylene: Fullerene-like Properties in a Nonalternant Cyclopentafused Aromatic Hydrocarbon. *J. Am. Chem. Soc.* **2002**, *124*, 136–143.

(78) Koper, C.; Sarobe, M.; Jenneskens, L. W. Redox Properties of Non-Alternant Cyclopenta-Fused Polycyclic Aromatic Hydrocarbons: The Effect of Peripheral Pentagon Annelation. *Phys. Chem. Chem. Phys.* **2004**, *6*, 319–327.

(79) Daniel, G. B.; Nachimuthu, K.; Nallasivam, J. L. Functionalization of [C60]-Fullerene: A Recent Update. *Chemistry – An Asian Journal* **2025**, *20*, e202401800.

(80) Wood, J. D.; Jellison, J. L.; Finke, A. D.; Wang, L.; Plunkett, K. N. Electron Acceptors Based on Functionalizable Cyclopenta[*Hi*]Aceanthrylenes and Dicyclopenta[*de,Mn*]Tetracenes. *J. Am. Chem. Soc.* **2012**, *134*, 15783–15789.

(81) Lee, C.-H.; Plunkett, K. N. Orthogonal Functionalization of Cyclopenta[Hi]Aceanthrylenes. *Org. Lett.* **2013**, *15*, 1202–1205.

(82) Schierl, C.; Alex, W.; Mateo, L. M.; Ballesteros, B.; Shimizu, D.; Osuka, A.; Torres, T.; Guldi, D. M.; Bottari, G. Quadrupolar Cyclopenta[Hi]aceanthrylene-Based Electron Donor-Acceptor-Donor Conjugates: Charge Transfer versus Charge Separation. *Angew Chem Int Ed* **2019**, *58*, 14644–14652.

(83) Urgel, J. I.; Bock, J.; Giovannantonio, M. D.; Ruffieux, P.; Pignedoli, C. A.; Kivala, M.; Fasel, R. On-Surface Synthesis of π-Conjugated Ladder-Type Polymers Comprising Nonbenzenoid Moieties. *RSC Adv.* **2021**, *11*, 23437–23441.

(84) Modelli, A.; Mussoni, L.; Fabbri, D. Electron Affinities of Polycyclic Aromatic Hydrocarbons by Means of B3LYP/6-31+G* Calculations. *J. Phys. Chem. A* **2006**, *110*, 6482–6486.

(85) Zhu, X.; Bheemireddy, S. R.; Sambasivarao, S. V.; Rose, P. W.; Torres Guzman, R.; Waltner, A. G.; DuBay, K. H.; Plunkett, K. N. Construction of Donor–Acceptor Polymers via Cyclopentannulation of Poly(Arylene Ethynylene)s. *Macromolecules* **2016**, *49*, 127–133.

(86) Jellison, J. L.; Lee, C.-H.; Zhu, X.; Wood, J. D.; Plunkett, K. N. Electron Acceptors Based on an All-Carbon Donor–Acceptor Copolymer. *Angew Chem Int Ed* **2012**, *51* (49), 12321–12324.

(87) Chen, W.; Sun, F.; Guo, J.; Qie, F.; Jia, X.; Shi, C.; Zhen, Y. Substituent Tailoring Anti-Aromaticity and Charge Transport Polarity of Cyclopenta[Hi]Aceanthrylenes. *J. Mater. Chem. C* **2024**, *12*, 18238–18242.

(88) Fernández, Á. C.; Rivero, S. M.; Chaurasia, S.; Torres, T.; Casado, J.; Bottari, G. Enhancing the Cumulene Character of One-Dimensional Acetylene-Based Systems by Stimuli-Induced Planarization of Their Two Pro-Diradicaloid Cyclopenta[h,i]Aceanthrylene Units. *Angew Chem Int Ed* **2024**, *n/a* (n/a), e202419832.

(89) Schierl, C.; Pardo, V.; Bottari, G.; Guldi, D. M.; Torres, T. Cyclopenta[Hi]Aceanthrylene Decorated with Multiple and Long Alkoxy Chains: Physicochemical Properties and Single-

Walled Carbon Nanotubes' Exfoliation Capability. *ECS J. Solid State Sci. Technol.* **2020**, *9*, 051011.

(90) Darzi, E. R.; White, B. M.; Loventhal, L. K.; Zakharov, L. N.; Jasti, R. An Operationally Simple and Mild Oxidative Homocoupling of Aryl Boronic Esters To Access Conformationally Constrained Macrocycles. *J. Am. Chem. Soc.* **2017**, *139*, 3106–3114.

(91) Van Raden, J. M.; White, B. M.; Zakharov, L. N.; Jasti, R. Nanohoop Rotaxanes from Active Metal Template Syntheses and Their Potential in Sensing Applications. *Angew Chem Int Ed* **2019**, *58*, 7341–7345.

(92) Otteson, C. E.; Levinn, C. M.; Van Raden, J. M.; Pluth, M. D.; Jasti, R. Nanohoop Rotaxane Design to Enhance the Selectivity of Reaction-Based Probes: A Proof-of-Principle Study. *Org. Lett.* **2021**, *23*, 4608–4612. https://doi.org/10.1021/acs.orglett.1c01348.

(93) Schaub, T. A.; Prantl, E. A.; Kohn, J.; Bursch, M.; Marshall, C. R.; Leonhardt, E. J.; Lovell, T. C.; Zakharov, L. N.; Brozek, C. K.; Waldvogel, S. R.; Grimme, S.; Jasti, R. Exploration of the Solid-State Sorption Properties of Shape-Persistent Macrocyclic Nanocarbons as Bulk Materials and Small Aggregates. *J. Am. Chem. Soc.* **2020**, *142*, 8763–8775.

(94) Hermann, M.; Wassy, D.; Esser, B. Conjugated Nanohoops Incorporating Donor, Acceptor, Hetero- or Polycyclic Aromatics. *Angew Chem Int Ed* **2021**, *60*, 15743–15766.

(95) Bruno, N. C.; Tudge, M. T.; Buchwald, S. L. Design and Preparation of New Palladium Precatalysts for C–C and C–N Cross-Coupling Reactions. *Chem. Sci.* **2013**, *4*, 916–920.

(96) Hart, L. F.; Hertzog, J. E.; Rauscher, P. M.; Rawe, B. W.; Et., A. Material Properties and Applications of Mechanically Interlocked Polymers. *Nature Reviews Materials* **2021**.

(97) Zhang, J.; Ma, P. X. Cyclodextrin-Based Supramolecular Systems for Drug Delivery: Recent Progress and Future Perspective. *Advanced Drug Delivery Reviews* **2013**.

(98) Xu, Y.; Kaur, R.; Wang, B.; Minameyer, M. B.; Gsänger, S.; Meyer, B.; Drewello, T.; Guldi, D. M.; von Delius, M. Concave–Convex π–π Template Approach Enables the Synthesis of [10]Cycloparaphenylene–Fullerene [2]Rotaxanes. *J. Am. Chem. Soc.* **2018**, *140*, 13413–13420.

(99) Narita, N.; Kurita, Y.; Osakada, K.; Ide, T.; Kawai, H.; Tsuchido, Y. A Dodecamethoxy[6]Cycloparaphenylene Consisting Entirely of Hydroquinone Ethers: Unveiling in-Plane Aromaticity through a Rotaxane Structure. *Nat Commun* **2023**, *14*, 8091.

(100) Bu, A.; Gao, J.-N.; Chen, Y.; Xiao, H.; Li, H.; Tung, C.-H.; Wu, L.-Z.; Cong, H. Modular Synthesis of Improbable Rotaxanes with All-Benzene Scaffolds. *Angew Chem Int Ed* **2024**, *n/a* (n/a), e202401838.

(101) Aucagne, V.; Hänni, K. D.; Leigh, D. A.; Lusby, P. J.; Walker, D. B. Catalytic "Click" Rotaxanes: A Substoichiometric Metal-Template Pathway to Mechanically Interlocked Architectures. *J. Am. Chem. Soc.* **2006**, *128*, 2186–2187.

(102) Aucagne, V.; Berná, J.; Crowley, J. D.; Goldup, S. M.; Hänni, K. D.; Leigh, D. A.; Lusby, P. J.; Ronaldson, V. E.; Slawin, A. M. Z.; Viterisi, A.; Walker, D. B. Catalytic "Active-Metal" Template Synthesis of [2]Rotaxanes, [3]Rotaxanes, and Molecular Shuttles, and Some Observations on the Mechanism of the Cu(I)-Catalyzed Azide−Alkyne 1,3-Cycloaddition. *J. Am. Chem. Soc.* **2007**, *129* (39), 11950–11963.

(103) Patrick, C. W.; Woods, J. F.; Gawel, P.; Otteson, C. E.; Thompson, A. L.; Claridge, T. D. W.; Jasti, R.; Anderson, H. L. Polyyne [3]Rotaxanes: Synthesis via Dicobalt Carbonyl Complexes and Enhanced Stability. *Angew Chem Int Ed* **2022**, *61*, e202116897.

(104) May, J. H.; Van Raden, J. M.; Maust, R. L.; Zakharov, L. N.; Jasti, R. Active Template Strategy for the Preparation of π-Conjugated Interlocked Nanocarbons. *Nat. Chem.* **2023**, *15*, 170–176.

(105) May, J. H.; Fehr, J. M.; Lorenz, J. C.; Zakharov, L. N.; Jasti, R. A High-Yielding Active Template Click Reaction (AT−CuAAC) for the Synthesis of Mechanically Interlocked Nanohoops. *Angewandte Chemie International Edition* **2024**, *63*, e202401823.

(106) Patrick, C. W. Towards Polyyne Rotaxanes and Catenanes. **2022**.

(107) Patel, V. K.; Kayahara, E.; Yamago, S. Practical Synthesis of [n]Cycloparaphenylenes (N=5, 7–12) by H2SnCl4-Mediated Aromatization of 1,4-Dihydroxycyclo-2,5-Diene Precursors. *Chemistry – A European Journal* **2015**, *21*, 5742–5749.

(108) Fan, Y.-Y.; Chen, D.; Huang, Z.-A.; Zhu, J.; Tung, C.-H.; Wu, L.-Z.; Cong, H. An Isolable Catenane Consisting of Two Möbius Conjugated Nanohoops. *Nat Commun* **2018**, *9*, 3037.

(109) Terabayashi, T.; Kayahara, E.; Zhang, Y.; Mizuhata, Y.; Tokitoh, N.; Nishinaga, T.; Kato, T.; Yamago, S. Synthesis of Twisted [n]Cycloparaphenylene by Alkene Insertion. *Angew Chem Int Ed* **2023**, *62*, e202214960.

(110) Song, J. Y.; Park, S. N.; Lee, S. J.; Kim, Y. K.; Yoon, S. S. Novel Fluorescent Blue-Emitting Materials Based on Anthracene-Fluorene Hybrids with Triphenylsilane Group for Organic Light-Emitting Diodes. *Dyes and Pigments* **2015**, *114*, 40–46.

(111)Zhao, Z.; Yu, S.; Xu, L.; Wang, H.; Lu, P. Novel, Yellow-Emitting Anthracene/Fluorene Oligomers: Synthesis and Characterization. *Tetrahedron* **2007**, *63*, 7809–7815.

(112) Yao, J.; Liu, X.; Li, S.; Pi, M.; Yang, J.; Zhang, D.; Tang, C. W.; Dong, S.-C. Enhancing Operational Lifetime of Blue Organic Light-Emitting Diodes Through Targeted Deuteration of Host Materials. *Advanced Functional Materials* **2026**, *36*, e25930.

(113) Dietrich-Buchecker, C.; Colasson, B.; Fujita, M.; Hori, A.; Geum, N.; Sakamoto, S.; Yamaguchi, K.; Sauvage, J.-P. Quantitative Formation of [2]Catenanes Using Copper(I) and Palladium(II) as Templating and Assembling Centers: The Entwining Route and the Threading Approach. *J. Am. Chem. Soc.* **2003**, *125*, 5717–5725.

(114) Girardot, C.; Lemercier, G.; Mulatier, J.-C.; Andraud, C.; Chauvin, J.; Baldeck, P. L. Novel 5-(Oligofluorenyl)-1,10-Phenanthroline Type Ligands: Synthesis, Linear and Two-Photon Absorption Properties. *Tetrahedron Letters* **2008**, *49*, 1753–1758.

(115) Zhang, W.; Abdulkarim, A.; Golling, F. E.; Räder, H. J.; Müllen, K. Cycloparaphenylenes and Their Catenanes: Complex Macrocycles Unveiled by Ion Mobility Mass Spectrometry. *Angewandte Chemie* **2017**, *129*, 2689–2692.

(116) Dietrich-Buchecker, C.; Sauvage, J.-P. Templated Synthesis of Interlocked Macrocyclic Ligands, the Catenands. Preparation and Characterization of the Prototypical Bis-30 Membered Ring System. *Tetrahedron* **1990**, *46*, 503–512.

(117) Segawa, Y.; Kuwayama, M.; Hijikata, Y.; Fushimi, M.; Nishihara, T.; Pirillo, J.; Shirasaki, J.; Kubota, N.; Itami, K. Topological Molecular Nanocarbons: All-Benzene Catenane and Trefoil Knot. *Science* **2019**, *365*, 272–276.

(118) Fan, Y.-Y.; Chen, D.; Huang, Z.-A.; Zhu, J.; Tung, C.-H.; Wu, L.-Z.; Cong, H. A Conjugated Covalent Template Strategy for All-Benzene Catenane Synthesis. *Nat Commun* **2018**, *9*, 3037.

(119) Steudel, F. M.; Ubasart, E.; Leanza, L.; Pujals, M.; Parella, T.; Pavan, G. M.; Ribas, X.; von Delius, M. Synthesis of C60/[10]CPP-Catenanes by Regioselective, Nanocapsule-Templated Bingel Bis-Addition. *Angew Chem Int Ed* **2023**, *62*, e202309393.

(120) Ubasart, E.; Borodin, O.; Fuertes-Espinosa, C.; Xu, Y.; García-Simón, C.; Gómez, L.; Juanhuix, J.; Gándara, F.; Imaz, I.; Maspoch, D.; Von Delius, M.; Ribas, X. A Three-Shell

Supramolecular Complex Enables the Symmetry-Mismatched Chemo- and Regioselective Bis-Functionalization of C60. *Nat. Chem.* **2021**, *13*, 420–427.

(121) Shi, W.; Hu, Y.; Leanza, L.; Shchukin, Y.; Hoffmann, P. A.; Li, M.; Ning, C.; Cao, Z.; Xu, Y.; Du, P.; Von Delius, M.; Pavan, G. M.; Xu, Y. Ring-in-Ring Assembly Facilitates the Synthesis of a [12]Cycloparaphenylene ABC-Type [3]Catenane. *Angew Chem Int Ed* **2025**, *64*, e202421459.

(122) Ishibashi, H.; Rondelli, M.; Shudo, H.; Maekawa, T.; Ito, H.; Mizukami, K.; Kimizuka, N.; Yagi, A.; Itami, K. Noncovalent Modification of Cycloparaphenylene by Catenane Formation Using an Active Metal Template Strategy. *Angew Chem Int Ed* **2023**, *n/a* (n/a), e202310613.

(123) Fujinaga, M.; Murafuji, T.; Kurotobi, K.; Sugihara, Y. Polyborylation of Azulenes. *Tetrahedron* **2009**, *65*, 7115–7121.

(124) Narita, M.; Murafuji, T.; Yamashita, S.; Fujinaga, M.; Hiyama, K.; Oka, Y.; Tani, F.; Kamijo, S.; Ishiguro, K. Synthesis of 2-Iodoazulenes by the Iododeboronation of Azulen-2-Ylboronic Acid Pinacol Esters with Copper(I) Iodide. *J. Org. Chem.* **2018**, *83*, 1298–1303.